

Polarimetric Modeling of  
Remotely Sensed Scenes in the Thermal Infrared

by

Michael G. Gartley

B.S. Physics, Binghamton University, 1995

M.S. Materials Science and Engineering, Rochester Institute of Technology, 1997

A dissertation submitted in partial fulfillment of the  
requirements for the degree of Doctor of Philosophy  
in the Chester F. Carlson Center for Imaging Science  
Rochester Institute of Technology

May 2007

Signature of the Author \_\_\_\_\_

Accepted by \_\_\_\_\_  
Coordinator, Ph.D. Degree Program Date



CHESTER F. CARLSON CENTER FOR IMAGING SCIENCE  
ROCHESTER INSTITUTE OF TECHNOLOGY  
ROCHESTER, NEW YORK

CERTIFICATE OF APPROVAL

---

Ph.D. DEGREE DISSERTATION

---

The Ph.D. Degree Dissertation of Michael G. Gartley  
has been examined and approved by the  
dissertation committee as satisfactory for the  
dissertation required for the  
Ph.D. degree in Imaging Science

---

Dr. John R. Schott, dissertation Advisor

---

Dr. Carl Salvaggio

---

Dr. Anthony Vodacek

---

Dr. Surrendra Gupta

---

Date



DISSERTATION RELEASE PERMISSION  
ROCHESTER INSTITUTE OF TECHNOLOGY  
CHESTER F. CARLSON CENTER FOR IMAGING SCIENCE

Title of Dissertation:

**Polarimetric Modeling of  
Remotely Sensed Scenes in the Thermal Infrared**

I, Michael G. Gartley, hereby grant permission to Wallace Memorial Library of R.I.T. to reproduce my thesis in whole or in part. Any reproduction will not be for commercial use or profit.

Signature \_\_\_\_\_ Date \_\_\_\_\_



# Polarimetric Modeling of Remotely Sensed Scenes in the Thermal Infrared

by

Michael G. Gartley

Submitted to the  
Chester F. Carlson Center for Imaging Science  
in partial fulfillment of the requirements  
for the Doctor of Philosophy Degree  
at the Rochester Institute of Technology

## Abstract

This dissertation develops a polarimetric thermal infrared (IR) framework within the Digital Image and Remote Sensing Image Generation (DIRSIG) software tool enabling users in the remote sensing community to conduct system level trades and phenomenology studies. To support polarized reflection and emission modeling within DIRSIG, a generalized bi-directional reflectance distribution function (BRDF) is presented. This generalized form is a 4x4 element Mueller matrix that may be configured to resemble the commonly utilized Beard-Maxwell or Priest-Germer BRDF models. A polarized emissivity model is derived that leverages a hemispherical integration of the polarized BRDF and Kirchoff's Law.

A portable experimental technique for measuring polarized long-wave IR emissivity is described. Experimental results for sixteen target and background materials are fit to the polarized emissivity model. The resulting model fit parameters are ingested by DIRSIG to simulate polarized long-wave infrared scene phenomenology.

Thermally emitted radiance typically has a vertical polarization orientation, while reflected background radiance is polarized horizontally. The balance between these two radiance components dictates what polarized signature (if any) is detected for a given target. In general, specular targets have a stronger emission polarization signature compared to diffusely scattering targets consistent with visible polarimetry findings. However, the influence of reflected background radiance can reduce the polarimetric signature of specular targets below a detectable threshold. In these situations, a diffusely scattering target may actually exhibit a polarization signature stronger than a specular target material. This interesting phenomenology is confirmed by experimental scene collections and DIRSIG simulations. Understanding polarimetric IR phenomenology with this level of detail is not only key for system design, but also for determining optimal collection geometries for specific tactical missions.



## Acknowledgements

I would like to thank my research committee members: John Schott, Carl Salvaggio, Tony Vodacek and Vinnie Gupta. My dissertation would not have been possible without your consistent support, feedback and steady guidance. Thank you to Vinnie for supporting me throughout all of my graduate work at RIT. You've taught me core engineering principles that I utilize every day and have been a guiding force for me since 1995. Thank you to Tony for asking the difficult questions - the ones I dreaded but knew I needed to answer. Thanks to Carl for working with me in developing creative solutions to get my experimental technique producing usable results. A special thanks to John Schott who has been patient beyond expectation and relentless in keeping me driven towards results oriented work and focused on finishing. It has been a pleasure and honor to work under the wing of a true leader in the field of remote sensing. Thank you to Joe Pow for lending me his LWIR camera equipment, most of the time on very short notice. Thank you to Cindy Schultz for always keeping me in her radar and helping me stay on top of my academic schedule.

Working with the DIRSIG development team has not only been intellectually stimulating, but also a lot of fun. Scott Brown's technical background and understanding of all things polarimetric was key to getting my simulations accurate. Thanks to Niek Sanders and Adam Goodenough for enthusiastically responding to my nit-picks on how DIRSIG handles hemispherical integration and background sampling, and creating custom builds at a moments notice.

Thanks to my previous and current employers, Bausch & Lomb, Eastman Kodak Company, and ITT Corporation for their continuous financial support.

Most importantly, I would like to thank my family for their unconditional moral support. My mother has always encouraged me to achieve any goal I set my mind to, no matter how long it takes. Thank you to my children Evan and Lila for keeping me smiling and focused on what really matters in life. Thank you to my wonderful wife Karen for always cheering me on, accommodating my chaotic work schedule, and selflessly putting aside her own needs to allow me to "just finish one more thing".



# Contents

Acknowledgements	ix
Table of Contents	xi
List of Figures	xiv
List of Tables	xviii
Definition of Terms	xxi
<b>1 Introduction and Objectives</b>	<b>1</b>
1.1 Introduction . . . . .	1
1.2 Objectives of Work . . . . .	2
1.3 Scope of Work . . . . .	3
1.4 Organization of Dissertation . . . . .	3
<b>2 Theory and Background</b>	<b>5</b>
2.1 Electromagnetic Radiation . . . . .	5
2.1.1 Electromagnetic Radiation as a Wave . . . . .	6
2.1.2 Electromagnetic Radiation as a Particle . . . . .	7
2.2 Blackbody Emission . . . . .	9
2.3 Polarization of Light . . . . .	11
2.3.1 Stoke's Vector . . . . .	13
2.3.2 Mueller Matrices . . . . .	15
2.3.3 Stoke's Vector Measurement . . . . .	16
2.4 Reflection and Emission of Light . . . . .	18
2.4.1 Fresnel Reflection and Transmission . . . . .	19
2.4.2 Real-world Reflection and Transmission . . . . .	23
2.5 Bidirectional Reflectance Distribution Function . . . . .	25
2.5.1 Torrance-Sparrow BRDF . . . . .	27
2.5.2 Beard-Maxwell BRDF . . . . .	29
2.5.3 Priest-Germer Model . . . . .	30

2.6	Theory Summary . . . . .	32
<b>3</b>	<b>Prior Work and Recent Advancements</b>	<b>33</b>
3.1	Polarimetric Emission Measurements . . . . .	33
3.1.1	Jordan and Lewis . . . . .	33
3.1.2	Gurtan and Dahmani . . . . .	35
3.2	Applications of Polarimetric Infrared Imaging . . . . .	38
3.2.1	LWIR Polarimetric Imaging of Space Objects . . . . .	38
3.2.2	Detection of Man-made Objects . . . . .	41
3.3	Chapter Summary . . . . .	46
<b>4</b>	<b>Infrared Radiometry</b>	<b>47</b>
4.1	Review of Radiometric Concepts . . . . .	47
4.2	Atmosphere in the Infrared . . . . .	48
4.3	Material Properties Important in Infrared . . . . .	51
4.4	Governing Radiometric Equation for Infrared . . . . .	52
4.5	Chapter Summary . . . . .	54
<b>5</b>	<b>Polarized BRDF and Emissivity Model</b>	<b>55</b>
5.1	Polarized Specular Component . . . . .	56
5.1.1	Fresnel Mueller Matrix . . . . .	56
5.1.2	Probability Distribution Function . . . . .	61
5.1.3	Shadowing and Obscuration Function . . . . .	63
5.2	Unpolarized Component . . . . .	64
5.3	Effect of Parameters on pBRDF . . . . .	64
5.3.1	Complex index of refraction . . . . .	64
5.3.2	Sigma value . . . . .	66
5.3.3	Shadowing and Obscuration Function Parameters . . . . .	69
5.4	Spectral Interpolation . . . . .	69
5.5	Polarized Emissivity . . . . .	74
5.6	Chapter Summary . . . . .	77
<b>6</b>	<b>Measurement of Polarized Emissivity</b>	<b>81</b>
6.1	Measurement Approach . . . . .	81
6.1.1	Radiometric Framework . . . . .	82
6.1.2	Imaging System Design . . . . .	85
6.1.3	Imaging System Calibration . . . . .	90
6.1.4	Image Collections . . . . .	93
6.1.5	Processing of Image Data . . . . .	95
6.2	Measurement Results . . . . .	107
6.3	Emissivity Model Parameter Fitting . . . . .	115
6.3.1	Parameter Fitting Step 1 . . . . .	115

6.3.2	Parameter Fitting Step 2 . . . . .	116
6.3.3	Parameter Fitting Step 3 . . . . .	117
6.4	Measurement Error and Uncertainty Analysis . . . . .	123
6.4.1	Polarizer Orientation Angle Error . . . . .	123
6.4.2	Camera Calibration Error . . . . .	123
6.4.3	Sample Temperature Assumption Error . . . . .	124
6.4.4	Downwelled Radiance Calculation Error . . . . .	124
6.4.5	Uncertainty due to Foil Perfect Reflector Assumption . . . . .	125
6.4.6	Image Level Noise Uncertainty . . . . .	126
6.4.7	Total Measurement Uncertainty . . . . .	127
6.5	Experimental Summary . . . . .	128
<b>7</b>	<b>DIRSIG Simulations</b>	<b>133</b>
7.1	DIRSIG4 Overview . . . . .	133
7.2	Implementation . . . . .	134
7.3	Verification . . . . .	140
7.3.1	Polarized BRDF . . . . .	140
7.3.2	Polarized DHR . . . . .	141
7.3.3	Background Reflectance Sampling . . . . .	145
7.3.4	Polarization Orientation . . . . .	147
7.3.5	Scene 1 - Backyard Target Range . . . . .	152
7.3.6	Scene 2 - Automobiles . . . . .	156
7.3.7	Scene 3 - Man-made Targets in Natural Background . . . . .	160
7.4	Configuring Materials With Limited Characterization . . . . .	167
7.5	DIRSIG Simulation Summary . . . . .	169
<b>8</b>	<b>Future Work</b>	<b>171</b>
8.1	Polarimetric Thermal IR Imaging System Improvements . . . . .	171
8.2	Midwave IR Phenomenology . . . . .	172
8.3	Generation of Polarized Megascene . . . . .	172
	<b>Appendix</b>	<b>174</b>
<b>A</b>	<b>IDL Source Code for Polarized BRDF</b>	<b>175</b>
<b>B</b>	<b>IDL Source Code for Polarized DHR</b>	<b>179</b>
<b>C</b>	<b>IDL Source Code for Calculating Polarized Emissivity</b>	<b>181</b>
<b>D</b>	<b>Template to configure polarized material in DIRSIG</b>	<b>183</b>
<b>E</b>	<b>Generic Rad Solver Technical Brief</b>	<b>185</b>

<b>F Polarization Orientation Technical Brief</b>	<b>199</b>
<b>G Polarized Emissivity Measurement Procedure</b>	<b>205</b>
G.1 Required Equipment . . . . .	205
G.2 Experimental Technique . . . . .	207
<b>H Detailed Critique of DIRSIG Simulations</b>	<b>211</b>
H.1 Backyard Scene . . . . .	211
H.2 Car Scene . . . . .	214
H.3 B76 Scene . . . . .	216
H.4 Spheres Scene . . . . .	219
H.5 DIRSIG Simulation Differences Summary . . . . .	221
<b>Bibliography</b>	<b>223</b>

# List of Figures

2.1	Illustration of light wave . . . . .	7
2.2	Electromagnetic spectrum . . . . .	8
2.3	Blackbody spectral radiance . . . . .	11
2.4	Illustration of polarization types . . . . .	12
2.5	Comparison of Torrance Sparrow BRDF to experimental data . . . . .	28
2.6	Comparison between Priest-Germer BRDF and experimental data . . . . .	31
3.1	Surface slope distribution for glass . . . . .	34
3.2	DOLP as a function of emission angle . . . . .	35
3.3	Spectral index of refraction for glass . . . . .	36
3.4	Spectral DOLP for glass . . . . .	37
3.5	DOLP for painted glass . . . . .	37
3.6	Simulation of GPS satellite . . . . .	39
3.7	Modeled DOLP for reentry vehicles . . . . .	40
3.8	Polarization images of landmines . . . . .	42
3.9	Polarization images of tripwires . . . . .	43
3.10	Polarization images of landmines in vegetation . . . . .	45
3.11	Polarization images of vehicles in tree shadows . . . . .	45
4.1	Spectral transmission of atmosphere . . . . .	49
4.2	Spectral plot of DOLP of downwelled skydome radiance . . . . .	50
5.1	Polarized BRDF angles relative to macro surface normal . . . . .	58
5.2	Polarized BRDF angles relative to micro-surface normal $\hat{z}_\mu$ and macro-surface normal $\hat{z}$ . . . . .	59
5.3	Plots of Gaussian slope probability functions . . . . .	62
5.4	Plots of Cauchy surface slope probability functions . . . . .	63
5.5	Plots showing effect of index of refraction on pBRDF . . . . .	67
5.6	Plots showing effect of $\sigma$ on pBRDF . . . . .	68
5.7	Plots showing effect of $\sigma$ on pBRDF . . . . .	70
5.8	Plots showing effect of shadowing function on pBRDF . . . . .	71
5.9	Plots showing effect of $\sigma$ on polarized emissivity . . . . .	75

5.10	Plots showing effect of shadowing function on polarized emissivity . . .	76
5.11	Plots showing effect of unpolarized terms on polarized emissivity . . .	77
5.12	Illustration of dominant polarization state for reflected and emitted light	79
6.1	Illustration of relevant radiometric terms . . . . .	83
6.2	EZTherm LWIR camera and IR wire grid polarizer . . . . .	86
6.3	Illustration showing how a wire grid polarizer works . . . . .	88
6.4	Spectral transmission of WGP . . . . .	89
6.5	Illustration of camera and stage alignment . . . . .	90
6.6	LWIR EZTherm camera calibration curve. . . . .	91
6.7	Example of LWIR camera image of blackbody cavity. . . . .	92
6.8	Illustration showing importance of including a diffuse and a glossy calibration target . . . . .	94
6.9	Processing flow for experimentally acquired image data . . . . .	96
6.10	Image examples showing effect of polarizer reflectance . . . . .	98
6.11	Illustration of radiance reaching camera for WGP calibration image acquisition . . . . .	98
6.12	Example of SLAR radiance image . . . . .	99
6.13	Processing paths for Stoke's generated imagery and emissivity measurements . . . . .	100
6.14	Image examples of processed Stoke's radiance bands $S_0$ , $S_1$ , and $S_2$ . . . . .	102
6.15	Image example of targets for emissivity measurement . . . . .	103
6.16	Image example showing regions of interest drawn with the ENVI ROI tool . . . . .	104
6.17	Color photos of natural target materials . . . . .	108
6.18	Color photos of construction target materials . . . . .	108
6.19	Color photos of miscellaneous target materials . . . . .	109
6.20	Polarized emissivity after fitting step 1 . . . . .	115
6.21	Polarized emissivity after fitting steps 2 and 3 . . . . .	116
6.22	Measured and modeled polarized emissivity for bark and brick . . . . .	119
6.23	Measured and modeled polarized emissivity for cement and soil . . . . .	119
6.24	Measured and modeled polarized emissivity for fresh asphalt and flat black paint . . . . .	120
6.25	Measured and modeled polarized emissivity for glossy black paint and glass . . . . .	120
6.26	Measured and modeled polarized emissivity for grass and glossy tan paint . . . . .	121
6.27	Measured and modeled polarized emissivity for car hood and particle board . . . . .	121
6.28	Measured and modeled polarized emissivity for pine and shingle . . . . .	122

6.29	Measured and modeled polarized emissivity for snow and weathered asphalt . . . . .	122
6.30	Plot of modeled and measured polarized emissivity for flat black painted target. The error bars show the calculated level of total measurement uncertainty at the 1-sigma level. . . . .	129
6.31	Plot of modeled and measured polarized emissivity for flat black painted target. The error bars show the calculated level of total measurement uncertainty at the 2-sigma level. . . . .	130
7.1	An example of a DIRSIG image . . . . .	134
7.2	Images of a hot sphere on cold ground . . . . .	138
7.3	Images of cold sphere on hot ground . . . . .	139
7.4	Images of a hot sphere on hot ground . . . . .	140
7.5	Points utilized to verify polarized BRDF . . . . .	141
7.6	DIRSIG simulations showing the effect of a recent code change to incorporate relative orientation of each facet relative to camera coordinates	149
7.7	Measured and DIRSIG images showing a sphere sitting on snow with a glossy plate in front with a sun elevation of 18 degrees . . . . .	150
7.8	Measured and DIRSIG images showing a sphere sitting on snow with a glossy plate in front at night under a starry sky . . . . .	151
7.9	Illustration of target placement for Scene 1 . . . . .	152
7.10	Digital camera photo of backyard target range . . . . .	153
7.11	Measured and DIRSIG images of backyard target scene . . . . .	154
7.12	Illustration of target placement for Scene 1 with pool . . . . .	155
7.13	Measured and DIRSIG images of backyard scene with pool behind targets	156
7.14	Digital camera image of three automobiles utilized for test scene . . . . .	157
7.15	Measured and DIRSIG images of cars . . . . .	159
7.16	Digital camera photo of man made targets placed in the open away from trees. . . . .	160
7.17	Illustration of target placement for Scene 3 with targets out in the open	161
7.18	Measured and DIRSIG $S_0$ images of targets outside B76 . . . . .	162
7.19	Measured and DIRSIG $S_1$ images of targets outside B76 . . . . .	163
7.20	Digital camera photo of man made targets placed within a grove of trees.	164
7.21	Illustration of target placement for Scene 3 with targets embedded in cluster of trees . . . . .	165
7.22	Measured and DIRSIG $S_0$ images of targets outside B76 . . . . .	166
7.23	Measured and DIRSIG $S_1$ images of targets outside B76 . . . . .	166
E.1	The data matrix for an arbitrary BRDF model . . . . .	193
E.2	The result of non-negative factorization of $Y$ into $G$ (left) and $F$ (right) using $J\_RANK = 8$ . . . . .	194

E.3	10,000 samples from the model with the given BRDF data and using an exitant vector at $45^\circ$ . . . . .	195
E.4	Reconstructions of the original BRDF data matrix after using increasing J_RANK values (a-d). Note that the 32x3 (JxK) rank reconstruction is almost identical to the original. . . . .	196
F.1	Illustration of global coordinates, facet normal, incident and exitant ray directions. . . . .	201
F.2	Illustration showing projection of facet normal into ray s-p plane. . . . .	202
G.1	Photo of camera and polarizer stage . . . . .	206
G.2	Photo of sample stage with tip-tilt capability . . . . .	206
G.3	Photo of sample stage loaded with material samples and foil targets . . . . .	207
G.4	Photo of tripod (without camera and polarizer loaded), sample stage with targets, and foil placed behind stage to reflect sky . . . . .	208
H.1	Comparison of DIRSIG and measured thermal IR images of targets in backyard scene . . . . .	212
H.2	Comparison of DIRSIG and measured thermal IR images of targets in backyard scene with a kiddie pool behind them . . . . .	212
H.3	Comparison of DIRSIG and measured thermal IR images of three automobiles on asphalt . . . . .	214
H.4	Comparison of DIRSIG and measured thermal IR images of Building 76 target scene . . . . .	216
H.5	Comparison of DIRSIG and measured thermal IR images of Building 76 target scene with targets embedded in trees . . . . .	217
H.6	Comparison of DIRSIG and measured thermal IR images of spheres during the day . . . . .	219
H.7	Comparison of DIRSIG and measured thermal IR images of spheres at night . . . . .	220

# List of Tables

2.1	Index of refraction for a variety of dielectric materials . . . . .	23
2.2	Description of Beard-Maxwell Functions and Inputs . . . . .	29
4.1	Thermal conductivity values for a few materials[41] . . . . .	51
4.2	Specific heat capacity values[39] . . . . .	52
6.1	LWIR camera calibration curve data points in degrees F. . . . .	92
6.2	Table of SLAR radiance values . . . . .	105
6.3	Table of SLAR Stoke's vector components . . . . .	105
6.4	Table of Stoke's emissivity values . . . . .	106
6.5	Polarized emissivity results for tree bark . . . . .	108
6.6	Polarized emissivity results for brick . . . . .	110
6.7	Polarized emissivity results for cement . . . . .	110
6.8	Polarized emissivity results for soil . . . . .	110
6.9	Polarized emissivity results for fresh asphalt . . . . .	111
6.10	Polarized emissivity results for flat black paint . . . . .	111
6.11	Polarized emissivity results for glossy black paint . . . . .	111
6.12	Polarized emissivity results for glass . . . . .	112
6.13	Polarized emissivity results for grass . . . . .	112
6.14	Polarized emissivity results for glossy tan paint . . . . .	112
6.15	Polarized emissivity results for a car hood . . . . .	113
6.16	Polarized emissivity results for particle board . . . . .	113
6.17	Polarized emissivity results for a pine board . . . . .	113
6.18	Polarized emissivity results for roofing shingle . . . . .	114
6.19	Polarized emissivity results for snow . . . . .	114
6.20	Polarized emissivity results for weathered asphalt . . . . .	114
6.21	Summary of polarized BRDF parameters that produce a polarized emissivity best fit to experimentally measured emissivity. . . . .	118
6.22	Downwelled skydome radiance reflected from a perfect infrared reflec- tor as a function of surface roughness $\sigma$ . . . . .	125

7.1	Comparison of DIRSIG and IDL DHR results for a flat black painted surface . . . . .	143
7.2	Comparison of DIRSIG and IDL DHR results for a smooth 100% reflecting surface . . . . .	144
7.3	Comparison of DIRSIG and IDL DHR results for a glossy black painted surface . . . . .	145
7.4	Comparison of DIRSIG and IDL integration of reflections from background hemisphere from a cold target surface. . . . .	148

## Nomenclature

The following tables provide a list of the variables and acronyms utilized in this document. The acronyms are listed alphabetically. The variables are arranged alphabetically starting with English letters, followed by greek letters.

Acronym	Description
BB	BlackBody
BRDF	Bidirectional Reflectance Distribution Function
DIRSIG	Digital Image and Remote Sensing Image Generation
DOLP	Degree Of Linear Polarization
DOP	Degree Of Polarization
IR	InfraRed
LWIR	Long Wave InfraRed
MODTRAN	MODerate resolution radiative TRANsfer model
MODTRAN-P	Polarized MODTRAN
MWIR	Mid Wave InfraRed
NEDT	Noise Equivalent Delta Temperature
SLAR	Surface leaving, aperture reaching
WGP	Wire Grid Polarizer

Symbol	Description	Units
$B$	Bias parameter of probability distribution function	-
$c$	Speed of light	$m/s^2$
$E$	Irradiance	$\frac{W}{cm^2}$
$f_{BM}$	Beard-Maxwell BRDF function	$sr^{-1}$
$f_{PG}$	Priest-Germer BRDF function	$sr^{-1}$
$f_{pBRDF}$	Polarized ShellTarget DIRSIG BRDF	$sr^{-1}$
$f_{TS}$	Torrance-Sparrow BRDF function	$sr^{-1}$
$L$	Radiance	$\frac{W}{cm^2 sr}$
$L_{100}$	Aperture reaching radiance from an IR reflector	$\frac{W}{cm^2 sr}$
$L_{BB}$	Blackbody badiance	$\frac{W}{cm^2 sr}$
$L_{EAR}$	Entrance aperture reaching radiance	$\frac{W}{cm^2 sr}$
$L_{dw}$	Downwelled radiance	$\frac{W}{cm^2 sr}$
$L_{meas}$	Measured radiance	$\frac{W}{cm^2 sr}$
$L_{SLAR}$	Surface leaving, aperture reaching radiance	$\frac{W}{cm^2 sr}$
$L_{uw}$	Upwelled radiance	$\frac{W}{cm^2 sr}$
$M$	Mueller matrix	-
$\tilde{n}$	Complex index of refraction	-
$r_p$	Fresnel parallel reflectance coefficient	-
$r_s$	Fresnel perpendicular reflectance coefficient	-
$\vec{S}$	Stokes vector	-
$S_0$	Total intensity component of Stokes vector	-
$S_1$	Linearly polarized Stokes component ( $I_0 - I_{90}$ )	-
$S_2$	Linearly polarized Stokes component ( $I_{45} - I_{135}$ )	-
$t_p$	Fresnel parallel transmission coefficient	-
$t_s$	Fresnel perpendicular transmission coefficient	-
$\alpha$	Polarizer rotation angle	Deg
$\epsilon$	Emissivity	-
$\lambda$	Wavelength	$\mu m$
$\Omega$	Shadowing function adjustment parameter	-
$\psi$	Digital protractor measurement angle	Deg
$\rho$	Reflectivity	-
$\rho_{DHR}$	Directional hemispherical reflectivity	-
$\rho_D$	Diffuse reflectivity	-
$\rho_p$	Reflectivity of polarizer	-
$\rho_V$	Volume reflectivity	-
$\tau$	Shadowing function adjustment parameter	-
$\tau_p$	Transmission of polarizer	-
$\theta_i$	Incident zenith angle	Deg
$\theta_N$	Zenith angle of a microfacet relative to surface normal	Deg
$\theta_r$	Reflected zenith angle	Deg

# Chapter 1

## Introduction and Objectives

### 1.1 Introduction

Remote sensing is a discipline primarily focused on measuring material properties from a distance. Originally, remote sensing systems were air or spaceborne, film based camera systems designed to capture monochrome photographs in the visible region of the electromagnetic spectrum. During World War I, remote sensing flourished as a method of gaining military intelligence. These airborne instruments were able to capture photographs of areas where access was denied by conventional land based assets.

Since World War I, remote sensing has evolved dramatically from monochrome film cameras to multispectral and hyperspectral digital collection systems. Passive imaging is common in the visible region, near infrared (IR), short wave infrared, mid wave infrared and long wave infrared regions of the spectrum. Exploitation of the spectral nature of scene reflections and thermally emitted radiance has aided analysts in characterizing the environment, defeating enemy denial and deception tactics, and detecting critical target signatures to name a few.

Most recently, the remote sensing community has explored systems equipped to

collect polarized image data. Although most naturally occurring materials do not have a significant polarimetric signature [28] (except for water), many man made materials indeed do. Remote sensing polarimetry has demonstrated value in many areas such as astronomy [30], man made target cueing[23], decoy discrimination[20], and surface land mine detection[8] to name a few.

Given the growing level of interest the remote sensing community has in polarimetry, it follows that there should be a scene simulation tool to aid in system level design trades and algorithm development work. Currently there is no rigorous scene modeling tool for simulating infrared polarimetric scenes available to the community. This dissertation work is meant to address this need by working with the DIRSIG team to equip the Digital Imaging and Remote Sensing Image Generation (DIRSIG) tool with such a capability.

## 1.2 Objectives of Work

The primary objective of this work is to equip DIRSIG with the capability to accurately model remotely sensed scenes imaged with polarimetric infrared imaging systems. Specific tasks include:

1. Design, assemble, and test an infrared imaging system with polarization measurement capability.
2. Develop an experimental technique to measure polarized emissivity curves for a wide variety of man-made and naturally occurring materials.
3. Identify a suitable polarized thermal emission model that exists and can be integrated into DIRSIG in order to enable accurate polarimetric infrared scene simulations.
4. Verify the DIRSIG capability against experimentally acquired image data.

## 1.3 Scope of Work

This dissertation is meant to investigate polarization in the longwave region (8-14 microns) of the electromagnetic spectrum. Although data will not be acquired in the midwave region (3-5 microns), the experimental method and model implementation described here is believed to be applicable for midwave polarization.

In addition, the modeling and experimental collections within this work are focused only on measuring linear polarization. Although circular polarization may be present to an extent in some scenes with man-made objects, the minimal intelligence value that circular polarization detection adds does not warrant inclusion into system design and modeling efforts at this time.

Throughout this work, we consider all materials to have a surface texture that is azimuthally isotropic. This is an acceptable assumption for most man-made and naturally occurring materials of interest in a remotely sensed scene.

Finally, every effort has been made to thermally stabilize target and background materials before experimental collections were performed. We therefore make the assumption that all materials are thermally stable during a single polarization measurement (typically lasting 15-20 seconds). However the error introduced by a temperature drift is considered in the error and uncertainty analysis portion of the work.

## 1.4 Organization of Dissertation

Chapter 2 presents polarimetry from an introductory physics point of view. This theoretical background is followed by an overview of prior work and recent advancements in IR Polarimetry in Chapter 3.

Chapter 4 extends introductory polarimetry presented in Chapter 2 to more advanced radiometric concepts. Specifically this chapter will cover properties of the atmosphere in the IR and major sources of radiance in this region of the spectrum.

The conclusion of this chapter will present a polarized version of the governing radiometric equation in the IR.

Chapter 5 describes the chosen polarized emissivity model in detail. Chapter 6 details the experimental collection system design, measurement method, and data analysis technique utilized to fit to the polarized emissivity model.

Previous works [29][17] have developed a framework within DIRSIG to handle polarized radiometry in the visible region of the spectrum. Chapter 7 describes how this framework will be extended to support rendering scenes polarimetrically in the IR region of the spectrum and the results of a comparison of modeled and actual thermal IR images.

# Chapter 2

## Theory and Background

This chapter presents a brief description of electromagnetic radiation and how it interacts with matter. Section 2.1 describes the nature of electromagnetic radiation from a historical context, specifically how it has both particle-like and wave-like properties. Section 2.2 presents the theory behind thermal emission of electromagnetic radiation as described by the Planck blackbody equation. Section 2.3 goes beyond the amplitude and wavelength properties of light and examines the polarization nature of light. Section 2.4 describes how electromagnetic radiation behaves upon striking a material interface. Section 2.5 describes how empirical bi-directional reflectance distribution functions and emissivity models can produce accurate and computationally efficient results utilizing the physics-based theory presented in Section 2.4.

### 2.1 Electromagnetic Radiation

Electromagnetic radiation is characterized by its wavelength, its amplitude (or intensity), and its polarization state.

### 2.1.1 Electromagnetic Radiation as a Wave

As early as the late 17th century, physicists such as Robert Hooke and Christian Huygens theorized that visible light was a wave [27]. Their theory predicted this wave-like nature could enable light to interfere with itself, which was confirmed by Thomas Young and his famous double-slit experiment in the 18th century. Thomas Young also proposed that each color of visible light had a characteristic wavelength.

Throughout the 19th century, Physicists found success treating light as a plane wave propagating through space. In 1845, Michael Faraday experimentally found the polarization state of light could be altered by a magnetic field [27]. This effect is nowadays referred to as Faraday rotation. Faraday's work sparked James Clerk Maxwell to investigate and learn that visible light was actually just a form of radiation possessing both an electric and a magnetic field propagating through free space at a constant speed [10]. In 1873, Maxwell published his theory of the behavior of electromagnetic radiation that is now referred to as Maxwell's equations of electromagnetism. Maxwell proposed the constant speed of light  $c$  could be expressed in terms of the permittivity  $\epsilon_0$  and permeability  $\mu_0$  of free space. The constant  $c$  is  $2.9979 \cdot 10^8$  meters/second, while the permittivity and permeability of free space are  $8.85412 \cdot 10^{-12}$  farads/meter and  $4\pi \cdot 10^{-7}$  henries/meter respectively.

$$c = \frac{1}{\sqrt{\epsilon_0 \mu_0}} \quad (2.1)$$

Electromagnetic radiation was described as a solution to Maxwell's equations, having the general form [10]

$$\vec{E}(z, t) = A e^{\omega t + \vec{k} \cdot \vec{z} + \phi} \quad (2.2)$$

where  $A$  is the magnitude of the electric field,  $\omega$  is the angular frequency,  $\vec{k}$  is the wave vector,  $t$  is time,  $\vec{z}$  is the direction of propagation, and  $\phi$  is a constant representing

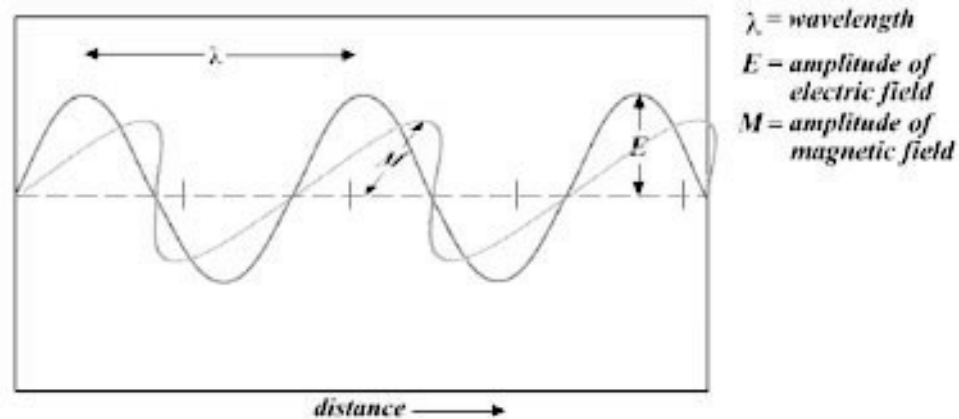


Figure 2.1: Illustration of a light wave propagating through space[40].

a phase shift. The angular frequency and wave vector are related by the following relationship.

$$|k| = \frac{\omega}{c} = \frac{2\pi}{\lambda} \quad (2.3)$$

Figure 2.1 shows an illustration of the alternating electric and magnetic fields that are a solution to Maxwell's equations. The figure is reproduced from reference [40].

Maxwell's equations verified that visible light, radio waves, and infrared radiation were all forms of electromagnetic radiation. What distinguished these different forms of radiation was their wavelength. Figure 2.2 summarizes the various forms of electromagnetic radiation as a function of wavelength. This figure is from reference [35].

### 2.1.2 Electromagnetic Radiation as a Particle

Although the wave theory of light received a significant amount of experimental success in the 17th and 18th centuries, one experimental anomaly did not fit the theory. Scientists were perplexed by the photoelectric effect, which showed that light incident on a metal surface produced a current flow across an applied voltage gap [27]. The understanding was that the light was ejecting electrons from the metal surface

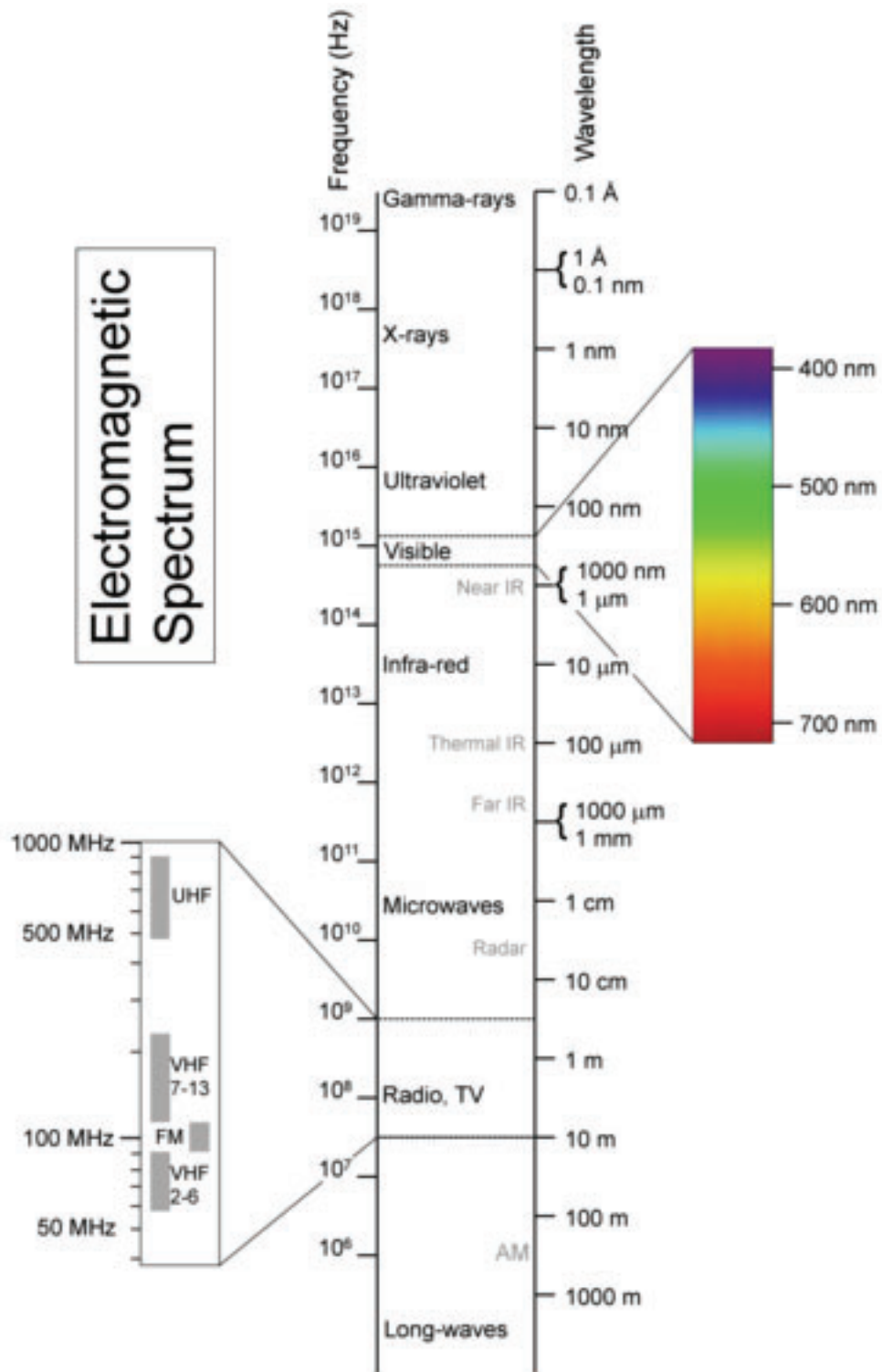


Figure 2.2: The electromagnetic spectrum [35].

and the voltage was inducing a current flow across a gap. What puzzled scientists was that the maximum energy of the ejected electrons was not proportional to the intensity of the light incident on the metal surface, but inversely proportional to the wavelength of the light.

In 1905 Albert Einstein was able to explain the photoelectric effect by treating light as coming in discrete units of energy he termed *light quanta* [27]. In 1923, the Compton effect experimentally showed light behaving again as particles confirming Einstein's earlier particle description. Einstein's continued work led to the concept of an elementary particle known as the *photon*. A photon possesses a characteristic wavelength and energy. The wavelength  $\lambda$  is in units of distance and is related to its frequency  $f$  and the speed of light  $c$  by the equation

$$f\lambda = c \tag{2.4}$$

This combination of experimental results provided physicists with the notion that not only electromagnetic radiation, but all matter, possesses both wave-like and particle-like properties. In 1924 deBroglie hypothesized that any piece of matter has a characteristic wavelength, the deBroglie wavelength given by

$$\lambda_D = \frac{h}{p} \tag{2.5}$$

where  $\lambda$  is the wavelength,  $h$  is Planck's constant and  $p$  is the momentum of the piece of matter.

## 2.2 Blackbody Emission

In 1862, Gustov Kirchoff coined the term *blackbody* to describe an object that reflects no light. Although a blackbody material was not known to exist naturally at the time,

experimentalists could approximate the behavior of a blackbody by a cavity having a small aperture. Light entering the cavity would have to bounce around several times before having a chance of exit, therefore forcing almost every photon entering the cavity to be absorbed before having a chance to exit.

In 1900, Max Planck was able to empirically derive a formula describing the radiation exiting the blackbody cavity [27]. This formula related the intensity of the radiation to the temperature of the blackbody cavity. In order to derive this empirical formula from a first principles point of view, Planck had to envision that the cavity was filled with a finite number of oscillators each having a quantized value of energy. This quantized value of energy (in units of Joules) was written by Planck as

$$E = hf = \frac{hc}{\lambda} \quad (2.6)$$

From Planck's derivation came Planck's law of blackbody radiation.

$$I(f, T) = \frac{2hf^3}{c^2(e^{hf/kT} - 1)} \quad (2.7)$$

which has units of Joules per unit time per steradian per unit of frequency. An alternate form of the Planck blackbody equation [26] is written in terms of radiance

$$L(\lambda, T) = \frac{2hc^2}{\lambda^5} \frac{1}{e^{\frac{hc}{\lambda kT}} - 1} \quad (2.8)$$

which has units of  $\frac{W}{cm^2 sr \mu m}$ . Figure 2.3 shows a few examples of blackbody radiance (Equation (2.8)), as a function of temperature and wavelength. The spectral radiant output of the sun is commonly approximated by a 5800K blackbody curve.

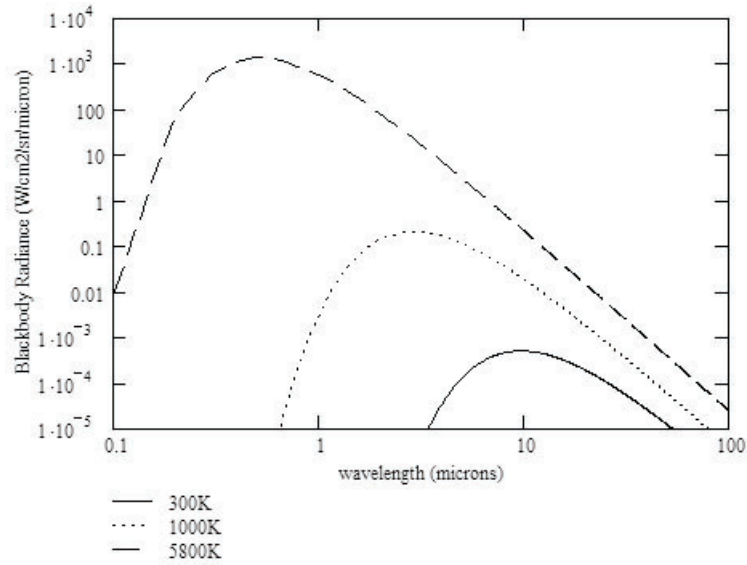


Figure 2.3: Spectral radiance output from blackbodies at 5800K (dashed) 1000K (dotted) and 300K (solid).

## 2.3 Polarization of Light

In addition to amplitude and wavelength, another distinguishing characteristic of light is its polarization state. The polarization state of a transverse light wave is the direction of oscillation of the electric field, in the plane perpendicular to the direction of motion. If we follow the convention described above for coordinate axes, the  $\hat{x}$  and  $\hat{y}$  directions are in the plane perpendicular to the direction of travel,  $\hat{z}$ .

When the  $\vec{x}$  and  $\vec{y}$  component of the electric field oscillate completely in phase, this is known as *linear polarization*. When the  $\vec{x}$  and  $\vec{y}$  components oscillate with the same amplitude and are exactly 90 degrees out of phase, this is known as *circular polarization*. Finally, if the  $\vec{x}$  and  $\vec{y}$  components satisfy neither of the previous two cases, the resulting polarization state is known as elliptical polarization, in that the shape traced in the x-y plane through a full oscillation cycle is an ellipse. Figure 2.4 demonstrates each of these three polarization states. This figure is reprinted from reference [38].

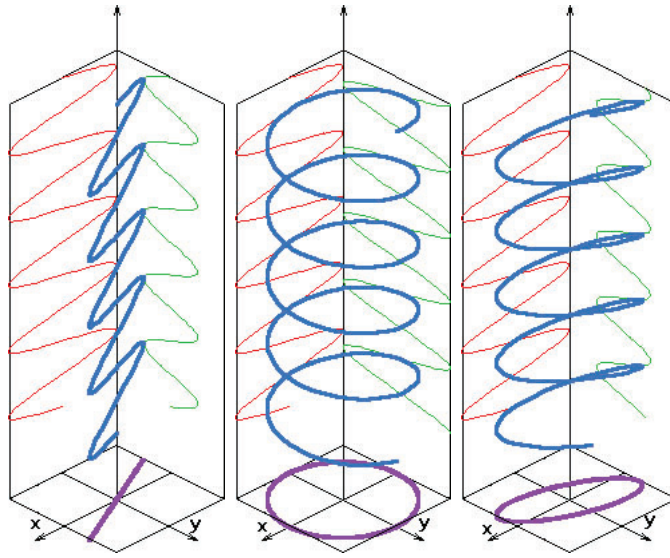


Figure 2.4: Illustration showing linear (left), circular (middle), and elliptical (right) polarization states [38]

Everyone encounters some form of light polarization when they are outside during the daytime. The light coming down from the skydome has a characteristic polarization due to the Rayleigh scattering of sunlight through the atmosphere [14]. However, the downwelled skydome light is only partially polarized.

Another example of naturally occurring light polarization is when light is reflected from the surface of water. The reflected light is linearly polarized and can be reduced by sunglasses that serve as polarization filters. This is why fishermen prefer polarized sunglasses, because it allows them to block out most of the reflected light from the water's surface and see into the water better. The level of polarization of light reflected from water can be much greater than that of the downwelled skydome light.

This leads us to make a distinction between the polarization state of coherent and incoherent light. Although coherent light can have the property of being 100% polarized in one state, it is rarely encountered in remote sensing applications.

Incoherent light is a combination of electromagnetic radiation possessing multiple phase values, wavelength values and polarization states. The overall polarization state

of incoherent light must be described by a formalism that supports partial, linear, circular and elliptical polarization states.

### 2.3.1 Stoke's Vector

In 1852, George Gabriel Stokes developed a system for describing the polarization state of incoherent radiation [10]. The system involved replacing scalar radiation intensity values with 4 element column vectors. These column vectors are commonly referred to as Stoke's vectors.

$$\vec{S} = \begin{pmatrix} S_0 \\ S_1 \\ S_2 \\ S_3 \end{pmatrix} \quad (2.9)$$

For a given amount of incoherent radiation, a Stoke's vector contains the total electromagnetic radiation intensity incident onto an imaging system in the 1st element,  $S_0$ . The light intensity may be represented by the magnitude of the electric field vector, irradiance, radiance, or any other radiometric quantity. For our description, we will present the Stoke's vector in terms of the quantity irradiance (defined in Chapter 4). The  $S_0$  irradiance element is proportional to the square of the magnitude of the electric field vector described previously, and can be expressed in terms of observed irradiance as

$$S_0 = E_x + E_y \quad (2.10)$$

The  $S_1$  element is defined as the difference between polarization in the  $\hat{x}$  direction and  $\hat{y}$  degree direction. A positive value of  $S_1$  describes light that is more polarized in the  $\hat{x}$  direction, while a negative value describes light that is more polarization in the  $\hat{y}$  direction.

$$S_1 = E_x - E_y \quad (2.11)$$

To aid in describing the  $S_2$  element, we refer to the direction that is halfway between  $+\hat{x}$  and  $+\hat{y}$  as the  $\hat{a}$  direction and the direction that is halfway between  $-\hat{x}$  and  $+\hat{y}$  as the  $\hat{b}$  direction. Sometimes the  $\hat{x}$ ,  $\hat{y}$ ,  $\hat{a}$ , and  $\hat{b}$  directions are also known as the 0, 90, 45, and 135 degree directions respectively. Sometimes the  $\hat{x}$  and  $\hat{y}$  directions are referred to as the horizontal and vertical directions respectively. No matter what nomenclature is utilized, care must be taken to properly define the orientation of these axes relative to some master coordinate system (such as Earth Center Fixed).

$$S_2 = E_a - E_b \quad (2.12)$$

The  $S_2$  element contains the amount of polarization that exists in either the  $\hat{a}$  or  $\hat{b}$  directions. A positive value of  $S_2$  indicates preferential polarization in the  $\hat{a}$  direction, while a negative value indicates a preferential polarization in the  $\hat{b}$  direction.

The  $S_3$  element of the Stoke's vector contains the amount of circular polarization. A positive value of  $S_3$  indicates more left circular polarization, while a negative value indicates a more right circular polarization value.

$$S_3 = E_{rc} - E_{lc} \quad (2.13)$$

Other quantities may be derived from this four element Stoke's vector. The *degree of polarization* (DOP) is commonly utilized and is expressed as

$$DOP = \frac{\sqrt{S_1^2 + S_2^2 + S_3^2}}{S_0} \quad (2.14)$$

Monochromatic coherent light has the property that  $DOP = 100\%$ , while incoherent light has  $DOP < 100\%$ .

Another common value that is derived from the 4-element Stoke's vector is the

*degree of linear polarization* (DOLP) and is given by

$$DOLP = \frac{\sqrt{S_1^2 + S_2^2}}{S_0} \quad (2.15)$$

### 2.3.2 Mueller Matrices

Just as the 4 element Stoke's vector replaces scalar radiometric quantities, the 4x4 Mueller matrix replaces scalar transmission and reflectivity values. A generic Mueller matrix is given by equation (2.16).

$$M = \begin{pmatrix} m_{00} & m_{10} & m_{20} & m_{30} \\ m_{01} & m_{11} & m_{21} & m_{31} \\ m_{02} & m_{12} & m_{22} & m_{32} \\ m_{03} & m_{13} & m_{23} & m_{33} \end{pmatrix} \quad (2.16)$$

The Mueller matrix operates on an input Stoke's vector to produce an output Stoke's vector, demonstrated by equation (2.17).

$$\vec{S}_{out} = M\vec{S}_{in} \quad (2.17)$$

The Mueller matrix for transmission of light through a linear polarizer oriented at an angle  $\theta$  to the horizontal direction is written as

$$M(\theta) = \frac{1}{2} \begin{pmatrix} 1 & \cos(2\theta) & \sin(2\theta) & 0 \\ \cos(2\theta) & \cos^2(2\theta) & \cos(2\theta)\sin(2\theta) & 0 \\ \sin(2\theta) & \cos(2\theta)\sin(2\theta) & \sin^2(2\theta) & 0 \\ 0 & 0 & 0 & 0 \end{pmatrix} \quad (2.18)$$

The following four equations show the exact Mueller matrix values for perfect

linear polarizers oriented at angles of 0, 90, 45, and 135 degrees.

$$M(0^\circ) = \frac{1}{2} \begin{pmatrix} 1 & 1 & 0 & 0 \\ 1 & 1 & 0 & 0 \\ 0 & 0 & 0 & 0 \\ 0 & 0 & 0 & 0 \end{pmatrix} \quad (2.19)$$

$$M(90^\circ) = \frac{1}{2} \begin{pmatrix} 1 & -1 & 0 & 0 \\ -1 & 1 & 0 & 0 \\ 0 & 0 & 0 & 0 \\ 0 & 0 & 0 & 0 \end{pmatrix} \quad (2.20)$$

$$M(45^\circ) = \frac{1}{2} \begin{pmatrix} 1 & 0 & 1 & 0 \\ 0 & 0 & 0 & 0 \\ 1 & 0 & 1 & 0 \\ 0 & 0 & 0 & 0 \end{pmatrix} \quad (2.21)$$

$$M(135^\circ) = \frac{1}{2} \begin{pmatrix} 1 & 0 & -1 & 0 \\ 0 & 0 & 0 & 0 \\ -1 & 0 & 1 & 0 \\ 0 & 0 & 0 & 0 \end{pmatrix} \quad (2.22)$$

In addition to transmission, Mueller matrices are also utilized to quantify reflection of polarized light at an interface. The mathematics of how these reflection Mueller matrices are arrived at are presented in Chapter 5.

### 2.3.3 Stoke's Vector Measurement

There are various methods utilized to measure the Stoke's vector for light incident onto a camera focal plane. Some methods might involve multiple cameras, each

equipped with a unique polarization filter, pointed at the same object. Other methods utilize a single camera with an adjustable filter or filter wheel in front of the camera aperture. No matter which camera approach is utilized, multiple frames of data utilizing multiple filter orientations and types must be utilized in order to generate a Stoke's vector representation of a scene.

One combination of polarization filters aims at determining both the linear and circular polarization state, namely the  $S_1$ ,  $S_2$ , and  $S_3$  components of the Stoke's vector. This can be achieved by imaging a scene with a combination of polarization filters that includes a 50% neutral density filter, 2 linear polarizers and a circular polarizer. Let the irradiance values detected at the focal plane corresponding to each filter be denoted by  $I_{ND}$ ,  $I_0$ ,  $I_{45}$ , and  $I_{rc}$ . The resulting Stoke's vector can be assembled by the following combinations of intensity bands.

$$S_0 = 2I_{ND} \quad (2.23)$$

$$S_1 = 2I_0 - 2I_{ND} \quad (2.24)$$

$$S_2 = 2I_{45} - 2I_{ND} \quad (2.25)$$

$$S_3 = 2I_{rc} - 2I_{ND} \quad (2.26)$$

This approach is attractive, in that it allows one to fill out the entire Stoke's vector given only four measurements. However, in signal starved situations, one can take advantage of a series of four linear polarizer orientations at the expense of not being able to measure circular polarization. In most polarimetric remote sensing applications this is an acceptable trade.

Utilizing either a single rotatable linear polarizer, or a series of 4 linear polarizers oriented at angles of 0, 45, 90, and 135 degrees relative to the plane of incidence of the camera, permits calculation of the linear polarization elements of the Stoke's

vector. Let us assume that the sensed irradiance values through the 0, 45, 90, and 135 degree filter orientations are given by  $I_0$ ,  $I_{45}$ ,  $I_{90}$ , and  $I_{135}$ . The Stoke's vector may be calculated as follows.

$$S_0 = \frac{1}{2}(I_0 + I_{90} + I_{45} + I_{135}) \quad (2.27)$$

$$S_1 = I_0 - I_{90} \quad (2.28)$$

$$S_2 = I_{45} - I_{135} \quad (2.29)$$

$$S_3 = 0 \quad (2.30)$$

Although the  $S_0$  element can be calculated utilizing only  $S_0 + S_{90}$  or  $S_{45} + S_{135}$ , noisy scenes show benefit from summing all four intensity bands. However it should be noted that good intensity band to intensity band registration is required, otherwise summing all four bands instead of only two will result in a  $S_0$  image with increased blur. It should also be noted that the  $S_0$  through  $S_2$  bands can be derived from a series of only 3 linear polarizer orientations (0deg, 60deg, and 120deg). However the signal to noise performance of the resulting Stoke's images utilizing only three orientations is inferior to utilizing the above mentioned series of 4 polarizer orientations.

## 2.4 Reflection and Emission of Light

Passive remote sensing applications rely on reflected and thermally emitted radiance from scene surfaces. Daytime collections utilize the sun and skydome as sources to illuminate the scene. Nighttime collections commonly utilize the moon and man-made lights as sources of irradiance. Remote sensing in the short and mid-wave regions of the electromagnetic spectrum take advantage of both reflected radiance and thermally emitted radiance, while long wave infrared collections rely primarily on thermally emitted radiance. Modeling of thermally emitted blackbody radiance

was covered previously in Section 2.3.

Kirchoff's law of thermal radiation[10] states that for a given amount of incident radiance, any radiance that is not reflected or transmitted through the material is absorbed and then thermally emitted. Kirchoff's law assumes the object is in thermal equilibrium. His law is a conservation of energy written in terms of reflectivity, transmission and emissivity.

$$\tau(\lambda) + \rho(\lambda) + \epsilon(\lambda) = 1 \quad (2.31)$$

Now that we understand the energy conservation relationship existing between transmission, reflection and emission, we need to understand how these quantities are determined.

### 2.4.1 Fresnel Reflection and Transmission

One of the most straightforward reflection models is the Fresnel reflection model. Fresnel reflection theory utilizes the material property known as *index of refraction*. The index of refraction of a material is the scale factor by which the propagation of electromagnetic radiation slows down relative to the speed of light in a vacuum  $c$ . The index of refraction is written as

$$n = \sqrt{\frac{\epsilon_1 \mu_1}{\epsilon_0 \mu_0}} \quad (2.32)$$

where  $\epsilon_1$  and  $\mu_1$  are the permittivity and permeability of the material respectively. The quantity  $\epsilon$ , not to be confused with emissivity, is also referred to as the *dielectric constant* of a material.

The speed of light in the material is then given by

$$v = \frac{c}{n} \quad (2.33)$$

For most materials, the index of refraction is complex and wavelength dependent. The complex index of refraction is written as

$$\tilde{n} = n - i\kappa \quad (2.34)$$

where  $n$  is the index of refraction as defined above in equation 2.32 and  $\kappa$  is referred to as the material's *extinction coefficient*, and  $i = \sqrt{-1}$ . The spectral nature of the index of refraction is what causes light dispersion into its spectral components when going through a prism.

Fresnel's law of reflectance assumes that light is incident onto a perfectly flat surface of complex index of refraction  $\tilde{n}$ . The zenith angle  $\theta_i$  the incident light makes with the surface normal is equal to the zenith angle  $\theta_r$  that the reflected angle makes with the surface normal. However the angle of the transmitted light is different and given by the well known *Snell's Law*,

$$\tilde{n}_i \sin \theta_i = \tilde{n}_t \sin \theta_t \quad (2.35)$$

where  $\tilde{n}_i$  is the index of refraction of the medium the light is incident from and  $\tilde{n}_t$  is the index of refraction of the material the light transmits into.

An interesting situation, known as *total internal reflection*, occurs when the light moves from a high index of refraction material to a low index of refraction material. When the light is incident on this high-to-low interface, there is a critical angle for which light will no longer transmit through the interface and all light will be reflected from it. This critical angle is given by,

$$\theta_c = \sin^{-1}\left(\frac{\tilde{n}_{high}}{\tilde{n}_{low}}\right) \quad (2.36)$$

where  $\tilde{n}_{high}$  and  $\tilde{n}_{low}$  are the index of refraction of the high and low index of refraction

materials respectively.

The *Fresnel Equations* define the magnitude of the light transmitted and reflected as a function of the complex index of refraction of both materials. The Fresnel equations express the magnitude of light in terms of the  $s$  and  $p$  components of the electric field. The  $s$  component refers to the component of the electric field that is perpendicular to the plane of incidence, where the plane of incidence is defined as the plane containing the incident ray vector and the surface normal vector. The  $p$  component is the component of the electric field that is parallel to the plane of incidence. Therefore, the Fresnel equations are inherently polarimetric in their treatment of reflection and transmission.

The magnitude of the  $s$  and  $p$  components of the reflectance are given by,

$$r_s(\theta_i) = \frac{2\tilde{n}_i \cos \theta_i}{\tilde{n}_i \cos \theta_i + \sqrt{\tilde{n}_t^2 - \tilde{n}_i^2 \sin^2 \theta_i}} \quad (2.37)$$

$$r_p(\theta_i) = \frac{2\tilde{n}_i \tilde{n}_t \cos \theta_i}{\tilde{n}_t^2 \cos \theta_i + \tilde{n}_i \sqrt{\tilde{n}_t^2 - \tilde{n}_i^2 \sin^2 \theta_i}} \quad (2.38)$$

while the  $s$  and  $p$  components of transmission are given by,

$$t_s(\theta_i) = \frac{\tilde{n}_i \cos \theta_i - \sqrt{\tilde{n}_t^2 - \tilde{n}_i^2 \sin^2 \theta_i}}{\tilde{n}_i \cos \theta_i - \sqrt{\tilde{n}_t^2 + \tilde{n}_i^2 \sin^2 \theta_i}} \quad (2.39)$$

$$t_p(\theta_i) = \frac{\tilde{n}_t^2 \cos \theta_i - \tilde{n}_i \sqrt{\tilde{n}_t^2 - \tilde{n}_i^2 \sin^2 \theta_i}}{\tilde{n}_t^2 \cos \theta_i + \tilde{n}_i \sqrt{\tilde{n}_t^2 - \tilde{n}_i^2 \sin^2 \theta_i}} \quad (2.40)$$

where the angle  $\theta_t$  has been replaced by  $\sqrt{\tilde{n}_t^2 - \tilde{n}_i^2 \sin^2 \theta_i}$  via Snell's law.

These above magnitudes correspond to the electric field, however the energy of light is actually proportional to the square of the electric field. Therefore, the quantities we are interested in for modeling reflection in remote sensing applications are given by,

$$\rho_s = r_s^2 \quad (2.41)$$

$$\rho_p = r_p^2 \quad (2.42)$$

$$\tau_s = t_s^2 \quad (2.43)$$

$$\tau_p = t_p^2 \quad (2.44)$$

A more common form of the Fresnel equations breaks the complex index of refraction down into its real and imaginary components, makes the assumption that the incident medium is air ( $n = 1$ ), and the assumption that the permeability of the air and target material are essentially the same. These two assumptions are known to be valid for most remote sensing applications. The Fresnel equations now reduce to

$$\rho_s(\theta_i) = \frac{(A - \cos \theta_i)^2 + B^2}{(A + \cos \theta_i)^2 + B^2} \quad (2.45)$$

$$\rho_p(\theta_i) = \rho_s \frac{(A - \sin \theta_i \tan \theta_i)^2 + B^2}{(A + \sin \theta_i \tan \theta_i)^2 + B^2} \quad (2.46)$$

where the quantities  $A$  and  $B$  are given by

$$A = \sqrt{\frac{\sqrt{4n^2\kappa^2 + (n^2 - \kappa^2 - \sin^2 \theta_i)^2} + n^2 - \kappa^2 - \sin^2 \theta_i}{2}} \quad (2.47)$$

$$B = \sqrt{\frac{\sqrt{4n^2\kappa^2 + (n^2 - \kappa^2 - \sin^2 \theta_i)^2} - n^2 + \kappa^2 + \sin^2 \theta_i}{2}} \quad (2.48)$$

Some common values of index of refraction for various dielectric materials (materials having  $\kappa = 0$ ) are given in the table below. These values are reprinted from Reference [36].

Table 2.1: Index of refraction for a variety of dielectric materials

<i>Material</i>	$n@λ = 589nm$
Vacuum	1 (exactly)
Air @ STP	1.0002926
Water Ice	1.31
Liquid Water (20C)	1.333
Teflon	1.35 - 1.38
Acrylic glass	1.490 - 1.492
Rock salt	1.516
Crown glass (pure)	1.50 - 1.54
Salt (NaCl)	1.544
Polycarbonate	1.584 - 1.586
Flint glass (pure)	1.60 - 1.62
Crown glass (impure)	1.485 - 1.755
Flint glass (impure)	1.523 - 1.925
Diamond	2.419
Gallium(III) phosphide	3.5
Gallium(III) arsenide	3.927
Silicon	4.01

### 2.4.2 Real-world Reflection and Transmission

As stated in the previous section, Fresnel reflectance equations assume a perfectly flat material surface. Although not perfectly flat, materials such as glass, glossy plastics, and still water are close enough for Fresnel equations to predict reflection and transmission magnitudes and directions. Reflectance that is well modeled by the Fresnel equations is often referred to as *specular reflectance*. In addition, the term *specular direction* is sometimes utilized and refers to the direction dictated by Fresnel reflectance. The specular direction refers to a reflected zenith angle that is equal to the incident zenith angle and has an azimuth angle exactly 180 degrees relative to the incident light.

However, most materials that are imaged in remote sensing applications are not perfectly flat. Most materials have a surface roughness that may be on the scale of microns, centimeters, inches or even meters. In many cases, surface roughness actually

exists on many scales of measurement. For example, plowed soil has both a millimeter scale roughness due to individual soil particles and a meter scale roughness due to plowing. Another example that is commonly modeled as having roughness on two scales is ocean water. One scale is on the order of meters and takes into consideration waves and another roughness scale considers the froth that exists on wave crests.

In terms of reflection, a *Lambertian surface* is completely the opposite of a specular surface. A Lambertian surface has no specularly reflected component and reflects radiance equally in all directions in the hemisphere above its surface. Lambertian surfaces are also sometimes referred to as *perfectly diffuse* surfaces.

In the preceding example of Fresnel reflectance, the reflectance magnitude was completely determined based upon the optical properties of the materials and the angle of incidence. In addition, the reflected energy is only directed in the plane of incidence at the reflected angle,  $\theta_r$ , where  $\theta_r = \theta_i$  per the law of reflection. However, this is only true for perfectly planar or smooth surfaces which also have no internal scatter. A quick look around is all it takes to realize that most surfaces are not perfect mirror surfaces, and even mirror surfaces are not perfect. Also obvious is the fact that objects have color different than the illumination source, which is not accounted for by the Fresnel equations.

In addition to first surface scattering, there is also *volume scattering* that occurs in many materials of interest in remote sensing applications. Volume scattering occurs when light is transmitted initially through the surface and then is scattered internally within the material and reflected back out through the surface again. The random nature of the light bouncing around inside a material and then exiting the surface forces volume scattered light to have no preferential polarization state (randomly polarized). For a more detailed description of the physical mechanisms involved in volume scattering, the reader is referred to Shell (2005)[29].

## 2.5 Bidirectional Reflectance Distribution Function

As described in the previous section, the reflectance of a surface is dependent upon its bulk material properties and surface texture (or roughness). The bidirectional reflectance distribution function (BRDF) is a common metric within the remote sensing community. For a given incident irradiance direction, the BRDF describes what fraction of the incident irradiance is scattered into any solid angle within the hemisphere above a surface per unit solid angle. The BRDF is defined as the ratio of the scattered radiance to the incident irradiance as a function of incident and reflected angles by [26]

$$\rho(\theta_i, \phi_i, \theta_r, \phi_r, \lambda) = \frac{dL(\theta_r, \phi_r, \lambda)}{dE(\theta_i, \phi_i, \lambda)} \quad (2.49)$$

where  $\rho(\theta_i, \phi_i, \theta_r, \phi_r, \lambda)$  is the BRDF,  $dL(\theta_r, \phi_r, \lambda)$  is the reflected radiance, and  $dE(\theta_i, \phi_i, \lambda)$  is the incident irradiance. This quantity has units of inverse steradians. The incident irradiance can be expressed in terms of the incident radiance as [26]

$$dE(\theta_i, \phi_i, \lambda) = dL(\theta_i, \phi_i, \lambda) \cos \theta_i d\omega_i \quad (2.50)$$

where  $\omega_i$  is the solid angle within which the incident irradiance is contained.

The directional hemispherical reflectance (DHR) of a surface is defined as the ratio of the total energy reflected into the entire hemisphere above a sample surface to the total energy incident from a particular direction. DHR is a function of incident zenith angle, incident azimuth angle, and wavelength.

$$\rho_{DHR}(\theta_i, \phi_i, \lambda) = \int \rho(\theta_i, \phi_i, \theta_r, \phi_r, \lambda) \cos \theta_r d\omega_r \quad (2.51)$$

For the purpose of this dissertation, the assumption is made that all material surfaces are azimuthally symmetric. This means that instead of specifying both a  $\phi_i$  and  $\phi_r$  angle, we can simply specify a relative azimuthal angle between the

incident and reflected directions  $\Delta\phi$ . This assumption allows us to rewrite how we parameterize the BRDF function as  $\rho(\theta_i, \theta_r, \Delta\phi, \lambda)$ .

In addition, we can express the above integral in a form that puts the integration into terms of zenith and azimuthal angle as follows,

$$\rho_{DHR}(\theta_i, \phi_i, \lambda) = \int_0^{2\pi} \int_0^{\pi/2} \rho(\theta_i, \theta_r, \Delta\phi, \lambda) \cos \theta_r \sin \theta_r d\theta_r d\phi \quad (2.52)$$

. Recall that perfectly diffuse Lambertian reflectors have no angle dependence to the reflectance function. This results in a simple expression for Lambertian BRDF in terms of the DHR,

$$\rho(\theta_i, \theta_r, \Delta\phi, \lambda) = \rho(\lambda) = \frac{\rho_{DHR}}{\pi}. \quad (2.53)$$

For perfectly reflecting materials, the DHR is equal to 1 by definition.

Utilizing Kirchoff's law of thermal radiation, the emissivity of a material can be expressed in terms of the diffuse hemispherical reflectance (assuming the material does not transmit any light).

$$\epsilon(\theta_i, \lambda) = 1 - \int_0^{2\pi} \int_0^{\pi/2} \rho(\theta_i, \theta_r, \Delta\phi, \lambda) \cos \theta_r \sin \theta_r d\theta_r d\phi \quad (2.54)$$

$$= 1 - \rho_{DHR}(\theta_i, \lambda) \quad (2.55)$$

.

Now that the BRDF quantity has been defined, the following sub-sections introduce specific forms of the BRDF commonly utilized in remote sensing applications. For the remainder of the text, we utilize the variable  $f$  to denote a BRDF quantity that is model specific.

### 2.5.1 Torrance-Sparrow BRDF

K.E. Torrance and E.M. Sparrow wrote an important paper in 1967 [31] that described how one might model surface reflectivity away from the specular peak. In fact, slightly rough surfaces actually show a peak in reflectivity that is *not* in the specular direction. Explaining this off-specular peak appeared to be the motivation for Torrance and Sparrow to introduce the concept of combining a diffuse and a specular reflection term into a single model.

The Torrance and Sparrow model makes the geometric optics assumption, namely that the majority of the surface roughness occurs on a scale much larger than the wavelength of light scattered from it. This eliminates the need to model diffractive interference at the scattering interface.

This model makes the assumption that a rough surface is simply a super-position of small "mirror-like" surfaces that are oriented at various angles relative to the overall surface normal. In fact, they modeled the probability of finding such a surface at an angle  $\alpha$  from the surface normal as a Gaussian,

$$P(\alpha) = be^{-c^2\alpha^2} \quad (2.56)$$

where  $c$  is a constant related to the amount of surface roughness and  $b$  is a scale factor. A larger value of  $c$  corresponds to a larger relative surface roughness.

The Torrance and Sparrow BRDF takes the form,

$$f_{TS} = \frac{F(\theta'_i, \tilde{n})A_f G(\theta_{ip}, \theta_{rp})P(\alpha)}{4 \cos \theta_i \cos \theta_r} + \frac{a}{d\omega_i} \quad (2.57)$$

where  $A_f$  is the area of a facet,  $d\omega$  is the reflected solid angle,  $\theta'_i$  is the angle of incidence relative to a local facet normal, and  $\theta_{ip}$  and  $\theta_{rp}$  are angles relating the angle of incidence, angle of reflection, surface and facet normals. The reader is referred to the original paper for a description of how to calculate these two angles. The

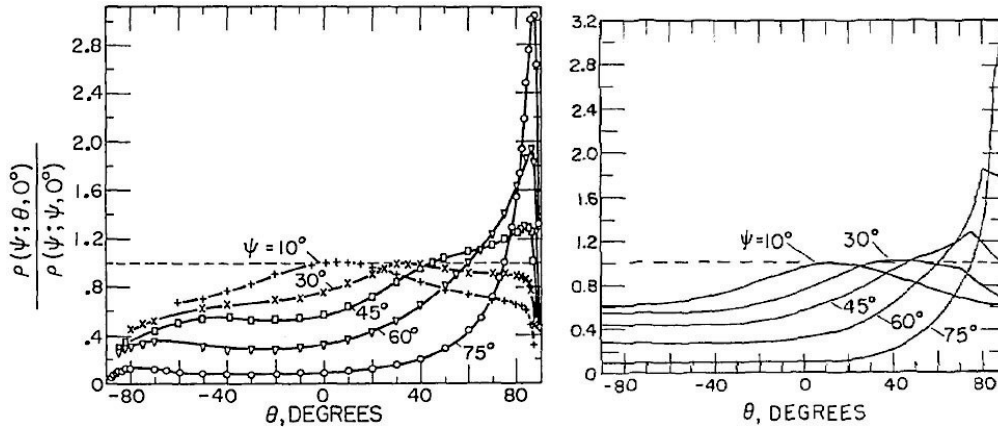


Figure 2.5: Comparison of experimental (left) BRDF measurements of Aluminum and the modeled BRDF (right). The variables  $\psi$  and  $\theta$  correspond to the zenith angles of incidence and reflection[31].

function  $G$  is an attenuation factor that considers shadowing of reflected radiance and masking of incident radiance due to the facet distribution. The function  $F$  is the Fresnel reflectance for an angle of incident given by  $\theta'_i$  for a material of complex index of refraction  $\tilde{n}$ . The constant  $a$  in the volume term represents the fraction of the incident radiance that is scattered diffusely and is given by

$$a = \frac{L_i}{L_r \cos \theta_i} \quad (2.58)$$

The plots in Figure 2.5 demonstrate the agreement found by the authors between their BRDF model and experimentally measured results. The authors utilize the variable  $\psi$  to describe the zenith angle of incidence and the angle  $\theta$  to describe the reflected zenith angle. For the plots in Figure 2.5, the authors plot the BRDF in the specular plane ( $\phi_i = \phi_r + \pi$ ) normalized by the BRDF value at the specular direction ( $\psi = \theta$  or  $\theta_i = \theta_r$ ). The Torrance and Sparrow BRDF model was able to capture the off-specular reflectance peak phenomenon introduced by surface roughness.

Another commonly utilized, physics-based BRDF model was developed by Beard and Maxwell.

Table 2.2: Description of Beard-Maxwell Functions and Inputs

variable	description
$f_{BM}$	total BRDF
$R(\beta, n, k)$	Fresnel reflection coefficient for angle $\beta$ and index of refraction $n - ik$
$\beta$	specular angle relative to normal of surface scattering element
$BRDF_{FS}$	first surface BRDF based on experimental measurements
$\theta_N$	zenith of scattering element relative to the material surface normal
$\theta_i$	incident direction zenith angle
$\theta_r$	reflected direction zenith angle
$\phi_i$	incident direction azimuth angle
$\phi_r$	reflected direction azimuth angle
SO	shadowing and obscuration function
$\rho_D$	diffuse scattering parameter
$\rho_V$	volumetric scattering parameter
$n - ik$	complex index of refraction of material
$\sigma$	mean square value of the total slope at a point on the surface
$B$	facet normal distribution BIAS parameter
$\Omega, \tau$	parameters for shadowing and obscuration model

### 2.5.2 Beard-Maxwell BRDF

The non-conventional exploitation factors (NEF) database [18] is a software package commonly utilized by people in the remote sensing community for modeling surface reflectance and emission properties. The NEF database contains material properties at visible and infrared wavelengths for a wide variety of man-made and some naturally occurring materials. The NEF database utilizes a modified version of the BRDF model[16] published by Beard and Maxwell in 1973.

The NEF implementation of the Beard-Maxwell BRDF has the functional form

$$f_{BM}(\theta_i, \phi_i, \theta_r, \phi_r) = R(\beta, n, k) \frac{BRDF_{FS}(\theta_N) \cos^2(\theta_N)}{R(0, n, k) \cos(\theta_i) \cos(\theta_r)} SO(\beta, \theta_N, \tau, \Omega) + \rho_D + \frac{2\rho_V}{\cos(\theta_I) + \cos(\theta_R)} \quad (2.59)$$

The input parameters and functions are described in table 2.5.2. The function  $BRDF_{FS}(\theta_N)$  is a measurement based quantity utilized to experimentally derive the

$\tau$  and  $\Omega$  parameters for the shadowing and obscuration function.

$$\overline{BRDF}_{FS}(\theta_N) = \frac{R(0, n, k)B}{4 \cos^3(\theta_N)(\sigma^2 + \tan^2(\theta_N))} \quad (2.60)$$

Substituting equation (2.60) back into equation (2.59), the NEF implementation of the Beard-Maxwell BRDF is written as

$$f_{BM}(\theta_i, \phi_i, \theta_r, \phi_r) = \frac{R(\beta, n, k)B}{4 \cos(\theta_i) \cos(\theta_r)} \frac{SO(\beta, \theta_N, \tau, \Omega)}{\cos(\theta_N)(\sigma^2 + \tan^2(\theta_N))} + \rho_D + \frac{2\rho_V}{\cos(\theta_I) + \cos(\theta_R)} \quad (2.61)$$

where the shadowing and obscuration function  $SO$  is expressed in terms of the parameters  $\tau$  and  $\Omega$  and dependent on the angles  $\beta$  and  $\theta_N$ . The shadowing and obscuration takes on the functional form

$$SO(\beta, \theta_N, \tau, \Omega) = \frac{1 + \frac{\theta_N}{\Omega} e^{-2\beta/\tau}}{1 + \frac{\theta_N}{\Omega}} \quad (2.62)$$

It should be noted that the NEF database includes a diffuse, Lambertian-like, scattering term  $\rho_d$  not included in the original Beard-Maxwell model. Inclusion of this term demonstrated a better fit between the model and experimental measurement results for the it's developers.

Although the Beard-Maxwell model is inherently polarized by the Fresnel reflectance term, the authors (and the NEF database adaptation) does not take advantage of this feature. Therefore, a BRDF model that is inherently polarized and does indeed leverage the polarization is needed.

### 2.5.3 Priest-Germer Model

In 2000, Richard Priest and Thomas Germer [21] introduced a BRDF model similar in nature to the Beard-Maxwell and Torrance-Sparrow models. However, their model

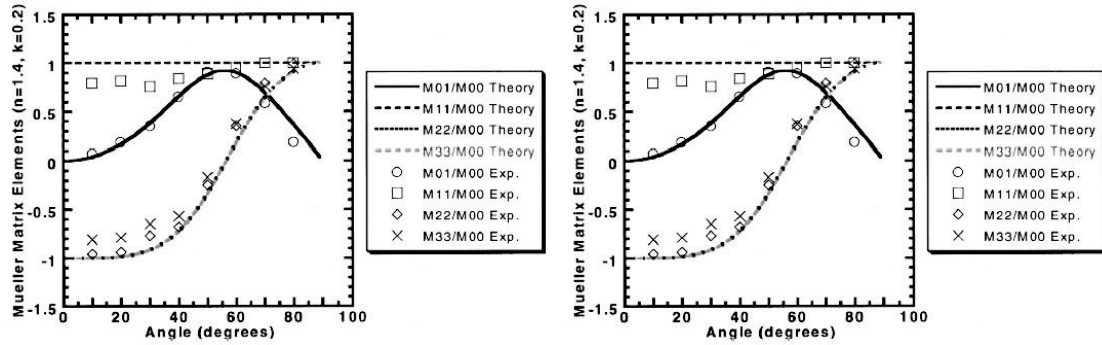


Figure 2.6: Agreement between Priest-Germer BRDF model and experimental measurements for a low reflectivity sample (left) and high reflectivity sample (right) [21]

utilizes a 4x4 element Mueller matrix for the Fresnel scattering factor in order to predict a polarized BRDF. The Priest-Germer model takes the form

$$f_{PG}(\theta_i, \theta_r, \Delta\phi) = \frac{1}{2\pi} \frac{1}{4\sigma^2} \frac{1}{\cos^4 \theta} \frac{e^{-(\tan^2 \theta / 2\sigma^2)}}{\cos \theta_i \cos \theta_r} M(\theta_i, \theta_r, \Delta\phi) \quad (2.63)$$

where  $\sigma$  is a surface roughness parameter,  $\theta$  is a derived angle presented later in equation 5.10, and  $M_{j,k}$  is the 4x4 element Mueller scattering matrix based on the  $s$  and  $p$  Fresnel reflection coefficients. The components of the Mueller matrix are derived in Chapter 6.

One advantage of this BRDF model is its simplicity. The only parameters it required as inputs (besides scattering angles) are the complex index of refraction of the scattering material and the slope variance  $\sigma$  of the material's surface roughness. Another advantage of this model is they have derived all of the functions required to fully determine the polarization state of reflected radiance.

In 2002, Germer published a paper showing agreement between his model and experimental polarimetric measurements of a low reflectivity and high reflectivity sample. The agreement between the model and measurements are shown in the Figure 2.6.

## 2.6 Theory Summary

This chapter has presented an overview of important discoveries in optics and how they contributed to the wave and particle theories of light. The wave theory of light is relevant to this work, in that the Fresnel reflection equations are based on it. The particle theory of light is also vital in understanding the scientific basis for blackbody radiation, another key aspect to modeling in the infrared.

Next, the concept of polarization was introduced and described utilizing the Stoke's vector formalism. Although not directly measurable, the Stoke's radiance vector is easily derived from a series of intensity measurements leveraging multiple polarizer orientation angles.

Finally, the concept of a BRDF was presented in order to address the need for this dissertation to describe optical scattering from real-world surfaces. Relevant BRDF models are described leading up to the development of a more generalized BRDF (Chapter 4). The equations utilized to compute a directional emissivity from the BRDF are also derived in order to support a polarized emissivity model.

# Chapter 3

## Prior Work and Recent Advancements

Although rare, polarimetric IR imaging related topics have received some attention in the literature over the past 20 years. The experimental and theoretical work in polarimetric IR spans a range of applications, including but not limited to: astronomy[30], observations of space objects[20], characterization of polarized material emissivity[11, 12], target cueing[24], and decoy discrimination.

### 3.1 Polarimetric Emission Measurements

Various authors have published on their experimental methods and results in the area of emission polarization. This section briefly reviews a few papers relevant to my dissertation.

#### 3.1.1 Jordan and Lewis

In 1994, Jordan and Lewis published a paper[11] outlining their experimental measurement of the emission polarization from glass and aluminum. Their work focused

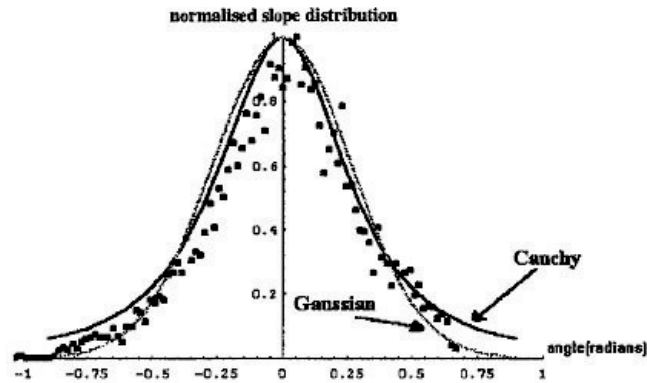


Figure 3.1: Measured surface slope distribution for a roughened glass sample

primarily on the wavelength region of 10 to 11 microns, dictated by their optical coatings and detector spectral response.

Jordan and Lewis examined both smooth and sand-blasted versions of aluminum and glass, mounted to a thermal bath to maintain a sample temperature of approximately 70C. The intent of heating the sample was to keep the thermally emitted radiance level well above the ambient radiance that might be reflected from the sample surfaces. A combination of a rotatable linear polarizer and a quarter wave plate enabled measurements of all 4 stokes parameters ( $S_0$ ,  $S_1$ ,  $S_2$ , and  $S_3$ ).

The surface roughness was measured utilizing a Talysurf surface profilometer. The surface surface slope distributions for each sample were found to lie in between a Gaussian and a Cauchy distribution (see Figure 3.1).

The authors found the  $S_2$  and  $S_3$  Stoke's components of the thermally emitted radiance to be zero within the noise level of the measurements. The partial polarization of all samples showed the  $S_1$  radiance to always be negative, indicative of a partial  $p$  polarization.

In 1996, the same authors published another paper[12] utilizing the same polarized emission results. However this paper utilized an active technique to measure the complex index of refraction of their materials at 10.6 microns. In addition this followup paper developed a model to estimate polarized emissivity of a material given

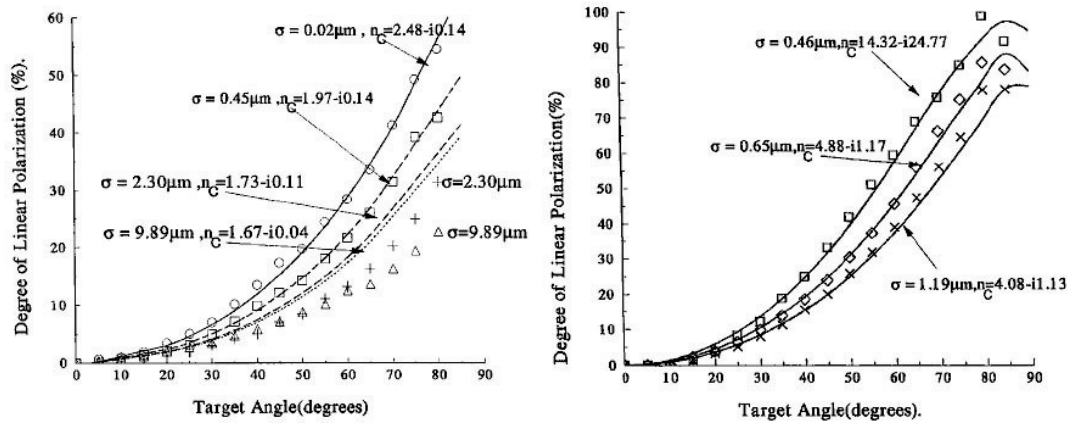


Figure 3.2: DOLP as a function of emission angle for various glass (left) and aluminum (right) surfaces

the (1) complex index of refraction and (2) rms surface slope distribution as inputs. Figure 3.2 is taken from this work and shows excellent agreement between their model and the experimental results. The model is not presented here, but the reader is directed to the publication[12] for further details.

### 3.1.2 Gurtan and Dahmani

Gurtan and Dahmani published a paper in 2005 describing their experimental work in the area of emission polarization. This work is interesting because the authors built a polarimetric FTIR spectrometer, enabling polarized spectral measurements. The FTIR instrument was outfitted with a wire grid polarizer and a quarter wave retarder plate. This spectrometer configuration enabled measurement of all 4 Stoke's vector components between 4.5 and 13.0 microns.

The primary material examined by Gurtan and Dahmani was borosilicate glass. Included in their work was the complex index of refraction ( $n$  and  $k$ ) values, over the same wavelength range (see Figure 3.3) the FTIR covered, to facilitate evaluating a simple Fresnel model.

In order to examine the effect of surface roughness on the emission polarization,

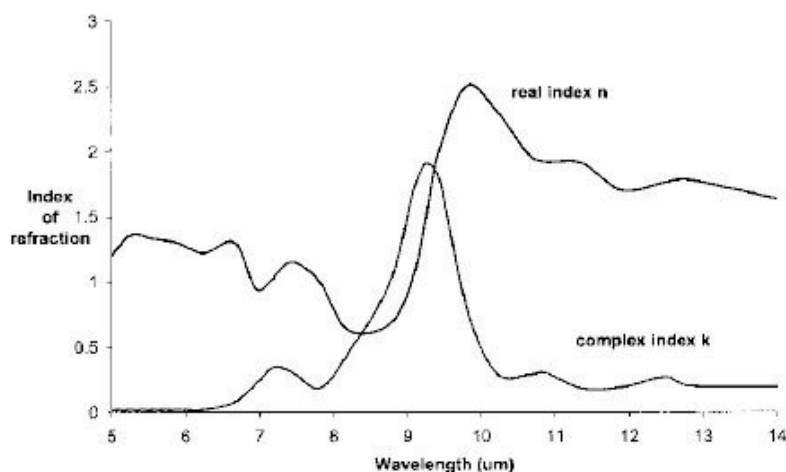


Figure 3.3: Index of refraction for borosilicate glass between 4.5 and 13.0 microns

the author's sandblasted glass samples to various degrees. In addition to glass, they measured a Krylon Black paint coating and a CARC green paint coating on smooth borosilicate glass substrates. The degree of roughness was quantified by a surface profilometer. From the profilometer traces, the authors calculated root-mean-square (rms) surface roughness ( $R_a$ ) and rms surface slope roughness of all surfaces they examined. The authors found the rms surface slope distribution to follow a Gaussian distribution.

The polarized emission measurements showed that for all materials, the  $S_2$  and  $S_3$  components of the emitted stoke's radiance vector was zero to within the noise of the measurement. For the smooth glass samples, the author's found excellent agreement between measurement and Fresnel predicted degree of emission polarization (see Figure 3.4). However this agreement was only reported at one wavelength (9.5 microns), so it is not known how well the agreement was over the entire spectral range measured.

The emission polarization measurements were taken for emission angles between 10 and 80 degrees. The authors found  $\leq 2\%$  DOLP for all samples at an emission angle of 10 degrees. However the DOLP reached about 55% for the smooth glass

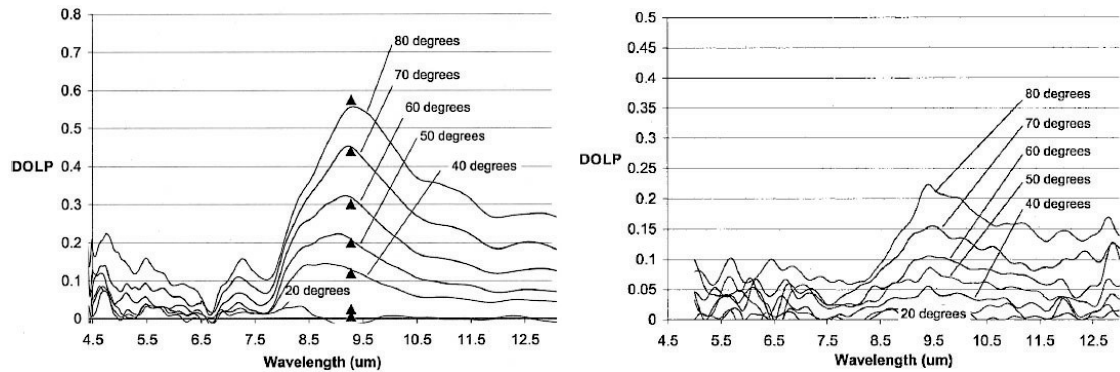


Figure 3.4: DOLP as a function of wavelength and emission angle for smooth (left) and moderately rough (right) surfaces

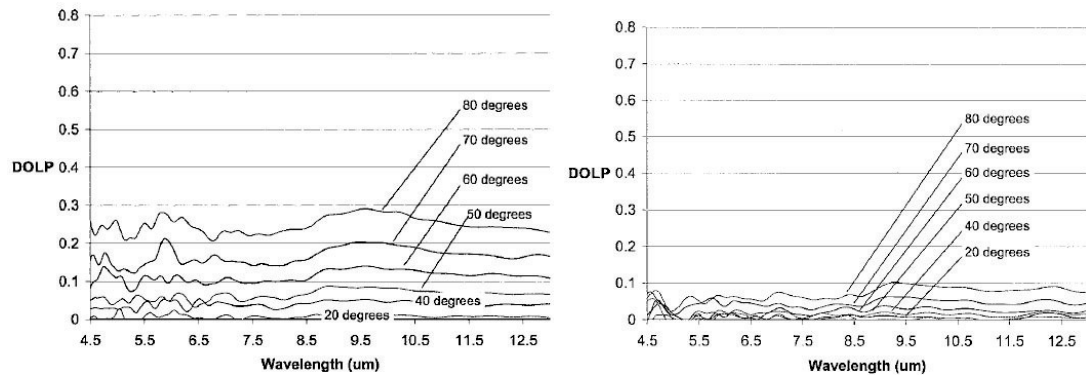


Figure 3.5: DOLP as a function of wavelength and emission angle for Krylon black coated (left) and CARC green coated (right) glass surfaces

sample at an emission angle of 80 degrees, and around 20% for all 3 of their sand-blasted glass samples. The CARC green painted glass sample showed almost no emission polarization at most emission angles (max 8% @ 80 degrees). The Krylon black painted sample showed an emission polarization increasing to about 25% at the max emission angle of 80 degrees.

## 3.2 Applications of Polarimetric Infrared Imaging

This section of Chapter 3 reviews a few examples of work intended to explore how polarimetric infrared imaging may be applied to operational scenarios.

### 3.2.1 LWIR Polarimetric Imaging of Space Objects

Mark Pesses and John Tan are researchers that have published work [20] on polarimetric simulation of space objects in the long-wave infrared. The intent of the work was to examine the potential utility of polarimetric LWIR imaging versus unpolarized LWIR imaging. The authors utilized SAIC's 3-D LWIR spectropolarimetric signature model called *Polar Heat*.

The first utility example presented was polarimetric images of a spinning GPS satellite vehicle. The images were rendered utilizing a CAD model of a GPS spacecraft containing over 10,000 individual facets. The solar array panels were assumed to be constructed of quartz glass, while the surface of the spacecraft bus and antennas were assumed to be constructed of aluminum and silver respectively. The authors compared the utility of  $S_0$ , DOLP, and  $S_0/S_1$  image products to aid in exploitation of the GPS spacecraft images (see Figure 3.6). It was found that the DOLP image products showed the largest level of contrast as the GPS spacecraft spun, potentially providing more information to an image analyst looking to solve an intelligence problem.

Pesses and Tan also examined the case of imaging small objects in low earth orbit and objects in geosynchronous orbit. In both of these cases, the spacecraft cannot be spatially resolved. However, they generated a time varying polarimetric signature model that algebraically added together the polarization effects of all portions of the target into one signal. A preliminary analysis showed that for space object identification, the polarimetric rotation signature will be more useful than the current hyperspectral rotation signatures. However, the authors did not back up this claim.

Finally, Pesses and Tan present the challenging task that a ballistic missile de-

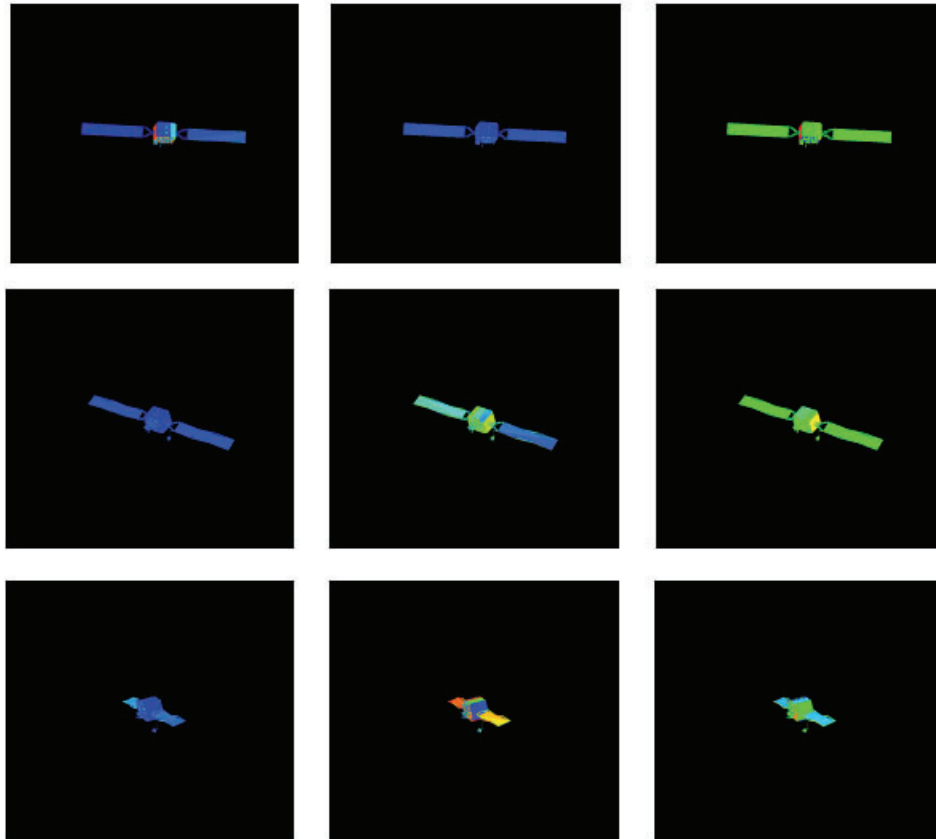
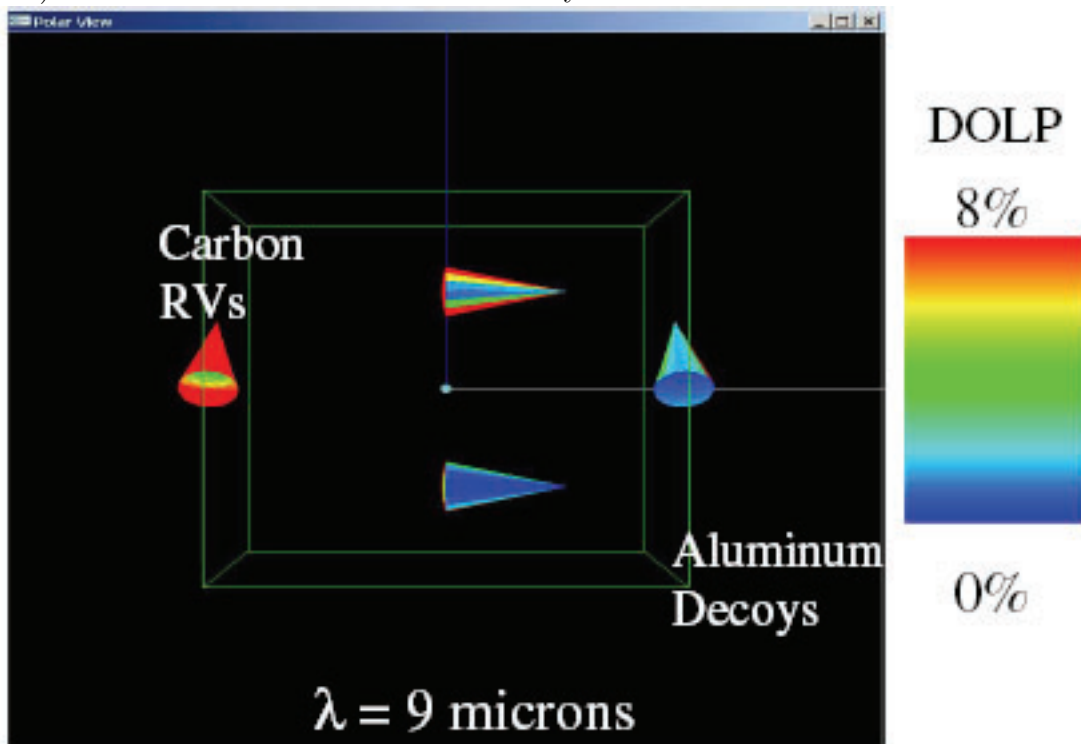


Figure 3.6: The left column shows three different false color views of a GPS in 10 micron S0 light. The middle column shows three different views of a GPS in 10 micron DOLP light. The right column shows three different views of a GPS in 10 micron S0/S1 light.

Figure 3.7: Comparison of modeled DOLP values for 2 carbon coated reentry vehicles (RVs) and 2 aluminum coated balloon decoys.



fense system has of distinguishing between reentry vehicles and balloon decoys. The author's polarimetrically modeled these targets utilizing the SAIC Polar Heat model (Figure 3.7). Polar Heat is outfitted with both Fresnel and BRDF reflectance models, in addition to incoherent scattering effects. The author's discovered the actual reentry vehicles to have 2-4x more DOLP signature than the aluminum coated decoy balloons.

### 3.2.2 Detection of Man-made Objects

Polarization measurements in the infrared have demonstrated utility for the detection of man-made objects in natural backgrounds. One example that has been studied extensively, both with modeling and experimental collections, is the detection of surface laid landmines and tripwires.

Goran Forssel, of the Swedish Defence Research Agency, has published many papers examining the utility of polarized image collections in the infrared for detection of landmines and trip wires. One such publication[8] specifically compares detection of these objects in a non-polarized IR image against a degree of linear polarization (DOLP) image.

Although unpolarized thermal imagery can sometimes easily detect surface laid landmines, the detection becomes quite challenging after the mines begin to be covered by surrounding vegetation and dust from the ground. The problem of detecting tripwires is even more challenging, in that for most cases the wire width is much smaller than the ground sampling distance of the detector making unpolarized radiance measurements (IR or visible) useless.

The images contained in Figure 3.8 are taken from this paper. As a test scenario, Forssel laid five mines on a dry grass ground with no covering and two mines covered with dry grass. The visible image (top) shows the uncovered mines designated by the number 1 and the covered mines designated by the number two. The four crosses in

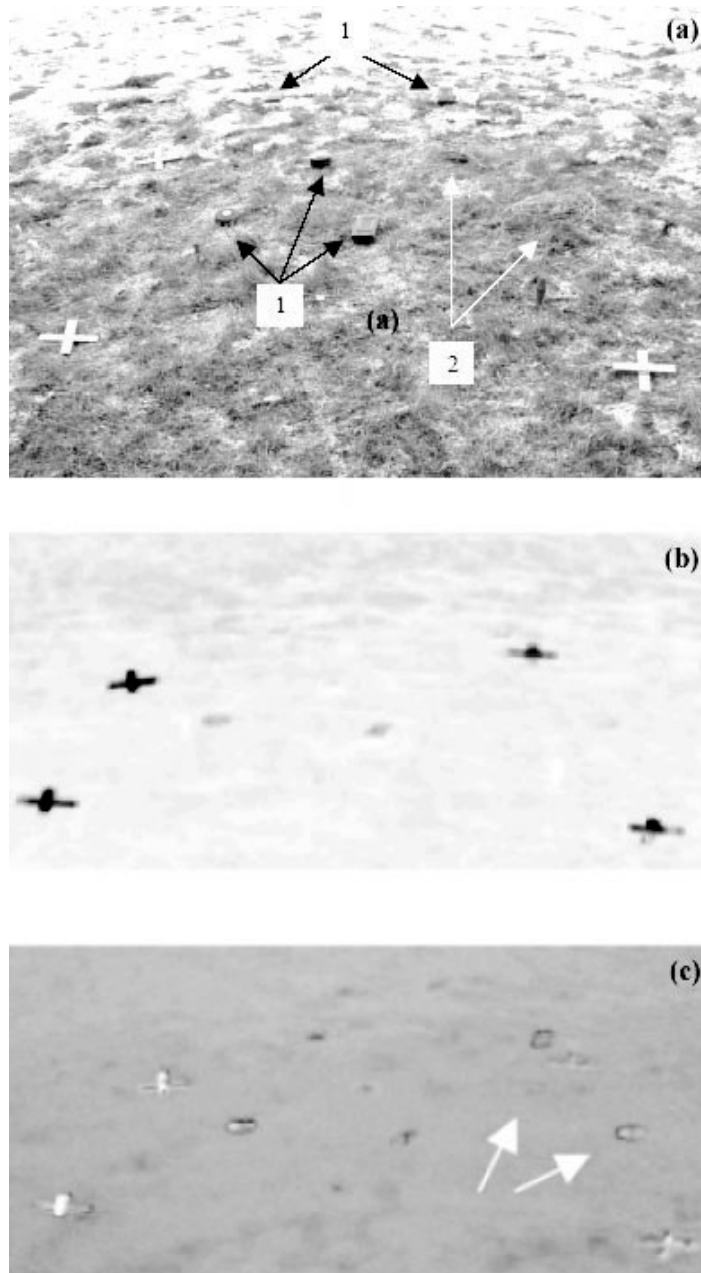


Figure 3.8: Visible contextual image (top) showing five surface laid landmines and two landmines covered by dry grass. Unpolarized IR (middle) and DOLP (bottom) images of the same scene.

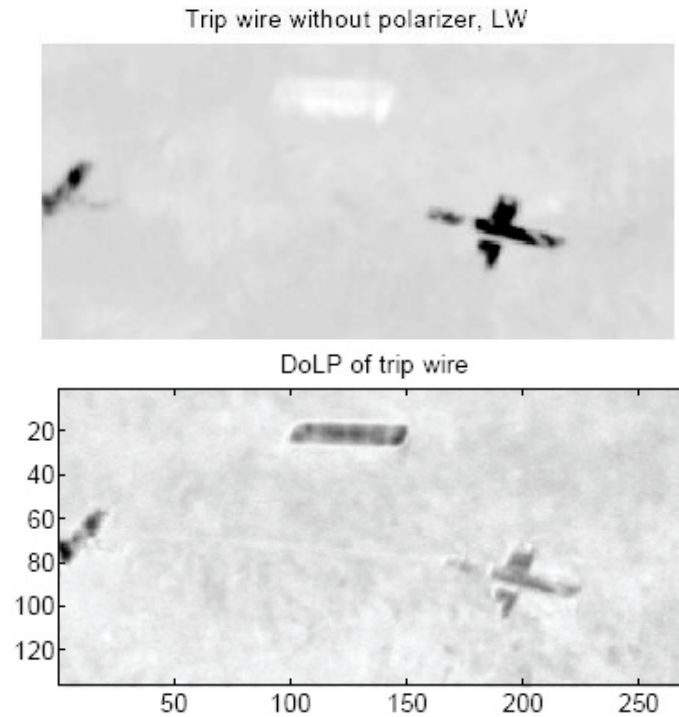


Figure 3.9: Unpolarized IR (left) and DOLP IR image of a trip wire between two fiducial markers.

the scene are placed as reference markers, but not meant to actually be targets for detection. The unpolarized IR image show two of the five uncovered mines clearly visible above the background. However, all five of the uncovered mines are visible within the DOLP image. In addition, one of the covered mines is also visible within the DOLP image and one is not (white arrows).

Forsell also examines a scene where a trip wire is placed across a foot path. The trip wire is only 1.5 mm in diameter and is not visible within the unpolarized IR radiance image. However, Forsell is able to detect the presence of the trip wire clearly in the DOLP image. The images in figure 3.9 are taken from his work to demonstrate this utility of IR polarimetric imaging.

Frank Cremer of Delft University in the Netherlands has examined the utility of MWIR polarimetric measurements to solve the same problem. In a paper in 2002[3], Cremer presents an example where surface laid landmines are difficult to detect with unpolarized MWIR radiance images. However with the addition of a polarizer, he is able to easily detect the presence of landmines.

Figure 3.10 shows a series of images presented by Cremer. Two visible images show the location of the five mines before and after vegetation has grown around them. Next, the figure presents a broadband unpolarized MWIR image where three of the five mines are visible. The  $S_1$  polarization image (labeled Q) shows all five mines to have some polarimetric contrast, while the  $S_2$  polarization image (U) shows minimal contrast.

Another application of LWIR polarimetric imaging is detection of vehicles in a cluttered background. Tyo et al published a passive IR polarimetry review paper in August of 2006 [32]. Figure 3.11 shows an example of two vehicles inside a shadow on the edge of a forest. The vehicle is not visible in the visible multispectral image or the unpolarized LWIR image. However adding LWIR polarization as another degree of freedom brings the vehicle out of the background and significantly enhances the ability for detection.

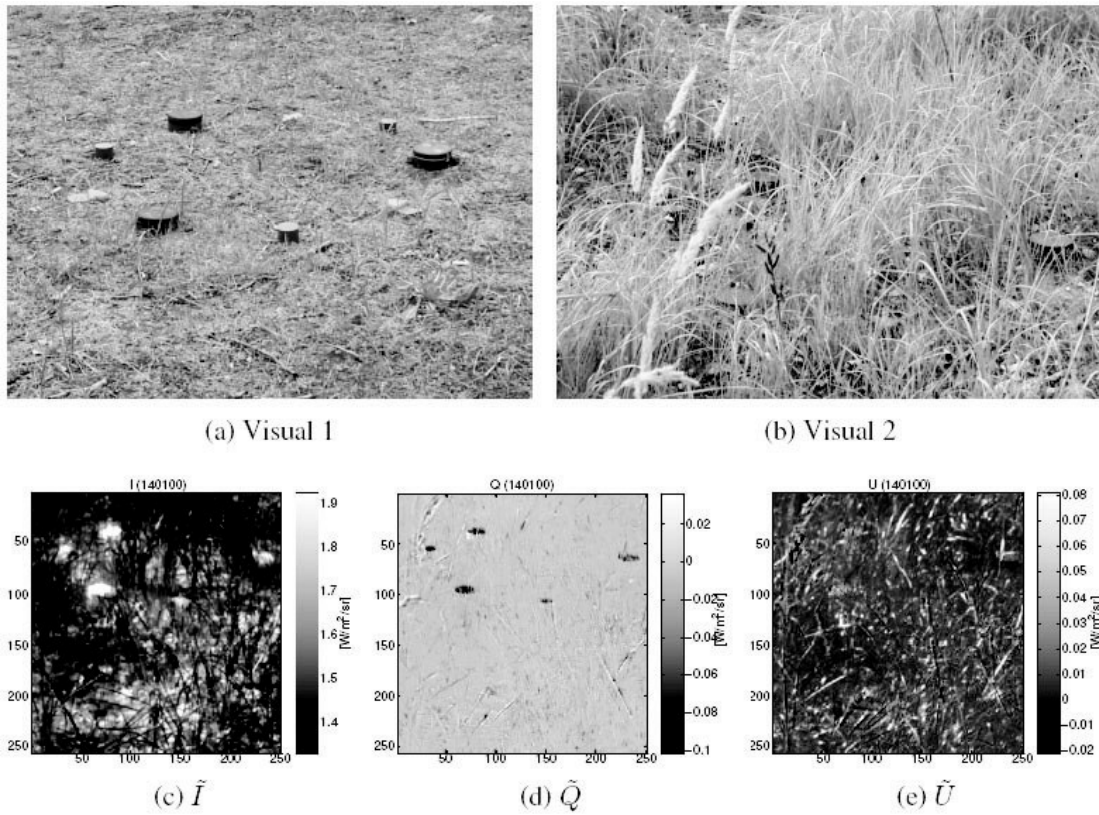


Figure 3.10: Visible images of mines (a) before and (b) after vegetation has grown around them, (c)  $S_0$  IR image, (d)  $S_1/Q$  IR image and (e)  $S_2/U$  IR image of mines embedded in vegetation.

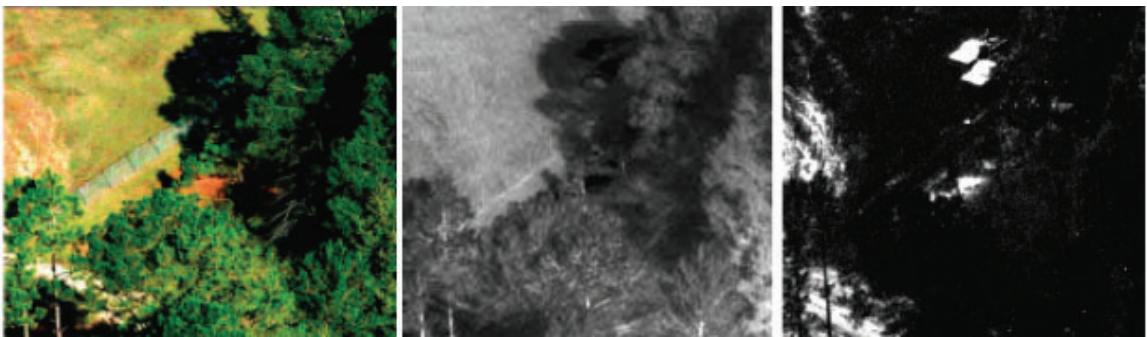


Figure 3.11: Multispectral visible (left), unpolarized MWIR (middle), and degree of polarization MWIR image (right) of vehicles in tree shadows.

### 3.3 Chapter Summary

The first half of this chapter has presented a selection of experimental work geared towards characterizing polarization phenomenology in the infrared. Most of the cited works are material specific to either glass or aluminum. The intent of presenting this work is to familiarize the reader with what levels of polarization to expect for a few man-made materials as a function of emission angle.

The second half of this chapter introduces the reader to recent applications of polarimetric infrared imaging systems. The cited works are very specific to certain operational scenarios (such as a vehicle in a shadow, or image simulation of a GPS satellite) where measuring polarization adds value.

# Chapter 4

## Infrared Radiometry

### 4.1 Review of Radiometric Concepts

In chapter two, we introduced the concept of Stoke's Vectors, blackbody emission, and BRDF models. This section of Chapter 4 describes how the energy contained within each of these variables may be quantified.

Energy is a fundamental physical unit that is measured in Joules. Although we can express a quantity of electromagnetic radiation in terms of its energy, it typically makes more sense to express the *power* of the light in units of Watts (Joules/s). For example, laser output is typically specified in units of Watts because we are interested in the energy output rate. The power is calculated in terms of energy output  $E$  of a unit of time  $\Delta T$

$$P = \frac{E}{\Delta T} \quad (4.1)$$

In remote sensing applications, it may sometimes be more useful to express power in terms of photons per second. This conversion is easily done when one knows the wavelength of the light for a coherent source

$$P_{ph} = \frac{E}{\Delta T} \frac{\lambda}{hc} \quad (4.2)$$

or the wavelength distribution of the light output from an incoherent source,

$$P_{ph} = \frac{1}{\Delta T} \int \frac{\lambda E(\lambda) d\lambda}{hc} \quad (4.3)$$

As an example, let us calculate the power output (in photons/s) from a 1mW HeNe laser source. Assume the wavelength is 650 nm. The power output then becomes,

$$P_{ph} = 1mW \frac{650nm}{hc} = 3.26995 \cdot 10^{15} \frac{photons}{s} \quad (4.4)$$

The amount of power incident onto a surface is expressed in terms of *irradiance*. Irradiance is commonly expressed in units of  $\frac{W}{cm^2}$  or  $\frac{photons}{cm^2s}$ . Irradiance is calculated from the incident power  $P$  and illuminated area  $A$  from the equation [26]

$$E = \frac{P}{A} \quad (4.5)$$

Perhaps the most common radiometric term utilized in remote sensing applications is *radiance*. Radiance is defined as the power coming from a projected area element  $dA \cos\theta$  into a solid angle  $d\Omega$  and is calculated from the equation [26]

$$L = \frac{dP}{dA d\Omega \cos\theta} = \frac{dE}{d\Omega \cos\theta} \quad (4.6)$$

and commonly has units of  $\frac{W}{cm^2sr}$  or  $\frac{photons}{cm^2sr s}$ .

## 4.2 Atmosphere in the Infrared

The atmosphere is made up of a complex mix of water vapor, oxygen, carbon dioxide and other molecular species. The presence of these molecules dictates what wavelengths of light transmit well and what wavelengths are strongly attenuated by the atmosphere.

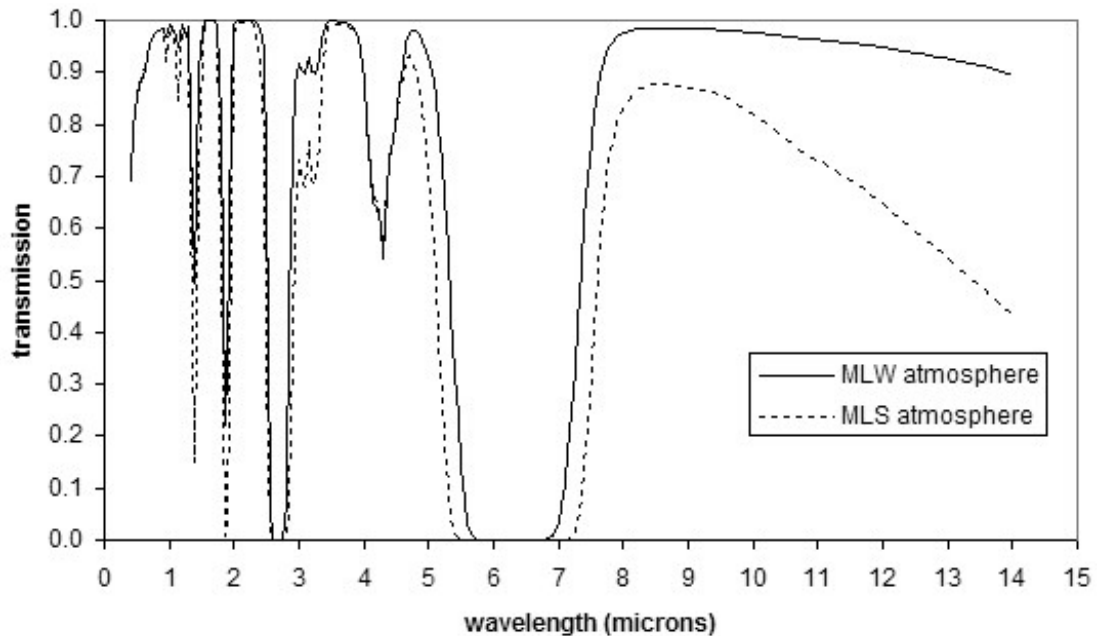


Figure 4.1: Plot of atmosphere transmission between space and ground for a nadir view geometry under MODTRAN mid-latitude summer (MLS) and mid-latitude winter (MLW) both with 23km visibility conditions.

The plot in figure 4.1 shows the transmission loss between space and ground for a nadir view geometry. These values are leveraged from a MODTRAN4v2r1 [1] run configured to have a mid-latitude summer atmosphere (dotted line) and a mid-latitude winter atmosphere (solid line) both with 23km nautical visibility and utilizing a rural aerosol model. The strong absorption features present between 2.5 and 2.8 microns are the divide between the short-wave IR and mid-wave IR regions of the spectrum. Similarly, the strong absorption by the atmosphere between about 5.3 and 7.3 microns is what divides the mid-wave IR region from the long-wave IR region. Atmospheric transmission within the long-wave IR region is excellent, coming in at greater than 90% between 7.8 and 14 microns for a mid-latitude winter atmosphere.

Although there is a strong polarization to downwelled skydome radiance in the visible region of the electromagnetic spectrum, the polarized component of downwelled infrared radiance is negligible. This fact is demonstrated by plotting the downwelled

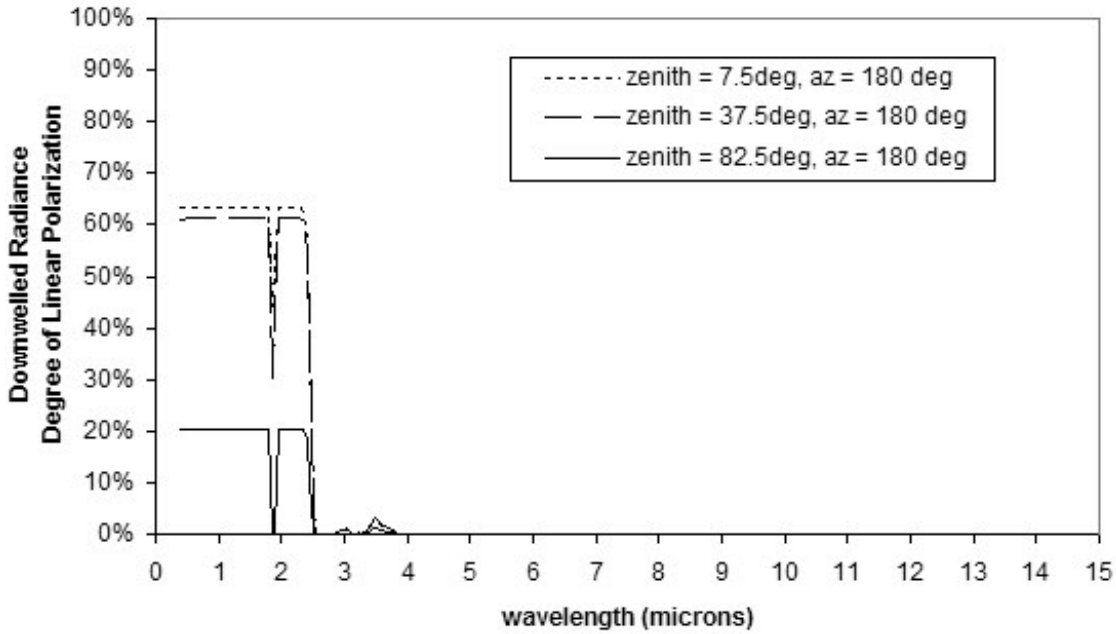


Figure 4.2: Plot showing degree of polarization of downwelled radiance for a Modtran4P atmosphere

radiance from a three different zenith directions at a relative azimuth to the sun of 180 degrees. The sky is modeled to have the sun at a 45 degree zenith angle. The data is derived from a MODTRAN4v2r1-P run [7] (Figure 4.2) assuming a mid-latitude summer atmosphere with 23km visibility. The degree of polarization in the plot was calculated from the ratio of polarized solar radiance to total radiance (thermal and solar)

$$DOP = \frac{\sqrt{(S_1^{solar})^2 + (S_2^{solar})^2}}{S_0^{thermal} + S_0^{solar}} \quad (4.7)$$

Now that the properties of the atmosphere in the infrared have been briefly presented, it follows that we examine bulk material properties important for infrared imaging applications.

Table 4.1: Thermal conductivity values for a few materials[41]

Material	Thermal conductivity ( $\frac{W}{mK}$ )
Copper	385-401
Aluminum	205-237
Steel	36-54
Concrete	0.8-1.28
Glass	0.8-0.93
Soil	0.17-1.13
Water	0.6
Wood	0.09 - 0.21
Air	0.024 - 0.026

### 4.3 Material Properties Important in Infrared

Typically with infrared scene simulation, the user does not have information about the temperature of each individual scene element. When this is the case, a thermodynamic model may be utilized to predict the effect of the diurnal cycle on scene element temperatures. A thermodynamic model, such as THERM available within DIRSIG, utilizes thermal conductivity, solar absorptivity, 48 hour weather history, heat capacity, and material thickness.

*Solar absorptivity* is a measure of how much solar irradiance is absorbed by a material. This term is commonly utilized when referring to absorbed solar irradiance in the visible and near-IR portion of the electromagnetic spectrum. From a pure physics point of view, solar absorptivity is the same physical quantity as solar emissivity.

*Thermal conductivity* is a basic material property that is a measure of it's ability to conduct heat. Thermal conductivity is commonly expressed in units of Watts per meter per degree Kelvin. Table 4.1 lists approximate thermal conductivity values for a select group of materials.

*Specific heat capacity*, sometimes referred to as specific heat, is the measure of how much heat energy is required to raise the temperature of a material by 1 degree. The units of specific heat capacity are Joules per gram per degree Kelvin. Table 4.2

Table 4.2: Specific heat capacity values[39]

Material	Specific Heat ( $\frac{J}{gK}$ )
Asphalt	0.92
Brick	0.84
Concrete	solid 0.88
Glass, silica	0.84
Glass, crown	0.67
Glass, flint	0.503
Glass, pyrex	0.753
Granite solid	0.790
Marble, mica	0.880
Sand solid	0.835
Soil solid	0.80
Wood solid	0.42

lists the heat capacity of a range of materials relevant to modeling of remotely sensed scenes.

## 4.4 Governing Radiometric Equation for Infrared

Schott [26] expresses the total effective aperture reaching (EAR) radiance  $L_{EAR}$  as shown below in equation (4.8).

$$L_{EAR} = \left( E_s \cos \sigma \tau_1 \frac{\rho}{\pi} + \epsilon L_{BB} + F(E_{ds} + E_{dc}) \frac{\rho_d}{\pi} + (1 - F)(L_{bs} + L_{bc}) \rho_d \right) \tau_2 + L_{us} + L_{uc} \quad (4.8)$$

This governing equation all of the potentially significant radiance terms that are either reflected or emitted from the target, background, and atmospheric paths towards a remote sensor.

The first term in the governing equation is due to solar irradiance reflected by the target into the direction of the sensor. The top of the atmosphere solar irradiance  $E_s$  is attenuated by the path transmission loss  $\tau_1$  between the sun and the target. This

irradiance is then reflected by the target, having a reflectivity of  $\rho$ , towards the sensor. For this version of the governing equation it is assumed that the target material has Lambertian reflectance properties.

The next term in the governing equation is the target self-emission term. The target, having an emissivity of  $\epsilon$  emits a fraction of the blackbody radiance  $L_{BB}$  towards the sensor. The blackbody radiance is temperature dependent as described in Chapter 2. Although this term can be quite insignificant when modeling  $L_{EAR}$  in visible and NIR wavelengths, it is a major contributor at longer wavelengths such as the LWIR region considered in this work.

Not only does the governing equation consider reflected solar irradiance, but it also includes reflected downwelled sky radiance. The downwelled sky radiance includes a term for both solar scattered irradiance  $E_{ds}$  (think of the blue sky) and the irradiance due to thermal emission from the skydome. The downwelled irradiance is scaled by a factor  $F$ , having a value of 0 to 1, due to potential background objects. Consider the case of a target that is imaged near a building. The building may take up a significant portion of the hemisphere above the target, effectively blocking the skydome irradiance terms, but introducing background terms of it's own.

The background radiance contributors are included by the terms  $L_{bs}$  and  $L_{b\epsilon}$ , which are due to reflected solar radiance and background emitted radiance incident onto the target surface. Since the background objects will take up only a fraction of the hemisphere above the target, their radiance terms are scaled by the factor  $(1 - F)$ .

The final terms in the governing equation are the upwelled radiance terms. The first upwelled term  $L_{us}$  is due to solar irradiance that is scattered by the atmosphere back towards the sensor. The other upwelled radiance term  $L_{u\epsilon}$  is due to thermal emission of the atmosphere towards the sensor.

It is implied in that the reflectivity, emissivity, path transmissions, solar irradiance, downwelled and upwelled irradiance values in the governing equation are wavelength

dependent. A version of the governing radiometry equation applicable to thermal IR will be presented in Chapter 6.

## 4.5 Chapter Summary

This chapter takes the theory presented in Chapter 2 a step further into the realm of radiometry and introduces relevant radiometric quantities. Most importantly, the governing equation is introduced in the context of infrared scene modeling.

Next, the spectral transmission and degree of polarization of the atmosphere is described by presenting results from MODTRAN runs. Finally, since thermodynamic modeling is a key feature of DIRSIG to be exploited for this work, the material properties relevant to this feature are introduced to the reader.

# Chapter 5

## Polarized BRDF and Emissivity Model

The chosen reflectance and emissivity model for this work was developed as a generalization of the BRDF models discussed in Section 2.5. Upon close inspection, it is apparent the Beard-Maxwell model, the Torrance-Sparrow model, and the Priest-Germer model all have the same general form [9, 29].

The polarized bi-directional reflectivity distribution function (BRDF) is generalized to include a polarized specular component and an un-polarized volume component (although in reality, the volume component may contribute a small amount to the overall polarization of reflectance, this model treats the volume term is completely unpolarized).

$$f_{pBRDF} = f_{spec} + f_{vol} = f_{polarized} + f_{unpolarized} \quad (5.1)$$

The polarized component of the BRDF is a 4x4 element Mueller matrix and is developed in section 5.1. The unpolarized component is a scalar that is presented in section 5.2.

## 5.1 Polarized Specular Component

The specular component of the polarized BRDF is based upon a statistical distribution  $P(\theta_N)$  of a Fresnel reflection Mueller matrix  $M$ . In addition, we include a shadowing and obscuration function  $SO(\theta, \beta, \tau, \Omega)$ . These functions and associated inputs are discussed below.

$$f_{spec} = \frac{M(\beta, n, k)SO(\theta, \beta, \tau, \Omega)P(\theta_N, \sigma, B)}{4\cos(\theta_i)\cos(\theta_r)} \quad (5.2)$$

### 5.1.1 Fresnel Mueller Matrix

As stated in Chapter 2, the Fresnel reflectance from a surface is a function of the complex index of refraction of the material  $n + ik$ , and the angle of incidence. The Fresnel reflectance function assumes a perfectly smooth surface, forcing the reflection to have the same zenith angle as the incident ray. However, as stated in Chapter 2, there is a polarization effect built into the Fresnel reflectance functions which are the basis of the polarized BRDF function.

Expressions for the  $s$  and  $p$  components of Fresnel reflectance were introduced in equations (2.37) and (2.38) in terms of the complex index of refraction  $\tilde{n}$ . However, a more convenient form of these equations, expressed below, is entirely in terms of real quantities.

$$\rho_s(\beta, n, k) = \frac{(A - \cos(\beta))^2 + B^2}{A + \cos(\beta)^2 + B^2} \quad (5.3)$$

and

$$\rho_p(\beta, n, k) = \rho_s \frac{(A - \sin(\beta)\tan(\beta))^2 + B^2}{A + \sin(\beta)\tan(\beta)^2 + B^2} \quad (5.4)$$

where  $\beta$  is the angle of incidence onto a micro-facet (which is different than the

incident zenith angle onto the macro surface  $\theta_i$ ), and A and B are given below as

$$A = \sqrt{\frac{\sqrt{C} + D}{2D}} \quad (5.5)$$

$$B = \sqrt{\frac{\sqrt{C} - D}{2D}} \quad (5.6)$$

$$C = 4n^2k^2 + D^2 \quad (5.7)$$

$$D = n^2 - k^2 - \sin(\beta)^2 \quad (5.8)$$

Priest and Germer[21] break down a roughened surface into a series of perfectly flat micro-facet surfaces, each of which can be treated as having a Fresnel reflectance function. The geometry of incident and reflected directions dictate which facet orientation is considered for the polarized BRDF.

It should be noted that there are three levels of surfaces that are of worth mentioning at this point. The surface of interest is defined as having a macro-surface normal direction  $\hat{z}$ . Within the surface of interest, there exists a series of micro-facets, each having a unique micro-facet normal direction  $\hat{z}_\mu$ . Finally, the macro-surface may also be expressed in some global coordinate system having its own "up" direction. Therefore, care must be taken to specifically state which scattering angles are relative to which surfaces.

Assume an incident ray having a zenith angle of  $\theta_i$  and a reflected ray having a zenith angle of  $\theta_r$  and an azimuth angle  $\phi$  relative to the incident ray. These angles are relative to the local macro-facet normal direction  $\hat{z}$ , not a global normal or "up" direction and not the micro-facet normal. The incident ray and macro surface normal define the *plane of incidence*, shown as the light blue plane in Figure 5.1. The reflected ray and the macro surface normal become the *plane of reflection*, shown as the light orange plane in the figure below.

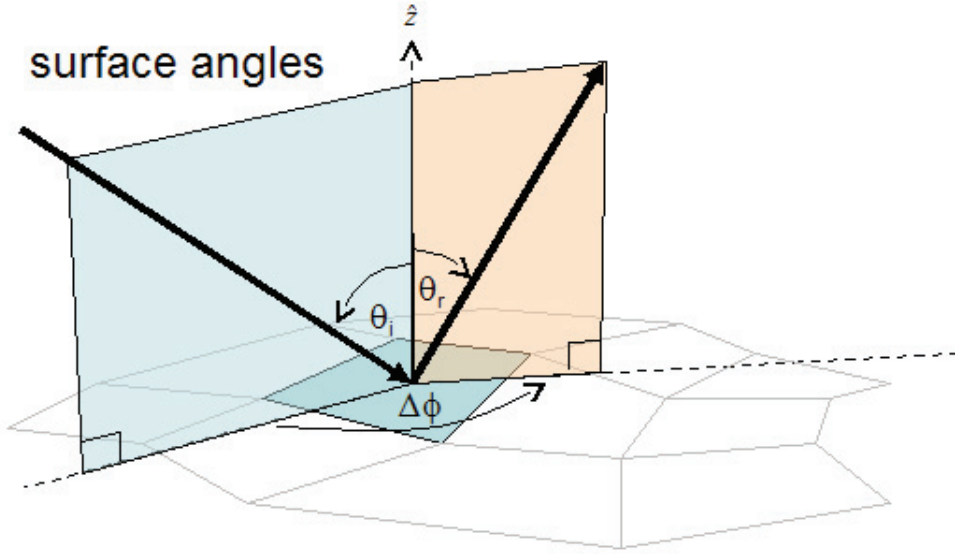


Figure 5.1: Polarized BRDF angles relative to macro surface normal  $\hat{z}$

An expression for the angle  $\beta$  in terms of the incident and reflected ray zenith and azimuth angles.

$$\cos(2\beta) = \cos(\theta_i)\cos(\theta_r) + \sin(\theta_i)\sin(\theta_r)\cos(\phi_r - \phi_i) \quad (5.9)$$

The angle  $\theta_N$  is the angle between the micro-facet normal and the macro surface normal, and is defined in terms of the incident and reflected ray zenith angles and the angle  $\beta$  (see Figure 5.2).

$$\cos(\theta_N) = \frac{\cos(\theta_i) + \cos(\theta_r)}{2\cos(\beta)} \quad (5.10)$$

There is only one such micro-facet that will reflect the incident ray into the direction of the reflected ray. This micro-facet is at an angle  $\theta_N$  relative to the macro-surface normal. The incident and reflected ray both have a zenith angle of  $\beta$  relative to the micro-facet normal. The angle  $\eta_i$  is the angle between the plane of incidence onto the micro-surface and the plane of incidence onto the macro surface. The angle

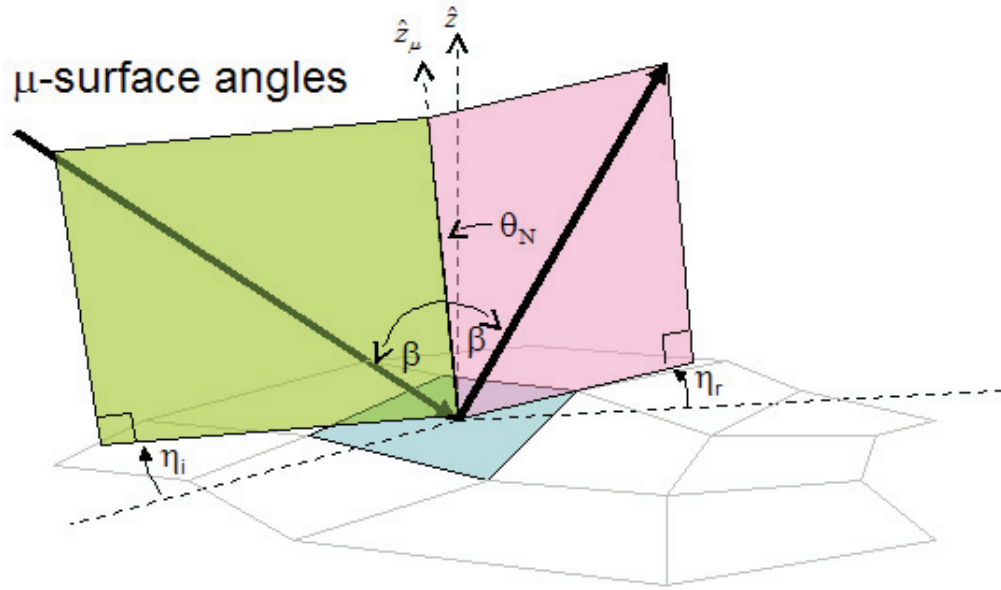


Figure 5.2: Polarized BRDF angles relative to micro-surface normal  $\hat{z}_\mu$  and macro-surface normal  $\hat{z}$

$\eta_r$  is the angle between the plane of reflection from the micro-surface and the plane of reflection from the macro surface.

$$\cos(\eta_i) = \frac{\cos(\theta_N) - \cos(\theta_i)\cos(\beta)}{\sin(\theta_i)\sin(\beta)} \quad (5.11)$$

$$\cos(\eta_r) = \frac{\cos(\theta_N) - \cos(\theta_r)\cos(\beta)}{\sin(\theta_r)\sin(\beta)} \quad (5.12)$$

Finally, a Fresnel Mueller reflection matrix is derived by first writing the  $s$  and  $p$  component of the reflected electric field in terms of the incident electric field vector  $s$  and  $p$  components and the angles  $\eta_r$  and  $\eta_i$ .

In Jones vector notation, the magnitude of the reflected electric field from a material interface is given by

$$\begin{pmatrix} E_s^r \\ E_p^r \end{pmatrix} = \begin{pmatrix} \cos(\eta_r) & \sin(\eta_r) \\ -\sin(\eta_r) & \cos(\eta_r) \end{pmatrix} \begin{pmatrix} r_s & 0 \\ 0 & r_p \end{pmatrix} \begin{pmatrix} \cos(\eta_i) & -\sin(\eta_i) \\ \sin(\eta_i) & \cos(\eta_i) \end{pmatrix} \begin{pmatrix} E_s^i \\ E_p^i \end{pmatrix} \quad (5.13)$$

where the Fresnel reflectance factors  $r_s$  and  $r_p$  are the same as presented in Equations 2.37 and 2.38. This expression can be re-written in a more simple form relating the incident and reflected Jones vectors by a single Jones matrix,

$$\begin{pmatrix} E_s^r \\ E_p^r \end{pmatrix} = \begin{pmatrix} T_{ss} & T_{ps} \\ T_{sp} & T_{pp} \end{pmatrix} \begin{pmatrix} E_s^i \\ E_p^i \end{pmatrix} \quad (5.14)$$

From the Jones matrix  $T$  we can write the Mueller matrix as

$$M_{00} = |T_{ss}|^2 + |T_{sp}|^2 + |T_{ps}|^2 + |T_{pp}|^2 \quad (5.15)$$

$$M_{01} = |T_{ss}|^2 + |T_{sp}|^2 - |T_{ps}|^2 - |T_{pp}|^2 \quad (5.16)$$

$$M_{02} = T_{ss}T_{ps}^* + T_{ss}^*T_{ps} + T_{sp}T_{pp}^* + T_{sp}^*T_{pp} \quad (5.17)$$

$$M_{03} = i(T_{ss}T_{ps}^* - T_{ss}^*T_{ps} + T_{sp}T_{pp}^* - T_{sp}^*T_{pp}) \quad (5.18)$$

$$M_{10} = |T_{ss}|^2 - |T_{sp}|^2 + |T_{ps}|^2 - |T_{pp}|^2 \quad (5.19)$$

$$M_{11} = |T_{ss}|^2 - |T_{sp}|^2 - |T_{ps}|^2 + |T_{pp}|^2 \quad (5.20)$$

$$M_{12} = T_{ss}T_{ps}^* + T_{ss}^*T_{ps} - T_{sp}T_{pp}^* - T_{sp}^*T_{pp} \quad (5.21)$$

$$M_{13} = i(T_{ss}T_{ps}^* + T_{ss}^*T_{ps} - T_{sp}T_{pp}^* + T_{sp}^*T_{pp}) \quad (5.22)$$

$$M_{20} = T_{ss}T_{sp}^* + T_{ss}^*T_{sp} + T_{ps}T_{pp}^* + T_{ps}^*T_{pp} \quad (5.23)$$

$$M_{21} = T_{ss}T_{sp}^* + T_{ss}^*T_{sp} - T_{ps}T_{pp}^* - T_{ps}^*T_{pp} \quad (5.24)$$

$$M_{22} = T_{ss}T_{pp}^* + T_{ss}^*T_{pp} + T_{ps}T_{sp}^* + T_{ps}^*T_{sp} \quad (5.25)$$

$$M_{23} = i(T_{ps}T_{sp}^* - T_{ps}^*T_{sp} - T_{ss}T_{pp}^* + T_{ss}^*T_{pp}) \quad (5.26)$$

$$M_{30} = i(T_{ss}T_{sp}^* - T_{ss}^*T_{sp} + T_{ps}T_{pp}^* - T_{ps}^*T_{pp}) \quad (5.27)$$

$$M_{31} = i(T_{ss}T_{sp}^* - T_{ss}^*T_{sp} - T_{ps}T_{pp}^* + T_{ps}^*T_{pp}) \quad (5.28)$$

$$M_{32} = i(T_{ss}T_{pp}^* - T_{ss}^*T_{pp} + T_{ps}T_{sp}^* - T_{ps}^*T_{sp}) \quad (5.29)$$

$$M_{30} = T_{ss}T_{pp}^* + T_{ss}^*T_{pp} - T_{ps}T_{sp}^* + T_{ps}^*T_{sp} \quad (5.30)$$

Utilizing these Mueller matrix elements, we can therefore write the reflected Stoke's vector in terms of the incident Stoke's vector from a flat material interface as

$$\begin{pmatrix} S_0^r \\ S_1^r \\ S_2^r \\ S_3^r \end{pmatrix} = \begin{pmatrix} M_{00} & M_{10} & M_{20} & M_{30} \\ M_{01} & M_{11} & M_{21} & M_{31} \\ M_{02} & M_{12} & M_{22} & M_{32} \\ M_{03} & M_{13} & M_{23} & M_{33} \end{pmatrix} \begin{pmatrix} S_0^i \\ S_1^i \\ S_2^i \\ S_3^i \end{pmatrix} \quad (5.31)$$

### 5.1.2 Probability Distribution Function

Since most surfaces we will encounter in our modeling efforts will not be perfectly flat, we can take advantage of a facet probability distribution function. A probability distribution allows us to express a non-flat surface in terms of flat micro-facets that are oriented at an angle  $\theta$  relative to the macrosurface plane. Figure 5.2 shows an illustration of how we can represent a roughened surfaces as a series of flat micro-facets with different orientations.

A common micro-facet distribution function is the Gaussian distribution. This function is given in terms of a bias parameter  $B$  and a roughness parameter  $\sigma$ . Specifically, this distribution function is a Gaussian of the local surface slope  $\tan(\theta)$  with a variance of  $\sigma^2$ .

$$P_G(\theta, B, \sigma) = \frac{B e^{-\frac{\tan(\theta)^2}{2\sigma^2}}}{2\pi\sigma^2 \cos(\theta)^3} \quad (5.32)$$

Figure 5.3 shows examples of this distribution function as a function of reflected zenith angle and relative azimuth between the incident and reflected directions.

The Cauchy distribution, expressed in equation (5.33) is most commonly utilized

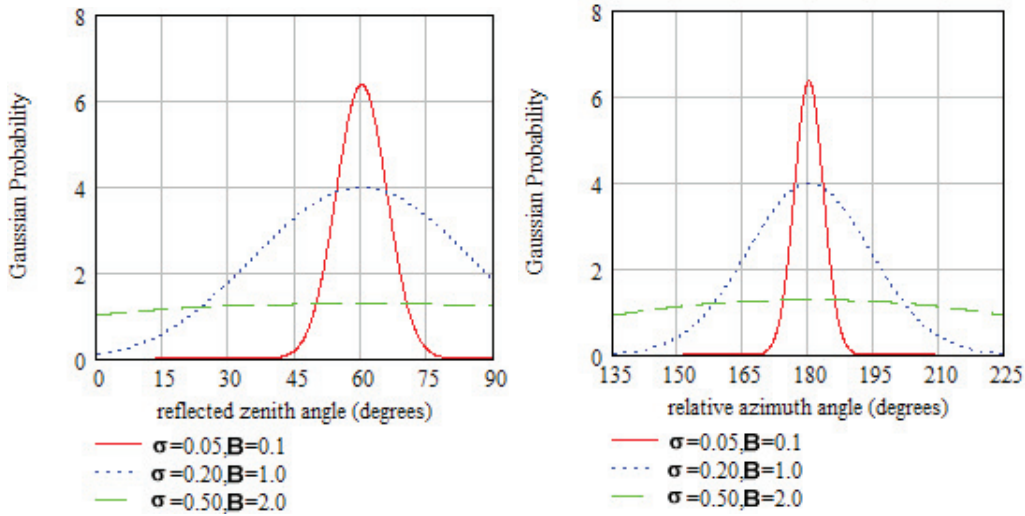


Figure 5.3: Plots showing dependence of Gaussian distribution function on scattered zenith angle

by the NEF database for use in calculating the Beard-Maxwell BRDF. Plots of the Cauchy surface slope distribution function for different values of BIAS ( $B$ ) and  $\sigma$  are presented in Figure 5.4.

$$P_C(\theta, B, \sigma) = \frac{B}{\cos(\theta)(\sigma^2 + \tan(\theta)^2)} \quad (5.33)$$

Figure 5.4 shows a plot of the Cauchy probability distribution as a function of reflected zenith and azimuth angles.

The Cauchy distribution requires an approximately 5x increase in the bias parameter  $B$  to get results similar to the Gaussian function with an identical value of  $\sigma$ . With this adjustment, the general shape of the two distribution functions is similar. However, further inspection shows the Cauchy function to have a higher probability away from the specular direction, but a more narrow specular lobe relative to the Gaussian function.

Although the surface distribution functions are comparable, I prefer to utilize the Gaussian distribution due to the fact that it's easier to normalize and relate to

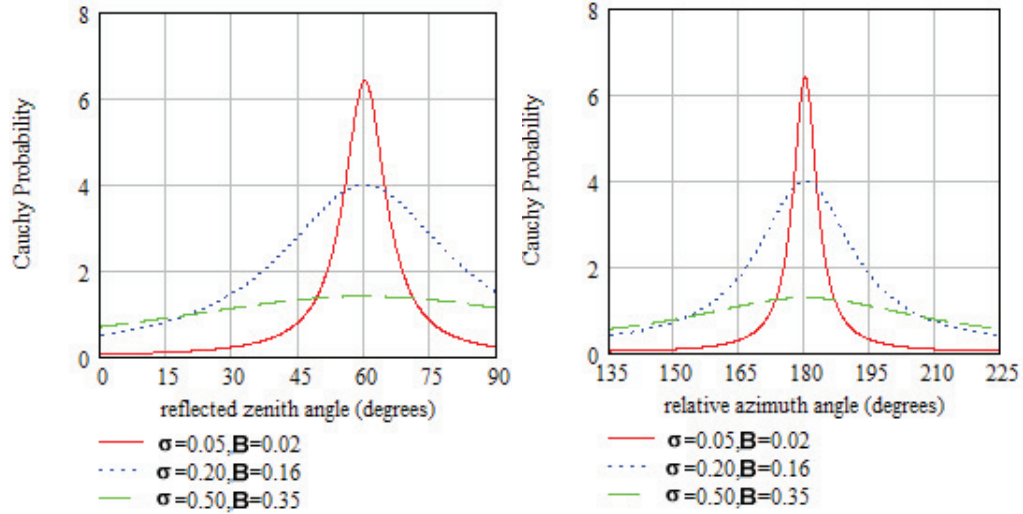


Figure 5.4: Plots showing depending of Cauchy distribution function on scattered zenith angle

reflectivity. For example, a perfectly reflecting surface (having infinite complex index of refraction) modeled with a Gaussian surface slope distribution and BIAS parameter of 1.0 and results in a directional hemispherical reflectivity of 1.0.

### 5.1.3 Shadowing and Obscuration Function

The shadowing and obscuration function serves the purpose of accounting for shadowing and obscuration effects resulting from very rough surfaces. The particular function utilized by the Beard-Maxwell BRDF model is preferred due to its maturity within the NEF database. Equation (5.34) presents the function utilized by the Beard-Maxwell BRDF model, implemented in the NEF database.

$$SO(\theta, \beta, \tau, \Omega) = \frac{1 + \frac{\theta}{\Omega} e^{-2\beta/\tau}}{1 + \frac{\theta}{\Omega}} \quad (5.34)$$

A *stronger* (smaller values of  $\tau$  and  $\Omega$ ) shadowing and obscuration function reduces surface reflectance for higher roughness surfaces by considering that oblique incident and reflected angle scattering has a higher probability of being shadowed or

re-reflected in another direction by a micro-facet.

## 5.2 Unpolarized Component

In addition to the polarized Fresnel component of the BRDF, there is also an unpolarized scattering component. This un-polarized component has a *volume* scattering term  $\rho_v$  and a *diffuse* scattering term  $\rho_d$ .

$$f_{vol}(\theta_i, \theta_r) = \rho_d + \frac{2\rho_v}{\cos(\theta_i) + \cos(\theta_r)} \quad (5.35)$$

The diffuse scattering term is analogous to Lambertian reflectivity, where by definition there is no angular dependence to scattering and the result is completely unpolarized. The volume scattering term, also un-polarized, represents radiance that is absorbed and reflected immediately back out due to sub-surface scattering.

## 5.3 Effect of Parameters on pBRDF

This section examines the effect that various input parameters have on the value of the pBRDF function described above. All examples in this section utilized the values of  $\rho_v=0$ ,  $\rho_d=1e-4$ , and Gaussian probability function with  $B=1.0$ . This set of parameter values is intended to help investigate the sensitivity of the specular (polarizing) component of the pBRDF.

### 5.3.1 Complex index of refraction

The complex index of refraction  $\tilde{n}$  has a real component  $n$  and a complex component  $\kappa$ . In general, increasing the value of the complex index of refraction (either  $n$  or  $\kappa$  or both) has the effect of raising the unpolarized reflectivity. A perfect dielectric reflector has a real valued index of refraction of infinity. A perfect metal reflector

has a complex valued index of refraction of infinity. Assuming a material allows no transmission, a blackbody emitter would be modeled by a real valued index of refraction of 1.0.

For this example, the values of  $\tilde{n}$  were picked to be 3.2-0.2i, 1.5-2.15i, and 1.5-5.0i. These values do not represent any material specifically, but are meant merely for the illustrative purposes of this section. The first two values of  $\tilde{n}$  have the same complex magnitude when calculated by the formula

$$|\tilde{n}| = \sqrt{(n - 1)^2 + \kappa^2} \quad (5.36)$$

while the third value of  $\tilde{n}$  has a magnitude value that is much higher.

For unpolarized incident radiance, the components of the pBRDF Mueller matrix (recall equation 5.31) that drive the Stoke's vector of the reflected ray are the  $M_{00}$ ,  $M_{10}$ , and  $M_{20}$  components. Figure 5.5 shows these components plotted for the case of incident and reflected zenith angles of 45 degrees, and a surface roughness value of  $\sigma=0.10$ . There are many important qualitative conclusions that can be drawn from these plots, namely:

1. Increasing the value of  $n$  and/or  $\kappa$  has the effect of increasing the total reflectivity (captured by  $M_{00}$  element of pBRDF Mueller matrix).
2. Increasing the value of  $n$  and/or  $\kappa$  has the effect of lowering the values of the polarized components  $M_{10}$ , and  $M_{20}$  of the pBRDF Mueller matrix.
3. Changing the  $n$  and  $\kappa$  values, but keeping the value of  $|\tilde{n}|$  (as defined in equation 5.36) constant, does not effect of the polarized components  $M_{10}$ , and  $M_{20}$  of the pBRDF Mueller matrix. What this means is that the  $M_{10}$ , and  $M_{20}$  components appear to be driven primarily by the value of  $|\tilde{n}|$ , regardless of the combination of  $n$  and  $\kappa$  utilized to produce the value of  $|\tilde{n}|$ .

4. Changing the  $n$  and  $\kappa$  values, but keeping the value of  $|\tilde{n}|$  (as defined in equation 5.36) constant, does change the value of the total reflected radiance component  $M_{00}$ . The change is not well defined and could be studied further at a later date.

### 5.3.2 Sigma value

For this example, an incident angle of 22.5 degrees was chosen and a relative azimuth between them of 170 degrees. The out of plane value of relative azimuth was chosen in order to show the contrast in the  $M_{20}$  component. When the scattering is exactly in-plane (relative azimuth between incident and reflected ray is 180 degrees), the  $M_{20}$  component is very close to zero.

The plots in figure 5.6 show the  $M_{00}$ ,  $M_{10}$ , and  $M_{20}$  components of the pBRDF Mueller matrix for  $\sigma$  values of 0.1, 0.2, and 0.5 as a function of reflected zenith angle. Upon inspection, it is obvious that increasing the value of  $\sigma$  tends to flatten the  $M_{00}$ ,  $M_{10}$ , and  $M_{20}$  curves and shift the peaks to higher zenith angles. This phenomena of shifting the reflectance peak away from the specular angle was what motivated Torrance and Sparrow to derive their BRDF model.

Another way to demonstrate the effect of altering the  $\sigma$  value is to plot the  $M_{00}$ ,  $M_{10}$ , and  $M_{20}$  components versus relative azimuth. These plots are presented in Figure 5.7. For this example, the incident and reflected zenith angles were held at 22.5 degrees. Inspection of these curves shows that an increase in the value of  $\sigma$  tends to flatten the  $M_{00}$  and  $M_{10}$  curves, but keep their specular peak in-plane at a relative azimuth of 180 degrees. However, it is interesting to note that the peak values of the  $M_{20}$  component occur outside of the specular plane and are pushed further away from it by larger values of  $\sigma$ . In addition, it should be noted that the asymmetry the  $M_{20}$  component has about the specular azimuth angle of 180 degrees is what drives the  $S_2$  component of thermally emitted radiance down to virtually zero.

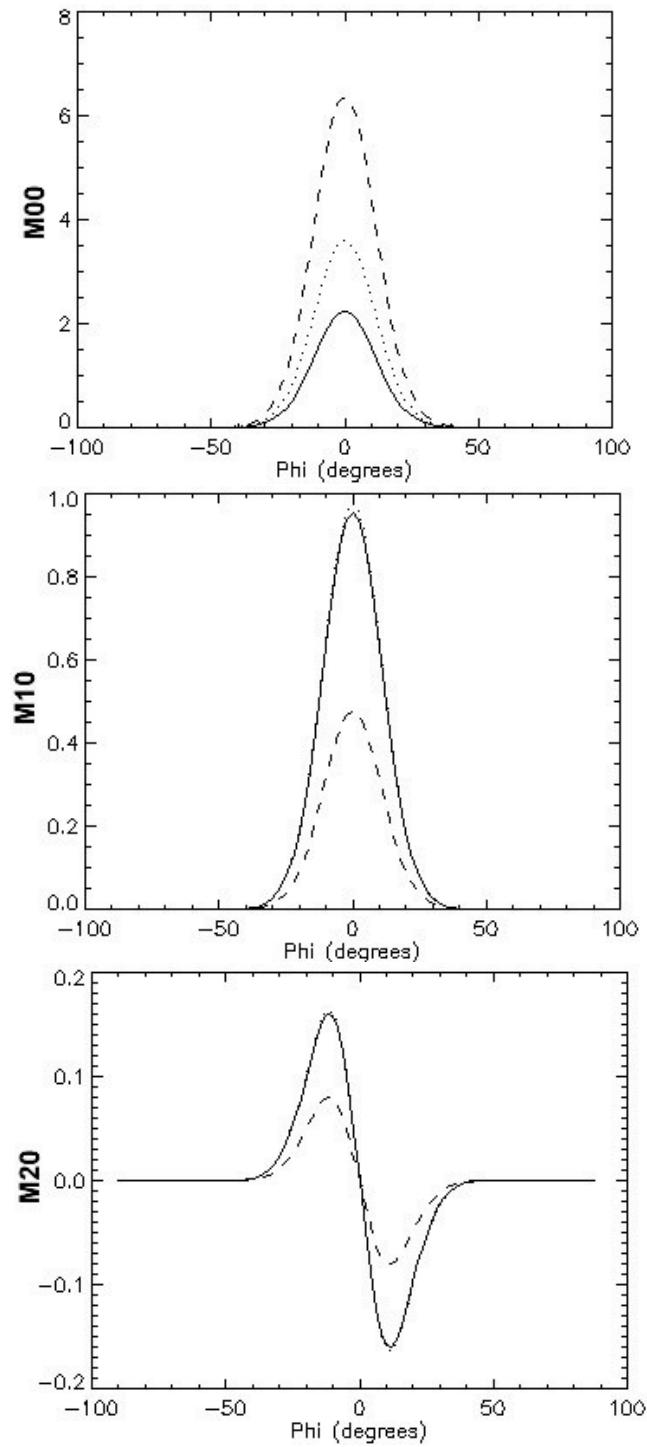


Figure 5.5: Plots of  $M_{00}$  (top),  $M_{10}$  (middle), and  $M_{20}$  (bottom) components of pBRDF as a function of reflected azimuth angle showing the sensitivity of the pBRDF to index of refraction. The solid curves correspond to  $\tilde{n} = 3.2 - 0.2i$ , dotted curves to  $\tilde{n} = 1.5 - 2.15i$ , and dashed curves to  $\tilde{n} = 1.5 - 5.0i$ .

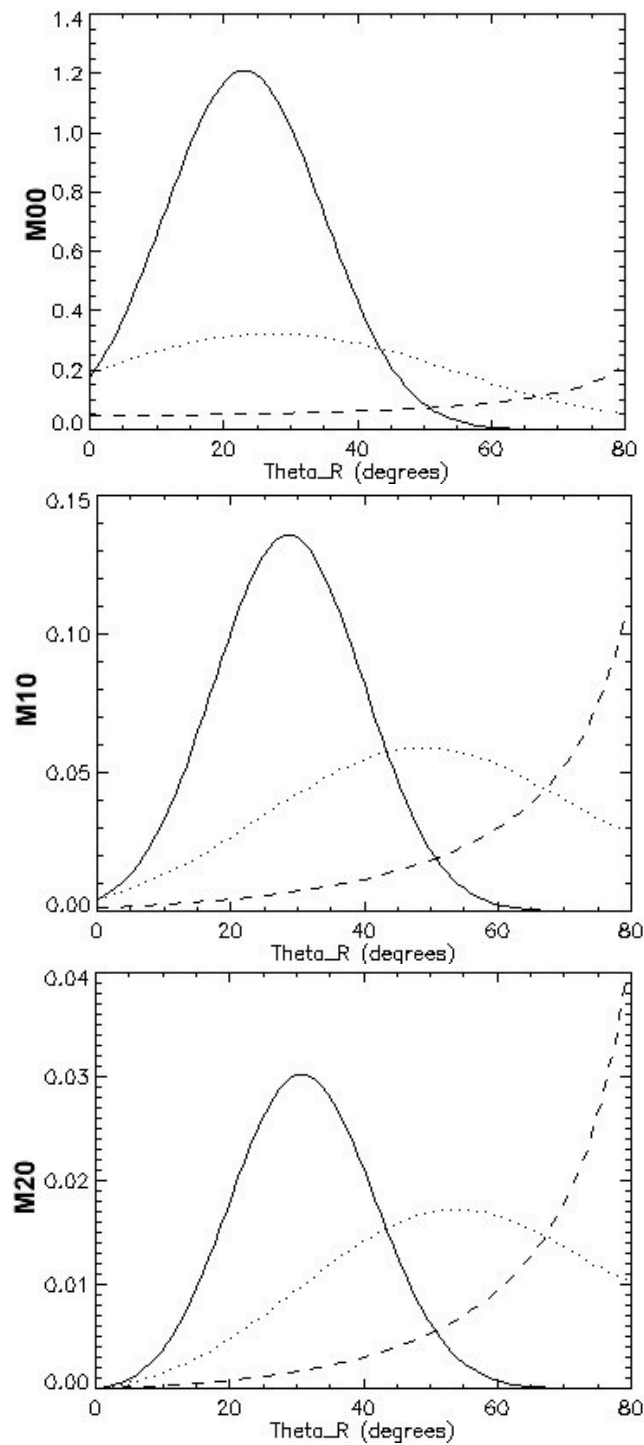


Figure 5.6: Plots of  $M_{00}$  (top),  $M_{10}$  (middle), and  $M_{20}$  (bottom) components of pBRDF as a function of reflected zenith angle showing the sensitivity of the pBRDF to surface roughness. The solids curves correspond to  $\sigma=0.1$ , dotted curves  $\sigma=0.2$ , and dashed curves  $\sigma=0.5$ .

### 5.3.3 Shadowing and Obscuration Function Parameters

For this example, an incident angle of 22.5 degrees was chosen and a relative azimuth between them of 180 degrees. The shadowing and obscuration function parameters chosen for the example are for a strong  $[\tau=0.1, \Omega=0.1]$ , moderate  $[\tau=0.5, \Omega=1.0]$  and weak  $[\tau=5, \Omega=10]$  shadowing and obscuration function. In that the effect of shadowing and obscuration is also driven by surface roughness,  $\sigma$  values of 0.05, 0.25, and 0.40 were chosen to plot.

The plots in figure 5.8 qualitatively demonstrate that increasing the strength of the shadowing and obscuration function has the tendency to decrease the overall reflectance from the surface, which is expected. For the smoothest surface ( $\sigma=0.05$ ), the shape of the  $f_{00}$  curve does not change much. However as the surface becomes increasingly rough, a stronger shadowing and obscuration function tends to bring out more of a specular peak but at a reduced magnitude relative to a scattering produced by a weaker shadowing and obscuration function.

## 5.4 Spectral Interpolation

The NEF database [18], primarily concerned with the value of  $M_{00}$ , performs a spectral interpolation of the modified Beard-Maxwell BRDF by the following equation.

$$\rho(\lambda) = \rho_{DHR}^{meas}(\lambda) \left( \frac{\rho(\lambda_j)}{\rho_{DHR}^{calc}(\lambda_j)} \frac{\lambda_k - \lambda}{\lambda_k - \lambda_j} + \frac{\rho(\lambda_k)}{\rho_{DHR}^{calc}(\lambda_k)} \frac{\lambda - \lambda_k}{\lambda_k - \lambda_j} \right) \quad (5.37)$$

where  $\lambda$  is the wavelength of interest,  $\lambda_j$  is a wavelength lower than  $\lambda$  for which BRDF parameters exist,  $\lambda_k$  is a wavelength higher than  $\lambda$  for which BRDF parameters exist,  $\rho_{DHR}^{meas}$  is an experimentally measured DHR, and  $\rho_{DHR}^{calc}$  is a calculated DHR based on hemispherical integration of the BRDF. This approach is simply a linear interpolation between wavelengths where BRDF parameters exist, weighted by an adjustment utilizing measured hemispherical reflectance.

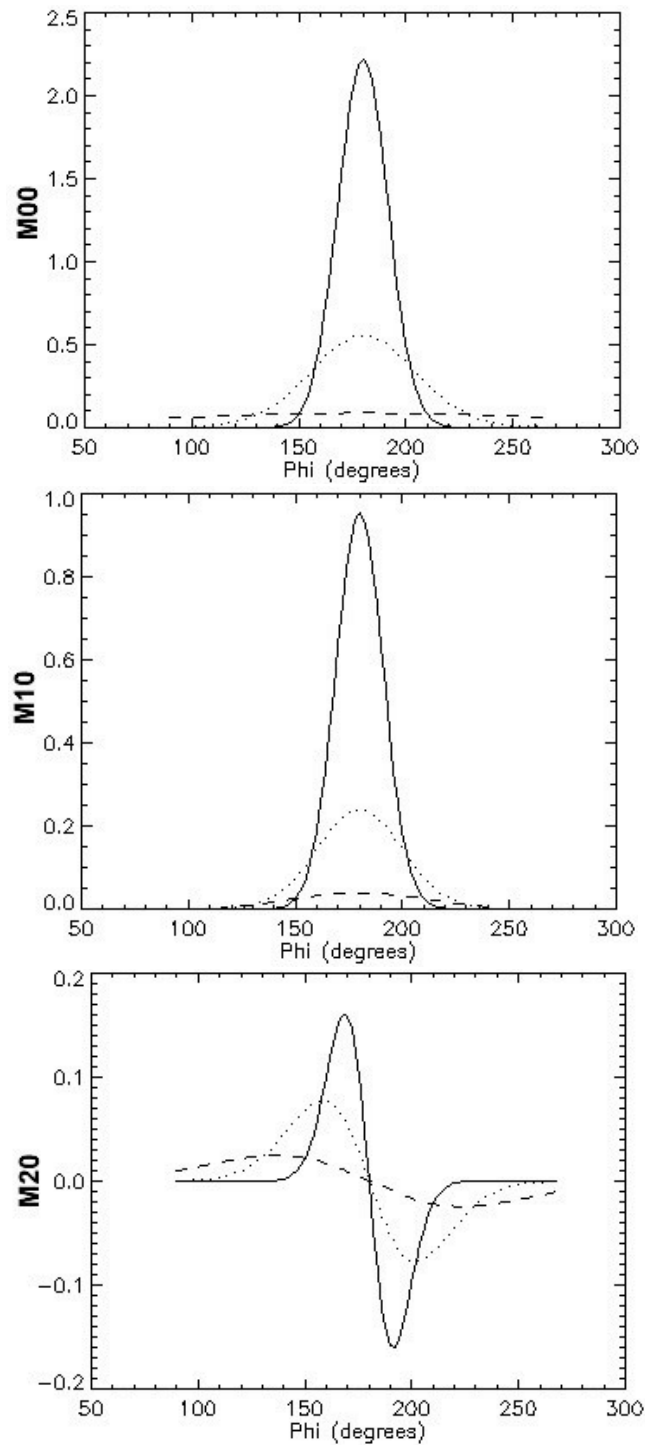


Figure 5.7: Plots of  $M_{00}$  (top),  $M_{10}$  (middle), and  $M_{20}$  (bottom) components of pBRDF as a function of reflected azimuth angle showing the sensitivity of the pBRDF to surface roughness. The solids curves correspond to  $\sigma=0.1$ , dotted curves  $\sigma=0.2$ , and dashed curves  $\sigma=0.5$ .

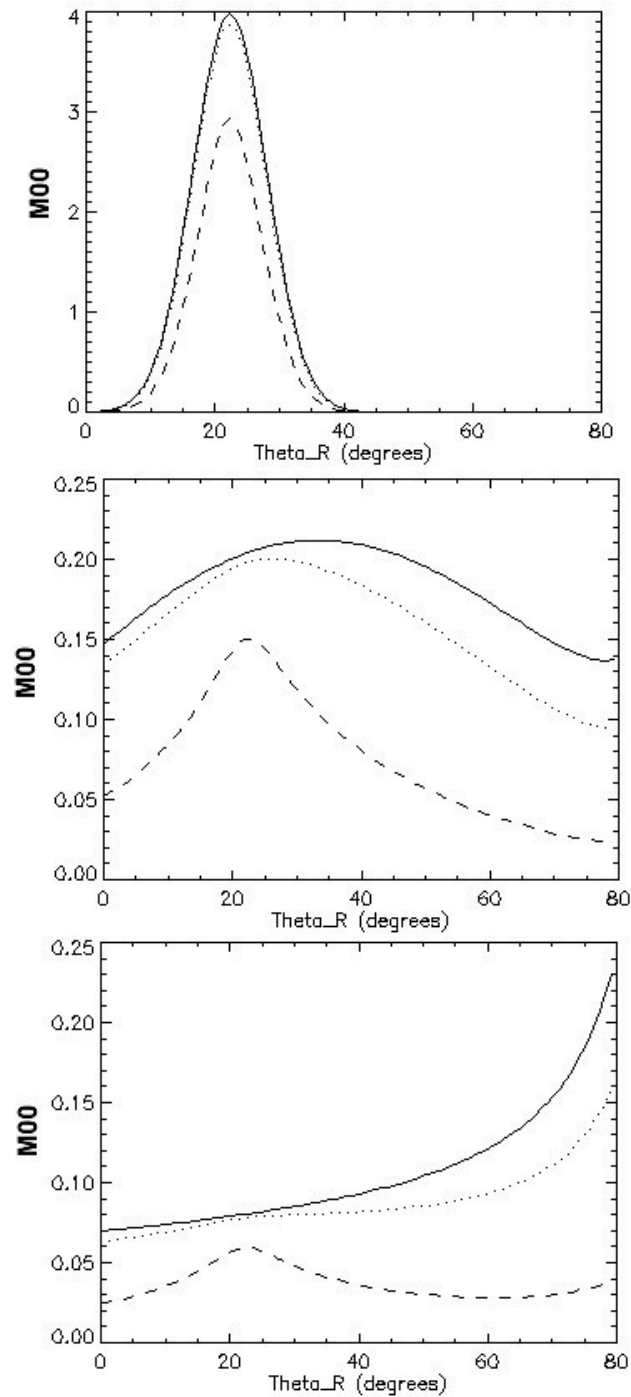


Figure 5.8: Plots of pBRDF component  $M_{00}$  for various shadowing and obscuration parameter values for surface roughness values of 0.05 (top), 0.25 (middle), and 0.40 (bottom). Solid lines for  $[\tau=5.0, \Omega=10.0]$ , dotted lines for  $[\tau=0.5, \Omega=1.0]$  and dashed lines for  $[\tau=0.1, \Omega=0.1]$  show the sensitivity of the pBRDF to the shadowing and obscuration function parameters and surface roughness.

Shell [29] points out that an analogous linear interpolation of a 4x4 Mueller matrix pBRDF is not appropriate. He proposes an alternate interpolation technique. This technique performs a linear interpolation on the product of the probability distribution function and shadowing and obscuration function (Equation 5.38), a linear interpolation on the real portion of the index of refraction  $n$  (Equation 5.39), a linear interpolation on the complex portion of the index of refraction  $\kappa$  (Equation 5.40), and a linear interpolation of the diffuse and volume scattering terms.

$$p(B, \sigma, \lambda)SO(\tau, \Omega, \lambda) = p(B, \sigma, \lambda_j)SO(\tau, \Omega, \lambda_j) \left( \frac{\lambda_k - \lambda}{\lambda_k - \lambda_j} \right) + p(B, \sigma, \lambda_k)SO(\tau, \Omega, \lambda_k) \left( \frac{\lambda - \lambda_j}{\lambda_k - \lambda_j} \right) \quad (5.38)$$

$$n(\lambda) = n(\lambda_j) \left( \frac{\lambda_k - \lambda}{\lambda_k - \lambda_j} \right) + n(\lambda_k) \left( \frac{\lambda - \lambda_j}{\lambda_k - \lambda_j} \right) \quad (5.39)$$

$$\kappa(\lambda) = \kappa(\lambda_j) \left( \frac{\lambda_k - \lambda}{\lambda_k - \lambda_j} \right) + \kappa(\lambda_k) \left( \frac{\lambda - \lambda_j}{\lambda_k - \lambda_j} \right) \quad (5.40)$$

Shell approaches the unpolarized pBRDF component spectral interpolation in the same manner as the NEF modeling document does for spectrally interpolating the Beard-Maxwell BRDF. The interpolation is a linear interpolation between hemispherical integration of the unpolarized pBRDF term at wavelengths possessing pBRDF fit parameters, weighted by an experimentally derived unpolarized hemispherical reflectance. This concept takes on the form

$$\rho_{vol}(\lambda) = \rho_{DHR}^{vol-meas}(\lambda) \left( \frac{\rho_{vol}(\lambda_j)}{\rho_{DHR}^{vol-calc}(\lambda_j)} \frac{\lambda_k - \lambda}{\lambda_k - \lambda_j} \right) + \left( \frac{\rho_{vol}(\lambda_k)}{\rho_{DHR}^{vol-calc}(\lambda_k)} \frac{\lambda - \lambda_j}{\lambda_k - \lambda_j} \right) \quad (5.41)$$

where  $\rho_{vol}$  is the value of the unpolarized  $f_{00}$  component of the pBRDF. The term

$\rho_{DHR}^{vol-calc}$  is a hemispherical integration of the unpolarized term of the BRDF at a reference wavelength that has pBRDF parameters defined

$$\rho_{DHR}^{vol-calc} = \pi\rho_D + 4\rho_V \quad (5.42)$$

The derivation of equation 5.42 is given in Shell [29]. The parameter  $\rho_{DHR}^{vol-meas}(\lambda)$  is derived by subtracting out the modeled polarized DHR from the measured value of the DHR

$$\rho_{DHR}^{vol-meas}(\lambda) = \rho_{DHR}^{meas}(\lambda) - \rho_{DHR}^{spec}(\lambda) \quad (5.43)$$

The term  $\rho_{DHR}^{spec}(\lambda)$  is the linearly interpolated value of the polarized component of the pBRDF between the value of the pBRDF evaluated at the reference wavelengths  $\lambda_j$  and  $\lambda_k$

$$\rho_{DHR}^{spec}(\lambda) = \frac{\rho_{DHR}^{spec}(\lambda_k) - \rho_{DHR}^{spec}(\lambda_j)}{\lambda_k - \lambda_j} \lambda + \rho_{DHR}^{spec}(\lambda_j) - \frac{\rho_{DHR}^{spec}(\lambda_k) - \rho_{DHR}^{spec}(\lambda_j)}{\lambda_k - \lambda_j} \lambda_k \quad (5.44)$$

Finally, the spectrally interpolated pBRDF is given by

$$\rho_{pBRDF}(\lambda) = \rho_{polarized}(\lambda) + \rho_{vol}(\lambda) \quad (5.45)$$

We have developed a detailed description of a generalized polarimetric BRDF. The next section describes how polarized thermal emissivity is derived from the polarized BRDF.

## 5.5 Polarized Emissivity

The polarized emissivity utilizes the concept of energy conservation. Recall from Chapter 2 that

$$\rho + \tau + \epsilon = 1 \quad (5.46)$$

where  $\rho$  is the hemispherical reflectivity,  $\tau$  is the transmission, and  $\epsilon$  is the emissivity of a material. In developing a polarized emissivity model, we assume that the material does not transmit radiance ( $\tau = 0$ ) in the infrared region of the spectrum and solve for emissivity in terms of hemispherical reflectivity

$$\epsilon(\theta) = 1 - \int f_{pBRDF}(\theta, \theta_r, \Delta\phi) \cos(\theta_r) d\Omega \quad (5.47)$$

The above integral can be re-written in terms of  $\theta_r$  and  $\phi_r$

$$\epsilon(\theta) = 1 - \int_0^{2\pi} \int_0^{\pi/2} f_{pBRDF}(\theta, \theta_r, \Delta\phi) \cos(\theta_r) \sin(\theta_r) d\theta_r d\phi_r \quad (5.48)$$

To understand how the different pBRDF inputs effect the behavior of the modeled emissivity, various examples are presented below.

As a baseline, a real valued index of refraction value of 1.5 was chosen. For the shadowing and obscuration function, values of 5 and 10 were chosen for the  $\tau$  and  $\Omega$  parameters respectively. The plot on the left of figure 5.9 shows the Stoke's  $S_0$  and  $S_1$  emissivity values as a function of emission angle and three different values of surface roughness  $\sigma$ . As expected, the  $S_0$  emissivity is quite flat for zenith values less than about 45 degrees. However the smoother surface ( $\sigma = 0.05$ )  $S_0$  falls off much faster for larger emission angles than does the moderately and severely rough surfaces.

The plot on the right of figure 5.9 shows the effect of changing the probability function bias value  $B$  on the  $S_0$  and  $S_1$  emissivity curves. Larger values of  $B$  have the effect of scaling the emissivity away from a perfect Lambertian blackbody ( $\epsilon(\theta) = 1.0$ ).

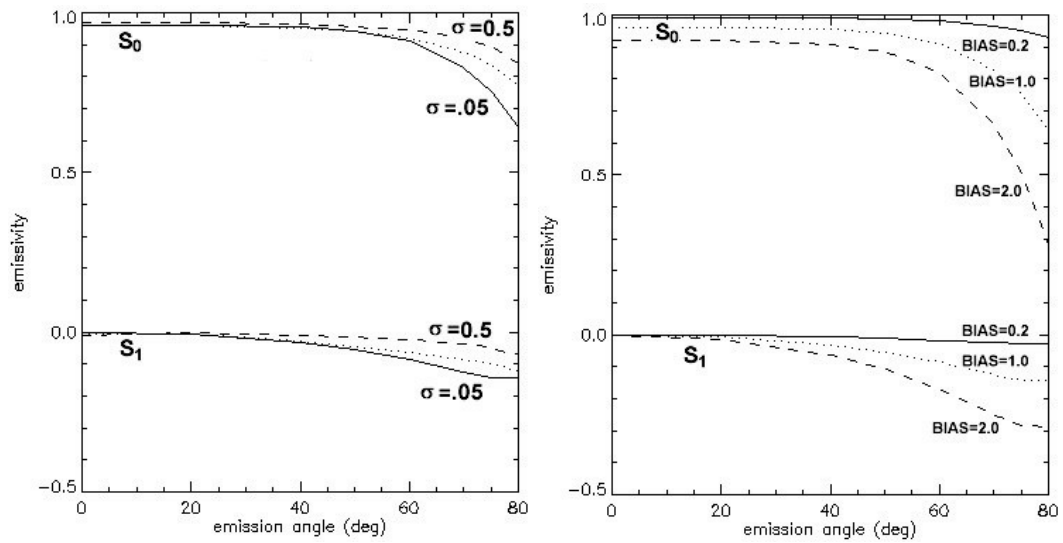


Figure 5.9: Plots showing effect of changing  $\sigma$  (left) value and  $B$  (right) value of pBRDF function on  $S_0$  and  $S_1$  emissivity.

The next series of emissivity plots, shown in figure 5.10, demonstrate the effect of altering the values of  $\tau$  and  $\Omega$  on the  $S_0$  and  $S_1$  emissivity curves. A complex index of refraction value of  $1.5-0.5i$  was chosen for these plots. Larger values of  $\tau$  and  $\Omega$  will relax the shadowing and obscuration function, such that they do not attenuate the reflections as much. Smaller values of  $\tau$  and  $\Omega$  produce a stronger shadowing and obscuration function, in that reflections are attenuated for rough surfaces at large incident and reflected zenith angles.

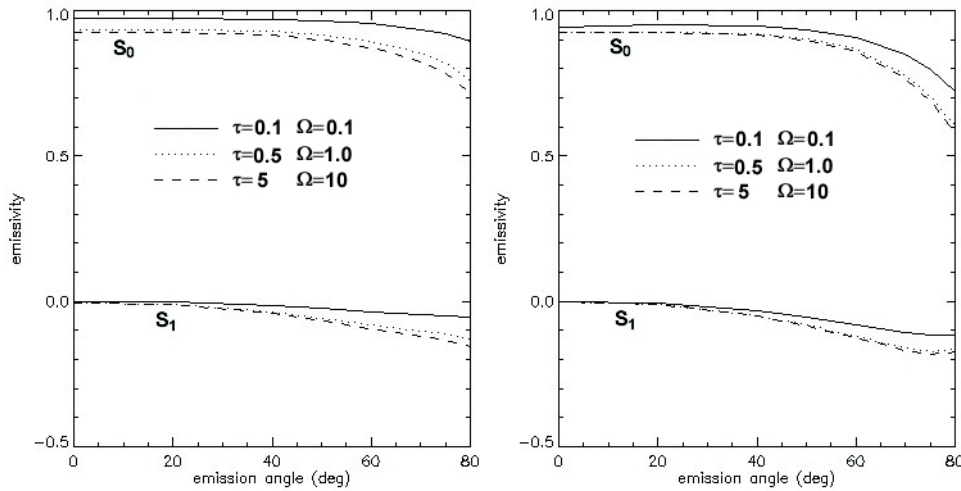


Figure 5.10: Plots showing the effect of changing the shadowing function parameters for a smooth (right) and moderately rough (left) surface.

The strongest shadowing and obscuration function was configured by the smallest values of  $\tau$  and  $\Omega$ , chosen to be 0.1 and 0.1 radians respectively. A moderate strength shadowing and obscuration function was configured by setting  $\tau$  and  $\Omega$  to 0.5 and 1.0 radians. The mildest form of the shadowing and obscuration function was generated by setting  $\tau$  and  $\Omega$  to 5.0 and 10.0 radians. The plots in figure 5.10 show that a stronger shadowing and obscuration function has the effect of (1) increasing the emissivity for all emission angles and (2) reducing the emissivity drop-off at large emission angles. As expected, the smoother surface (right side of figure) is slightly less effected by changing the shadowing and obscuration function parameters than the rougher surface (left side of figure).

Finally, a series of plots were generated to demonstrate the effect of altering the pBRDF diffuse scattering  $\rho_d$  and volume scattering  $\rho_v$  terms. For these examples, the bias value  $B$  of the probability distribution function was set to  $1e-6$ , effectively turning off the specular reflection portion of the pBRDF.

The plot on the left of Figure 5.11 shows the effect of changing the value of  $\rho_d$  on  $S_0$  emissivity. This term is essentially a Lambertian reflectance term, therefore no

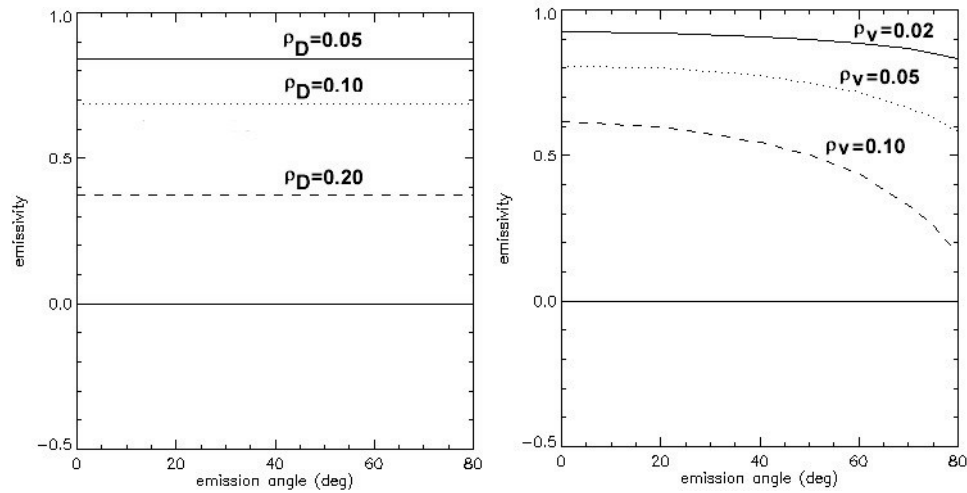


Figure 5.11: Plots showing  $S_0$  emissivity dependence on diffuse and volume scattering

angle dependence is present in the emissivity values as expected. Larger values of  $\rho_d$  result in smaller values of emissivity.

The plot on the right of Figure 5.11 demonstrates the effect of altering the value of  $\rho_v$  on emissivity. Increasing the value of  $\rho_v$  has the effect of reducing the emissivity, just as was demonstrated for the  $\rho_d$  term. However, the  $\rho_v$  term has an emission angle dependence, that the  $\rho_d$  term does not, that produces a gradual fall off in emissivity for larger emission angles. This fall off in emissivity is similar to the fall off produced by the Fresnel term, however it has no effect on the  $S_1$ ,  $S_2$ , or  $S_3$  terms of the emissivity Stoke's vector.

## 5.6 Chapter Summary

This chapter has presented the generalized polarimetric BRDF, originally examined in my dissertation proposal [9] and expanded upon in detail in Jim Shell's dissertation [29]. The polarized BRDF is powerful, in that it can mimic commonly utilized BRDFs (such as the Beard-Maxwell BRDF utilized by the NEF database) or be configured to describe new ones.

This chapter has examined the sensitivity of the generalized polarimetric BRDF and polarized emissivity model to key BRDF parameters. The generalized BRDF was found to be most sensitive to surface slope probability function parameters  $\sigma$  and *BIAS* as well as the unpolarized  $\rho_D$  and  $\rho_V$  components. For most material surfaces, the BRDF is quite insensitive to the shadowing and obscuration function configuration. The shadowing and obscuration function is most sensitive to its parameters  $\tau$  and  $\Omega$  when the surface roughness parameter  $\sigma$  is high (for example, greater than 0.4). However, in the cases where the surface roughness is high, it is usually more appropriate to capture the diffuse, de-polarizing scattering behavior in the  $\rho_D$  term, not in the specular term.

Finally, the sensitivity of the polarized emissivity model to the input parameters was also presented. The emissivity model was found to be somewhat over parameterized, in that the same emissivity curve is easily found utilizing various combinations of complex index of refraction and surface slope distribution function *BIAS* parameters. The values of the  $S_1$  component of the emissivity model are driven primarily by a combination of (1) the *BIAS* and complex index of refraction and (2) the surface slope variance (aka roughness) parameter  $\sigma$ . Due to the azimuthal symmetry assumed for surface roughness, the  $S_2$  parameter of thermal emissivity is always zero by definition. In all cases, we find the polarization of the modeled surfaces to always be negative (*p* polarized) in the  $S_1$  component and strongest at grazing angles. This general property of the polarimetric state of emitted radiance is in contrast to reflected light which is generally positive in the Stoke's  $S_1$  component (*s* polarized). Therefore, surfaces that have strong polarized reflection and emission properties may appear to have no polarization signature when the level of radiance reflected from the surface is comparable to the level of radiance thermally emitted from the surface (Figure 5.12).

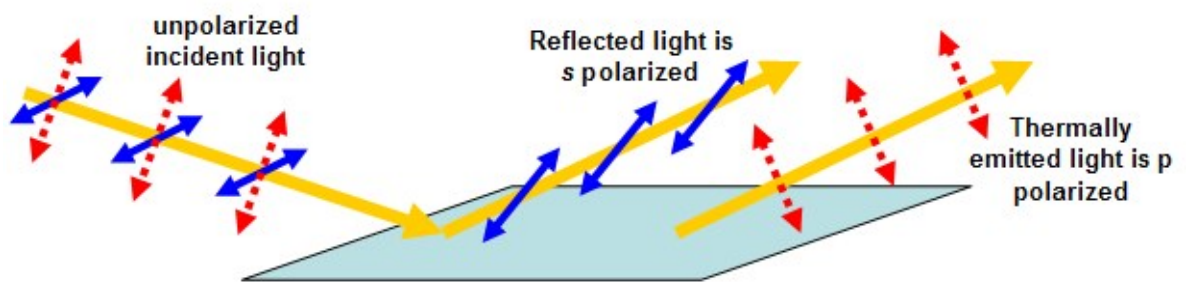


Figure 5.12: Illustration of dominant polarization state for reflected and emitted light



# Chapter 6

## Measurement of Polarized Emissivity

This chapter describes how polarized emissivity will be measured and infrared Stoke's imagery generated. Section 6.1 presents the radiometry that is relevant to the experimental technique, the imaging system design, calibration, and image collection techniques. Section 6.2 summarizes the polarized emissivity measurement results. Section 6.3 presents a technique and results for fitting the experimental results to the polarized emissivity model described in Chapter 5. Finally, Section 6.4 examines the errors associated with the experimental measurements.

### 6.1 Measurement Approach

Before making polarized emissivity measurements and generating infrared Stoke's image sets, it makes good sense to first understand the key radiometric terms involved in the radiance reaching the front of an IR polarimeter. A system design will be developed that pays careful attention to the environmental conditions as well as hardware constraints. The images collected and the algorithms utilized to extract

thermal emissivity from them will utilize the radiometric terms presented in 6.1.1 and the key design points in 6.1.2.

### 6.1.1 Radiometric Framework

Consider a generic infrared camera equipped with a linear polarizer having rotation capability. Let the rotation angle of the polarizer be designated by an orientation angle  $\alpha$ . Let us also assume that the target to camera path transmission loss is negligible.

There are a total of five radiometric terms (see Figure 6.1) that contribute to the total radiance reaching an infrared sensor through an infrared wire grid polarizer (WGP):

- Downwelled radiance reflected from target:  $\rho(\alpha)L_{dw}\tau_p$
- Thermally emitted radiance from target:  $\epsilon(\alpha)L_{BB}\tau_p$
- Upwelled radiance from the path between the target and polarizer:  $L_{uw}\tau_p$
- Downwelled radiance reflected from polarizer surface:  $\rho_p L_{dw}$
- Thermally emitted radiance from polarizer surface:  $\epsilon_p L_{BB}$

where  $L_{dw}$  represents the downwelled radiance,  $L_{uw}$  represents the upwelled radiance,  $\rho_p$  the reflectivity of the polarizer for randomly polarized light,  $\epsilon_p$  the emissivity of the polarizer,  $\tau_p$  the transmission of the polarizer for randomly polarized light,  $L_{BB}$  the radiance coming from a blackbody at ambient temperature,  $\epsilon(\alpha)$  the target emissivity, and  $\rho(\alpha)$  is the target reflectivity.

Therefore, the total radiance incident to the camera aperture is

$$L(\alpha) = \tau_p(\rho(\alpha)L_{dw} + L_{uw} + \epsilon(\alpha)L_{BB}(T)) + \epsilon_p L_{BB}(T) + \rho_p L_{dw} \quad (6.1)$$

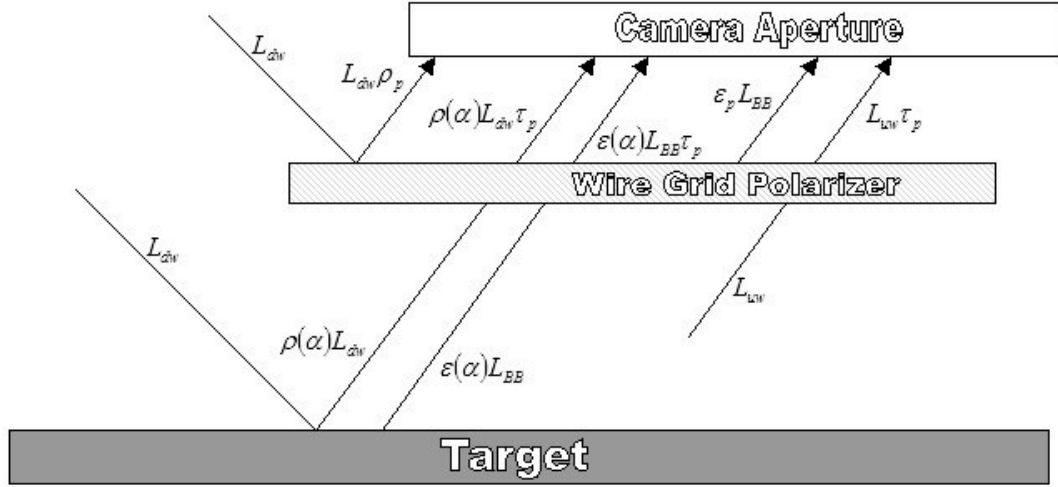


Figure 6.1: Illustration of relevant radiometric terms

where the variable  $T$  is the ambient air temperature.

For this experimental setup, we assume that the upwelled radiance between the sample and the camera is insignificant such that  $L_{uw} = 0$ . Now, the equation simplifies to

$$L(\alpha) = \tau_p(\rho(\alpha)L_{dw} + \epsilon(\alpha)L_{BB}(T)) + \epsilon_p L_{BB}(T) + \rho_p L_{dw} \quad (6.2)$$

Making the assumption that the emissivity of the wire grid polarizer is negligible [34] ( $\epsilon_p L_{BB} = 0$ ), we can solve for the target emissivity  $\epsilon(\alpha)$  as a function of WGP orientation angle  $\alpha$ ,

$$\epsilon(\alpha) = \frac{L(\alpha) - \tau_p L_{dw} - \rho_p L_{dw}}{\tau_p (L_{BB}(T) - L_{dw})} \quad (6.3)$$

Recall that if the emissivity of the wire grid polarizer is zero, we can write the Kirchoff's Law relation for the polarizer as

$$\tau_p + \rho_p = 1 \quad (6.4)$$

allowing us to reduce Equation 6.3 even further to

$$\epsilon(\alpha) = \frac{L(\alpha) - L_{dw}}{\tau_p(L_{BB}(T) - L_{dw})} \quad (6.5)$$

Ideally, we could utilize the internal calibration of the LWIR camera and derive the blackbody radiance term  $L_{BB}$  from the camera metadata. The camera metadata provides a relationship between digital count values and scene temperature assuming each material has an emissivity of 1.0 (this value is user selectable). Knowing the bandpass of the camera and the measured temperature allows us to derive an effective blackbody radiance value. However, repeated attempts demonstrated the internal calibration of the camera was not repeatable and accurate, requiring a user based calibration method (see Section 6.1.3).

In order to derive the downwelled skydome radiance term  $L_{dw}$  we can include a 100% long wave IR reflector in the scene. A readily available reflector in this wavelength region is Aluminum foil manufactured by Reynold's Wrap. In addition, we include a diffuse IR reflector and a specular IR reflector in each target scene. This feature allows us to choose an IR reflector that is closet to the surface roughness of the sample target of interest.

Plugging in values of  $\rho = 1$  and  $\epsilon = 0$  into equation 6.1 gives us the radiance  $L_{100}$  we expect to see at the camera aperture in the direction of the IR reflector.

$$L_{100}(T) = \tau_p L_{dw} + \epsilon_p L_{BB}(T) + \rho_p L_{dw} \quad (6.6)$$

We can again utilize equation 6.4 to further reduce this expression to

$$L_{100}(T) = L_{dw} \quad (6.7)$$

The next step is for us to solve for the target emissivity  $\epsilon(\alpha)$  utilizing our knowl-

edge of  $L_{dw}$  into equation 6.5,

$$\epsilon(\alpha) = \frac{L(\alpha, T) - L_{100}}{\tau_p(L_{BB}(T) - L_{100})} \quad (6.8)$$

### 6.1.2 Imaging System Design

Since we are primarily interested in measuring infrared emissivity, not reflectivity, we need to define the critical system design constraints.

- Thermal radiance incident onto the target sample surfaces must be kept much lower than the thermally emitted radiance. Inspection of equation 6.5 demonstrates that once the downwelled radiance level approaches the thermally emitted radiance level, the fraction is numerically unstable and noisy.
- The system must operate under nighttime conditions to avoid solar heating of target surfaces.
- The system must operate under ambient thermal conditions, requiring no sample heating or cooling.
- The camera must operate under ambient thermal conditions, requiring no cooling of the focal plane. This allows for rapid deployment of the imaging system to a wide variety of locations not equipped with a liquid coolant.
- The atmosphere conditions must be thermally stable. An acceptable rate of change in air temperature is  $< 1^\circ\text{C}$  per 30 minutes. Not only do we not want the sample temperatures to change during a measurement cycle, we also want the rate of change to be slow enough that the sample temperatures track well with the ambient air temperature in order to insure consistency between multiple samples within a scene.



Figure 6.2: EZTherm LWIR camera and IR wire grid polarizer

- A polarizer that has high transmission and high contrast ratio in the long wave region of the spectrum.
- An experimental setup capable of measuring emission zenith angles ranging from 0 to 80 degrees.

### LWIR Camera

To meet the camera design constraints, the EZTherm long wave infrared camera (Figure 6.2) was chosen for imaging. The focal plane array of this camera is an uncooled Barium-Strontium-Titanate (BST) material. Contrary to common CCD operation where charge is collected and proportional to scene intensity, the BST material produces a measurable resistance change as a function of temperature gradient. The focal plane has a temperature sweet spot where it is most sensitive, requiring active focal plane temperature control. The pixel pitch is 50 microns square and the array capable of 12-bit digitization. The camera is capable of measuring blackbody temperatures between -20C and 500C.

The effective focal length of the optics is 35 mm, while the primary aperture size is 29 mm resulting in a F/1.2 imager. The camera has a specified noise equivalent delta temperature of 0.080K. The manufacturer specs the camera to operate between -10C to +40C ambient air temperature.

The image data is accompanied by useful metadata such as air temperature, internal camera temperature, capture time and date. In addition, the camera is battery operated and housed in a camcorder case allowing collections almost anywhere.

### **Polarizer**

The polarizer chosen is a wire grid polarizer manufactured by Moletron (Figure 6.2). The polarizer has a 75 mm diameter clear aperture. The wire grid is a fine micro patterned mesh of aluminum wires on a ZnSe substrate. An important property of wire grid polarizers, whether in the visible region or infrared region of the spectrum, is that they both transmit and reflect light (see Figure 6.3). More specifically, light that oscillates parallel to the patterned lines of the wire grid is reflected while light that oscillates perpendicular to the grid pattern is transmitted. Wire grid polarizers are superior to the other types of polarizers due to their high contrast ratio and high transmission factors.

Simply putting the IR polarizer in front of the uncooled LWIR camera not only reduces the scene radiance incident on the camera aperture, it also reflects the thermally emitted radiance from the inside of the camera assembly. The first problem this causes is a non-uniform ghost image of the inside of the camera super-imposed onto the scene image. In addition, the shot noise induced by the ghost image drastically increases the NEDT of the resulting image.

The spectral transmission of the polarizer for incident radiance having its electric field vector perpendicular to the direction of the wire grid lines is shown in Figure 6.4. A perfect polarizer would nominally have a transmission value of 1 for this plot,

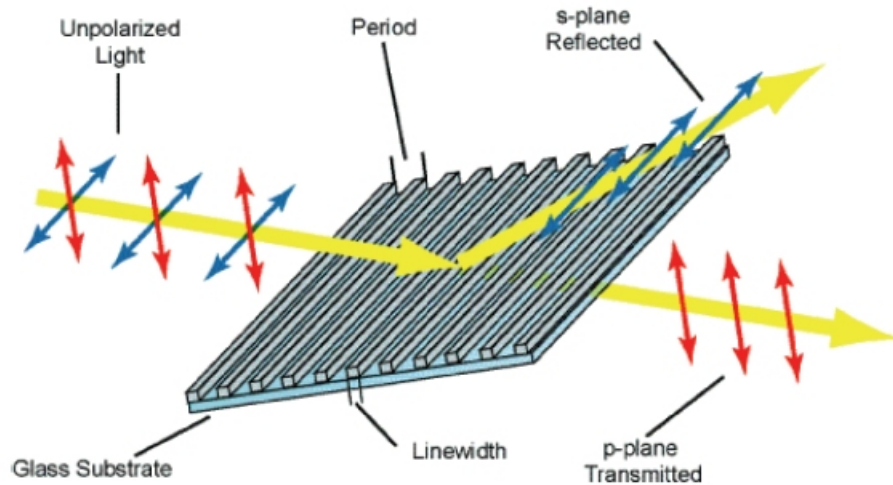


Figure 6.3: Illustration showing how a wire grid polarizer reflects one polarization state and transmits another (reprinted from Reference [37])

indicating that it transmits all light of the preferred polarization state. The contrast ratio, defined as the amount of light transmitted with the appropriate polarization state to the amount of light transmitted with the incorrect polarization state, is reported by the manufacturer to be better than 400:1.

The solution is to tip the polarizer at an angle relative to the camera aperture. The polarizer can be tipped to an angle that insures that the radiance reflected from its surface comes from a uniform and cold source. For this experimental setup, we choose to tip the polarizer such that it reflects the night time, cloud free sky.

Nominally, the camera and polarizer are oriented as shown in Figure 6.5 for best noise performance.

### Sample Platform

Since we have fixed the camera to have an approximate look angle of 45 degrees to the ground, the sample platform must be adjustable to allow measurement of emissivity for zenith angles between 0 and 80 degrees. This can be accomplished by assembling a sample stage that is approximately 24 x 24 inches in size attached to a camera tripod

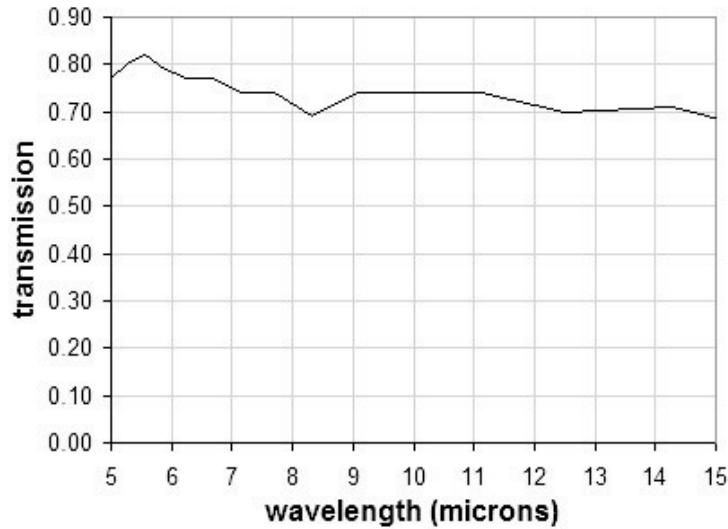


Figure 6.4: Spectral transmission of WGP for incident radiance with electric field vector perpendicular to the wire grid lines

with tip/tilt/rotate capability. The sample stage is made of lightweight particle board and fastened by machine screws to the camera tripod.

Accurate tip angle measurements are made possible by utilizing a Pro 360 Digital Protractor manufactured by Mitutoyo. The angular measurements are reported as a decimal number out to the tenth's place with a rms error specified as +/- 0.1 degrees.

Figure 6.5 shows the relative orientation of the imaging system and the sample platform. The digital protractor measures the angle  $\psi$ , which is related to the emission zenith angle to the camera by equation (6.9).

$$\theta_{emission} = 45^{\circ} - \psi \quad (6.9)$$

Orienting the sample platform at an angle of +45 degrees results in a sample zenith of 0 degrees towards the camera. Orienting the sample platform at an angle of 0 degree relative to the ground plane results in a measurement zenith angle of 45 degrees. As an extra degree of freedom, the camera tripod may be rotated about its primary axis to allow azimuthal rotation of sample surfaces.

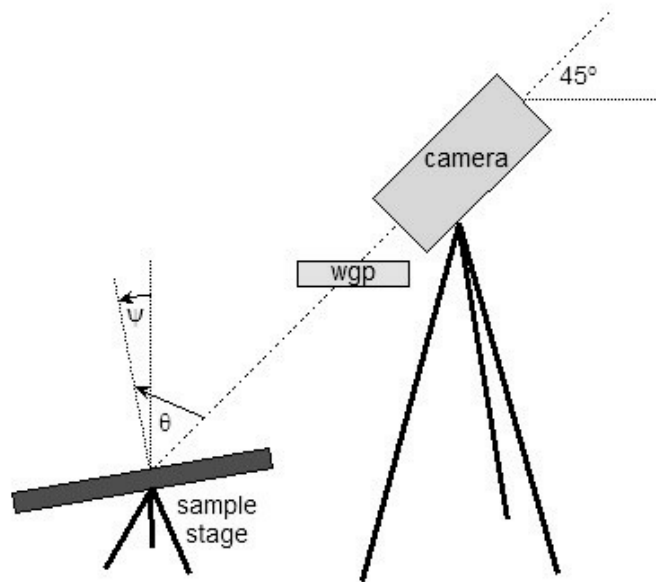


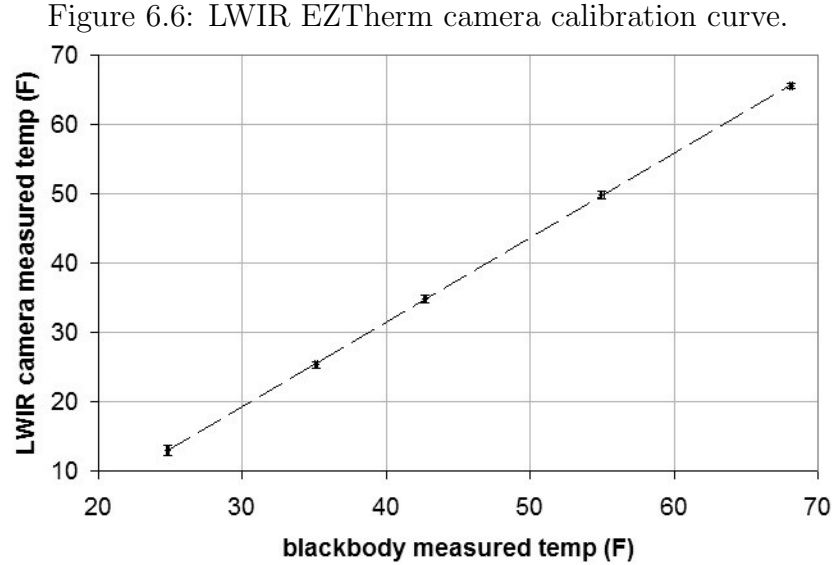
Figure 6.5: Illustration showing the relative alignment of the IR camera assembly and sample measurement stage

### 6.1.3 Imaging System Calibration

The LWIR EZTherm camera was calibrated by imaging into a blackbody cavity of known temperature. The blackbody cavity was constructed by cutting a small opening in a 4-square ball. A temperature probe was placed inside the blackbody cavity, through a back opening, to measure the blackbody temperature. The precision of this temperature measurement was  $\pm 0.1$  degrees F. Although the absolute accuracy of the temperature probe is not known, the temperature probe consistently measured the ambient air temperature in my house to within the precision (integer degree values) of my house thermostat.

The internal temperature of the blackbody cavity was varied by making initial measurements inside my house (ambient temperature between 18 and 20C initially). The blackbody temperature was then lowered by moving the calibration assembly outside and taking data points as the temperature dropped.

Figure 6.6 shows a plot of the original camera calibration curve measured on Dec



12, 2005. Although the camera derived temperature measurement deviated from the temperature probe measurement, there was a consistently linear relationship between the two. This linear relationship is utilized to convert camera derived temperature values to assumed scene temperature values.

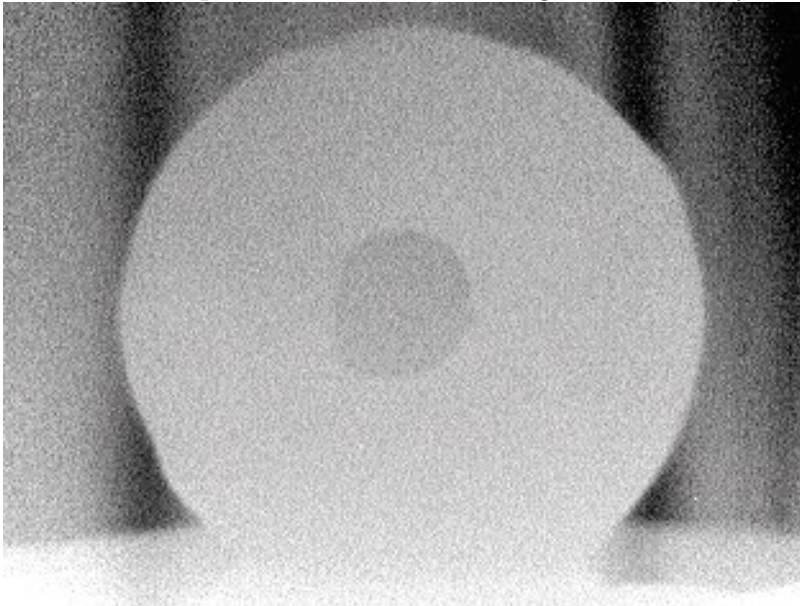
The camera image shown in Figure 6.7 is an example of one data point on the calibration curve. Rapid, in situ measurements of the blackbody cavity temperature were available from the camera interface without having to acquire an image. However the least significant figure of this measured temperature value was only to the tens place (ie. 52F) and not deemed to be enough. Therefore, a camera image was acquired for each temperature probe and analyzed in ENVI. The ENVI analysis consisted of drawing a region of interest over the entire cavity opening and calculating the average and standard deviation of the temperature within the cavity. The data in table 6.1 shows the measured temperature values and their associated uncertainty (the standard deviation for the camera measurement and the least significant digit of the temperature probe measurement).

This specific calibration curve was only applicable to the date on which it was

Table 6.1: LWIR camera calibration curve data points in degrees F.

Blackbody temp	uncertainty	LWIR Camera Measured Temp	uncertainty
24.8	0.1	13.0	0.7
35.1	0.1	25.3	0.5
42.7	0.1	34.8	0.6
55.0	0.1	49.8	0.5
68.1	0.1	65.6	0.4

Figure 6.7: Example of LWIR camera image of blackbody cavity.



acquired. The internal calibration of the camera response appeared to vary significantly from day to day, warranting a new calibration curve to be measured each time the camera was fired up.

#### 6.1.4 Image Collections

Two types of image collections were performed within the scope of this work. The first type of collection was done in order to experimentally determine the polarized emissivity of a wide variety of target and background materials, herein referred to as an *emissivity collection*. Emissivity collections required masking of the imaging system and operator with a wall of aluminum foil. In addition, the ground surrounding the target sample stage was also covered with aluminum foil. The intent of the aluminum foil in both cases is to limit infrared radiance from the camera, the operator, and the ground from reflecting off the target materials. The emissivity measurement technique works best when the amount of thermal radiance incident on the target surfaces is much less than the level of thermally emitted radiance. To accomplish this, the imaging measurements were always done at night under a starlit sky.

In addition, the emissivity collection scenarios required embedding a glossy (pressed flat) aluminum foil target and a diffuse aluminum foil target on the sample stage to facilitate accurate measurement of downwelled radiance. For smooth target surfaces such as glossy paints and glass, the flat aluminum target was utilized to determine downwelled radiance. For rough target surfaces such as flat (diffuse) paints and soil, the diffuse aluminum foil target was utilized to estimate the level of downwelled radiance.

The concept for this approach is to have the reflecting foil target approximate the reflectance distribution function of the target surface in order to more accurately determine how much radiance is indeed reflected from the target surface. For example, consider a scene with a majority of the hemisphere above the sample stage consisting

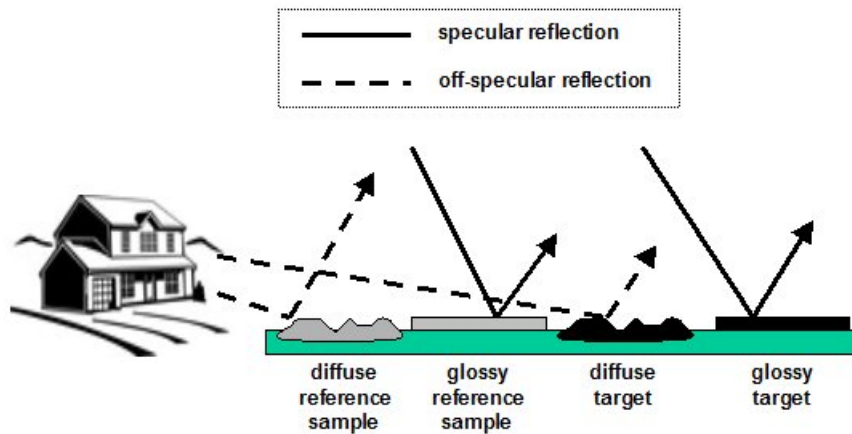


Figure 6.8: Illustration showing importance of including a diffuse and a glossy calibration target

of the skydome, except for a single house far off at a grazing angle (see Figure 6.8). When the camera is viewing close to nadir, a glossy target will not reflect the house but a diffuse target will partially reflect the house. It is important for the reflecting foil target to sample the hemisphere above the targets for incident radiance in a fashion similar to how the target does. Although there are many varying degrees of roughness that could be included to refine this concept, including simple types of reflecting targets is sufficient for this effort.

The second type of collection was performed to examine actual scenes with target materials embedded in backgrounds, herein referred to as *scene collections*. The scene collections are designed to capture both thermally emitted and reflected radiance from man-made target materials embedded in naturally occurring backgrounds. In this collection scenario, aluminum foil surrounding the camera and operator was not necessary due to the increased distance between the imaging system and the targets. A range between the imaging system and targets varied from 15 feet to about 150 feet.

Due to the imaging system design, both types of collection scenarios required a

cloud free sky due to the reflective nature of the wire grid polarizer. If any clouds were present over the target at imaging time, they were clearly visible on the resulting image collected. If the clouds were static (not moving), they could have been backed out during the polarizer reflected radiance correction step of the processing chain. However due to the temporal nature of collecting a calibration image for each polarizer orientation and a scene or measurement image for each polarizer orientation, the clouds would have to have been static over at least a 2 minute period of time. Clouds were encountered on many of the collections nights, and at no time where the clouds static enough to be removed during image processing. Therefore, it was learned that if one or more images in a given image set (4 scene/measurement images and 4 calibration images) contained clouds then the whole set was scrapped.

Additionally, a flat field blackbody calibration image was acquired at multiple times during each collection scenario. This calibration image has two functions: (1) to allow flat-fielding of the acquired imagery and (2) to determine the amount of downwelled radiance reflected from the back surface of the polarizer. Recall that any incident radiance not transmitted by the polarizer (Figure 6.4) is reflected from its surface.

### 6.1.5 Processing of Image Data

This section describes how a raw camera image is processed into a calibrated scene leaving radiance image. Figure 6.9 illustrates this image processing flow.

The EZTherm LWIR camera outputs a 320x240 pixel 12-bit digital count image and an 8-bit temperature image with some support graphics. An IDL function was written to convert the 12-bit raw image data to a 12-bit temperature image by correlating it with the 8-bit temperature image.

The raw 12-bit temperature image is then converted to a double precision calibrated temperature image utilizing the camera calibration curve determined according

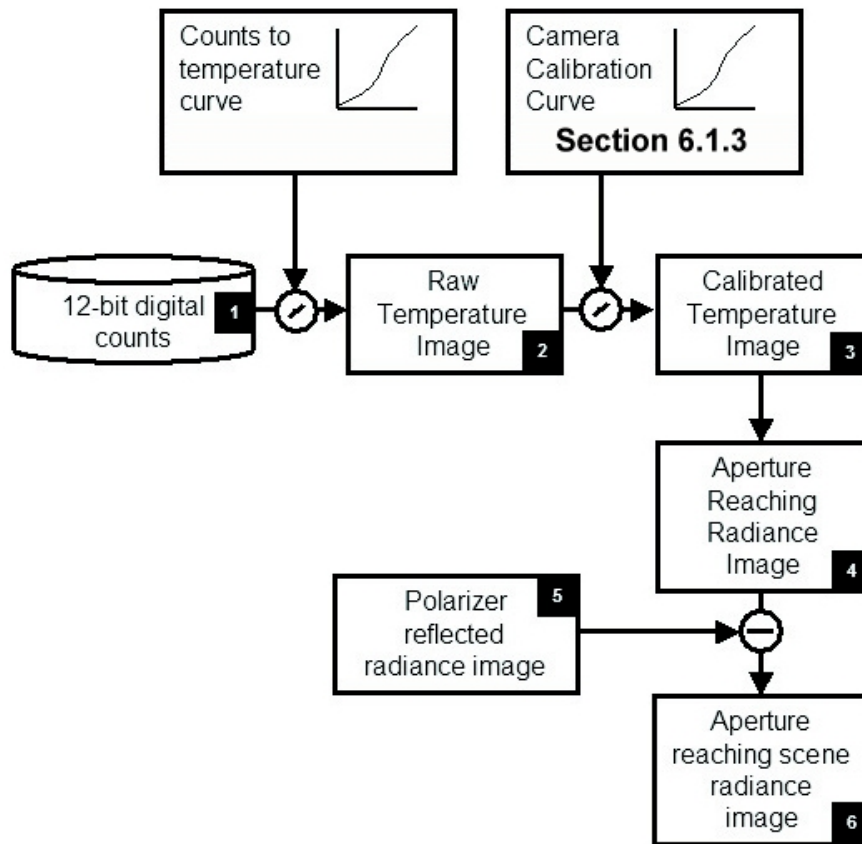


Figure 6.9: Processing flow for experimentally acquired image data

to the procedure described in Section 6.1.3.

Next, the calibrated temperature image is converted to a calibrated aperture reaching radiance image. The functional relationship between the calibrated temperature and aperture reaching radiance image is determined by fitting a 3rd order polynomial to the value of the following integral for temperatures between 220K to 320K in 1 degree increments.

$$L(T) = \int \frac{2hc^2}{\lambda^5} \frac{1}{e^{hc/\lambda kT} - 1} d\lambda \quad (6.10)$$

The 3rd order polynomial that was a best fit between radiance and temperature was found to be

$$L(T) = 0.010225614 + -1.012849 \cdot 10^{-4}T + 2.382483 \cdot 10^{-7}T^2 + 1.552269 \cdot 10^{-10}T^3 \quad (6.11)$$

The variance between the polynomial form and rigorous integration was found to be negligible.

The temperature to radiance conversion utilizes the knowledge that the temperatures reported by the camera correspond to blackbody temperatures (user selected emissivity = 1.0) and the camera has a bandpass of 8-14 microns. The actual spectral response of the camera is not known, so we assume a flat 8-14 micron spectral response as a first order estimate. This should be suitable, in that the radiometric estimates provided by the temperature to radiance conversion are meant to be order of magnitude accurate only and to capture the non-linear relationship between temperature and radiance. An example of a calibrated aperture reaching radiance image is shown on the left hand side of Figure 6.10.

Next, the calibrated aperture reaching radiance image is converted to an *aperture reaching, scene leaving* radiance image by removing the effects of the wire grid polarizer reflections. For each collection scenario, a flat aluminum foil target is placed

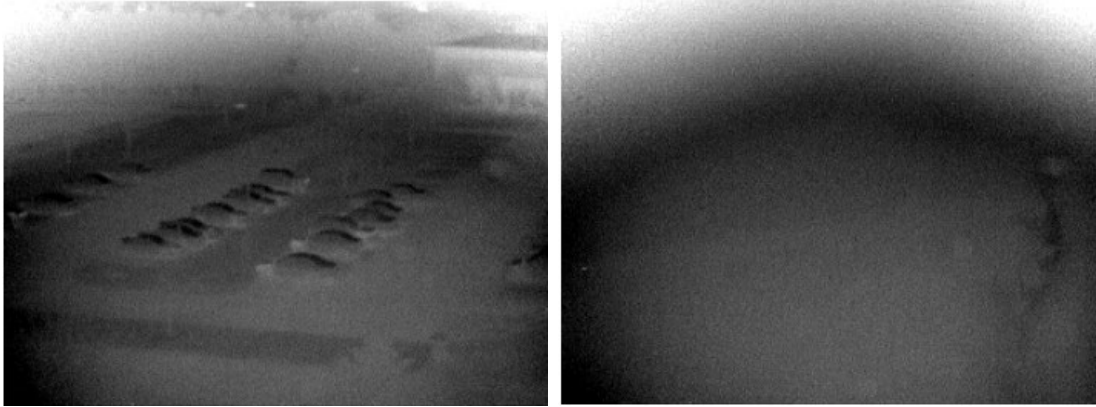


Figure 6.10: Image examples showing intensity image before removal of polarizer reflectance and the polarizer reflectance image

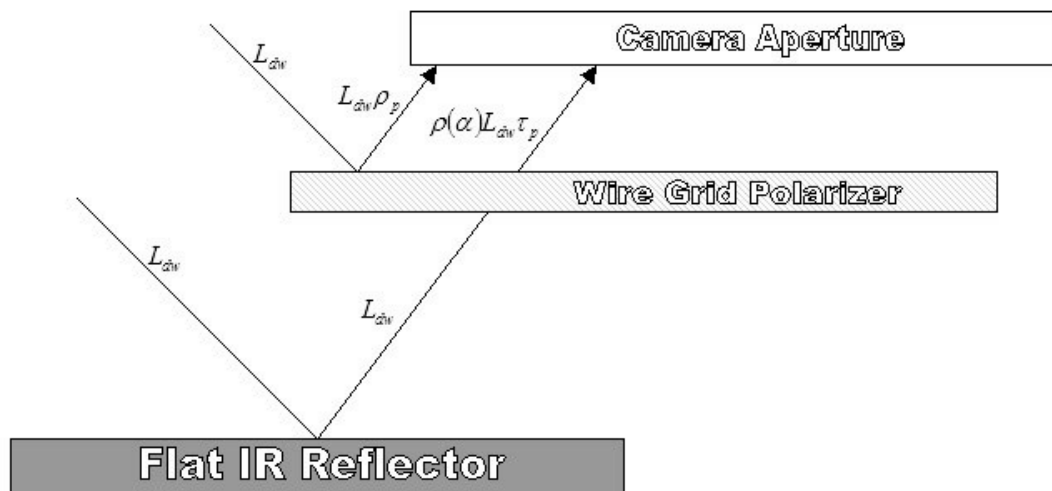


Figure 6.11: Illustration of radiance reaching camera for WGP calibration image acquisition



Figure 6.12: Example of surface leaving, aperture reaching radiance image, with polarizer at 0 degree orientation

in front of the wire grid polarizer such that it reflects the downwelled skydome radiance. The illustration in Figure 6.11 shows this configuration. An example of a WGP calibration image is shown on the right hand side of Figure 6.10. For the WGP calibration image, the governing equation is

$$L_{WGP} = \rho_p L_{dw} + \tau_p L_{dw} = L_{dw} \quad (6.12)$$

In order to remove only the polarizer reflected radiance, the WGP calibration image is scaled by  $(1 - \tau_p)$  which is the same as  $\rho_p$  (derived from Figure 6.4). In addition to removing polarizer reflected radiance, this processing step also serves as a flat-fielding step. The image presented in Figure 6.12 is an example of a scene leaving, aperture reaching radiance image.

Once the aperture reaching, scene leaving radiance image is produced, there are two distinct processing paths which may be followed. The flowchart in Figure 6.13 shows these two distinct data processing paths, one to generate Stoke's images of a scene and one to generate polarized emissivity values from a specific experimental setup.

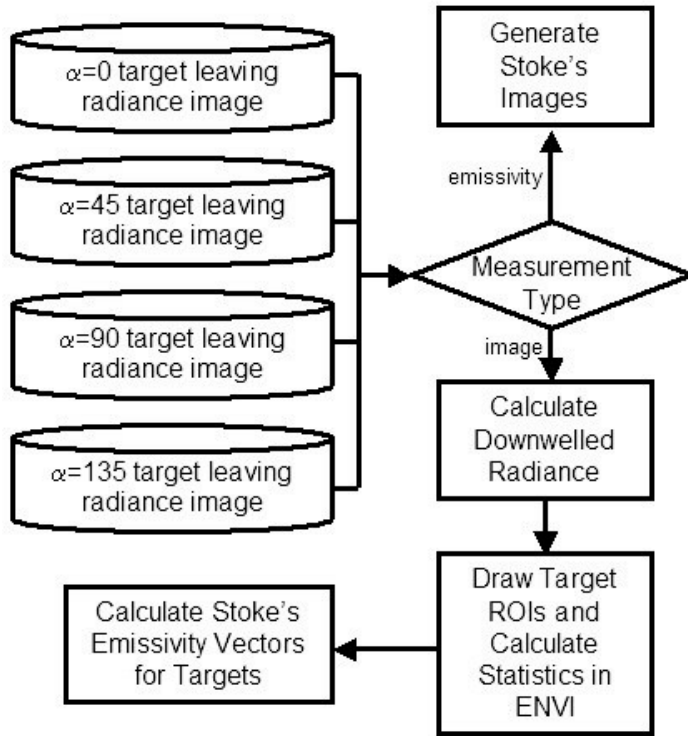


Figure 6.13: Processing paths for Stoke's generated imagery and emissivity measurements

### Processing for Stoke's Image Generation

For image data that is intended to be processed into Stoke's images, the four image bands are simply combined as shown in equations 6.13, 6.14, and 6.15 to form  $S_0$ ,  $S_1$  and  $S_2$  images. Recall that there is no  $S_3$  image data due to the lack of a circular polarizer in the experimental setup.

$$S_0 = \frac{1}{2}(L_{SLAR}(0) + L_{SLAR}(45) + L_{SLAR}(90) + L_{SLAR}(135)) \quad (6.13)$$

$$S_1 = L_{SLAR}(0) - L_{SLAR}(90) \quad (6.14)$$

$$S_2 = L_{SLAR}(45) - L_{SLAR}(135) \quad (6.15)$$

Recall that when the polarizer is oriented at 0 and 90 degrees, the camera system

is measuring the horizontal and vertical polarization states respectively of the scene leaving radiance.

Although the  $S_0$  images may be generated as a combination of the 0 and 90 or 45 and 135 radiance images, we have chosen to add all four images and then divide by 2 in order to reduce the NEDT of the resulting  $S_0$  image. Figure 6.14 shows an example of the Stoke's  $S_0$ ,  $S_1$ , and  $S_2$  images produced following this path.

### Processing for Polarized Emissivity Measurement

For image data that is collected for the purpose of target emissivity measurement, the processing chain differs from the Stoke's image generation chain described above (see Figure 6.13). The following example presents the processing utilized to calculate polarized emissivity on a series of targets from the August 8, 2006 collection. This specific example has the targets with a zenith angle of 40 degrees relative to the camera.

The images in Figure 6.15 show the target image before and after removal of the polarizer reflected radiance. These images correspond to steps 4 and 6 of the scene leaving, aperture reaching (SLAR) radiance processing flow (Figure 6.9).

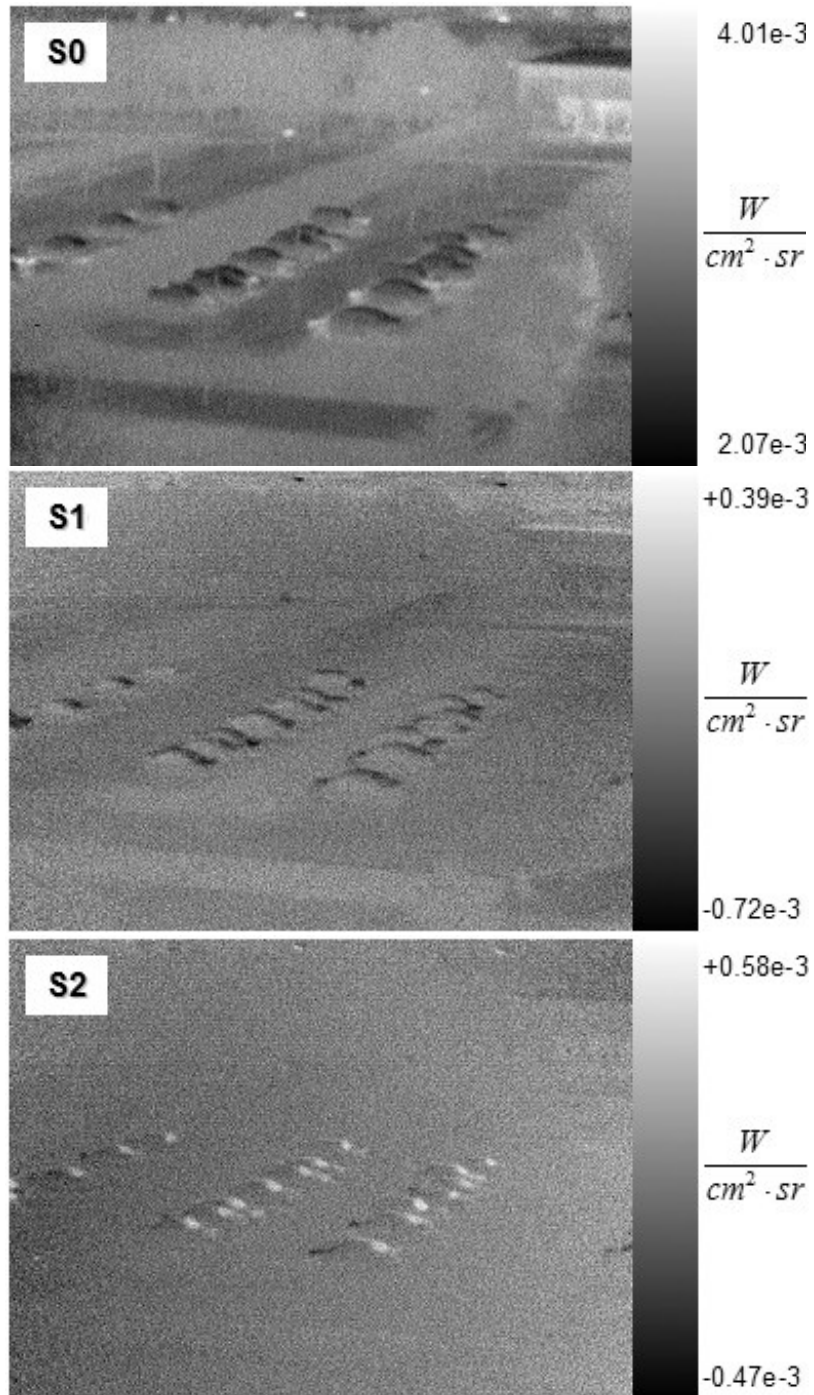


Figure 6.14: Image examples of processed Stoke's radiance bands  $S_0$ ,  $S_1$ , and  $S_2$

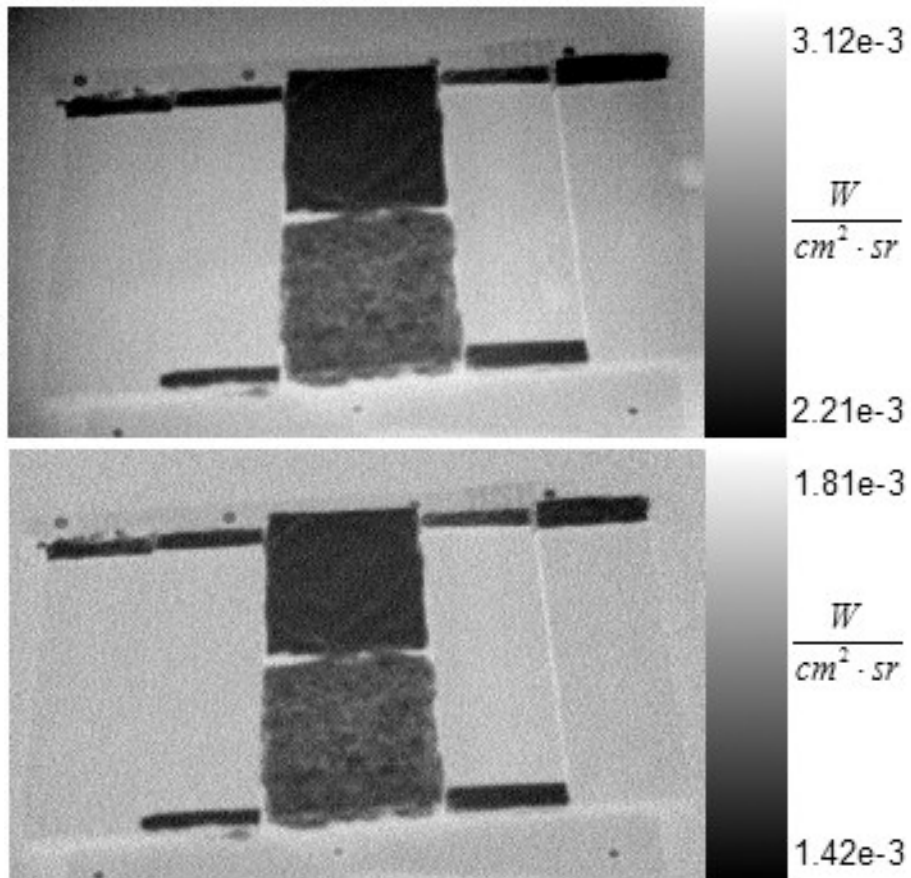


Figure 6.15: Image examples of targets setup for emissivity measurement (a) before removal of reflected polarizer radiance and (b) after removal of reflected polarizer radiance

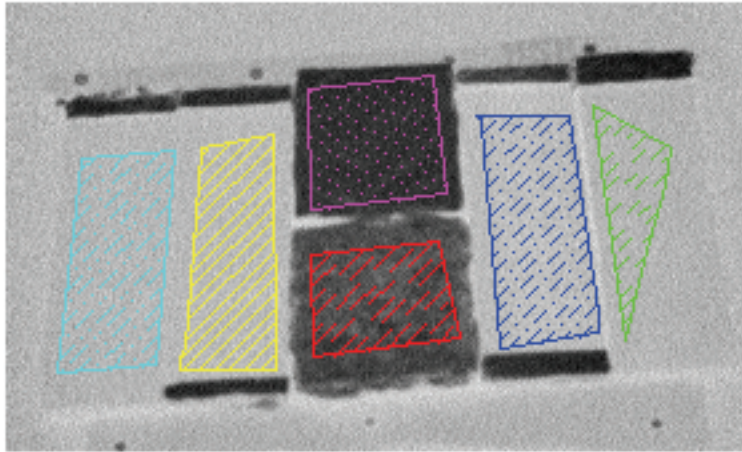


Figure 6.16: Image example showing regions of interest drawn with the ENVI ROI tool

After the four intensity band radiance images are corrected for polarizer reflected radiance, the images are imported into ENVI and target regions of interest (ROI) are setup. Specifically, a ROI is drawn over the flat and diffuse IR reflectors in order to determine the amount of downwelled radiance that each target is subjected to. Next, regions of interest are drawn over each target material. For this example, the targets are (from left to right) glossy black paint on wood, glossy tan paint on wood, flat IR reflector, diffuse IR reflector, bare pine wood, and ultra flat black paint on wood. Figure 6.16 shows the ROIs that were drawn for this example.

These target ROIs are drawn to encompass as much target surface as possible in order to increase the SNR of the statistics as well as best represent each target as a whole. From the target ROI statistics generated by ENVI, the average scene leaving, aperture reaching radiance is determined and the corresponding standard deviation. The data in table 6.2 represents the  $L_{SLAR}$  values for each target and polarizer orientation.

At this point, the radiometrically calibrated image data is represented by the

Table 6.2: Table of surface leaving aperture reaching radiance values

target	$L_{SLAR}(0)$	$L_{SLAR}(45)$	$L_{SLAR}(90)$	$L_{SLAR}(135)$
diffuse reflector	1.497E-03	1.495E-03	1.492E-03	1.488E-03
flat black paint	1.677E-03	1.672E-03	1.702E-03	1.665E-03
bare pine wood	1.691E-03	1.685E-03	1.726E-03	1.698E-03
glossy tan paint	1.684E-03	1.692E-03	1.706E-03	1.692E-03
glossy black paint	1.683E-03	1.686E-03	1.708E-03	1.696E-03
flat reflector	1.448E-03	1.442E-03	1.439E-03	1.437E-03

Table 6.3: Table of SLAR Stoke's vector components

target	$(S_0)_{SLAR}$	$(S_1)_{SLAR}$	$(S_2)_{SLAR}$
flat black paint	3.358E-03	-2.541E-05	7.148E-06
bare pine wood	3.400E-03	-3.530E-05	-1.286E-05
glossy tan paint	3.387E-03	-2.213E-05	3.818E-07
glossy black paint	3.387E-03	-2.563E-05	-1.003E-05

following governing equation

$$L_{SLAR}(\alpha) = \tau_p(1 - \epsilon(\alpha))L_{dw} + \tau_p\epsilon(\alpha)L_{BB} \quad (6.16)$$

where  $\alpha$  is the polarizer rotation angle. From the SLAR radiance at polarizer orientations of 0, 45, 90, and 135 degrees, we can calculate a SLAR Stoke's vector

$$\vec{S}_{SLAR} = \begin{pmatrix} \frac{1}{2}(L_{SLAR}(0) + L_{SLAR}(45) + L_{SLAR}(90) + L_{SLAR}(135)) \\ L_{SLAR}(0) - L_{SLAR}(90) \\ L_{SLAR}(45) - L_{SLAR}(135) \\ 0 \end{pmatrix} \quad (6.17)$$

The data in table 6.3 shows the SLAR radiance values in table 6.2 converted to Stoke's vector components via equation 6.17.

Knowing this Stoke's vector, we can rewrite equation 6.16 as

$$\vec{S}_{SLAR} = \tau_p(1 - \vec{\epsilon})L_{dw} + \tau_p\vec{\epsilon}L_{BB} \quad (6.18)$$

Table 6.4: Table of Stoke's emissivity vector values

target	$\epsilon_{S0}$	$\epsilon_{S1}$	$\epsilon_{S2}$
flat black paint	0.858	-0.058	0.016
bare pine wood	0.955	-0.081	-0.030
glossy tan paint	0.924	-0.051	0.001
glossy black paint	0.923	-0.059	-0.023

where  $\vec{\epsilon}$  is the polarized Stoke's emissivity vector. Solving for each component of the Stoke's emissivity vector, we find

$$\epsilon_{S0} = \frac{(S_0)_{SLAR} - \tau_p L_{dw}}{\tau_p L_{BB} - \tau_p L_{dw}} \quad (6.19)$$

$$\epsilon_{S1} = \frac{(S_1)_{SLAR}}{\tau_p L_{BB} - \tau_p L_{dw}} \quad (6.20)$$

$$\epsilon_{S2} = \frac{(S_2)_{SLAR}}{\tau_p L_{BB} - \tau_p L_{dw}} \quad (6.21)$$

Utilizing these equations, we can now numerically solve for the Stoke's emissivity vector components. The data in table 6.4 shows the resulting Stoke's emissivity vector components for the targets in this example. Recall that  $L_{BB}$  is derived knowing the ambient scene temperature and utilizing equation 6.11 ( $3.42 \cdot 10^{-3} W/cm^2/sr$  for this example),  $L_{dw}$  is derived from the in-scene infrared reflector panel, and  $\tau_p$  is the broad band polarizer transmission for randomly polarized light. In order to determine the  $\vec{S}_{SLAR}$  stoke's vector, we plug in the results from the ENVI region of interest analysis into equation 6.17.

## 6.2 Measurement Results

A total of 16 materials were chosen for polarized emission characterization by the method described in Section 6.1: snow, tree bark, soil, grass, particle board, brick, cement (aka concrete), roofing shingle, weathered and fresh asphalt, particle board, pine wood, flat black painted wood, glossy black painted wood, glossy tan painted wood, glass and a car hood. Digital camera images of these target and background materials are found in Figures 6.17, 6.18, and 6.19.

Measured Stoke's emissivity vector results as a function of zenith angle are shown in the tables below for all sixteen materials. The tree bark results are an average of measurements conducted on three different types of tree bark obtained from trees in Maplewood Park, Rochester, NY. The grass measurements were performed on a chunk of grass pulled from my lawn in early spring. At this time of year, the grass was a mixture of dead and green grass blades.

The flat black paint was Krylon brand ultra-flat finish. The glossy black paint was Krylon brand glossy finish. The glossy tan paint was a "desert tan" high solids enamel manufactured by LHB Industries.

The car hood sample was cut from a medium-blue colored sports car hood. The hood itself was obtained from a automobile repair shop. The glass sample was approximately 8 by 10 inches in size and was retrieved from a picture frame. The roofing shingle, concrete, brick, and asphalt samples were obtained from local construction sites.



Figure 6.17: Color digital camera photos of natural target materials: (a) snow, (b) tree bark (c) soil (d) grass.

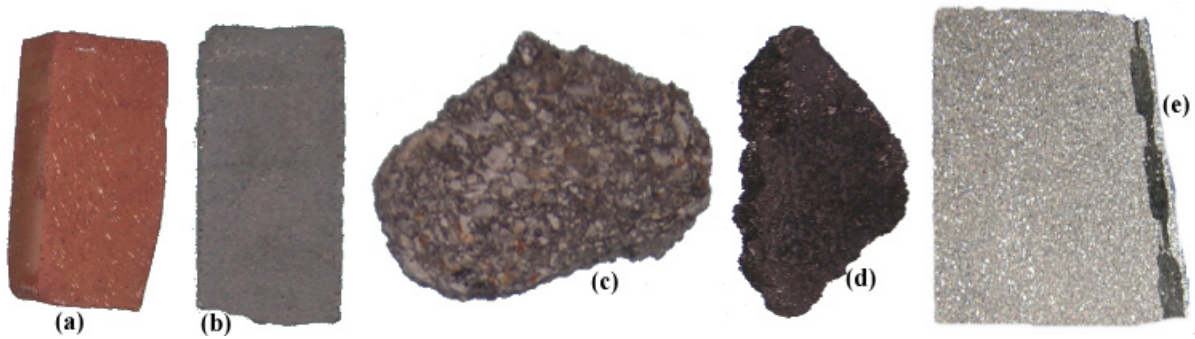


Figure 6.18: Color digital camera photos of construction target materials: (a) brick (b) cement (c) weathered asphalt (d) freshly coated asphalt (e) roofing shingle.

Table 6.5: Polarized emissivity results for tree bark

Angle (deg)	$S_0$	$S_1$	$S_2$
0.0	0.932	-0.004	0.024
10.0	0.903	0.036	-0.030
20.0	0.893	0.002	0.038
30.0	0.912	-0.021	0.001
40.0	0.910	0.035	0.028
50.0	0.882	0.007	0.033
60.0	0.895	-0.033	0.001
70.0	0.891	-0.037	-0.000
80.0	0.863	-0.038	0.027

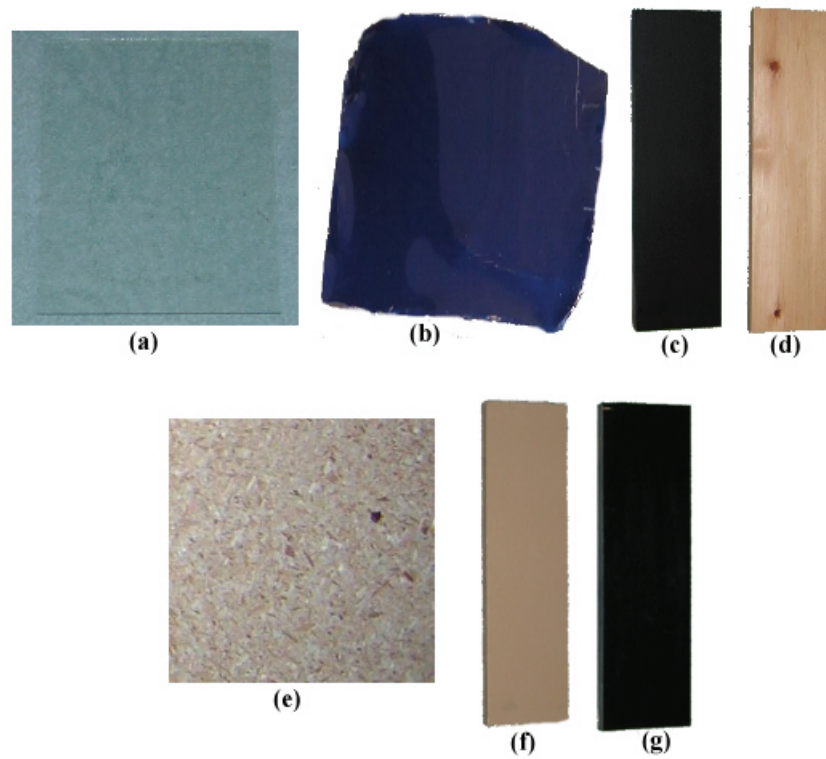


Figure 6.19: Color digital camera photos of miscellaneous target materials: (a) glass (shown sitting on top of a green towel) (b) car hood (c) ultra-flat black painted board (d) pine board (e) particle board (e) glossy tan painted board (f) glossy black coated board.

Table 6.6: Polarized emissivity results for brick

Angle (deg)	$S_0$	$S_1$	$S_2$
0.0	0.910	-0.017	0.012
10.0	0.915	-0.019	-0.020
20.0	0.905	-0.022	-0.004
30.0	0.910	-0.001	0.020
40.0	0.913	-0.018	-0.003
50.0	0.855	-0.017	-0.004
60.0	0.783	-0.032	0.012
70.0	0.660	-0.107	0.007

Table 6.7: Polarized emissivity results for cement

Angle (deg)	$S_0$	$S_1$	$S_2$
0.0	0.969	0.040	0.023
10.0	0.938	-0.010	0.017
20.0	0.935	-0.028	-0.019
30.0	0.937	-0.022	-0.003
40.0	0.937	-0.022	-0.001
50.0	0.940	-0.012	-0.010
60.0	0.922	-0.016	0.014
70.0	0.867	-0.025	-0.010
80.0	0.745	-0.049	-0.014

Table 6.8: Polarized emissivity results for soil

Angle (deg)	$S_0$	$S_1$	$S_2$
0.0	0.910	-0.001	0.009
10.0	0.920	-0.005	0.005
20.0	0.930	-0.011	-0.009
30.0	0.920	-0.017	0.003
40.0	0.880	-0.018	0.003
50.0	0.900	-0.018	-0.011
60.0	0.910	-0.015	0.003
70.0	0.930	-0.040	0.003
80.0	1.020	-0.029	-0.010

Table 6.9: Polarized emissivity results for fresh asphalt

Angle (deg)	$S_0$	$S_1$	$S_2$
0.0	1.008	-0.031	0.032
10.0	0.967	-0.011	-0.029
20.0	0.964	-0.021	-0.025
30.0	0.967	-0.033	0.005
40.0	0.950	-0.012	-0.027
50.0	0.952	-0.005	0.030
60.0	0.959	-0.028	-0.028
70.0	0.904	-0.054	0.005
80.0	0.856	-0.081	0.021

Table 6.10: Polarized emissivity results for flat black paint

Angle (deg)	$S_0$	$S_1$	$S_2$
0.0	1.100	0.009	0.020
10.0	0.942	-0.020	-0.012
20.0	0.924	-0.013	-0.041
30.0	0.906	-0.052	0.024
40.0	0.857	-0.059	0.017
50.0	0.912	-0.073	0.032
60.0	0.852	-0.081	0.012
70.0	0.740	-0.084	-0.035

Table 6.11: Polarized emissivity results for glossy black paint

Angle (deg)	$S_0$	$S_1$	$S_2$
0.0	0.993	0.020	0.022
10.0	0.936	-0.020	0.030
20.0	0.943	-0.019	0.012
30.0	0.936	-0.038	0.000
40.0	0.923	-0.059	0.012
50.0	0.853	-0.087	0.032
60.0	0.756	-0.124	-0.017
70.0	0.701	-0.159	-0.018

Table 6.12: Polarized emissivity results for glass

Angle (deg)	$S_0$	$S_1$	$S_2$
0.0	0.980	0.025	0.020
10.0	0.950	-0.010	0.010
20.0	0.940	-0.011	0.010
30.0	0.960	-0.029	-0.010
40.0	0.960	-0.047	-0.020
50.0	0.940	-0.075	0.030
60.0	0.910	-0.100	0.010
70.0	0.800	-0.140	-0.020

Table 6.13: Polarized emissivity results for grass

Angle (deg)	$S_0$	$S_1$	$S_2$
0.0	0.998	-0.020	-0.008
10.0	0.983	-0.013	-0.005
20.0	0.965	-0.013	-0.021
30.0	0.977	0.006	-0.013
40.0	0.977	0.029	0.004
50.0	0.974	0.006	-0.027
60.0	0.983	0.014	0.011
70.0	0.951	0.005	-0.010
80.0	0.934	0.029	0.026

Table 6.14: Polarized emissivity results for glossy tan paint

Angle (deg)	$S_0$	$S_1$	$S_2$
0.0	1.102	0.040	-0.030
10.0	0.938	-0.025	-0.019
20.0	0.940	-0.021	-0.003
30.0	0.935	-0.041	-0.016
40.0	0.914	-0.063	-0.019
50.0	0.849	-0.092	0.026
60.0	0.853	-0.118	0.015
70.0	0.723	-0.176	0.021

Table 6.15: Polarized emissivity results for a car hood

Angle (deg)	$S_0$	$S_1$	$S_2$
0.0	0.980	0.030	-0.013
10.0	0.953	-0.019	-0.012
20.0	0.941	-0.021	-0.008
30.0	0.955	-0.038	0.012
40.0	0.963	-0.057	0.021
50.0	0.942	-0.093	0.019
60.0	0.910	-0.138	0.012
70.0	0.799	-0.212	0.030

Table 6.16: Polarized emissivity results for particle board

Angle (deg)	$S_0$	$S_1$	$S_2$
0.0	0.909	-0.029	0.035
10.0	0.851	-0.014	-0.009
20.0	0.849	-0.033	0.014
30.0	0.844	-0.019	-0.003
40.0	0.820	-0.018	-0.019
50.0	0.802	-0.030	0.004
60.0	0.777	-0.042	0.010
70.0	0.694	-0.054	-0.012
80.0	0.521	-0.083	-0.014

Table 6.17: Polarized emissivity results for a pine board

Angle (deg)	$S_0$	$S_1$	$S_2$
0.0	0.950	0.030	0.024
10.0	0.925	-0.020	-0.012
20.0	0.942	-0.010	0.013
30.0	0.967	-0.083	0.051
40.0	0.954	-0.080	-0.030
50.0	0.920	-0.136	0.086
60.0	0.820	-0.145	-0.020
70.0	0.735	-0.178	0.049

Table 6.18: Polarized emissivity results for roofing shingle

Angle (deg)	$S_0$	$S_1$	$S_2$
0.0	1.020	-0.022	-0.010
10.0	0.903	-0.018	0.005
20.0	0.980	-0.022	0.012
30.0	0.900	-0.011	0.011
40.0	0.908	-0.038	0.012
50.0	0.957	-0.054	0.052
60.0	0.938	-0.061	-0.033
70.0	0.877	-0.091	-0.009
80.0	0.799	-0.118	0.019

Table 6.19: Polarized emissivity results for snow

Angle (deg)	$S_0$	$S_1$	$S_2$
0.0	0.920	0.021	0.011
10.0	0.845	0.019	0.019
20.0	0.877	0.002	-0.023
30.0	0.834	-0.021	-0.010
40.0	0.849	-0.017	-0.019
50.0	0.871	0.032	0.023
60.0	0.840	0.029	0.003
70.0	0.861	-0.003	0.023
80.0	0.801	0.042	0.017

Table 6.20: Polarized emissivity results for weathered asphalt

Angle (deg)	$S_0$	$S_1$	$S_2$
0.0	1.012	-0.037	-0.019
10.0	0.961	-0.033	0.020
20.0	0.950	-0.016	-0.030
30.0	0.951	-0.036	0.012
40.0	0.938	-0.027	-0.001
50.0	0.937	-0.035	-0.008
60.0	0.925	-0.034	0.012
70.0	0.880	-0.066	0.025
80.0	0.857	-0.128	0.030

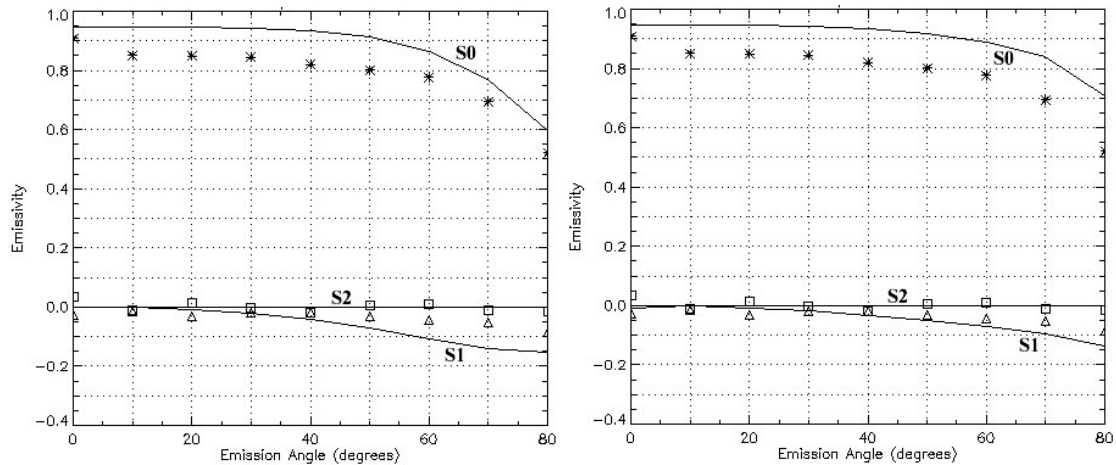


Figure 6.20: Plot of Stoke's emissivity before (left) and after (right) Step 1 of fitting process. The points represent measurements and the curves represent modeled data for a pine board. Step 1 of the fitting process consists of choosing the  $\sigma$  parameter such that the general shape of the  $S_1$  curve follows experimental data.

### 6.3 Emissivity Model Parameter Fitting

A manual procedure was utilized to fit the experimentally measured Stoke's  $S_0$  and  $S_1$  emissivity to the polarized emissivity model described in Chapter 5. The key model parameters driving the fit were determined to be the complex index of refraction, the diffuse reflectivity, and the probability distribution function  $\sigma$  and bias parameters. The following four steps were followed for each material.

#### 6.3.1 Parameter Fitting Step 1

As a starting point for each material, the  $\sigma$ , bias, and  $\tilde{n}$  values for a comparable NEF material were chosen. A visual assessment of the initial fit between model predicted and measured  $S_0$  and  $S_1$  emissivity was made. The left hand side plot in Figure 6.20 shows an example of the results for a pine board at this point.

Based on this assessment, the sigma value of emissivity model probability distribution function was varied such that the general shape of the modeled  $S_1$  curve

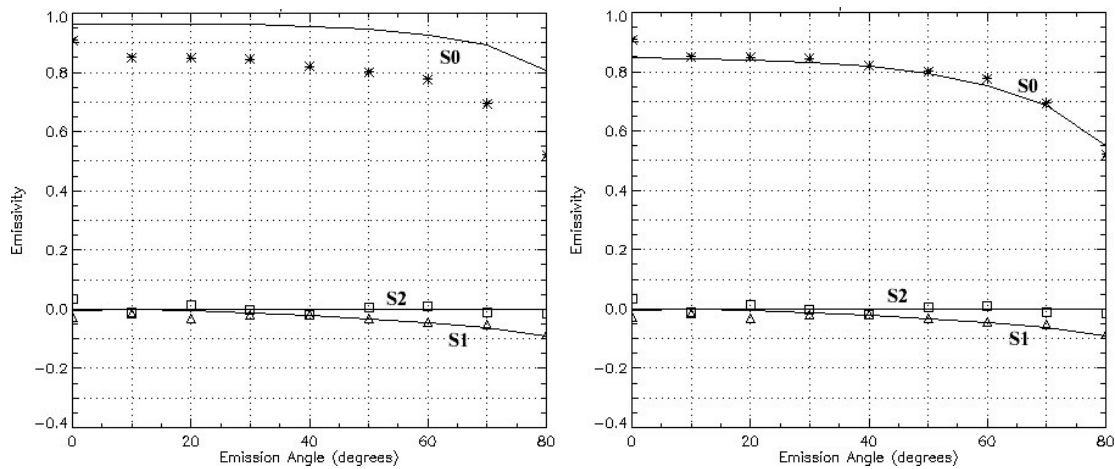


Figure 6.21: Plot of Stoke's emissivity after Step 2 (left) and after (right) Step 3 of fitting process. The points represent measurements and the curves represent modeled for a pine board. Step 2 consists of adjusting the polarized BRDF *BIAS* parameter to get the  $S_1$  modeled curve to match experimental data, while Step 3 consists of adjusting the  $\rho_v$  and  $\rho_d$  terms to drop the modeled  $S_0$  emissivity down to the experimental data.

followed the general shape of the measured  $S_1$  curve. The right hand side plot in Figure 6.20 shows an example of the results for a pine board after this step.

### 6.3.2 Parameter Fitting Step 2

Once a  $\sigma$  value was chosen, the bias value associated with the emissivity model probability distribution function was varied to bring the best visual fit of both the shape and magnitude of the  $S_1$  curve (in that the bias value directly scales the amount of modeled specular reflections and therefore the magnitude of the  $S_1$  curve). The left hand side plot in Figure 6.21 shows an example of the results for a pine board after this step.

### 6.3.3 Parameter Fitting Step 3

Once the  $\sigma$  and bias values are chosen, such that a good visual fit exists between measured and modeled  $S_1$  emissivity, the fit between the modeled and measured  $S_0$  emissivity was visually examined. Starting with a values of  $\rho_D = 0$  and  $\rho_V = 0$ , the modeled  $S_0$  emissivity was always higher than the measured value of  $S_0$  emissivity. Therefore, the final step was to vary the values of  $\rho_D$  and  $\rho_V$  to obtain the final fit. If the gap between the measured and modeled  $S_0$  curve was close to constant across all zenith angles, then only the value of  $\rho_D$  was increased. However, in some cases the gap between the measured and modeled  $S_0$  curves was slowly increasing with increasing zenith angle warranting an increase in both  $\rho_D$  and  $\rho_V$  to make up the difference. The right hand side plot in Figure 6.21 shows an example of the final modeled and measured results for a pine board.

The polarized BRDF parameters that produce the best fit Stoke's emissivity vector for emission angles between 0 and 80 degrees are listed in Table 6.21. Figures 6.22 through 6.29 show the agreement between the modeled (solid curves) and measured polarized emissivity (data points). The asterisks correspond to measured  $S_0$  emissivity, the triangles to measured  $S_1$ , and the squares to measured  $S_2$  emissivity.

All materials, except *hood* and *pine* show good agreement between the modeled and measured polarized emissivity. The car hood  $S_0$  and pine  $S_0$  modeled curves are lower than the experimentally measured  $S_0$  data. A set of polarized BRDF parameters does not exist that provide a good fit to both  $S_0$  and  $S_1$  curves for both of these materials, indicating that (1) the polarized BRDF is inadequate, (2) the experimentally measured  $S_0$  data has an error bias associated with it or (3) the experimentally measured  $S_1$  data has an error scale factor associated with it. The most likely root cause is (2), due to the assumption that all sample temperatures were ambient, but in reality the car hood and pine temperatures were not resulting in a bias in the measured  $S_0$  curve.

Table 6.21: Summary of polarized BRDF parameters that produce a polarized emissivity best fit to experimentally measured emissivity.

material	$\sigma$	bias	n	k	$\rho_D$	$\rho_V$	DHR
bark	0.10	0.20	1.3	0.0	3.1E-02	1.0E-07	0.1007
brick	0.04	1.30	1.3	0.0	3.0E-07	2.0E-02	0.0992
cement	0.10	0.70	1.3	0.0	3.0E-07	1.0E-03	0.0503
soil	0.10	0.05	1.3	0.0	2.5E-02	1.0E-07	0.0794
fresh asphalt	0.50	1.30	1.4	0.0	1.1E-05	1.0E-07	0.0286
flat black paint	0.25	1.30	1.3	0.4	1.1E-02	1.0E-07	0.0914
glossy black paint	0.05	1.30	1.4	0.4	1.1E-05	1.0E-07	0.0699
glass	0.01	1.15	1.5	0.0	6.0E-20	2.0E-08	0.0440
grass	0.10	0.20	1.3	0.0	6.1E-03	1.0E-07	0.0225
glossy tan paint	0.02	1.15	1.5	0.4	6.0E-20	2.0E-08	0.0725
hood of car	0.02	1.15	1.5	0.0	6.0E-20	2.0E-08	0.0453
particle board	0.25	0.80	1.3	0.4	1.0E-03	3.0E-02	0.1538
pine wood	0.12	1.00	1.8	0.8	1.0E-11	1.0E-07	0.1487
shingle	0.12	0.50	1.8	0.8	1.0E-20	1.0E-20	0.0743
snow	0.10	0.20	1.3	0.0	4.1E-02	1.0E-07	0.1322
weathered asphalt	0.30	0.50	2.0	0.5	3.0E-10	2.0E-10	0.0623

In addition, most of the measured emissivity curves show anomalous results at an emission angle of 0 degrees due to the fact that the target samples were reflecting the camera system and operator. This condition violates the assumption that the amount of background radiance reflected from the sample surfaces is minimized. Although the glossy and diffuse IR reflecting targets in the scene are meant to capture this background reflected radiance, the intensity of the radiance from the operator and camera requires a much better match in surface roughness between the reflectors and the sample surfaces for adequate removal of background radiance. Therefore, in most cases, the emissivity values at a zenith of 0 degrees were ignored during the parameter fitting process.

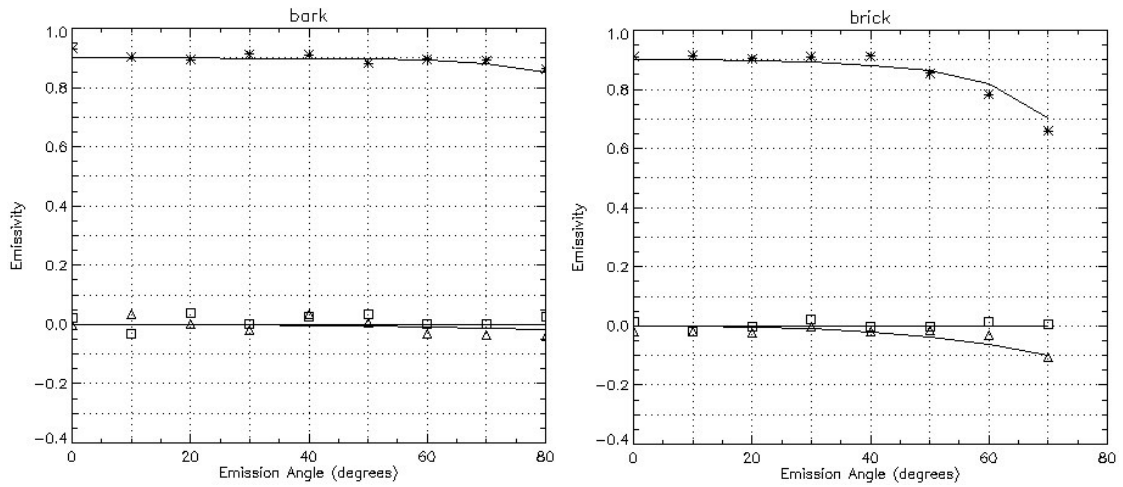


Figure 6.22: Emissivity model fit to experimentally measured emissivity for tree bark (left) and brick (right)

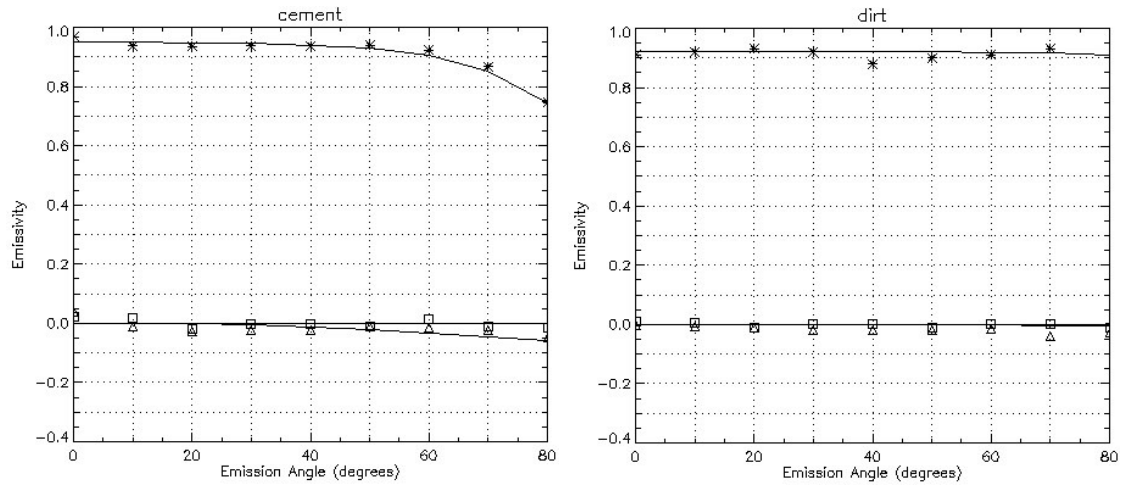


Figure 6.23: Emissivity model fit to experimentally measured emissivity for cement (left) and soil (right)

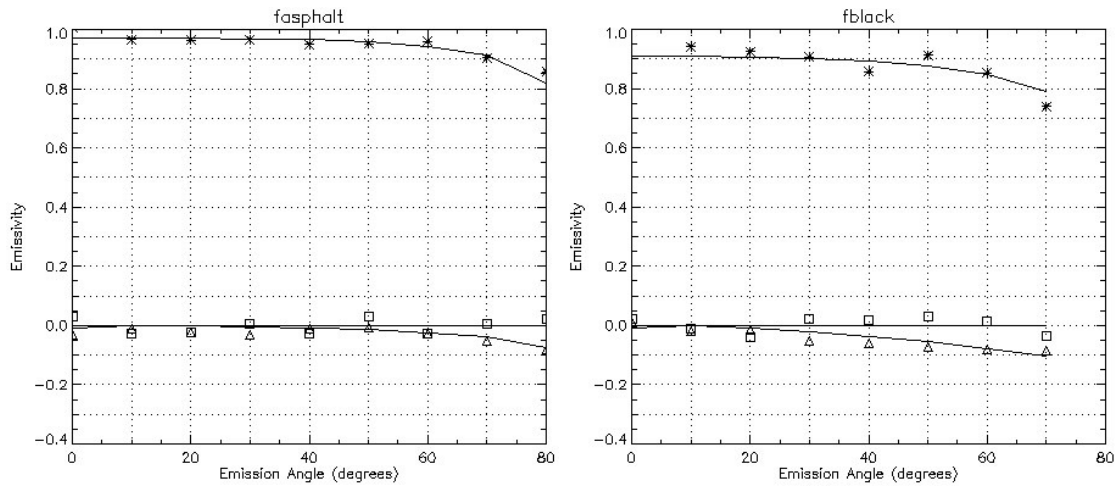


Figure 6.24: Emissivity model fit to experimentally measured emissivity for fresh asphalt (left) and flat black paint (right)

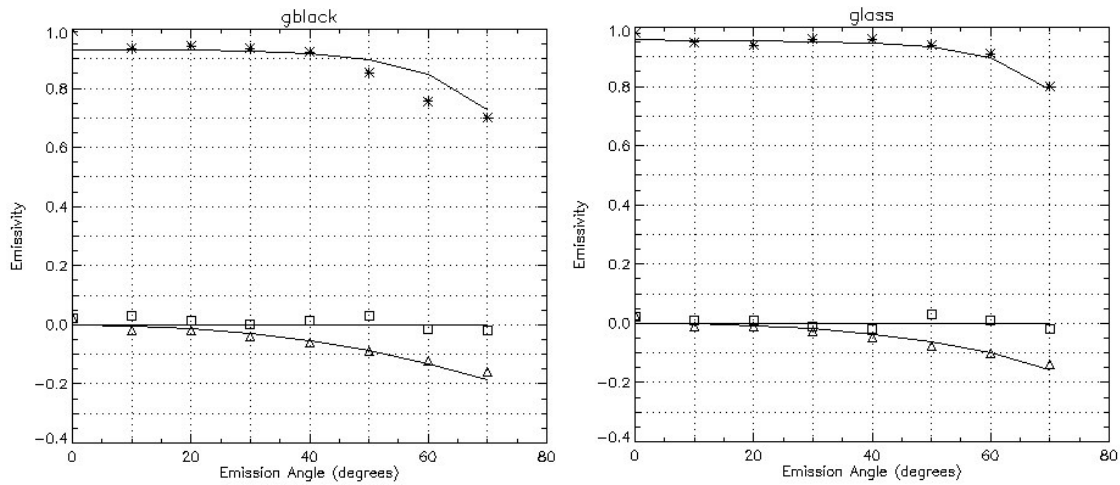


Figure 6.25: Emissivity model fit to experimentally measured emissivity for glossy black paint (left) and glass (right)

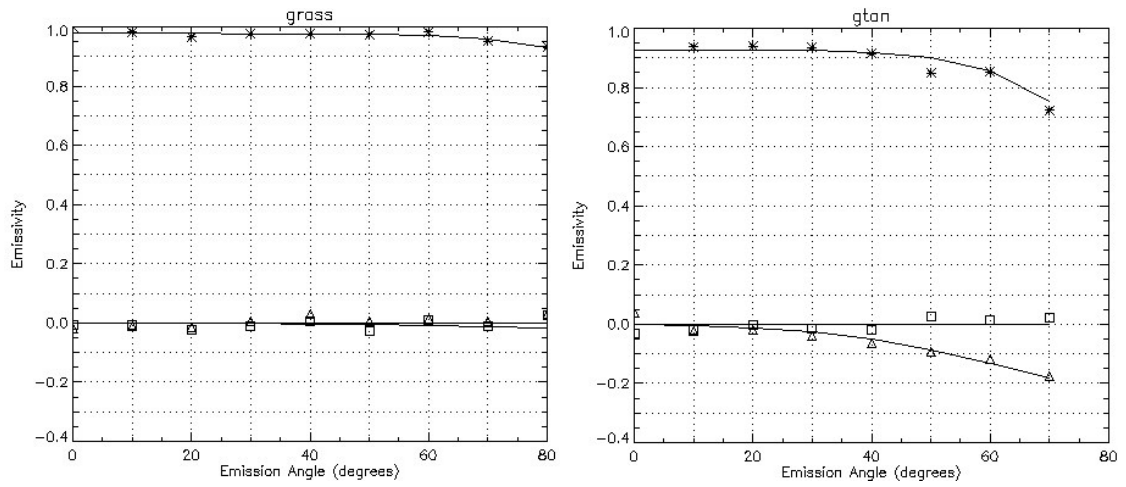


Figure 6.26: Emissivity model fit to experimentally measured emissivity for grass (left) and glossy tan paint (right)

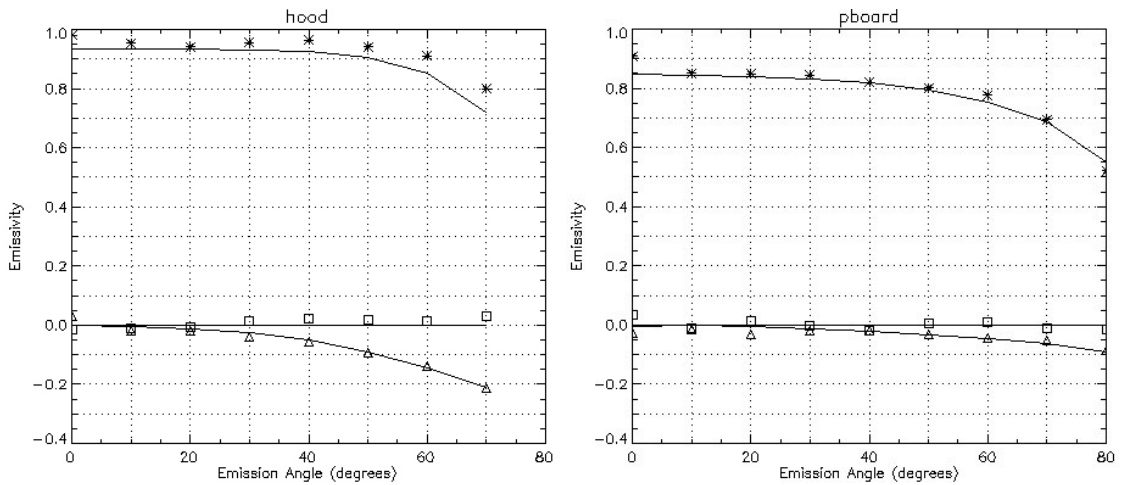


Figure 6.27: Emissivity model fit to experimentally measured emissivity for a car hood sample (left) and particle board (right)

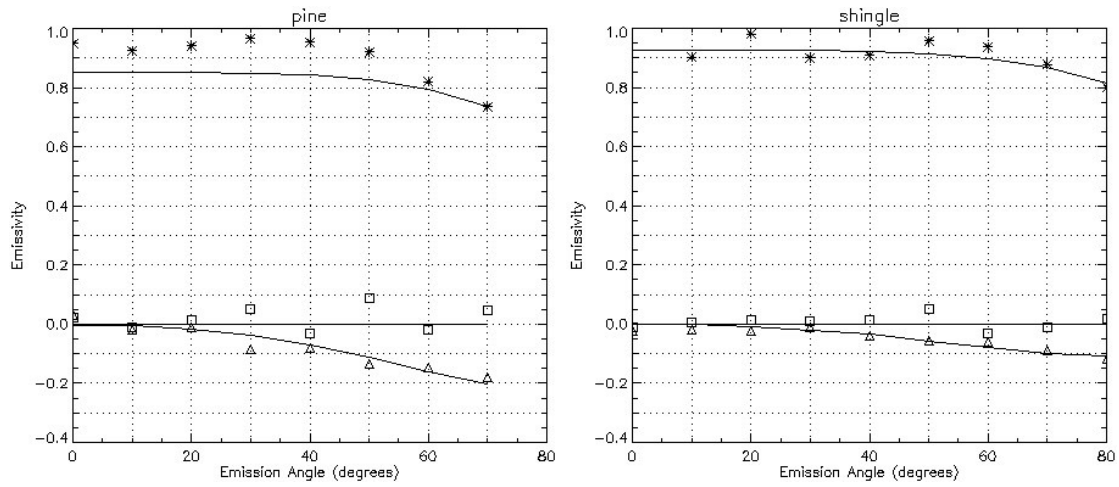


Figure 6.28: Emissivity model fit to experimentally measured emissivity for a pine board (left) and roofing shingle (right)

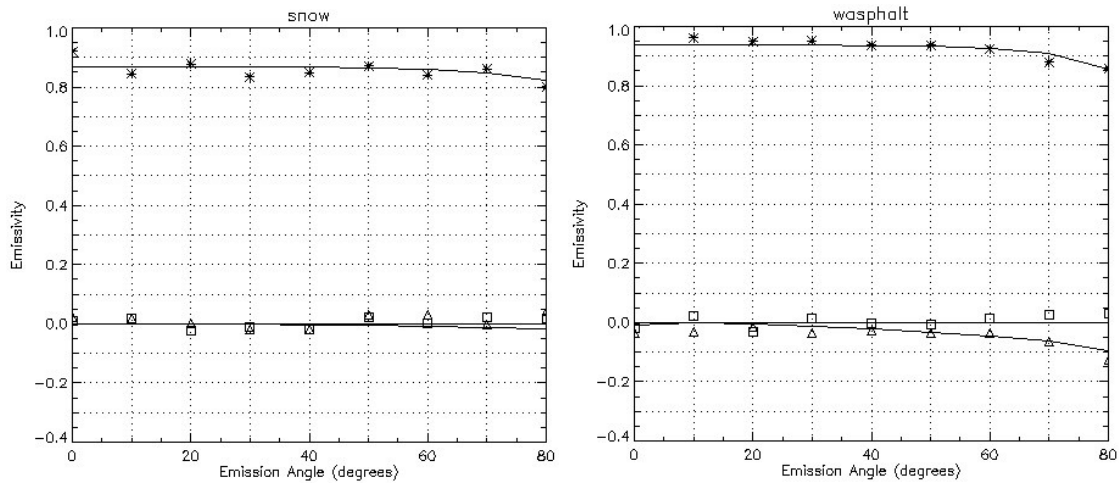


Figure 6.29: Emissivity model fit to experimentally measured emissivity for snow (left) and weathered asphalt (right)

## 6.4 Measurement Error and Uncertainty Analysis

This section describes the measurement error and Stoke's emissivity uncertainty analysis for materials characterized as described previously in this chapter.

### 6.4.1 Polarizer Orientation Angle Error

Care was taken to position the wire grid polarizer to known angle with accuracy of better than 2 degrees. The worst case scenario of the polarizer orientation being off by 2 degrees results in a relative total transmitted radiance (S0) uncertainty of 0.00% and 0.01% for an unpolarized and a 10% linearly polarized signal respectively. This relative uncertainty can be converted to an absolute uncertainty by multiplying by the measured radiance through the polarizer.

$$\Delta L_{WGP-\alpha} = \Delta L_{rel} L_{meas} \quad (6.22)$$

For a black painted surface at about 12.8C, the long-wave band integrated radiance has an uncertainty of  $\Delta L_{WGP-\alpha} = 5.628 \cdot 10^{-7} W/cm^2/sr$ .

### 6.4.2 Camera Calibration Error

Recall that before each radiometric experimental collection scenario, a calibration curve relating camera measured temperature and measured blackbody cavity temperature was acquired. In all cases, at least three data points were taken. The average root-mean-square error between the actual blackbody temperature values and the temperature values predicted by the least squares linear fit was 0.09C. However, the worst case error between the linear fit and a single measured data point was 0.20C. Utilizing equation 6.11, the uncertainty due to the calibration curve fit is  $\Delta L_{cal} = 1.43 \cdot 10^{-6} W/cm^2/sr$ .

### 6.4.3 Sample Temperature Assumption Error

Two key assumptions are made by the emissivity measurement technique described above. The first assumes that each target material being characterized has a surface temperature that tracks with the ambient air temperature. The second assumes that during the series of zenith angle and polarizer orientation angle combinations, the temperature of the samples does not vary significantly.

Experimental measurements of target surface temperatures for glossy black painted wood and flat black painted wood show the surface temperature stays within 0.5 degrees Celsius of the ambient air temperature. In addition, the same experimental measurements show that the target surface temperatures are constant to within 0.25 degrees Celsius over the 5 minutes required for a full series of polarizer angle and zenith angle image collections (approximately 36 images total).

Again, utilizing equation 6.11, we find the uncertainty in absolute radiance due to the target/ambient air assumption to be  $\Delta L_{tgt/amb} = 3.434 \cdot 10^{-6} W/cm^2/sr$ . In addition, the uncertainty in absolute measured radiance due to temporal drift of the target temperature is  $\Delta L_{drift} = 1.717 \cdot 10^{-6} W/cm^2/sr$ .

### 6.4.4 Downwelled Radiance Calculation Error

The two key assumptions that enable the calculation of the downwelled radiance term are (1) the roughness of the infrared calibration panel is comparable to the roughness of the target surface and (2) the downwelled radiance incident on the target surface is primarily isotropic.

If the downwelled radiance was perfectly isotropic (the same radiance coming from all directions), the roughness of the calibration panel would be irrelevant. However, since the downwelled skydome radiance is not isotropic we require the calibration panel roughness to roughly match the target sample roughness. Recall that each emissivity measurement scene contained a smooth infrared reflector panel and a dif-

Table 6.22: Downwelled skydome radiance reflected from a perfect infrared reflector as a function of surface roughness  $\sigma$ .

sigma	reflected skydome radiance ( $W/cm^2/sr$ )
0.05	6.487E-04
0.23	5.680E-04
0.50	5.071E-04

fuse (rough) infrared reflector panel.

In order to examine the worst case affect these two assumptions may have on the absolute radiance measurement, we assume the target surface has a roughness somewhere in between the roughness of either calibration panel. In the units of the polarized BRDF, a roughness ( $\sigma$ ) value of about 0.05 produces a very specular, glossy reflectance function. Conversely, a roughness value of about 0.5 produces a very diffuse, matte polarized BRDF reflectance function. Therefore, the worst cases scenario would be to have a target surface having a roughness of about 0.23 (halfway in between the smooth and diffuse reflector panels). Utilizing IDL engineering code that reads in the downwelled skydome radiance from a DIRSIG atmospheric database file, coupled with an IDL implementation of the polarized BRDF, we can estimate the effective downwelled radiance for surface roughness values of 0.05, 0.23, and 0.50. These values are shown in Table 6.22 for a mid-latitude winter atmosphere modified to have objects between 0 and 10 degrees above the horizon at ambient air temperature.

Based on this analysis, the uncertainty in the downwelled radiance due to mismatch in surface roughness between calibration panel and target surface is  $\Delta L_{dw/sigma} = 7.12 \cdot 10^{-5} W/cm^2/sr$ .

#### 6.4.5 Uncertainty due to Foil Perfect Reflector Assumption

The analytical approach of calculating the polarized thermal emissivity relies on the assumption that the aluminum foil utilized for flat-fielding and calculation of the downwelled radiance is a 100% infrared reflector. However, in this section we examine

the uncertainty introduced by this assumption, realizing that aluminum is typically a 98% reflector. Therefore, the radiance coming from the surface of the foil is not simply

$$L_{foil} = L_{dw} \quad (6.23)$$

but is actually

$$L_{foil} = 0.98L_{dw} + 0.02L_{BB} \quad (6.24)$$

where  $L_{BB}$  is the radiance coming from a blackbody at the ambient scene temperature. For this uncertainty analysis, the error in the radiance estimated as coming from the foil due to the 100% reflector assumption is  $\Delta L_{dw/\rho} = 1.178 \cdot 10^{-5} \text{ W/cm}^2/\text{sr}$ .

### 6.4.6 Image Level Noise Uncertainty

The image level noise consists of (1) NEDT of focal plane, (2) shot noise due to target radiance, and (3) shot noise due to skydome radiance reflected from wire grid polarizer. The EZTherm camera manufacturer specs the noise equivalent delta temperature (NEDT) at 0.080 Kelvin. However, characterization of the camera NEDT under collection conditions for this work show the NEDT averages about 0.150 to 0.200 Kelvin. Although the reason for this discrepancy is not known, there did appear to be a significant amount of sensor pattern noise that contributed to the overall noise of a constant radiance target. The presence of fixed pattern noise was easily discernible in the temporal video mode of the camera.

For a target temperature of approximately 1.7C, the NEDT due to the above three mentioned factors averages 0.92 Kelvin for a single frame of data. However after one considers the averaging of multiple pixels over a region of interest, we can express the NEDT in terms of the standard deviation of the mean. The standard deviation of the mean is utilized to express the uncertainty due to image level noise and is written in terms of the measured standard deviation  $\sigma_n$  and number of points  $n_{ROI}$  in the

region of interest

$$\Delta L_{noise} = \frac{\sigma_n}{\sqrt{n_{ROI}}} \quad (6.25)$$

For a region of interest having 100 pixels, this image level noise translates to an uncertainty in temperature space of 0.092 Kelvin and in radiance space of  $6.346 \cdot 10^{-6} W/cm^2/sr$ . It should be noted that for emissivity measurements near grazing zenith angles, the number of available points drops significantly.

### 6.4.7 Total Measurement Uncertainty

The total uncertainty in the S0 and S1 emissivity measurement is derived from the polarizer orientation angle uncertainty  $\Delta L_{WGP-\alpha}$ , the uncertainty in downwelled radiance measurement  $\Delta L_{dw/sigma}$ , the uncertainty due to calibration error  $\Delta L_{cal}$ , the uncertainty due to target temperature drift  $\Delta L_{drift}$ , the uncertainty due to target temperature mismatch from ambient air temp  $\Delta L_{tgt/amb}$ , and the uncertainty due to the camera level noise  $\Delta L_{noise}$ .

To calculate the total uncertainty in the polarized emissivity measurement, we follow a standard method of propagating measurement uncertainty. Recall that emissivity is derived from the equation

$$\epsilon = \frac{L_{meas} - L_{dw}}{\tau_p(L_{BB} - L_{dw})} \quad (6.26)$$

therefore the resulting equation for total uncertainty in a single (ie. single polarizer orientation angle) emissivity measurement is given by

$$\Delta\epsilon = \sqrt{\left(\frac{d\epsilon}{dL_{meas}}\right)^2 \Delta L_{meas}^2 + \left(\frac{d\epsilon}{dL_{BB}} \Delta L_{BB}\right)^2 + \left(\frac{d\epsilon}{dL_{dw}} \Delta L_{dw}\right)^2} \quad (6.27)$$

The uncertainty in downwelled radiance  $L_{dw}$ , the uncertainty in blackbody radiance

$L_{BB}$ , and the uncertainty in measured radiance  $L_{meas}$  are given by

$$\Delta L_{meas} = \sqrt{\Delta L_{noise}^2 + \Delta L_{WGP-\alpha}^2 + \Delta L_{drift}^2 + \Delta L_{amb/tgt}^2} \quad (6.28)$$

$$\Delta L_{dw} = \sqrt{\Delta L_{noise}^2 + \Delta L_{WGP-\alpha}^2 + \Delta L_{dw/\sigma}^2 + \Delta L_{dw/\rho}^2} \quad (6.29)$$

$$\Delta L_{BB} = \sqrt{\Delta L_{cal}^2 + \Delta L_{drift}^2 + \Delta L_{amb/tgt}^2} \quad (6.30)$$

For the case of a flat black paint measured with an ambient air temperature of about 55F, the total uncertainty in the emissivity measurement for a given polarizer orientation angle is +/- 0.0187. Note that the derived emissivity value for this configuration the actual emissivity measurement works out to be 0.9. The  $S_0$  emissivity measurement uncertainty for this scenario is driven primarily by the camera level noise and the assumption that the target temperature is at the ambient air temperature.

The plots in figures 6.30 and 6.31 show the emissivity results for the flat black painted wood target and the associated total 1 and 2-sigma measurement uncertainty respectively.

Since a Stoke's  $S_0$  emissivity value is a linear combination of all four polarizer angles divided by two, the resulting uncertainty is reduced by a factor of  $\sqrt{2}$ . However the opposite is true for the Stoke's S1 component of emissivity, where it is increased by a factor of  $\sqrt{2}$ .

## 6.5 Experimental Summary

This chapter has presented the design of a polarimetric LWIR imaging system. The imaging system is operated in either an emissivity or Stoke's image collection mode. The experimental technique (including all of it's intricacies) for deriving Stoke's emissivity as a function of zenith angle has been described in detail. Measured Stoke's

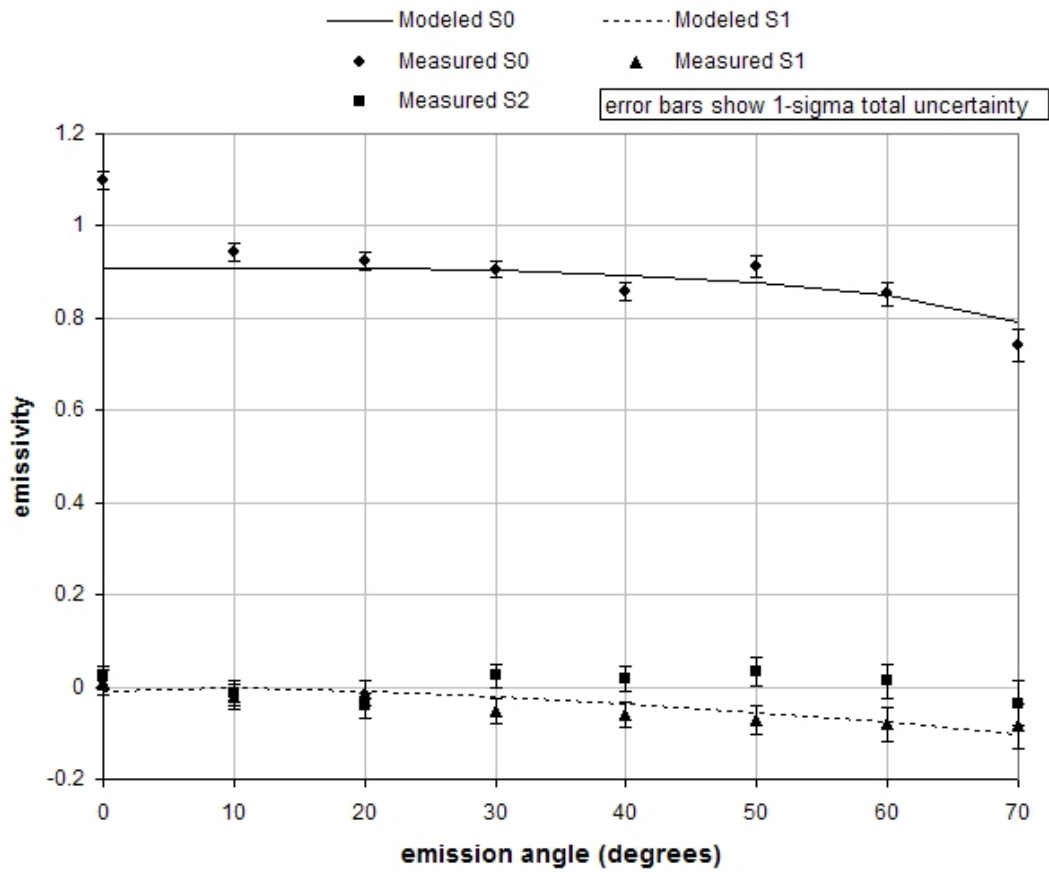


Figure 6.30: Plot of modeled and measured polarized emissivity for flat black painted target. The error bars show the calculated level of total measurement uncertainty at the 1-sigma level.

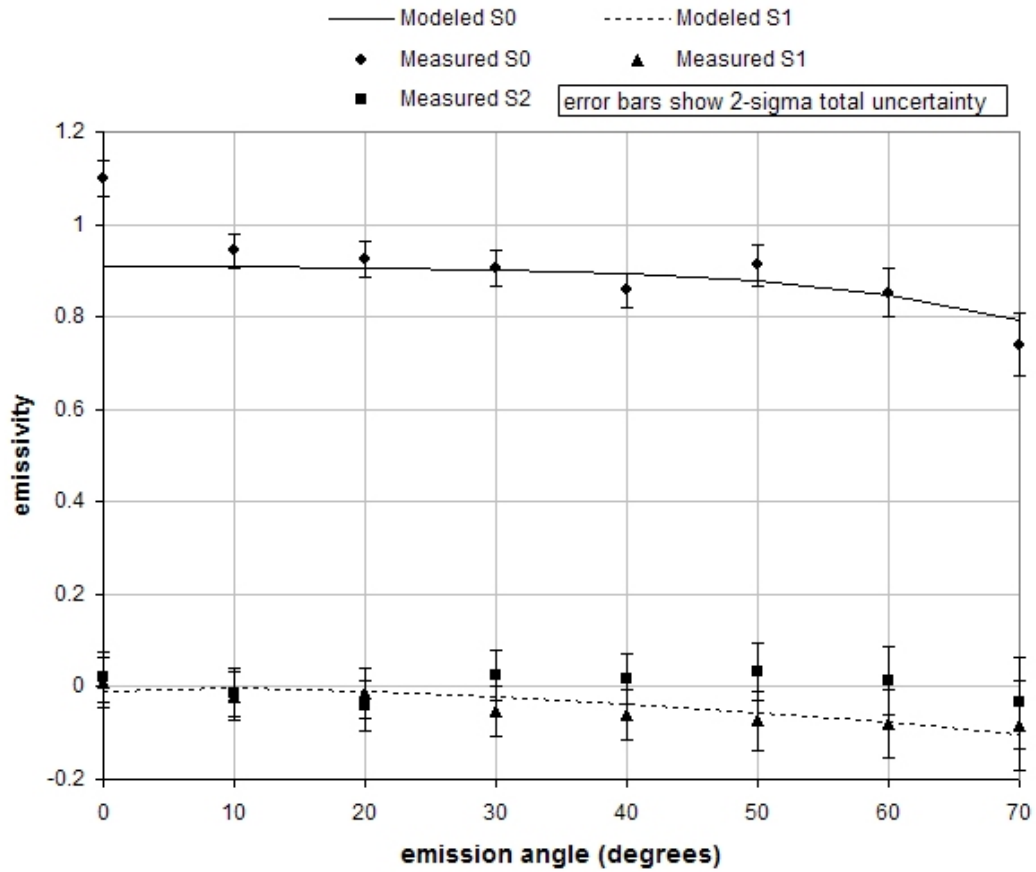


Figure 6.31: Plot of modeled and measured polarized emissivity for flat black painted target. The error bars show the calculated level of total measurement uncertainty at the 2-sigma level.

emissivity values for sixteen different target and background materials are listed. Finally, a summary of experimental error and propagation of uncertainty is detailed, showing the primary drivers to be camera level thermal and shot noise and the assumption that the targets begin and remain at the ambient air temperature throughout the experiment. The estimated level of uncertainty in the polarized emissivity values is consistent with the level of fit between measured and modeled data.



# Chapter 7

## DIRSIG Simulations

Previous work has equipped DIRSIG with the capability to handle polarized radiometry by means of Stoke's vectors, Mueller matrices, and a polarized BRDF. However, DIRSIG lacked the ability to model thermally emitted radiance polarimetrically, and had not been tested thoroughly for how well background reflected radiance was modeled in complex scenes.

This chapter presents a description and verification of an implementation to support polarized infrared scene simulations in DIRSIG. The polarized emissivity verification is carried out by means of a DIRSIG truth image against IDL engineering code, while the reflected background radiance verification is carried out by examining a carefully designed DIRSIG scene against IDL engineering code. The full scene simulation capability is verified by examining three different scenes, each with a specific purpose, against experimental measurements.

### 7.1 DIRSIG4 Overview

The Digital Imaging and Remote Sensing Image Generation (DIRSIG) model is a suite of software tools developed at the Rochester Institute of Technology. The main tool

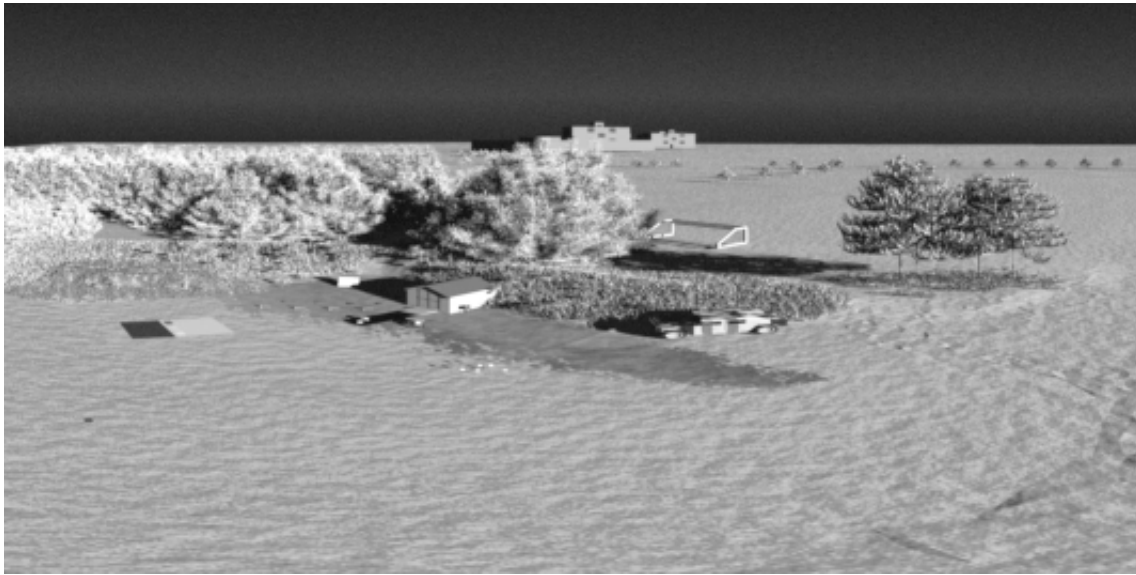


Figure 7.1: A DIRSIG simulated image of a portion of the RIT campus acquired with a near-infrared camera

renders scenes from a first principles, physics-based point of view. DIRSIG interfaces with both MODTRAN and FASCODE to model the scattering, transmission, and emission properties of the atmosphere. Figure 7.1 shows a near infrared simulation of the microscene created for model verification.

Version 4 of DIRSIG is a complete object oriented re-write of the original code base. DIRSIG4 supports broadband, multispectral, hyperspectral, visible and near IR polarimetric scene simulations. In addition, DIRSIG4 also supports active LAsER Detecting And Ranging (LADAR) scene simulations.

## 7.2 Implementation

Simulation of polarized infrared imagery is enabled by utilizing the ShellTarget reflectance property within the DIRSIG4 material database file (note: DIRSIG3 does not support this implementation).

```
MATERIAL_ENTRY {
```

```

NAME = WeatheredAsphalt
ID = 5
EDITOR_COLOR = 0.8200, 0.8200, 0.82003
SURFACE_PROPERTIES {
    REFLECTANCE_PROP_NAME = ShellTarget
    REFLECTANCE_PROP {
        BRDF_FIT_FILE = ./fit/wasphalt.fit
        EMISSIVITY_FILE = ./emissivity/wasphalt.ems
        DHR_NUM_ZENITH_BINS = 9
        DHR_MAX_ZENITH_ANGLE = 80.0
        DHR_INTEGRATION_DPFI = 1.0
        DHR_INTEGRATION_DTHETA = 1.0
    }
}

RAD_SOLVER_NAME = Generic
RAD_SOLVER {
    INITIAL_SAMPLE_COUNT = 1000
    MAX_BOUNCES = 2
    SAMPLE_DECAY_RATE = 5
    MU_SAMPLES = 20
    PHI_SAMPLES = 20
    ITERATIONS = 100
    J_RANK = 8
    K_RANK = 3
}

TEMP_SOLVER_NAME = Therm
TEMP_SOLVER {
    SPECIFIC_HEAT = 2.6689
    THERMAL_CONDUCTIVITY = 0.5000
    MASS_DENSITY = 111.4000
    SOLAR_ABSORPTION = 0.10
    THERMAL_EMISSIVITY = 0.9
    EXPOSED_AREA = 0.5
    THICKNESS = 1.0
    DOUBLE_SIDED = FALSE
}
}

```

A DIRSIG4 material entry has 3 important tagged components: SURFACE\_PROPERTIES, RAD\_SOLVER, and TEMP\_SOLVER. The polarized surface property, ShellTarget, is utilized by setting the tag

REFLECTANCE\_PROP\_NAME = ShellTarget.

The ShellTarget reflectance property has six configurable parameters. The BRDF\_FIT\_FILE tag contains the path and filename of the parameters utilized to configure the ShellTarget polarized BRDF. An example .fit file is shown below for reference.

```
SHELL_TARGET = 1.0

FIT_PARAMS {
  LAMBDA = 0.4
  N = 2.0
  K = 0.5
  DHR = 0.062274289

  ORIENT_PROB_NAME = Gaussian
  ORIENT_PROB {
    BIAS = 0.5
    SIGMA = 0.3
  }

  SHADOW_FUNCT_NAME = Maxwell-Beard
  SHADOW_FUNCT {
    TAU = 5
    OMEGA = 5
  }

  VOLUME_TERM_NAME = Maxwell-Beard
  VOLUME_TERM {
    RHO_D = 3e-10
    RHO_V = 2e-10
  }
}
```

In this .fit example, the ShellTarget BRDF is configured to have a complex index of refraction  $\tilde{n} = 2.0 - 0.5i$ , a Gaussian probability distribution function with  $\sigma = 0.3$  and  $BIAS = 0.5$ , a Maxwell-Beard shadowing and obscuration function with  $\tau = 5$  and  $\Omega = 5$ , and a Maxwell-Beard style unpolarized reflectance term with  $\rho_d = 3 \bullet 10^{-10}$  and  $\rho_v = 2 \bullet 10^{-10}$ .

For reference, recall the form of the polarized BRDF from Chapter 5 in equations 7.1, 7.2, and 7.3 below.

$$f_{pBRDF}(\theta_i, \theta_r, \phi) = f_{spec}(\theta_i, \theta_r, \phi) + f_{vol}(\theta_i, \theta_r) \quad (7.1)$$

$$f_{spec}(\theta_i, \theta_r, \phi) = \frac{M(\beta, n, k)SO(\theta, \beta, \tau, \Omega)P(\theta_N, \sigma, B)}{4\cos(\theta_i)\cos(\theta_r)} \quad (7.2)$$

$$f_{vol}(\theta_i, \theta_r) = \rho_d + \frac{2\rho_v}{\cos(\theta_i) + \cos(\theta_r)} \quad (7.3)$$

The EMISSIVITY\_FILE tag points to the spectral emissivity curve file for the material. The emissivity file is utilized by the spectral interpolation algorithm within the DIRSIG implementation of the polarized ShellTarget BRDF.

The diffuse hemispherical reflectance, which drives the thermal emissivity calculation, is calculated at a finite number of zenith angles, specified by the tag DHR\_NUM\_ZENITH\_BINS. For zenith angles in between these points, the DHR is interpolated. For most materials, calculating the DHR at 10 degree increments between 0 and 80 is suitable for good performance. The maximum allowable zenith angle utilized in the DHR integration is specified by the DHR\_MAX\_ZENITH\_ANGLE tag, however this angle does not restrict the maximum allowable angle of reflectance.

Finally, the tags DHR\_INTEGRATION\_DPFI and DHR\_INTEGRATION\_DTHETA control how finely the hemisphere is sampled during the DHR integration. Good performance has been found utilizing values of 1 degree for both variables, even for materials with a narrow specular lobe. For diffusely scattering materials, the DPFI and DTHETA parameters can be relaxed to 5 degrees and still provide numerically accurate DHR integrations.

Three versions of a simple DIRSIG scene, consisting of a sphere resting on an infinite plane, are presented to demonstrate the DIRSIG implementation of polarized emissivity.

Figure 7.2 shows the  $S_0$ ,  $S_1$  and  $S_2$  bands of a scene consisting of a hot sphere on a

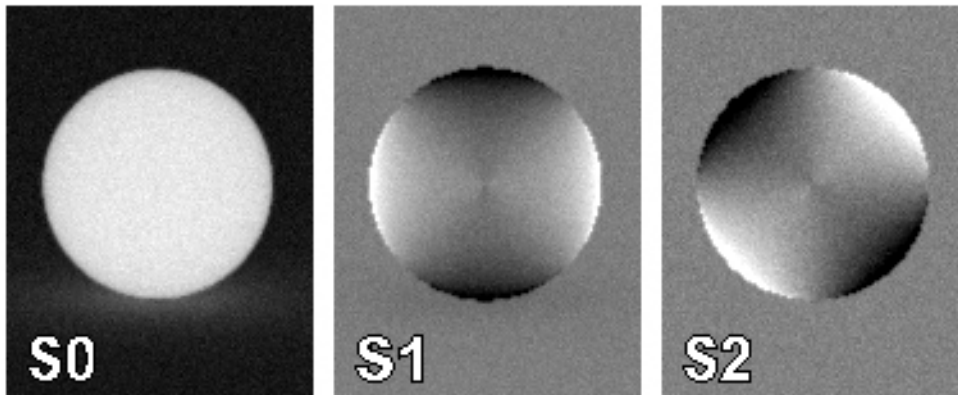


Figure 7.2: (a)  $S_0$ , (b)  $S_1$ , and (c)  $S_2$  images of a hot sphere on an cold surface.

relatively cold background under a cold and clear sky. The sphere surface is modeled to be painted with an ultra-flat Krylon black surface finish while the cold ground is modeled to be a non-polarized, diffuse surface.

The  $S_0$  band shows the expected phenomenology of a white hot sphere on cold black background. In addition, the  $S_0$  band also shows some diffusely reflected radiance coming from the sphere.

The  $S_1$  band shows alternating light and dark regions towards the edge of the sphere. This signature is due to thermal emission polarization and goes from light to dark around the edge due the orientation of the local facets relative to the camera. For example, we expect a negative (dark) emission polarization signature when a surface is flat to the ground. This is the signature that is seen on the top and bottom of the sphere due to the relative surface orientation of 0 and 180 degrees to the camera. The sides of the sphere have a relative orientation of 90 and 270 degrees relative to the camera, which causes the thermally emitted vertical polarization to appear horizontal (light). The  $S_2$  band show phenomenology similar to the  $S_1$  band, except the contrast is rotated by 45 degrees. Again, this effect is due to the thermally emitted polarization being vertical from the local surface, but appears to be non-vertical relative to the camera system.

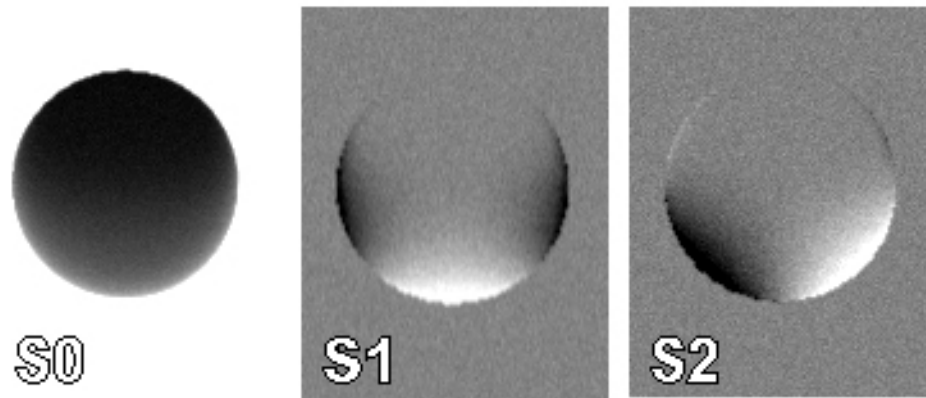


Figure 7.3: (a)  $S_0$ , (b)  $S_1$ , and (c)  $S_2$  images of a cold sphere on a hot surface.

Figure 7.3 shows the  $S_0$ ,  $S_1$ , and  $S_2$  bands of a scene consisting of a cold sphere on a relatively hot flat ground plane. The surfaces are modeled to have the same finishes as the previous example. The  $S_0$  image shows the expected tonal difference between the cold sphere and the hot background.

Due to the fact that the sphere is modeled to be very cold, there are no visible polarimetric signatures due to thermal emission from the sphere surface. There are polarization signatures in the  $S_1$  and  $S_2$  bands due to reflection from the warm ground however. In fact, the sign of the polarimetric signatures on the bottom half of the sphere (due to reflection) are opposite of the signatures seen in the previous example due to thermal emission. In this example, the sky is modeled to have no significant downwelled radiance component, therefore there is no reflected polarimetric signatures on the top half of the sphere.

A final example demonstrating the DIRSIG implementation of a polarized emissivity model is shown in Figure 7.4. This example is the most realistic of the three, in that both the sphere and the ground plane are modeled to have the same temperature. Both surfaces have finishes similar to the previous two examples, the sphere is painted with a flat black paint and the ground is modeled to be non-polarized and diffuse. Although at the same temperature, the ground plane has a lower amount of

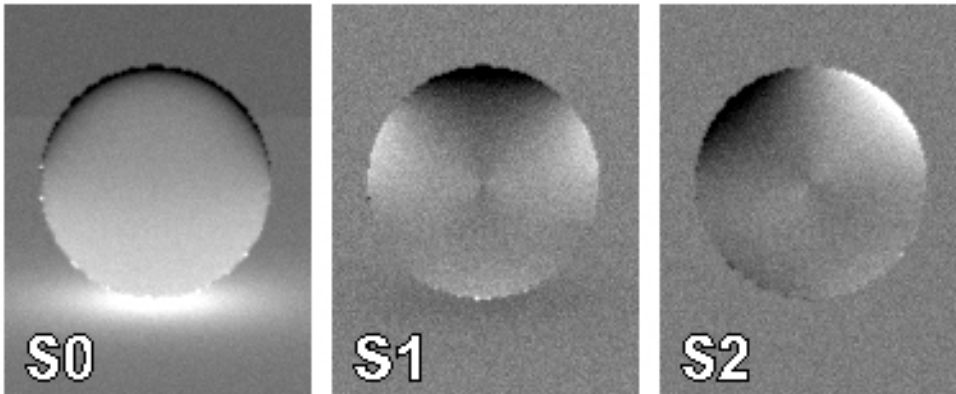


Figure 7.4: (a)  $S_0$ , (b)  $S_1$ , and (c)  $S_2$  images of a hot sphere on an hot surface.

thermally emitted radiance due to the viewing angle of the camera being about 70 degrees from the ground normal. In addition, the dynamic range of radiance values in the  $S_0$  band is much smaller compared to the two previous example, therefore the drop off in thermal emissivity at the edges of the sphere is much more noticeable.

The  $S_1$  and  $S_2$  bands of this example shows the strongest polarimetric signatures coming from the upper edges of the sphere. Although there is an equally strong thermally emitted  $S_1$  signature around the lower edges of the sphere, they are balanced out by the positive signature of the ground reflections. Therefore, only the top of the sphere that is open to the cold sky shows a significant polarimetric signature.

## 7.3 Verification

This section describes the polarized infrared scene simulation verification efforts.

### 7.3.1 Polarized BRDF

The polarized BRDF (CDSshellTarget class) was verified by the IDL code contained in Appendix B. Within the DIRSIG source code a debug output file was written for many incident/exitant ray directions by utilizing the points sent as input to the factored

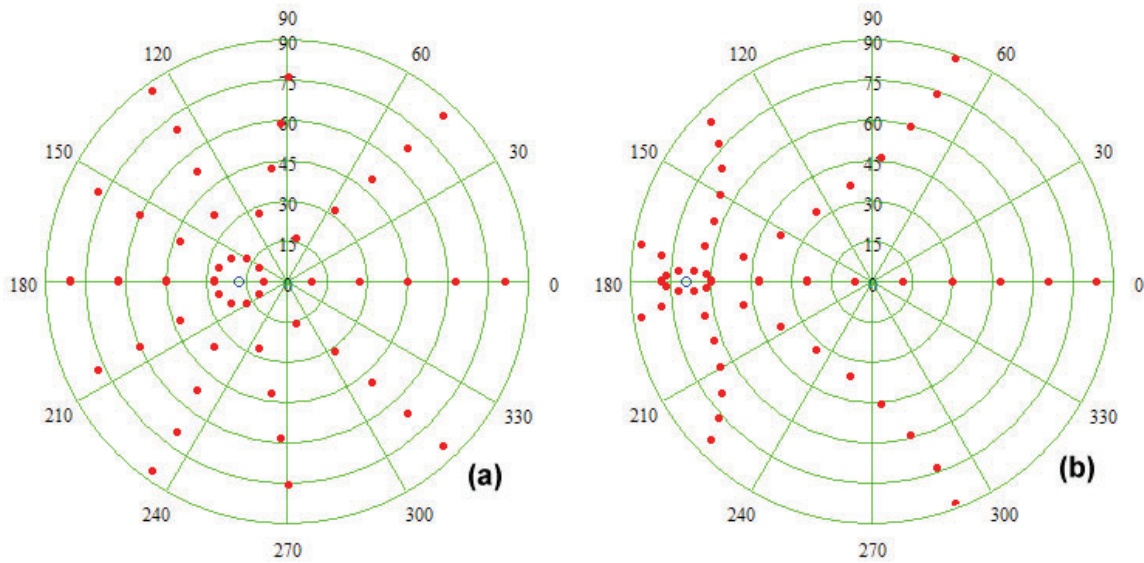


Figure 7.5: Locations of some of the viewing directions utilized to verify the DIRSIG polarized BRDF. The red dots show the exitant ray directions examined for a single given incident ray direction (a) zenith=18deg and (b) zenith=60deg. The blue dot shows the location of the perfectly specular reflection.

BRDF sampler (see Appendix E). Figure 7.5 shows an example of the reflected ray directions for two specific incident ray directions examined. The resulting polarized BRDF associated with a total of 10 incident ray directions. For each incident ray direction a total of 500 exitant ray directions were examined for a total of 5000 incident/exitant BRDF geometries.

The agreement between the DIRSIG calculated  $m_{00}$ ,  $m_{10}$ , and  $m_{20}$  components of the polarized BRDF and the same components of the IDL generated BRDF was better than 0.15% for a glossy IR reflector material, 0.5% for the glossy black material, and 0.01% for the flat black material.

### 7.3.2 Polarized DHR

The polarized directional hemispherical reflectance (DHR) is an integration of the polarized BRDF over the hemisphere above a sample surface. Verification of how

DIRSIG calculates polarized DHR is critical to accurate polarized emissivity modeling.

For this verification, six material surfaces were chosen and evaluated at zenith angles of 0, 10, 20, 30, 40, 50, 60, 70, and 80 degrees. The components of the 4x4 DHR Mueller Matrix that drive polarized thermal emission are the  $DHR_{00}$  and  $DHR_{10}$  components. This is due to the fact that polarized thermal emissivity is derived from the first row only of the DHR matrix, and the  $S_2$  component integrates to zero for any currently supported polarized BRDF surface (the only two supported surface slope probability distribution functions are azimuthally isotropic).

A custom DIRSIG build was generated that would output the polarized DHR (as it was calculated) to the console during program execution. Although an option exists to output the DHR to a truth image, the debug output to the console was preferred because it was found to be much more efficient.

Table 7.1 shows a comparison of polarized DHR results for a flat black painted surface. The difference between the DIRSIG and IDL engineering code evaluation of the  $S_0$  component ( $DHR_{00}$ ) is less than 0.002% for emission angles between 0 and 88 degrees. The  $S_1$  component ( $DHR_{10}$ ) of polarized DHR shows a difference of less than 0.000031% for emission angles between 0 and 89 degrees.

Table 7.2 shows a comparison of polarized DHR results for a smooth IR reflecting surface. The difference between the DIRSIG and IDL engineering code evaluation of the  $S_0$  component is less than 0.000003% for emission angles between 0 and 89 degrees. The  $S_1$  component of polarized DHR shows a difference of less than 0.001% for emission angles between 0 and 89 degrees. The percent difference in the  $S_1$  component of DHR are a bit larger near zero degrees zenith due to the values being very small and are limited by the reporting precision of 7 significant figures past the decimal place for the DIRSIG values.

Table 7.3 shows a comparison of polarized thermal emission results for a glossy

Table 7.1: Comparison of DIRSIG and IDL DHR results for a flat black painted surface

zenith angle (deg)	DIRSIG $S_0$	DIRSIG $S_1$	IDL $S_0$	IDL $S_1$	% $S_0$ difference	% $S_1$ difference
0.00	0.0916691	0.0087151	0.0916693	0.0087151	-0.000131%	0.000006%
4.94	0.0917343	0.0005552	0.0917344	0.0005552	-0.000131%	-0.000007%
9.89	0.0920172	0.0021796	0.0920173	0.0021796	-0.000130%	0.000000%
14.83	0.0925792	0.0049064	0.0925793	0.0049064	-0.000130%	-0.000002%
19.78	0.0935267	0.0087451	0.0935268	0.0087451	-0.000128%	-0.000002%
24.72	0.0950166	0.0136981	0.0950167	0.0136981	-0.000127%	-0.000004%
29.67	0.0972616	0.0197511	0.0972617	0.0197511	-0.000124%	-0.000001%
34.61	0.1005380	0.0268656	0.1005382	0.0268656	-0.000116%	-0.000001%
39.56	0.1051966	0.0349735	0.1051967	0.0349735	-0.000117%	-0.000002%
44.50	0.1116788	0.0439770	0.1116789	0.0439770	-0.000111%	-0.000002%
49.44	0.1205466	0.0537561	0.1205467	0.0537561	-0.000103%	-0.000001%
54.39	0.1325397	0.06419017	0.1325398	0.0641901	-0.000094%	-0.000002%
59.33	0.1486972	0.0752064	0.1486973	0.0752064	-0.000085%	-0.000001%
64.28	0.1706356	0.0868879	0.1706357	0.0868879	-0.000076%	-0.000001%
69.22	0.2012506	0.0997339	0.2012508	0.0997339	-0.000069%	-0.000001%
74.17	0.2467794	0.1153951	0.2467795	0.1153951	-0.000062%	-0.000005%
79.11	0.3245520	0.1393806	0.3245522	0.1393807	-0.000060%	-0.000011
84.06	0.5095600	0.1971688	0.5095603	0.1971689	-0.000068%	-0.000031%
89.00	1.0000000	0.3501299	1.0000000	0.3501299	0.000000%	0.000018%

Table 7.2: Comparison of DIRSIG and IDL DHR results for a smooth 100% reflecting surface

zenith angle (deg)	DIRSIG $S_0$	DIRSIG $S_1$	IDL $S_0$	IDL $S_1$	% $S_0$ difference	% $S_1$ difference
0.00	0.9969279	0.0000020	0.9969279	0.0000020	0.000000%	0.001174%
4.9	0.9956890	0.0000030	0.9956890	0.0000030	0.000000%	-0.000715%
9.89	0.9962411	0.0000121	0.9962411	0.0000121	0.000001%	-0.000240%
14.83	0.9966242	0.0000274	0.9966242	0.0000274	0.000000%	-0.000124%
19.78	0.9966968	0.0000491	0.9966968	0.0000491	0.000000%	-0.000024%
24.72	0.9966996	0.0000777	0.9966996	0.0000777	0.000000%	0.000040%
29.67	0.9966947	0.0001138	0.9966947	0.0001138	0.000000%	-0.000053%
34.61	0.9966864	0.0001582	0.9966864	0.0001582	0.000000%	-0.000019%
39.56	0.9966733	0.0002122	0.9966733	0.0002122	0.000000%	-0.000033%
44.50	0.9966532	0.0002779	0.9966532	0.0002779	0.000000%	-0.000022%
49.44	0.9966226	0.0003582	0.9966226	0.0003582	0.000000%	-0.000017%
54.39	0.9965763	0.0004580	0.9965764	0.0004580	0.000000%	-0.000004%
59.33	0.9965058	0.0005852	0.9965058	0.0005852	0.000000%	-0.000012%
64.28	0.9963913	0.0007544	0.9963913	0.0007544	0.000000%	-0.000015%
69.22	0.9960412	0.0009935	0.9960412	0.0009935	0.000000%	-0.000013%
74.17	0.9929339	0.0013589	0.9929339	0.0013589	0.000000%	-0.000022%
79.11	0.9720389	0.0019495	0.9720389	0.0019495	0.000003%	-0.000026%
84.06	0.9233799	0.0030243	0.9233799	0.0030243	0.000001%	-0.000043%
89.00	1.0000000	0.0078654	1.0000000	0.0078654	0.000000%	-0.000104%

Table 7.3: Comparison of DIRSIG and IDL DHR results for a glossy black painted surface

zenith angle (deg)	DIRSIG $S_0$	DIRSIG $S_1$	IDL $S_0$	IDL $S_1$	% $S_0$ difference	% $S_1$ difference
0.00	0.0701346	0.0004613	0.0701344	0.0004613	0.000269%	0.000009%
4.94	0.0700487	0.0006888	0.0700485	0.0006888	0.000269%	0.000003%
9.89	0.0701156	0.0027758	0.0701154	0.0027758	0.000269%	-0.000004%
14.83	0.0702700	0.0063214	0.0702698	0.0063214	0.000269%	-0.000003%
19.78	0.0706263	0.0114267	0.0706261	0.0114267	0.000267%	-0.000002%
24.72	0.0714008	0.0182364	0.0714007	0.0182364	0.000265%	-0.000007%
29.67	0.0729048	0.0269376	0.0729046	0.0269376	0.000259%	-0.000003%
34.61	0.0756019	0.0377568	0.0756017	0.0377568	0.000248%	-0.000005%
39.56	0.0801856	0.0509478	0.0801854	0.0509478	0.000233%	-0.000005%
44.50	0.0876900	0.0667661	0.0876898	0.0667661	0.000213%	-0.000006%
49.44	0.0996538	0.0854129	0.0996537	0.0854129	0.000184%	-0.000005%
54.39	0.1183666	0.1069258	0.1183664	0.1069259	0.000153%	-0.000006%
59.33	0.1472369	0.1309713	0.1472367	0.1309713	0.000120%	-0.000006%
64.28	0.1913454	0.1564576	0.1913452	0.1564576	0.000085%	-0.000005%
69.22	0.2581770	0.1807994	0.2581769	0.1807994	0.000057%	-0.000003%
74.17	0.3571440	0.1982976	0.3571439	0.1982976	0.000036%	0.000000%
79.11	0.4894236	0.1972356	0.4894235	0.1972356	0.000022%	0.000013%
84.06	0.6404931	0.1674667	0.6404931	0.1674667	0.000011%	0.000020%
89.00	1.0000000	0.1264528	1.0000000	0.1264527	0.000000%	0.000071%

black painted surface. The difference between the DIRSIG and IDL engineering code evaluation of the  $S_0$  component is less than 0.0003% for emission angles between 0 and 89 degrees. The  $S_1$  component of polarized DHR shows a difference of less than 0.00008% for emission angles between 0 and 89 degrees.

### 7.3.3 Background Reflectance Sampling

Although thermally emitted radiance can be the primary component in the  $S_0$  (total intensity) band, the  $S_1$  and  $S_2$  band signatures are very sensitive to background radiance reflected from each facet in the scene. In DIRSIG, Radiometry Solvers are algorithms to compute radiance leaving the surface of a scene element. The CDGener-

icRadSolver class is utilized by DIRSIG to handle integration of background radiance reflections. Adam Goodenough has written a detailed technical brief[5] describing how to configure and understand the operation of the Generic Rad Solver. This document is attached as an Appendix due to its importance for accurate polarimetric thermal IR scene modeling.

The Generic Rad Solver always samples the solar/lunar direction (if the sun or moon is in the sky) for reflected background radiance and then importance samples the rest of the hemisphere above each facet. The level of importance sampling performed is configured by the user within the DIRSIG material database file by utilizing the tags MU\_SAMPLES

In the visible region of the electromagnetic spectrum, the solar or lunar contribution is the primary source for radiance reflected from a facet surface. Of secondary importance is the downwelled skydome radiance, which has a moderately uniform distribution across the hemisphere. For visible applications, the Generic Rad Solver may be configured to operate in a very computationally efficient and accurate manner.

However, the dominate source of radiance in infrared scenes is not the sun, but potentially any object in the scene that is within the hemisphere above each facet element. Therefore, for accurate infrared scene simulations, the Generic Rad Solver must be configured such that it adequately samples all potential radiance sources in the hemisphere above each surface element. For a rigorous sampling of the hemisphere for background reflections, Goodenough recommends a value of 20 for the MU\_BINS and PHL\_BINS Generic Rad Solver parameters. In addition, he also recommends the parameters INITIAL\_SAMPLE\_COUNT set to 100, JRANK set to 16, KRANK set to 3 and ITERATIONS set to 1000.

In order to verify that the Generic Rad Solver is able to adequately sample a wide range of materials, a DIRSIG scene was constructed consisting of a glossy black surface, a glossy tan surface, a piece of pine wood, a flat black painted surface, a glossy

100% IR reflector, and a near-blackbody glossy surface. The near-blackbody surface is configured to have the same BRDF properties as the glossy black surface, except the BIAS parameter adjusted by a factor of 10 to result in less than 1% reflectance. All elements in this scene were configured to have a temperature of -120C in order to make the thermally emitted radiance component negligible. By design, the only source of radiance in this verification scene was the skydome resulting in only reflected skydome radiance reaching the sensor.

IDL code was written to integrate the reflected skydome radiance (read from the DIRSIG .adb file) over the hemisphere in 1 degree azimuth and elevation angle increments. A comparison of DIRSIG's GenericRadSolver modeling of reflected skydome radiance and the IDL code integration of reflected radiance is presented in Table 7.4. For all surfaces, glossy and diffuse (flat), there is an agreement to within about 5% or better. This level of agreement is acceptable, given the coarse and computationally efficient manner with which DIRSIG's GenericRadSolver determines reflected background radiance.

In addition, it should be noted that for most materials under ambient temperature conditions, the total radiance error due to a small error in the integration of background reflectance is small. For example, consider a material that has an emissivity of 0.9 in the thermal IR. Assuming the accuracy of the polarized emissivity is better than 0.0001% (see previous section) and the accuracy of the integration of background reflected radiance has an absolute accuracy of 5%, the overall radiance has an accuracy of 0.5%.

### 7.3.4 Polarization Orientation

A recent change was made to DIRSIG (see Appendix F) to correct the orientation of linear polarized radiance within the  $S_1$  and  $S_2$  bands. Previously, DIRSIG treated the orientation of linearly polarized light coming from each facet as though each facet

Table 7.4: Comparison of DIRSIG and IDL integration of reflections from background hemisphere from a cold target surface.

material	DIRSIG $S_0$	DIRSIG $S_1$	IDL $S_0$	IDL $S_1$	% $S_0$ difference	% $S_1$ difference
near blackbody	2.15E-07	1.65E-07	2.16E-07	1.66E-07	-0.80%	-0.73%
IR reflector	2.26E-04	5.92E-08	2.28E-04	5.94E-08	-0.68%	-0.42%
glossy black	2.11E-05	1.50E-05	2.00E-05	1.52E-05	5.25%	-1.12%
glossy tan	2.11E-05	1.46E-05	2.01E-05	1.48E-05	4.98%	-1.22%
pine	3.81E-05	1.94E-05	3.72E-05	1.97E-05	2.25%	-1.13%
flat black	2.54E-05	9.91E-06	2.55E-05	9.91E-06	-0.31%	-0.03%

was flat to the ground. However, one would actually expect the orientation of the linear polarization between the  $S_1$  and  $S_2$  bands to change as a function of the local facet normal orientation relative to the camera and global  $z$  (up) direction. The implementation of these specific changes are described in detail in Appendix F.

The simulated images in Figure 7.6 demonstrate the polarimetric phenomenology observed before and after the above mentioned change. This simulation shows a warm sphere sitting on a cold flat ground. Before the change was made, emissive polarization was always in the  $S_1$  band only, regardless of the orientation of the facet relative to the camera system. After the fix was made, emissive polarization does indeed show up in either the  $S_1$ ,  $S_2$  bands, or both depending on the orientation of the facet relative to the camera.

In order to verify these changes, experimental measurements of a flat-black painted sphere were conducted during the day (Figure 7.7) and at night (Figure 7.8). Simulations were run after this polarization orientation fix was made and confirm the fix to be correct. The simulations were configured to have target temperatures derived by THERM and thermodynamic properties similar to a paint from the DIRSIG desert scene. Both the day and night scenes were acquired in my backyard, and therefore had a significant level of objects in the background that contributed to surface reflections. The only objects considered in the simulations were two of the fences in my

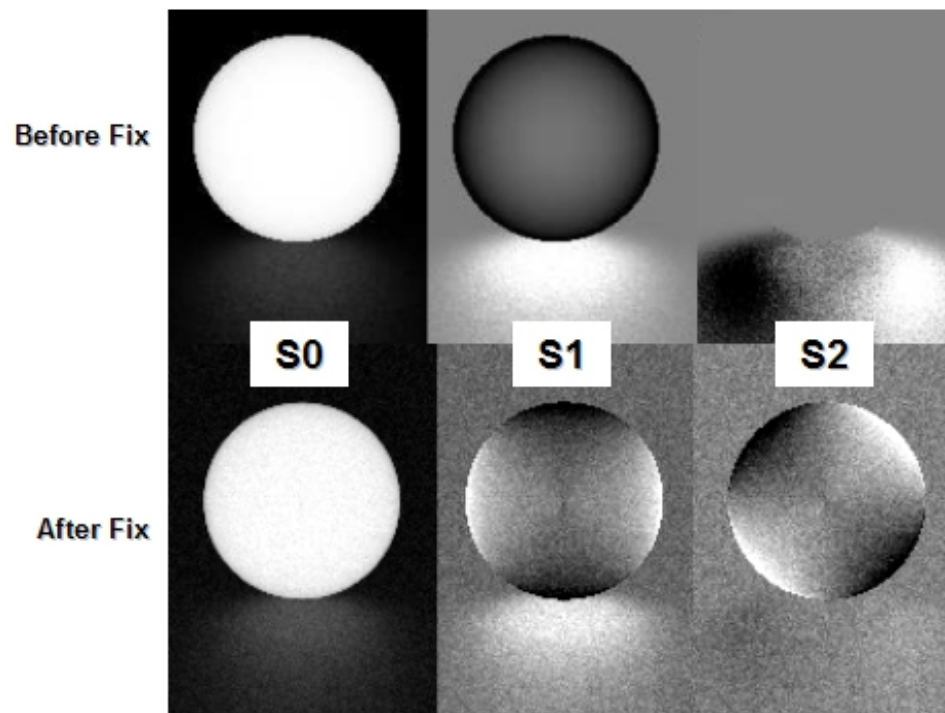


Figure 7.6: DIRSIG simulations showing the effect of a recent code change to incorporate relative orientation of each facet relative to camera coordinates

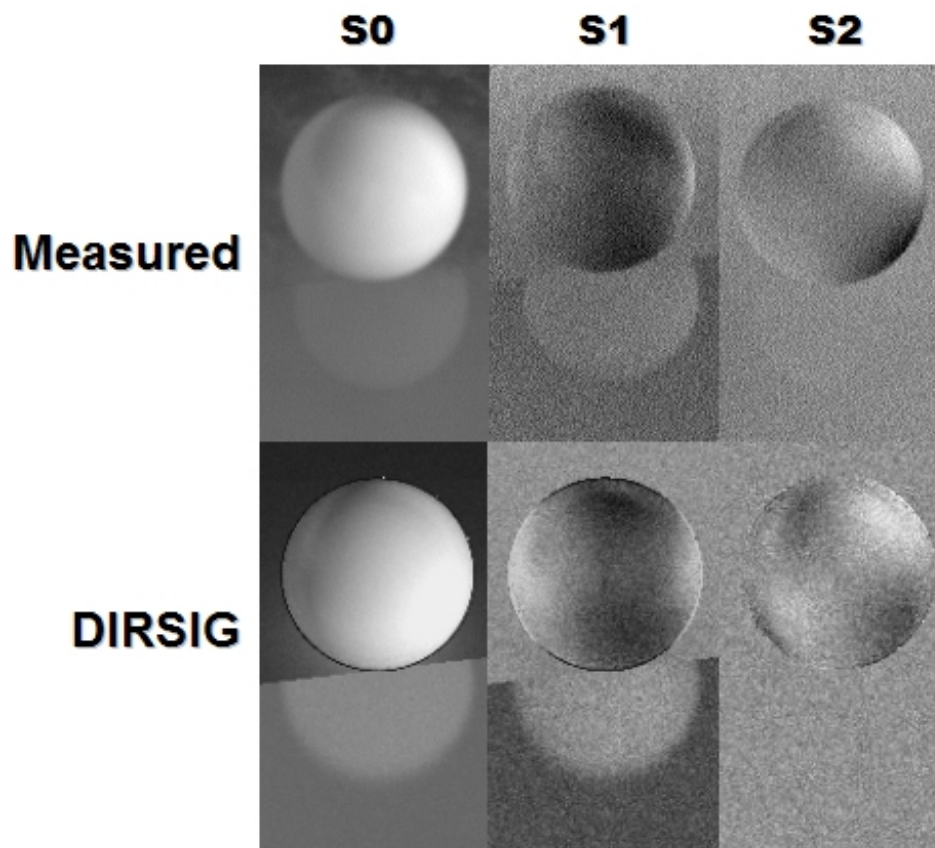


Figure 7.7: Measured and DIRSIG images showing a sphere sitting on snow with a glossy plate in front with a sun elevation of 18 degrees

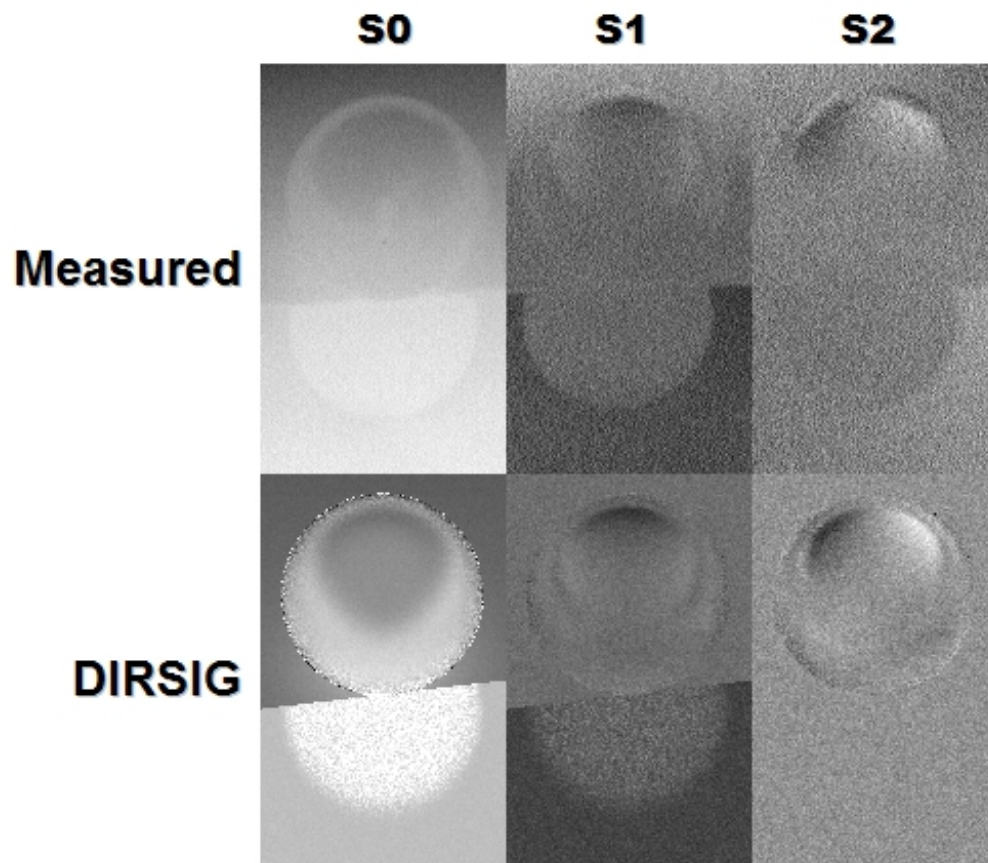


Figure 7.8: Measured and DIRSIG images showing a sphere sitting on snow with a glossy plate in front at night under a starry sky

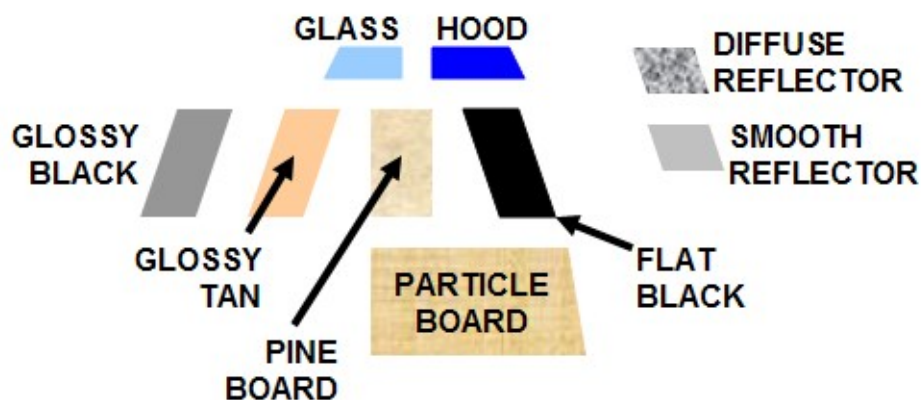


Figure 7.9: Illustration of target placement for Scene 1

yard and my house. Surrounding homes and trees were not included in the simulated scene. *The intention of the simulations was to verify the nature of the reflected and emitted scene phenomenology and angular dependence not to show an exact match.*

### 7.3.5 Scene 1 - Backyard Target Range

A scene in my backyard in North Chili, NY was constructed consisting of a series of painted target surfaces, a piece of a car hood, a piece of glass, and a smooth piece of pine wood (Figures 7.10 and 7.9). This scenario was setup to examine the effect of background clutter on the infrared polarimetric signatures of the target materials.

The imaging zenith angle was approximately 70 degrees from the ground normal, at a range of approximately 8 meters. The images were acquired under a starlit sky on August 21, 2006 between 11:00 and 11:30pm. At the time of image acquisition, the ambient air temperature was 12.9C.

Figure 7.11 shows the experimentally acquired  $S_0$  (a) and  $S_1$  (b) Stoke's image bands. The  $S_2$  Stoke's image band showed no polarimetric contrast, in that all targets were flat to the ground and had a surface normal almost completely in the plane of incidence. Note the ultra-flat black painted surface and the car hood show the

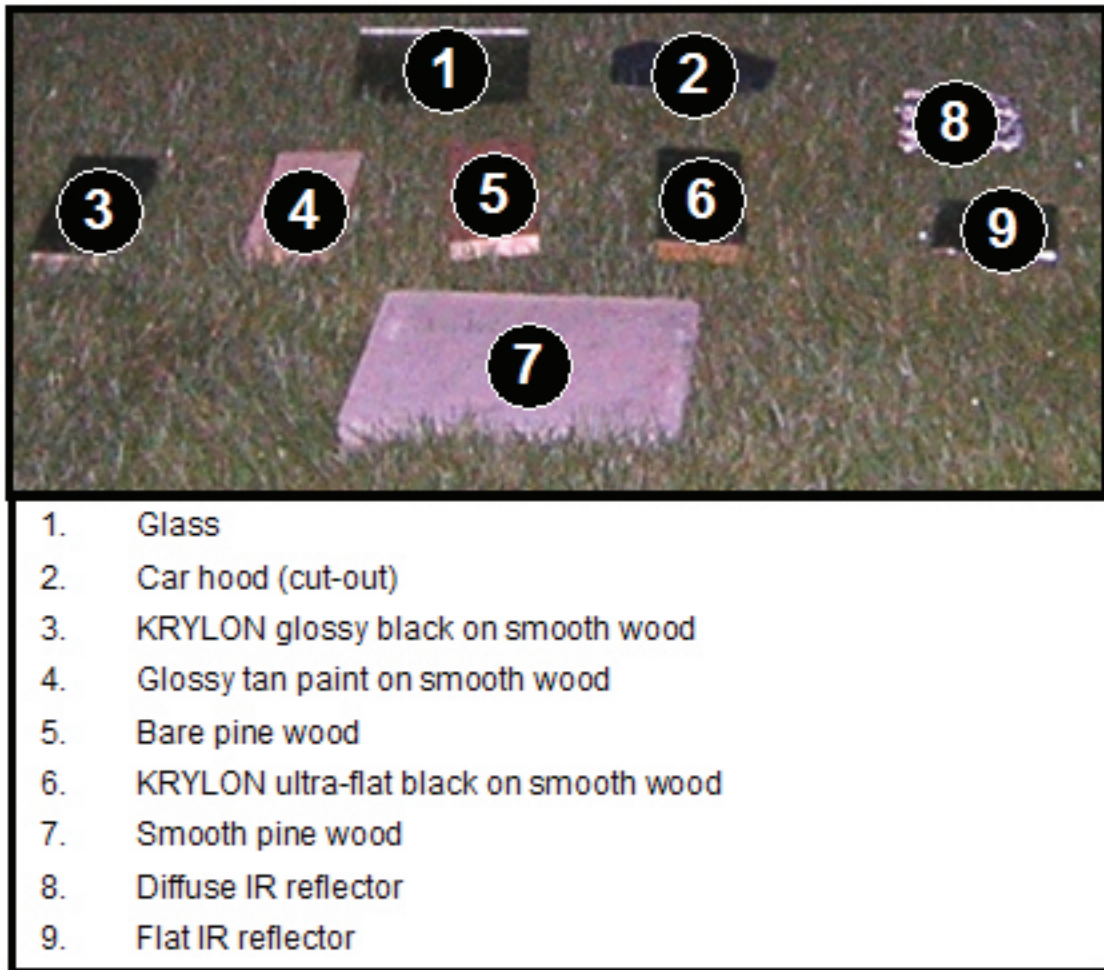


Figure 7.10: Digital camera photo of backyard target range

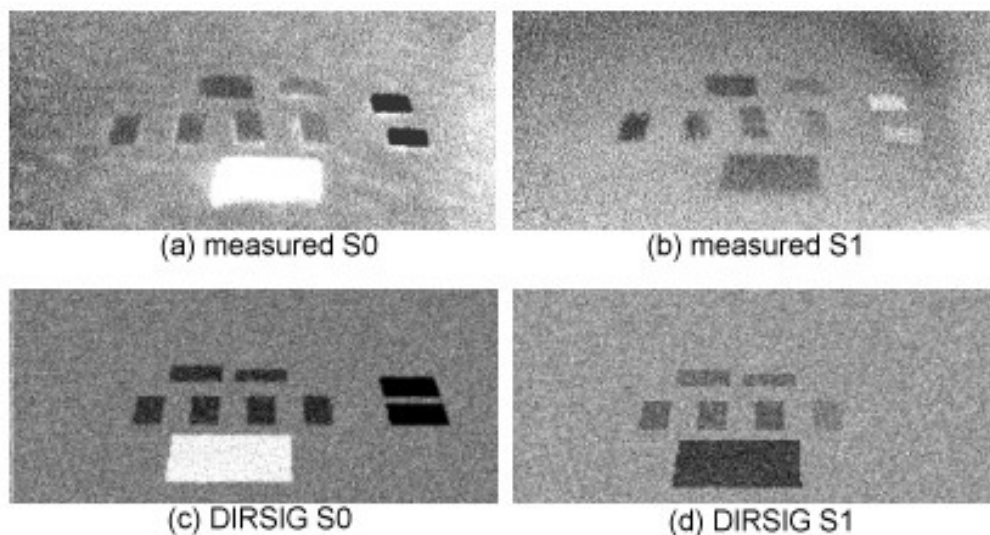


Figure 7.11: Images of backyard target range: measured (a)  $S_0$  (b)  $S_1$  and DIRSIG rendered (c)  $S_0$  (d)  $S_1$ . The IR reflectors were not rendered with polarimetric properties, therefore they do not have contrast in the DIRSIG  $S_1$  image.

least amount of contrast in the  $S_1$  band. Although this is expected for the diffusely scattering flat black surface, the car hood was not expected to have a diminished signature. However, close examination of the car hood sample after imaging operations were complete showed a small amount of dew.

Figure 7.11 also contains the DIRSIG simulated version of the backyard target scene. The simulated  $S_0$  (c) and  $S_1$  (d) images were post processed to contain the same level of noise as the measured  $S_0$  and  $S_1$  bands. There is excellent agreement between the simulated and actual  $S_0$  and  $S_1$  bands, except for the car hood sample as noted previously.

Note that the diffuse and specular IR reflectors in the scene have polarized component in the experimentally measured images, but not the DIRSIG measured images. The reflector targets were not experimentally characterized in this work, therefore the DIRSIG simulation treats them as un-polarized.

The same backyard target range was imaged with a large plastic kiddie pool positioned behind the targets (Figure 7.12). The intent of this scenario was to examine

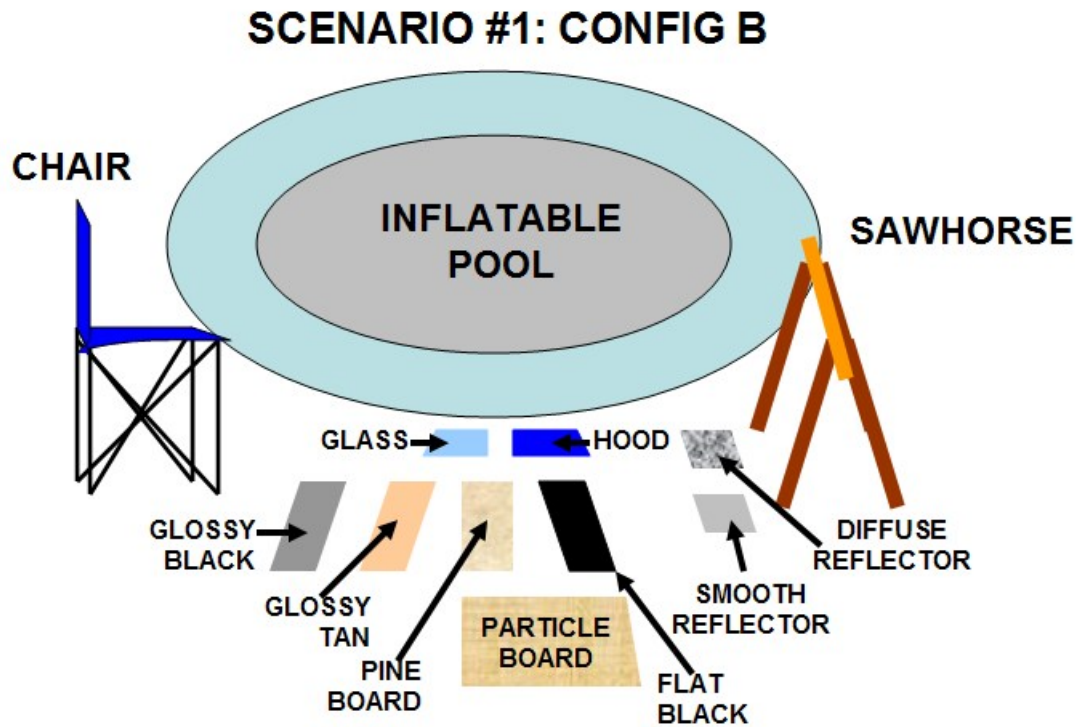


Figure 7.12: Illustration of target placement for Scene 1 with pool

the effect of adding a significant infrared source in the background hemisphere and examine its effect on the  $S_1$  band polarimetric signatures. Figure 7.13 shows the measured  $S_0$  (a) and  $S_1$  (b) bands next to the DIRSIG simulated  $S_0$  (c) and  $S_1$  (d) bands. The bright objects in the measured  $S_0$  image are a sawhorse (right) and a folding chair (left) utilized to hold the pool on its side behind the targets. The sawhorse and folding chair were not rendered in the DIRSIG simulation due to the fact that they did not provide a significant level of background radiance from the target surfaces.

Similar to the backyard scene with no pool, the agreement between the actual and simulated Stoke's bands is excellent. The effect of the pool is that it provides a source of radiance that is reflected from the target surfaces. This reflected radiance has a positive value in the  $S_1$  band that is almost equal in magnitude to the negative value

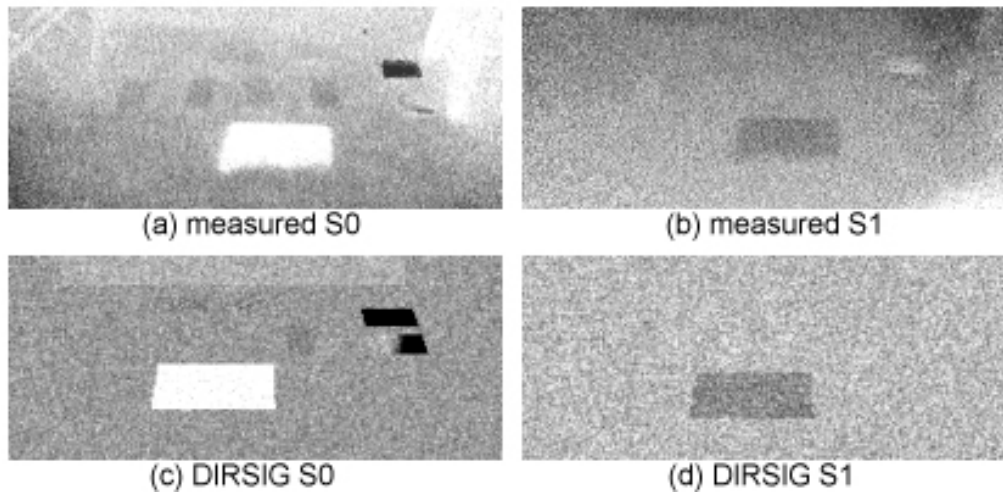


Figure 7.13: Images of background target range with pool behind targets: measured (a)  $S_0$  (b)  $S_1$  and DIRSIG rendered (c)  $S_0$  (d)  $S_1$ .

due to thermal emission in the  $S_1$  band. The result is essentially no polarimetric signature for most targets in the  $S_1$  band (at least within the limits of the image noise).

### 7.3.6 Scene 2 - Automobiles

The next scene was developed to verify the DIRSIG implementation of polarized infrared scene simulation with targets possessing complex geometry. This scene involves three automobiles on an asphalt surface. Figure 7.14 shows a digital camera photo of the scene containing a Volkswagen Beetle, a sedan, and a sport utility vehicle. The corresponding DIRSIG scene was constructed with a hatchback, a sedan, and a sport utility vehicle. The hatchback model was the closest available DIRSIG automobile to the actual Volkswagen Beetle.

The experimentally measured polarized images were acquired on April 7, 2006 between 10:30 and 11:00pm. The ambient air temperature was 6.1C.

Figure 7.15 shows the experimentally measured  $S_0$  (a),  $S_1$  (b), and  $S_2$  (c) images next to the DIRSIG simulated  $S_0$  (d),  $S_1$  (e), and  $S_2$  (f) images. What is most notable



Figure 7.14: Digital camera image of three automobiles utilized for test scene

within the polarized bands of the experimentally measured images are the surfaces facing the sky, such as the hoods and roofs, and the surfaces facing sideways. The surfaces facing the sky are expected to have a significant polarimetric  $S_1$  signature due to (1) the glossy nature of the car surfaces and (2) a lack of significant reflected background radiance to dampen the negative thermally emitted  $S_1$  signature. The surfaces facing sideways are expected to have a minimal polarimetric signature due to the balance between positive  $S_1$  reflected background radiance and negative  $S_1$  emitted radiance. This effect of negligible  $S_1$  signature on the car sides is observed experimentally as expected.

The DIRSIG versions of the  $S_0$ ,  $S_1$ , and  $S_2$  Stoke's bands require careful explanation. The DIRSIG  $S_0$  band agrees roughly with the measured  $S_0$  band. The roofs and car hood facing the sky are generally darker than the rest of the surfaces in the scene due to the minimal amount of reflected background radiance. The sides of the cars are brighter than the hoods and roofs in the DIRSIG  $S_0$  band as expected, but the effect is not as dramatic as what is seen experimentally. This may be due to incorrect modeling of the car temperatures as well as inadequate sampling of the background radiance reflected from the car sides.

The DIRSIG  $S_1$  and  $S_2$  bands correlate very well with the measured  $S_1$  and  $S_2$  bands. Specifically, the roofs and hoods of the cars show up as dark regions in both simulated and measured  $S_1$  image. In addition, there is also a slight brightening of the SUV windshield going from right to left due to the fact that the surface angle rolls away from the imager in this direction. In fact, this rolling away of the  $S_1$  signature on the SUV windshield shows up as a light to dark transition (from right to left) in both the measured and simulated  $S_2$  images.

In addition, the  $S_1$  and  $S_2$  signatures of the car sides show excellent agreement between measured and simulated imagery. The polarized signature from the car sides is actually within the noise of the camera due to the balance between thermally

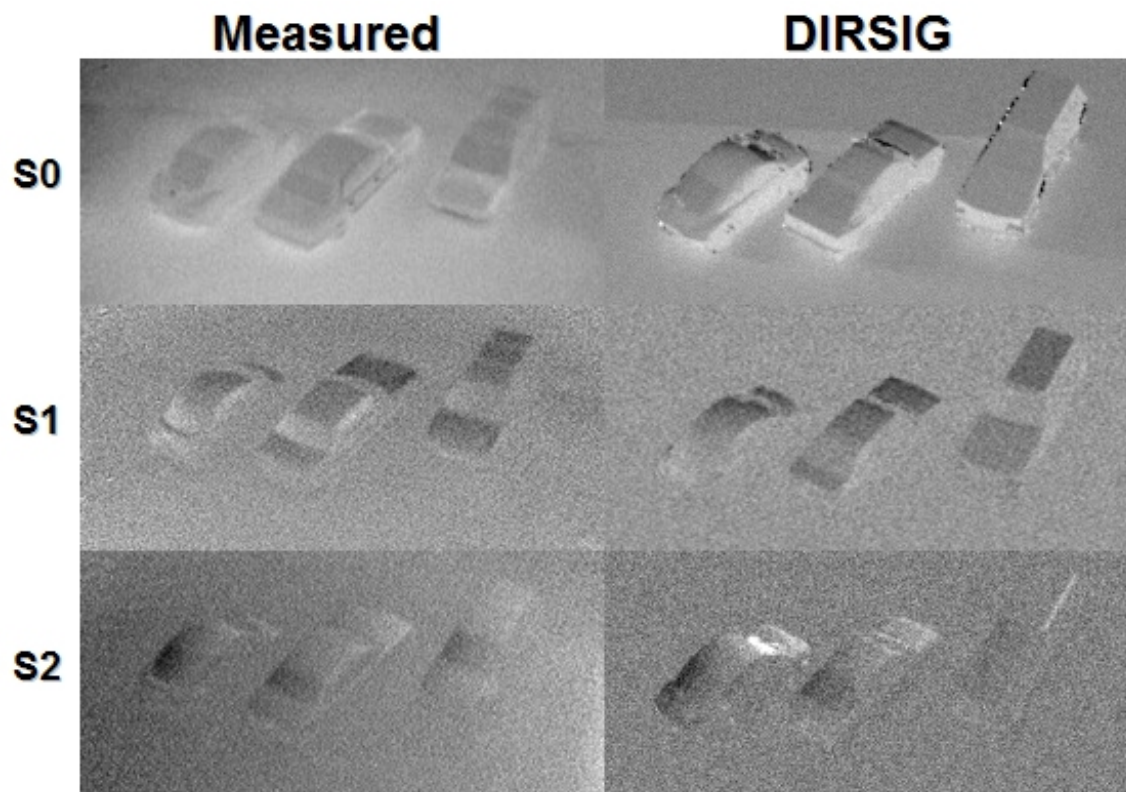


Figure 7.15: Images of automobiles: measured and DIRSIG rendered  $S_0$ ,  $S_1$  and  $S_2$ .

emitted radiance and reflected radiance.



Figure 7.16: Digital camera photo of man made targets placed in the open away from trees.

### 7.3.7 Scene 3 - Man-made Targets in Natural Background

The final scene constructed for verification of the DIRSIG implementation of polarized infrared scene simulation has man-made targets placed in a complex natural background. Specifically, 2'x2' painted panels, a car hood, a window, and a laminate floor plank were placed in the courtyard outside of Building 76 at the Rochester Institute of Technology campus. The courtyard consists of asphalt walkways, grassy areas and multiple kinds of trees.

Two versions of this scene were examined. The first version has the targets placed in the grass with no trees immediately overhead or behind them. The second version has the targets placed with minimal line of sight obscuration, but a significant level of tree cover overhead and immediately behind and on the sides of the targets. The intent of both of these scenarios was to keep the target geometry simple, but the background geometry complex and significant.

Figures 7.16 and 7.17 show the targets placed in front of the grove of trees. Figure



Figure 7.17: Illustration of target placement for Scene 3 with targets out in the open

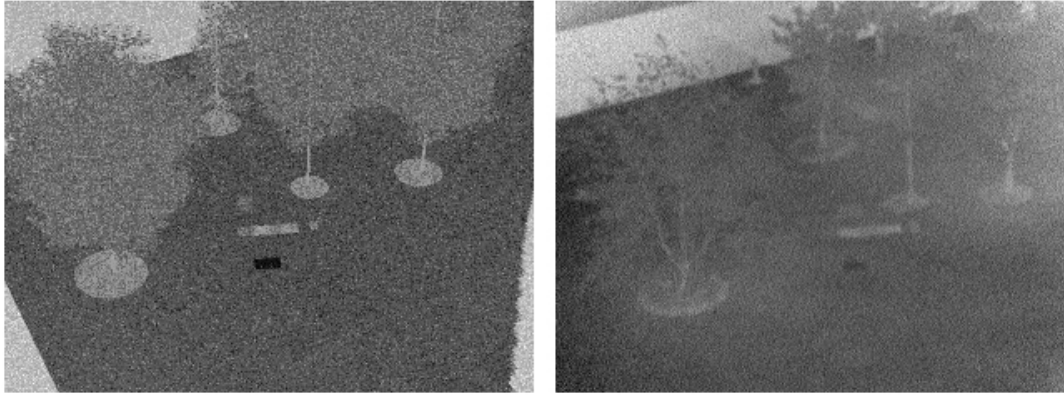


Figure 7.18:  $S_0$  images, (a) DIRSIG rendered (b) measured, of targets in open

7.18 shows the DIRSIG (a) and measured (b) versions of the  $S_0$  band for this first version of the scene. Figure 7.19 shows the DIRSIG (a) and measured (b)  $S_1$  band for this version of the scene. By design, there is good agreement between the measured and DIRSIG  $S_0$  bands because the thermodynamic properties of each scene material were tweaked to obtain this agreement. In the measured  $S_1$  band, 6 out of 7 of the targets are visible. The one target that is not detected is the window (which may have been due to dew accumulation on the window surface inhibiting the polarization signature). In fact, inspection of the targets after the imaging operation was complete showed dew on the painted panels – this most likely contributed to a reduction in the strength of the panel  $S_1$  signatures relative to the DIRSIG  $S_1$  signatures.

All 7 targets are detectable above the noise level in the DIRSIG simulated  $S_1$  band. The measured  $S_2$  band shows no polarimetric contrast within the noise level and is therefore not presented.

Note that the measured  $S_1$  image has a system artifact that appears to show a large dark and light region on the very right hand side of the image. This is not due to actual polarimetric contrast in the scene, but due to the size of the polarizer being slightly too small for the camera aperture.

Figure 7.20 shows a digital camera photo of the 7 targets placed within the grove

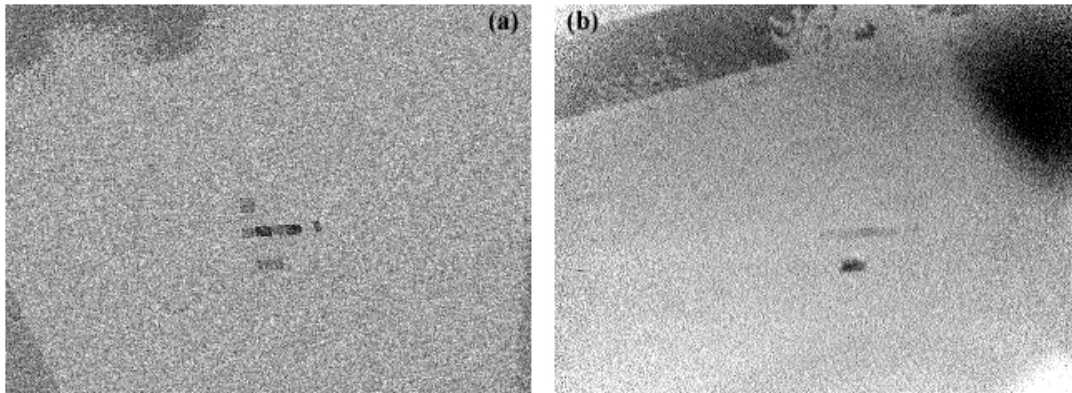


Figure 7.19:  $S_1$  images, (a) DIRSIG rendered (b) measured, of targets in open

of trees. Figure 7.22 shows the DIRSIG (a) and measured (b)  $S_0$  bands, while figure 7.23 shows the DIRSIG (a) and measured (b)  $S_1$  bands. As with the previous version of the scene, there is excellent agreement between the  $S_0$  bands by design. In the measured  $S_1$  band, only the car hood and the flat green painted panel are detected (2/7 targets). In the DIRSIG  $S_1$  band, the car hood, the flat green panel, the flat black panel and the window are detected (4/7 targets).

Although the agreement between measured and DIRSIG simulated  $S_1$  bands is not exact, it is obvious that DIRSIG does a good job integrating the effect of reflected background radiance diminishing polarimetric signatures. It should also be noted that the DIRSIG scene was constructed with tree sizes and types that most closely represented the trees that existed in the measured scene. However, differences between actual and simulated tree geometry and radiometric properties could have significant impacts on the amount of background radiance reflected from the man made target surfaces affecting the detectability in the  $S_1$  band.

It is anticipated that a more accurate correlation between the DIRSIG images and measured images would be found if the DIRSIG scene was configured closer to ground truth. For this dissertation, the significant level of tedious effort required to ground truth and configure the scene in DIRSIG was not justified. The point that



Figure 7.20: Digital camera photo of man made targets placed within a grove of trees.

DIRSIG does an excellent job integrating background reflections in definitely made with the current scene configuration.

Note that the measured  $S_1$  image has a system artifact that appears to show a large dark region on the very right hand side of the image. This is not due to actual polarimetric contrast in the scene, but due to the size of the polarizer being slightly too small for the camera aperture.

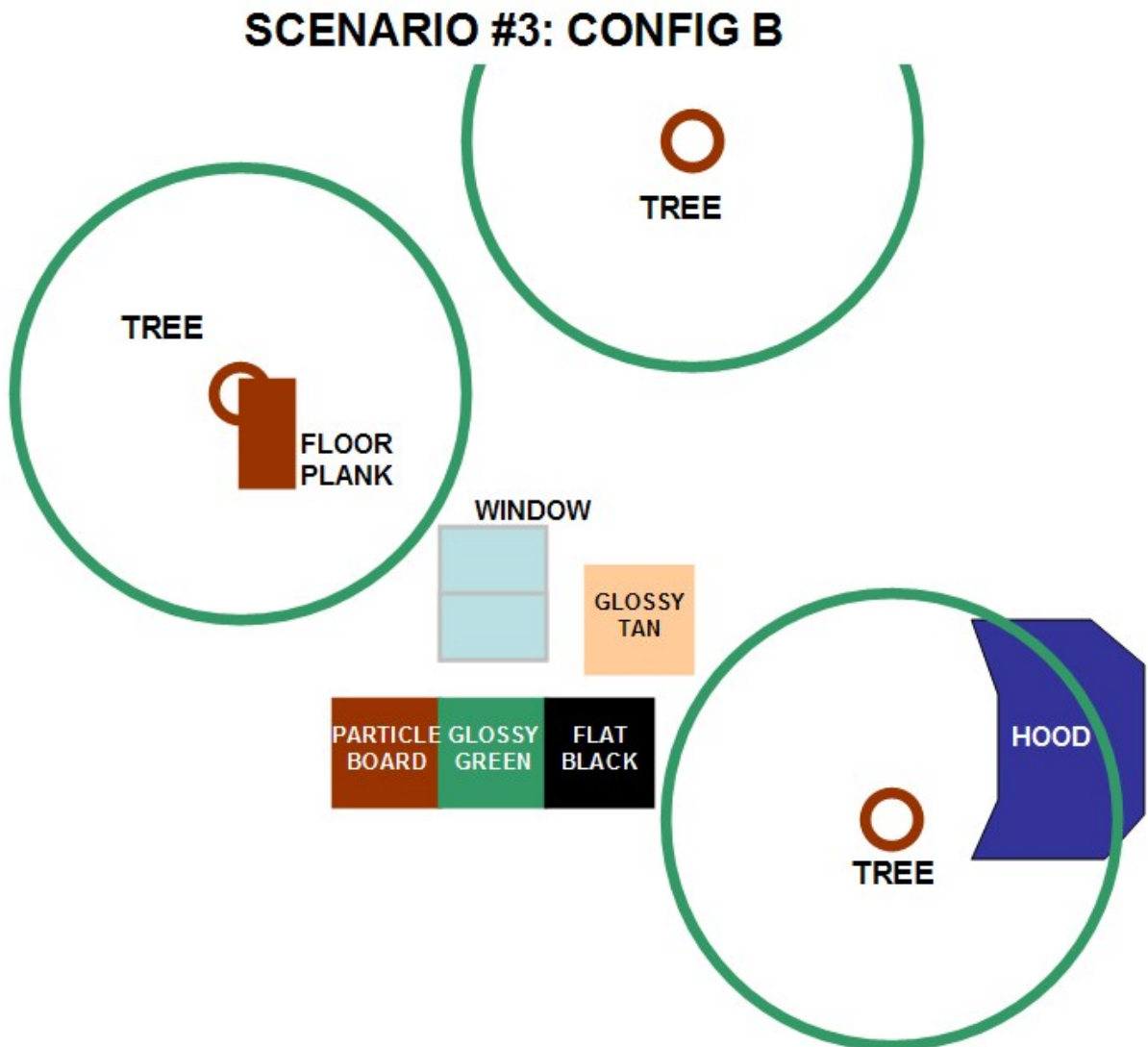


Figure 7.21: Illustration of target placement for Scene 3 with targets embedded in cluster of trees

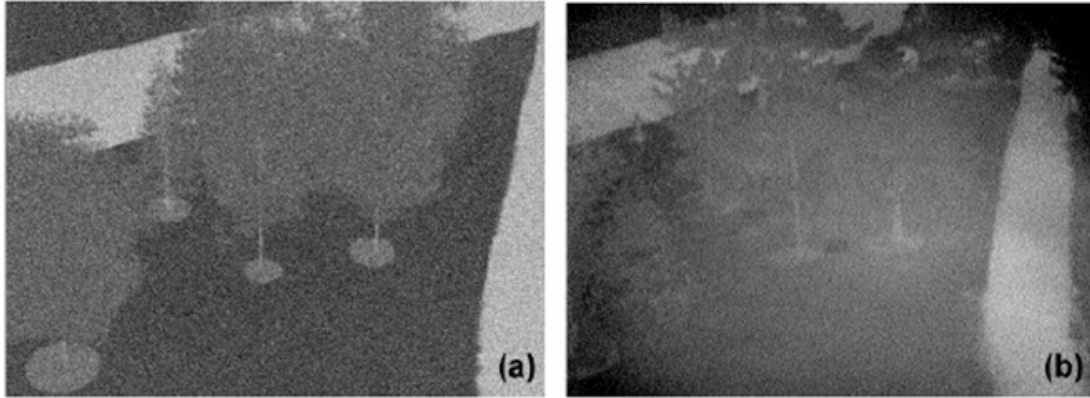


Figure 7.22:  $S_0$  images, (a) DIRSIG rendered (b) measured, of targets embedded in trees

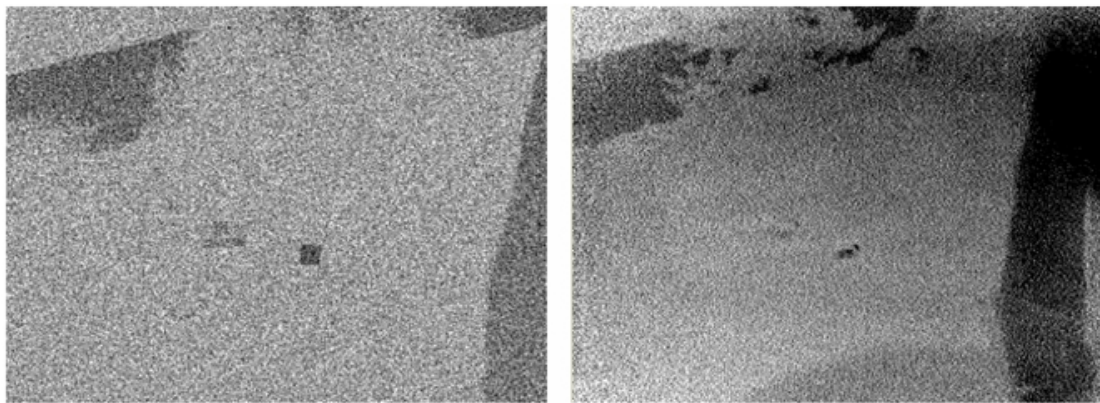


Figure 7.23:  $S_1$  images, (a) DIRSIG rendered (b) measured, of targets embedded in trees

## 7.4 Configuring Materials With Limited Characterization

A future DIRSIG user that would like to configure new materials for polarized infrared scene simulation can easily do so. The requirements for configuring a new material are (1) a hemispherical reflectivity or emissivity spectrum is available and (2) visual inspection of the material is possible.

When the following sequence of steps is followed, the user will have a usable and physically relevant DIRSIG material configured for polarimetric infrared scene simulations.

STEP 1: Visually inspect material reflectance properties in the visible region of the spectrum. Although the reflectance properties in the infrared may differ when the surface texture is very fine, in most cases the specular/diffuse nature carries over from the visible to the infrared region. From visual inspection, put the material into the category of either (1) glossy (2) matte (3) diffuse. The sun and/or artificial light sources are recommended to aid in this determination process.

A material classified as glossy will show reflections from the surface that are very crisp and well-defined, almost mirror-like. An example of such a material is a glossy paint on a plastic surface.

A material to be classified as matte will show subtle specular reflections, but in a very muddy fashion. An example of such a material is a flat painted surface. In most cases, mirror-like reflections are not visible from these types of surfaces. However solar and secondary light source reflections are slightly visible, but very muted compared to what is observed for a specular surface.

Finally, a material to be classified as diffuse will show no visible sign of a specular reflection. Examples of this type of material are easily found in the natural environment (dry grass and rough soil).

Based on the visual results of this step, assign a value of  $\sigma = 0.05, 0.2,$  or  $0.50$  for materials classified as glossy, matte, and diffuse respectively.

STEP 2: Decide whether a material reflectance is most likely due to (1) first surface reflections, (2) volume scattering, or (3) somewhere in between. Although this may seem a daunting task, a rough order guess is good enough for most purposes. Examples of primarily first surface reflective material are glass and metal surfaces. Examples of case (3), somewhere in between, are painted surfaces and bare plastic surfaces. Examples of case (2) are naturally occurring materials such as soil and snow.

Assign a *BIAS* value of 1.0, 0.5, and 0.01 to materials classified as having primarily first surface reflections, a mixture of volume and first surface reflections, and primarily volume reflections respectively.

STEP 3: Estimate a complex index of refraction for material of interest. The NEF database is a good resource for estimating a value for the complex index of refraction of the material of interest. However, if the NEF database is not available, we recommend a complex index of refraction of  $1.5 - 0.3i$  as a starting point.

STEP 4: Start a new .fit file based on the DIRSIG ShellTarget BRDF configuration template provide in Appendix D. Add the values of  $\sigma$ , *BIAS*, and  $\tilde{n}$  into the appropriate fields.

STEP 5: At this point, the user is likely not to know what the polarized emission signature of the material looks like as a function of zenith angle. This is precisely what Steps 1, 2, and 3, are meant to estimate based on observable material properties. In this step, the user will match the unpolarized directional hemispherical reflectance properties to what the IDL polarized BRDF tools (Appendices A, B, and C) estimate. In most cases, the initial model will predict emissivity values that are much higher than what is observed. When this is the case, the value of  $\rho_D$  is increased until the  $S_0$  component of polarized emissivity (or directional hemispherical reflectance) matches well with measured results. In cases where the initial configuration ( $\rho_D = 0$ ) produces

emissivity values that are lower than measured values, it is recommended that the user lowers the *BIAS* value of the surface slope probability distribution function in order to match measured to modeled results. The same result may be achieved by entering negative values of  $\rho_D$ , however this would cause simulation errors, in there is a significant probability of DIRSIG finding a negative BRDF for specific incident/reflected angle geometries.

## 7.5 DIRSIG Simulation Summary

This chapter has presented a verification of how DIRSIG models both polarized thermal emissivity and background reflected radiance. These two aspects of polarimetric infrared radiometry are key to accurate scene simulation.

Next, a daytime and a nighttime version of a scene containing a painted sphere in front of a glossy panel surface were imaged experimentally. The DIRSIG simulations of these scenes show excellent agreement with the experimentally observed phenomenology and provide a strong verification of DIRSIG's ability to keep track of polarization orientation angles.

In addition, three scenes were presented as a verification of DIRSIG's ability to simulate scenes polarimetrically in the infrared. The first scene was designed to have simple surface geometry and focus on the balance between thermally emitted polarization and background reflected polarization. This verification is considered a success.

The second scene (the three cars) examined DIRSIG's ability to simulate scenes polarimetrically with complex target geometry. This verification was considered a success because the DIRSIG  $S_1$  and  $S_2$  signatures originating from thermal emission and background reflections coming from a variety of surface orientations matched well with experimental measurements.

The third scene kept the target geometry simple, but created a complex back-

ground hemisphere full of radiance sources (trees). This final scene successfully demonstrated DIRSIG's ability to model polarimetric phenomenology of target materials in a complex natural background. Specifically, DIRSIG was able to capture the effect of background vegetation muting the polarimetric signature of line-of-sight visible man-made targets.

Finally, the last section presented a method for a future DIRSIG user's to estimate polarimetric properties of materials in the infrared without having to actually conduct measurements as was done for this project (Chapter 6).

# Chapter 8

## Future Work

This dissertation was meant to examine polarimetric phenomenology in the thermal IR region of the electromagnetic spectrum and determine how this could be implemented into DIRSIG. Now that the phenomenology has been explored and DIRSIG has been verified to accurately simulate it (Section 7.3), there are many opportunities for future work in the area of thermal IR polarimetry that could be of interest to RIT and the community at large.

### 8.1 Polarimetric Thermal IR Imaging System Improvements

An obvious area for future work is an improvement to the experimental polarized emissivity measurement hardware and measurement technique. The following ideas are presented for those willing to take on the challenge:

- Replace EZTherm LWIR camera with a radiometrically calibrated LWIR imager
- Remove the restriction of having to work outside under a cloud-free, starlit sky by building a cooled enclosure of known temperature to conduct the measure-

ments

- Outfit all target samples with thermocouples to actively monitor sample temperatures through the collection process
- Increase the number of reflecting calibration targets within the scene to encompass a wider variety of surface textures to better approximate the reflected component of radiance from target samples
- Construct a thermoelectrically cooled and temperature monitored cold plate to place above the wire grid polarizer for reduction in the image shot noise and an overall flatter field of view across the focal plane.

## 8.2 Midwave IR Phenomenology

Another area that would be very interesting to pursue for future work is to examine polarimetric phenomenology in the mid-wave region of the electromagnetic spectrum. In this situation, daytime phenomenology is distinct from nighttime phenomenology and may offer new and interesting observables.

## 8.3 Generation of Polarized Megascene

Develop a software utility to convert current Megascene material database file to new DIRSIG4 material entry format to enable polarimetric visible and infrared rendering of Megascene. This software tool could also automatically determine which materials to model polarimetrically and which to model with the ClassicEmissivity (unpolarized) property based on the values of the existing SPECULARITY and POLISHNESS parameters. Finally, the tool could actually perform the 'polarization' of the material entries in an automated fashion according to the procedure described in Section 7.4

replacing manual assessments of surface properties with parsing of current material entry parameters.



# Appendix A

## IDL Source Code for Polarized BRDF

The following is the IDL source code written to mimic the generalized polarimetric BRDF described in Chapter 5. This code has been tested on IDL5.5 and IDL6.3 and found to compile and execute with no errors.

```
FUNCTION pBRDF, thetaIN, thetaOUT, phi, $
    n, k, $
    sigma, BIAS, $
    omega, tau, $
    rhoV, rhoD, $
    verbose = verbose, $
    cauchy = cauchy

; // force phi between 0 and 2*PI
TWOPI = 2.0*!PI
if phi gt TWOPI then PHI = PHI - TWOPI
if phi lt 0d then PHI = PHI + TWOPI

; // calculate beta
beta = 0.5*acos(cos(thetaIN)*cos(thetaOUT)+sin(thetaIN)*$
    sin(thetaOUT)*cos(phi))

; // calculate thetaN
thetaN_arg = (cos(thetaIN)+cos(thetaOUT))/(2D*cos(beta))
if thetaN_arg lt -1.0 then thetaN_arg = -1.0
if thetaN_arg gt +1.0 then thetaN_arg = +1.0
thetaN = acos(thetaN_arg)
```

```

; // calculate etaI and etaR
etaI_arg = (cos(thetaN) - cos(thetaIN)*cos(beta))/sin(thetaIN)/sin(beta)
etaR_arg = (cos(thetaN) - cos(thetaOUT)*cos(beta))/sin(thetaOUT)/sin(beta)

if not finite(etaI_arg) then etaI_arg = 1.0
if not finite(etaR_arg) then etaR_arg = 1.0

if etaI_arg gt +1.0 then etaI_arg = +1.0
if etaR_arg gt +1.0 then etaR_arg = +1.0
if etaI_arg lt -1.0 then etaI_arg = -1.0
if etaR_arg lt -1.0 then etaR_arg = -1.0
if (PHI eq 0d) or (PHI eq !PI) then signEta = 0.0 else $
  if (PHI gt 0d)and(PHI lt !PI) then signEta = -1.0 else $
    signEta = +1.0
if etaI_arg eq 0d and etaR_arg eq 0d then signEta = +1.0

etaI = signEta * acos(etaI_arg)
etaR = signEta * acos(etaR_arg)

if keyword_set(verbose) then begin
  print,[thetaOUT, beta, thetaN, etaI, etaR],format='(5F11.4)'
  ENDIF

; // calculate fresnel reflectance factors
; // utilize the angle beta for Fresnel reflectance calculations

D = n^2 - k^2 - sin(beta)^2
C = 4*n^2*k^2 + D^2
B = sqrt((C^0.5 - D)/2D)
A = sqrt((C^0.5 + D)/2D)
rhoS = ((A - cos(beta))^2 + B^2) / $
        ((A + cos(beta))^2 + B^2)
rhoP = rhoS * ((A - sin(beta)*tan(beta))^2 + B^2) / $
        ((A + sin(beta)*tan(beta))^2 + B^2)
a_ss = rhoS^0.5
a_pp = rhoP^0.5

Tss = cos(etaI) * a_ss * cos(etaR) + sin(etaI) * a_pp * sin(etaR)
Tps = -cos(etaR) * a_ss * sin(etaI) + sin(etaR) * a_pp * cos(etaI)
Tsp = -sin(etaR) * a_ss * cos(etaI) + sin(etaI) * a_pp * cos(etaR)
Tpp = cos(etaI) * a_pp * cos(etaR) + sin(etaI) * a_ss * sin(etaR)

```

```

TssC = conj(Tss)
TpsC = conj(Tps)
TspC = conj(Tsp)
TppC = conj(Tpp)

if keyword_set(cauchy) then begin
  ; Cauchy probability function
  P = BIAS / (cos(thetaN)*(sigma^2 + tan(thetaN)^2))
endif else begin
; gaussian probability function
  P = BIAS*exp(-tan(thetaN)^2 / 2D / sigma^2) / $
      (2D*!DPI*sigma^2*cos(thetaN)^3)
endif

; Maxwell-Beard Shadowing function
S = (1D + thetaN/omega*exp(-2D*beta/tau)) / $
    (1 + thetaN/omega)

; Fresnel reflectance matrix, linear only elements
R = [[Tss*Tss + Tsp*Tsp + Tps*Tps + Tpp*Tpp, $
      Tss*Tss + Tsp*Tsp - Tps*Tps - Tpp*Tpp, $
      Tss*TpsC+ TssC*Tps+ Tsp*TppC+ TspC*Tpp, $
      0], $
     [Tss*Tss - Tsp*Tsp + Tps*Tps - Tpp*Tpp, $
      Tss*Tss - Tsp*Tsp - Tps*Tps + Tpp*Tpp, $
      Tss*TpsC+ TssC*Tps- Tsp*TppC- TspC*Tpp, $
      0], $
     [Tss*TspC+ TssC*Tsp+ Tps*TppC+ TpsC*Tpp, $
      Tss*TspC+ TssC*Tsp- Tps*TppC- TpsC*Tpp, $
      Tss*TppC+ TssC*Tpp- Tps*TspC- TpsC*Tsp, $
      0], [0,0,0,0d]] / 2D
;if keyword_set(verbose) then begin
; print,'fresnel matrix:'
; print,float(R)
; ENDIF

Fspec = R * P * S / (4D * cos(thetaIN)*cos(thetaOUT))

Fvol  = rhoD + 2D*rhoV/(cos(thetaIN) + cos(thetaOUT))

```

```
F = Fspec
F[0,0] = F[0,0] + Fvol

return, double(F)

END
```

# Appendix B

## IDL Source Code for Polarized DHR

The following is the IDL source code written to mimic the generalized polarimetric DHR calculation described in Chapter 5. This code has been tested on IDL5.5 and IDL6.3 and found to compile and execute with no errors.

```
FUNCTION pDHR, thetaIN, $
    n, k, $
    sigma, BIAS, $
    omega, tau, $
    rhoV, rhoD, $
    verbose = verbose, cauchy = cauchy
oversampleTHETA = 1d
oversamplePHI = 1d
sum = dblarr(4,4)
dt = 1d / oversampleTHETA * !DPI/180d ; deltaTheta = 1 deg
dp = 1d * !DPI/180d/oversamplePHI ; deltaPhi = 1 deg

for i=0, uint(89*oversampleTHETA) do begin
    thetaOUT = i/(90*oversampleTHETA)*!DPI/2d + 1e-4
    sinthetaOUT = sin(thetaOUT)
    costhetaOUT = cos(thetaOUT)
    for j= 0, uint(359*oversamplePHI) do begin
        phi = j*!dpi/360d*2./oversamplePHI + 1e-5
        if keyword_set(cauchy) then $
            result = pBRDF(thetaIN, thetaOUT, phi, n, k, sigma, $
                BIAS, omega, tau, rhoV, rhoD, /cauchy) else $
            result = pBRDF(thetaIN, thetaOUT, phi, n, k, sigma, $
                BIAS, omega, tau, rhoV, rhoD)
```

```
if not finite(result[0,0]) then begin
  print,'theta: ',thetaout*180./!pi
  print,'phi: ',phi*180./!pi
  return, 0
endif
sum = sum + result[0:2, 0]*sinthetaOUT*costhetaOUT
endfor
endfor
return, sum * dt * dp
END
```

# Appendix C

## IDL Source Code for Calculating Polarized Emissivity

The following is the IDL source code written to read in a DIRSIG .fit file and output the polarized emissivity. This code has been tested on IDL5.5 and IDL6.3 and found to compile and execute with no errors.

```
FUNCTION read_dot_fit, fn
openr, lun, fn, /get_lun
st = ''
results = {lambda: 0d, $
           n      : 0d, $
           k      : 0d, $
           bias   : 0d, $
           sigma  : 0d, $
           tau    : 0d, $
           omega  : 0d, $
           rhod   : 0d, $
           rhov   : 0d, $
           dhr    : 0d}
results = replicate(results,6)
i = -1
repeat begin
readf,lun, st
st1 = strsplit(st,',',/extract)
st1[0] = strcompress(st1[0], /remove_all)
if strpos(st1[0],'LAMBDA') ne -1 then begin
i = i + 1
results[i].lambda = float(st1[1])
endif
```

182 APPENDIX C. IDL SOURCE CODE FOR CALCULATING POLARIZED EMISSIVITY

```

if st1[0] eq 'N' then results[i].n = float(st1[1])
if st1[0] eq 'K' then results[i].k = float(st1[1])
if strpos(st1[0], 'DHR') ne -1 then results[i].dhr = float(st1[1])
if strpos(st1[0], 'BIAS') ne -1 then results[i].bias = float(st1[1])
if strpos(st1[0], 'SIGMA') ne -1 then results[i].sigma = float(st1[1])
if strpos(st1[0], 'RHO_D') ne -1 then results[i].RHOD = float(st1[1])
if strpos(st1[0], 'RHO_V') ne -1 then results[i].rhov = float(st1[1])
if strpos(st1[0], 'TAU') ne -1 then results[i].tau = float(st1[1])
if strpos(st1[0], 'OMEGA') ne -1 then results[i].omega = float(st1[1])
endrep until eof(lun)
close, lun
free_lun, lun
return, results
END

PRO dispDHR, st, angle

parms = read_dot_fit('c:\mat\' + st + '.fit')

n = parms[0].n
k = parms[0].k
BIAS = parms[0].bias
sigma = parms[0].sigma
tau = parms[0].tau ; *!PI/180D
omega = parms[0].omega ; *!PI/180D
rhoD = parms[0].rhod
rhoV = parms[0].rhov
rhoDHR = parms[0].dhr

F = dblarr(4,4)
F = pDHR(angle*!dpi/180d, $
          n, k, $
          sigma, BIAS, $
          omega, tau, $
          rhoV, rhoD)
print, 1-f[0,0], -f[1,0], -f[2,0]
ENDFOR
END

```

# Appendix D

## Template to configure polarized material in DIRSIG

The following is a template that may be filled out by the DIRSIG user to configure the polarized BRDF parameters of a new material. This configuration file is typically saved with the file extension .fit. It is required that this file has entries for at least two wavelengths. If no spectral information is known about the new material, just repeat the same values for another wavelength to make this file spectrally flat.

```
SHELL_TARGET = 1.0

FIT_PARAMS {
  LAMBDA = 8.0
  N = <insert real part of index of refraction>
  K = <insert complex part of index of refraction>
  DHR = <insert IDL code generated DHR>

  ORIENT_PROB_NAME = Gaussian
  ORIENT_PROB {
    BIAS = <insert probability function BIAS value>
    SIGMA = <insert surface slope variance value>
  }

  SHADOW_FUNCT_NAME = Maxwell-Beard
  SHADOW_FUNCT {
    TAU = <insert shadowing function parameter TAU>
    OMEGA = <insert shadowing function parameter OMEGA>
  }

  VOLUME_TERM_NAME = Maxwell-Beard
```

184 APPENDIX D. TEMPLATE TO CONFIGURE POLARIZED MATERIAL IN DIRSIG

```
VOLUME_TERM {
  RHO_D = <insert diffuse reflectivity term>
  RHO_V = <insert volume reflectivity term>
}

FIT_PARAMS {
  LAMBDA = 14.0
  N = <insert real part of index of refraction>
  K = <insert complex part of index of refraction>
  DHR = <insert IDL code generated DHR>

  ORIENT_PROB_NAME = Gaussian
  ORIENT_PROB {
    BIAS = <insert probability function BIAS value>
    SIGMA = <insert surface slope variance value>
  }

  SHADOW_FUNCT_NAME = Maxwell-Beard
  SHADOW_FUNCT {
    TAU = <insert shadowing function parameter TAU>
    OMEGA = <insert shadowing function parameter OMEGA>
  }

  VOLUME_TERM_NAME = Maxwell-Beard
  VOLUME_TERM {
    RHO_D = <insert diffuse reflectivity term>
    RHO_V = <insert volume reflectivity term>
  }
}
```

# Appendix E

## Generic Rad Solver Technical Brief

The following appendix is a document written by Adam Goodenough in support of the generic radiometry solver (aka Generic Rad Solver) that performs the core surface level radiometry and background sampling for polarized surfaces within DIRSIG.

### Overview

The goal of CDGenericRadSolver is to be able to effectively sample an unknown bi-directional reflectance distribution function (BRDF) in order to integrate the reflected radiance into a given direction. Assumptions were made about the BRDF in order to design this class:

1. The BRDF is not purely specular or purely diffuse  
*These types of BRDFs can be importance sampled directly and integrated using a Monte Carlo approach*
2. The BRDF cannot be analytically inverted  
*Again, a simple Monte Carlo approach would be more effective*
3. The BRDF is not highly dependent on secondary information in the hit  
*BRDF models that perform differently based on the GSD, for example*
4. The BRDF is made up of some arbitrary combination of diffuse, specular, retro-reflective, or other components  
*i.e. models or measurements where uniform sampling of the BRDF would not be efficient or effective*

These design restrictions dictated the type of radiometry solver that was developed and should be kept in mind when deciding whether to use CDGenericRadSolver for a particular BRDF model.

# Motivation/Background

This work represents a redesign of a pre-existing generic radiometry solver that used a somewhat straight-forward, uniform grid sampling of the BRDF for the non-solar contributions. There were a few problems with this approach:

1. Regular sampling of any space can lead to aliasing artifacts  
*This was mitigated to some extent in two dimensions by rotating the sample “disks” within the sampling dome*
2. Many (computationally expensive) samples could be wasted when the corresponding reflectance was relatively low
3. When the number of samples we wanted to take was few in number, it was very easy to miss high reflectance samples
4. There was no knowledge of the non-primary illumination sources which could be used to further direct the samples

The motivation for this class was the challenge to define a unified approach that addressed these problems. CDGenericRadSolver encompasses an attempted solution to items 1–3, but a general, integrated solution to item 4 does not yet exist in this format (see the note that follows).

*Note*

There are a number of techniques that use forward Monte Carlo propagation of “importons” (nodes that point back to important sampling directions) that could be used to address the illumination problem. The importons are stored in a structure such as a k-nearest neighbor map or facet caches and can be searched to find the important sample directions.

## Context

### Derivation

```

CDRadSolver
├── CDClassicRadSolver
├── CDMonteCarloRadSolver
├── ...
└── CDGenericRadSolver.....SUBJECT OF THIS BRIEF

```

## Components

<code>CDGenericRadSolver</code>	
└─ <code>CDFactoredSampler</code> .....	NEW CLASS, SEE <a href="#">APPENDIX</a>
└─ <code>CDSampleGen</code> .....	FOR SPHERE SECTION SAMPLES

## Approach

A threefold approach to sampling was taken in response to the problems posed previously. The three sampling components are listed below.

- The primary (solar) illumination vector is always sampled if it is on the same side of the geometry as the exitant vector
- An abstract representation of the entire BRDF is used to importance sample non-primary contributions (the user determines the number of these importance samples per generation via the interface)
- The un-sampled portions of the hemisphere integral are “cheaply” sampled to make sure that we don’t miss important source contributions

These three components ensure a thorough sampling of the surrounding space while attempting to make sure that each computationally expensive sample is as effective as possible. The parameters that are exposed to the user enable higher quality calculations at the expense of computational efficiency (or vice versa). Each component is now covered in detail.

### Primary illumination sample

Following the example of other radiometry solvers, `CDGenericRadSolver` makes sure to always sample the solar vector as provided by the atmosphere model. Under normal circumstances, the potential contribution from the sun is the most important in the BRDF integral, often orders of magnitude greater than other contributions.

Since it is quite possible for the surface being calculated to be facing away from the sun, we make sure to check whether the solar vector is in the hemisphere defined by the surface normal. This consists of taking the dot product of the normal and the solar vector, i.e.

————— *Check for a sun facing geometry* —————

```
bool sunFacing =
    CDVector::dotProduct(globalNormal,globalSolarVector)>=0;
```

The solid angle of the sun is calculated once (static) by placing a virtual solar disk at distance one (to make calculations easy) corresponding to the solar half angle provided by the atmosphere model,

*Solar solid angle calculation*

```
static double solarRadius = tan(getSimulation()->getAtmosphere()
    ->getSunHalfAngle());
static double solarSolidAngle = M_PI*solarRadius*solarRadius;
```

The appropriate geometry is calculated for the sample, but before any ray tracing begins, we make sure that the reflectance for that vector pair is significant (currently greater than 1e-6). The radiance from the solar vector is calculated via the usual DIRSIG problem/solution routines and the contribution is computed by applying the (already calculated) reflectance and solid angle.

*Note*

We do not consider the possibility of the sun being partially occluded (by geometry, clouds, or other phenomena) or spatially variant. Technically speaking, we should be sub-sampling the solar disk to compute an average “solar” radiance. However, since the reasons to do this are unlikely, this easier and more efficient approach was used.

Finally, we set the quad (see below) corresponding to the sun vector to the solar value calculated. If the solar solid angle is smaller than the quad solid angle then we calculate an approximate contribution from the remaining portion of the quad and add it to the stored value. If not, then we “squish” the entire contribution into one quad. This approach works since we make sure later that none of the sample vectors fall within the solar solid angle.

*Note*

Although the sun is usually the primary source in most DIRSIG scenes, it would be advantageous to abstract the concept of a primary source to be able to apply the same methods to a wider range of scenarios (low-light level/nighttime simulations for example). This approach would require significant changes to the code and a “global” concept of primary sources.

## BRDF importance samples

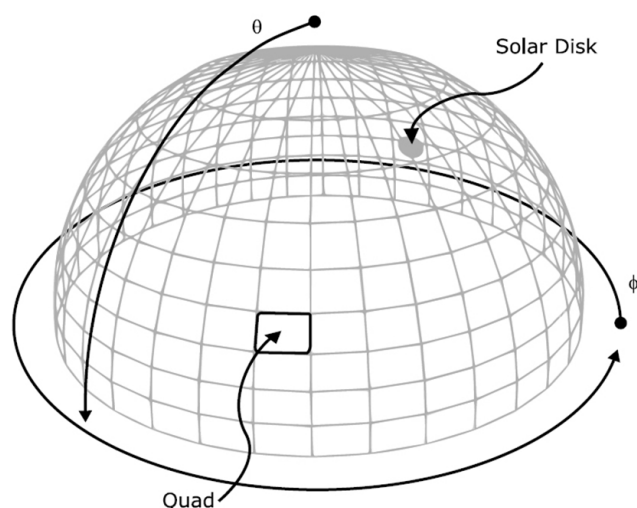


Figure 1: An illustration of the quad segmented concept of the BRDF hemisphere. A somewhat exaggerated projection of a solar disk onto the dome is shown.

The hemisphere corresponding to the contributions to the BRDF is modeled conceptually as a dome divided into quads that represent equal solid angles (see Figure 1). This setup enables us to use the same solid angle for each quad calculation and effectively gives each sample region the same weight.

At this point, we do *not* sample each quad in the hemisphere to calculate the contribution to the reflected radiance. Instead, we choose important samples from a pre-computed importance mapping of the BRDF using `CDFactoredSampler`. Using this method, it is quite possible to get many samples in a few quads and *no* samples in others. This is intentional. The idea here is that in important regions of the BRDF (as determined by the importance sampling) more samples are needed in order to calculate the average radiance from the quad. In other words, a mistake in a highly reflective quad is much more important than a mistake in a low reflectance quad, so we sample accordingly.

*Note*

When assigning the weights for the factored representation of the BRDF, the generic rad solver introduces an additional cosine weighting factor to the reflectance values.

The total number of samples used in this component of the model is determined by the user (see the interface that follows). Additionally, the user defines the number of quads to use in terms of the number of zenith and azimuth samples. Given the

sampling method, the effect of changing the number of quads is not particularly evident except for extreme values.

## Cheap source samples

As stated in the previous section, it is possible for some quads to not have had any samples taken in it and, therefore, not to have a computed contribution to the integral. The final component of the model is a “cheap” (computationally inexpensive) evaluation of whether there is a direct contribution to those quads (i.e. radiance incident from an official source or a emissive object). This is done by setting the generation of the sample to some arbitrarily high number. If the sample hits a source (e.g. the atmosphere) then the source radiance is returned. If the sample hits geometry then, by “convention” the radiometry solver computes the emitted radiance before checking the generation count (which, because of the high generation, should always result in the solver returning). The convention to add the emitted radiance before the generation check has been implemented in `CDGenericRadSolver` and `CDMonteCarloRadSolver`, but is not guaranteed for all rad solvers.

# User Interface

Recommended values for the parameters are given alongside the default values. These are intended to be used if a somewhat higher quality run is desired, but are not provided as the defaults since they can cause noticeable slow downs in either the initialization or run time (or both).

Parameter	Type	Default	Description or Link
INITIAL_SAMPLE_COUNT	int	10 ( <i>100</i> )	The number of importance samples in the first generation
MAX_BOUNCES	int	3 ( <i>5</i> )	The reflected contribution is not collected after the generation reaches this number
SAMPLE_DECAY_RATE	int	10 ( <i>3</i> )	Controls how many importance samples are taken after the first generation ( <a href="#">link</a> )
MU_SAMPLES	int	10 ( <i>20</i> )	Number of cosine distributed zenith angles in the quad representation
PHI_SAMPLES	int	10 ( <i>20</i> )	Number of azimuthal angles in the quad representation
J_RANK	string	8 ( <i>16</i> )	A parameter to the component CDFactoredSampler class ( <a href="#">See Appendix</a> )
K_RANK	string	2 ( <i>3</i> )	A parameter to the component CDFactoredSampler class ( <a href="#">See Appendix</a> )
ITERATIONS	long	100 ( <i>1000</i> )	A parameter to the component CDFactoredSampler class ( <a href="#">See Appendix</a> )

### SAMPLE\_DECAY\_RATE

The number of samples in the  $i$ th generation (where the first generation is  $i = 0$ ) is calculated as

$$\text{ceil} \left( \frac{\text{INITIAL\_SAMPLE\_COUNT}}{\text{SAMPLE\_DECAY\_RATE}^i} \right).$$

In other words, SAMPLE\_DECAY\_RATE describes how much the INITIAL\_SAMPLE\_COUNT is divided by after each generation (with a ceiling function that makes sure it never drops below one). Examples of different decay rates are shown in [Figure 2](#)

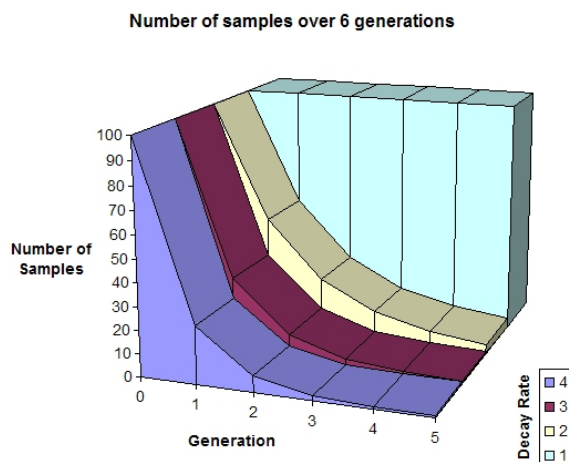


Figure 2: The effect of different decay rates on the number of samples at each generation. The INITIAL\_SAMPLE\_COUNT was set to 100

## Appendix

### CDFactoredSampler

**Overview** CDFactoredSampler represents a partial implementation of “Efficient BRDF Importance Sampling Using A Factored Representation” [13]. The implementation, at the time of writing, supports importance sampling, but not some of the additional functionality described in the paper (though it could be added to the given framework in the future). The code uses a half angle parametrization under the hood as suggested by the paper, but does not allow for arbitrary parametrization schemes. Despite some shortcomings compared to the original, the implementation is more than sufficient for the application given here.

*Note*

Unlike the version in the paper, this implementation is not intended to be used to represent BRDF models or data exactly, only to give a reasonable approximation for generating samples.

The current version represents a rewrite that de-couples CDFactoredSampler from the code that uses it. This is done by having the factored sampler request the values for the vector pairs that it needs and maintaining an internal representation of the data that is independent from the code that supplies the values. This is in contrast to the

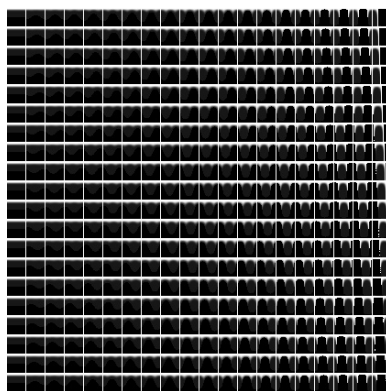


Figure E.1: The data matrix for an arbitrary BRDF model

original implementation which required a full understanding of the data structures to be useful.

**Motivation/Background** A bi-directional distribution function (BRDF) is a four-dimensional function in general (i.e. it takes both a source and exitant vector, each of which can be described by a zenith and azimuth angle). Storage for a sufficient number of source/exitant vector pairs presents a problem for efficient implementation of BRDF code. The approach taken here is to factor the matrix of data representing the BRDF using a non-negative matrix factorization (this allows sampling later on). An example of a BRDF data matrix is shown in Figure E.1 – the white lines segment off the specific BRDF corresponding to each exitant vector. The BRDF itself represents a simple diffuse + specular model where the specular portion is modeled as a phong-like lobe. The data shown uses twenty zenith samples and twenty azimuthal samples (in general, more zenith detail is needed). The black (zero-valued) portions of the BRDF data in the figure correspond to half-vectors that would lead to sample rays that are outside of the allowable hemisphere of vectors.

Factorization of the data matrix greatly decreases the storage requirements of the data at the expense of approximating the BRDF at high compression rates. Because of the parametrization into half vector space, the potential losses due to factorization are minimized. Additionally, the form of the factored data can be used to efficiently importance sample the BRDF given an exitant vector (see [13] for more details).

This technique is powerful and can potentially be used to construct fully independent BRDF models from measured data or complex models (see [13]). For this application, we will only use the “generic” sampling capabilities of the approach in order to produce random importance samples corresponding to the high reflectance regions of the BRDF being used.



Figure E.2: The result of non-negative factorization of  $Y$  into  $G$  (left) and  $F$  (right) using  $J\_RANK = 8$ .

**Approach** The process starts out by performing a non-negative factorization of the BRDF data matrix (matrix  $Y$ , to be consistent with the paper) into two new matrices,  $F$  and  $G$  as shown in Figure E.2.

The quality of the factorization is determined by the rank—in general, a higher rank equals a better reconstruction (this can be seen in Figure E.4). On the other hand, a higher rank means that more of the data is retained, leading to less data compression. In this case, a rank of 8 maintains a sufficient quality representation of the data. The original BRDF data matrix consisted of  $400 \times 400 = 160,000$  data points (from 20 zenith samples and 20 azimuth samples). After the first factorization this is knocked down to  $2 \times 400 \times 8 = 6,400$  data points. The next step in the process re-wraps the columns of the  $G$  matrix and factors each column representation into additional matrices (using a  $K\_RANK$  that can be very small (probably 2–4)). Finally, all of the data is organized so that it can be quickly indexed into and sampled (see [13] for details). Figure E shows 10,000 samples for a particular exitant angle.

The internal sampling obtains an entire hemispherical quad corresponding to the closest half vector (due to quantized sampling of the BRDF). We then sample uniformly within the quad to get the final half vector and compute the final source sample vector from that. The `CDSampleGen` class is used to generate uniform samples on a spherical quad.

**User Interface** The interface to `CDFactoredSampler` is not directly exposed to the user. The parametrization described here (with the exception of `IS_HEMISPHERE`) corresponds to the parameters in `CDGenericRadSolver` of the same name.

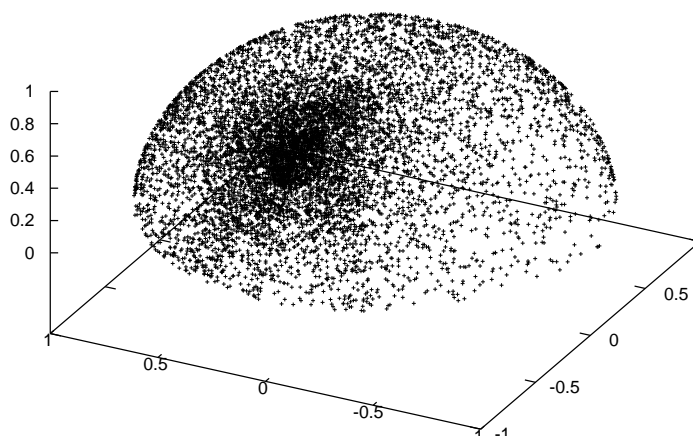


Figure E.3: 10,000 samples from the model with the given BRDF data and using an exitant vector at  $45^\circ$ .

Parameter	Type	Default	Description or Link
J_RANK	string	8	Along with K_RANK, sets the number of terms ( <a href="#">See Below</a> )
K_RANK	string	2	Along with J_RANK, sets the number of terms ( <a href="#">See Below</a> )
ITERATIONS	long	100	Number of iterations used to find the best fit factorization
<i>IS_HEMISPHERE</i>	bool	TRUE	Data and samples represent a hemisphere (as opposed to a full sphere) <a href="#">note</a>

### J\_RANK/K\_RANK

The two rank parameters control how many terms (factored matrices) are used to represent the full BRDF data matrix. The details are not particularly important (see [\[13\]](#)) but, in general, the J\_RANK should be used to set the quality and K\_RANK usually should be set to a low number such as 3, or even 2. The results of varying the J\_RANK for the BRDF already shown are shown in [Figure E.4](#).

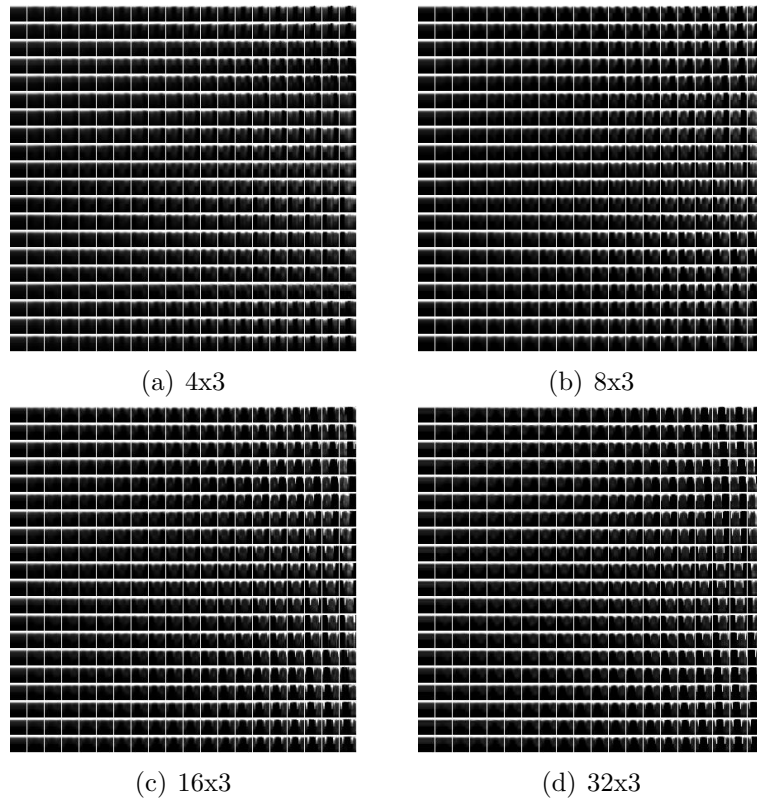


Figure E.4: Reconstructions of the original BRDF data matrix after using increasing J\_RANK values (a-d). Note that the 32x3 (JxK) rank reconstruction is almost identical to the original.

**A note on IS\_HEMISPHERE**

While it has not yet been tested, it is possible to use the factorization approach for spherical data (a full BDF (reflectance plus transmittance) for instance). Setting this parameter to false will make the code treat the given data as being on a sphere and will generate samples accordingly (hopefully). At the moment this parameter is not supported by CDGenericRadSolver.



# Appendix F

## Polarization Orientation Technical Brief

The following appendix is a document written to support a change to the DIRSIG CDGenericRadSolver class to enable correction of polarization orientation between facet local, incident ray, and exitant ray directions.

### Overview

The goal of this technical brief is to describe the convention utilized within DIRSIG to orient the  $S_1$  and  $S_2$  components of Stoke's polarization vectors.

### Motivation/Background

The motivation for this work was to determine how the orientation of linear polarization states could be handled within DIRSIG. Under the previous implementation, DIRSIG was not able to distinguish between polarized radiance emitted from a facet oriented towards the sky and polarized radiance emitted from a facet oriented sideways. This lack of distinction was due to the fact that all Stoke's vectors were calculated and reported at a facet local level. In order to remedy this problem, a convention is needed to orient all Stoke's vectors to a global coordinate system.

### Approach

#### Stoke's Vector

In 1852, George Gabriel Stokes developed a system for describing the polarization state of incoherent radiation. The system involved replacing scalar radiation intensity values with 4 element column vectors. These column vectors are commonly referred to as Stoke's vectors.

$$\vec{S} = \begin{pmatrix} S_0 \\ S_1 \\ S_2 \\ S_3 \end{pmatrix} \quad (\text{F.1})$$

For a given amount of incoherent radiation, a Stoke's vector contains the total electromagnetic radiation intensity incident onto an imaging system in the 1st element,  $S_0$ . The light intensity may be represented by the magnitude of the electric field vector, irradiance, radiance, or any other radiometric quantity. For our description, we will present the Stoke's vector in terms of the quantity irradiance. The  $S_0$  irradiance element is proportional to the square of the magnitude of the electric field vector described previously.

$$S_0 = E_s + E_p \quad (\text{F.2})$$

The  $S_1$  element is defined as the difference between polarization in the  $\hat{s}$  direction and  $\hat{p}$  direction. A positive value of  $S_1$  describes light that is more polarized in the  $\hat{s}$  direction, while a negative value describes light that is more polarization in the  $\hat{p}$  direction. The  $\hat{p}$  direction is described as the direction parallel to the plane of incidence, while the  $\hat{s}$  direction is perpendicular to the plane of incidence of a light ray. Sometimes the terms *horizontal* and *vertical* polarization are utilized in place of  $s$  and  $p$  polarization respectively.

$$S_1 = E_s - E_p \quad (\text{F.3})$$

To aid in describing the  $S_2$  element, we refer to the direction that is halfway between  $+\hat{s}$  and  $+\hat{p}$  as the  $\hat{a}$  direction and the direction that is halfway between  $-\hat{s}$  and  $+\hat{p}$  as the  $\hat{b}$  direction. Sometimes the  $\hat{s}$ ,  $\hat{p}$ ,  $\hat{a}$ , and  $\hat{b}$  directions are also known as the 0, 90, 45, and 135 degree directions respectively.

The  $S_2$  element contains the amount of polarization that exists in either the  $\hat{a}$  or  $\hat{b}$  directions. A positive value of  $S_2$  indicates preferential polarization in the  $\hat{a}$  direction, while a negative value indicates a preferential polarization in the  $\hat{b}$  direction.

$$S_2 = E_a - E_b \quad (\text{F.4})$$

The  $S_3$  element of the Stoke's vector contains the amount of circular polarization. A positive value of  $S_3$  indicates more left circular polarization, while a negative value indicates a more right circular polarization value.

$$S_3 = E_{lc} + E_{rc} \quad (\text{F.5})$$

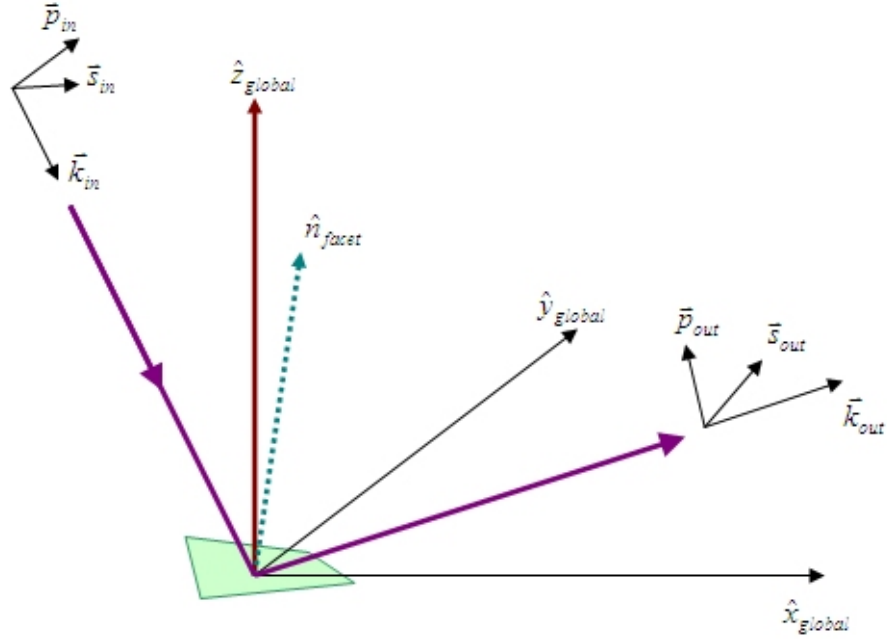


Figure F.1: Illustration of global coordinates, facet normal, incident and exitant ray directions.

The angle of polarization (AOP) is the relative angle between the  $S_1$  and  $S_2$  components of a Stoke's vector.

$$AOP = \frac{1}{2} \tan^{-1} \left( \frac{S_2}{S_1} \right) \quad (\text{F.6})$$

### Calculation of Ray $S$ and $P$ Directions

We define the  $s$ - $p$  polarization plane of a light ray to be the plane that has a normal that is the same as the direction of propagation of the ray  $\vec{k}$ . As a convention, we assume that the  $\hat{p}$  axis of the  $s$ - $p$  plane always points in the global  $\hat{z}$  direction. Figure F.1 shows an illustration of a light ray propagating in the direction  $\vec{k}_{in}$ , incident to a facet defined by its normal vector  $\hat{n}_{facet}$ .

The  $p$  and  $s$  axes of the ray's  $s$ - $p$  plane are found by

$$\hat{p} = \vec{k} \times (\hat{z} \times \vec{k}) \quad (\text{F.7})$$

$$\hat{s} = \vec{k} \times \hat{p} \quad (\text{F.8})$$

### Projection of Facet Normal into Ray S-P Plane

The local facet normal  $\hat{n}_{facet}$  is projected into the ray's  $s$ - $p$  plane by means of a similar

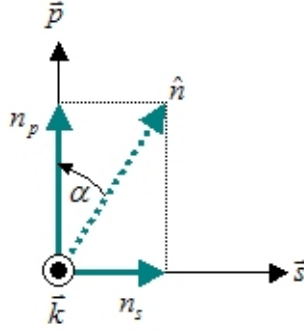


Figure F.2: Illustration showing projection of facet normal into ray s-p plane.

operation

$$\vec{n}_{sp} = \vec{k} \times (\hat{n}_{facet} \times \vec{k}) \quad (\text{F.9})$$

Figure F.2 shows the facet normal in the  $sp$  plane. The angle this projection makes with the global  $z$  direction (which is the same as the  $p$ -axis by the convention mentioned above) is the angle needed to rotate the  $S_1$  and  $S_2$  bands to go from the coordinate system of the incident ray to the facet local coordinate system. Therefore, the  $s$  and  $p$  components of the projected facet normal are calculated as follows

$$n_p = \vec{n}_{sp} \cdot \hat{p} \quad (\text{F.10})$$

$$n_s = \vec{n}_{sp} \cdot \hat{s} \quad (\text{F.11})$$

### Calculation of Rotation Angle

Finally, the rotation angle  $\alpha$  required to rotate from the incident vector polarization coordinates to the facet local polarization coordinates is simply

$$\alpha = -\tan^{-1} \left( \frac{n_s}{n_p} \right) \quad (\text{F.12})$$

In order to go from the facet local polarization coordinates to the exitant ray polarization coordinates, the rotation angle is

$$\alpha = \tan^{-1} \left( \frac{n_s}{n_p} \right) \quad (\text{F.13})$$

## DIRSIG Implementation

### CDMuellerMatrix

The computeLocalToGlobalRotation method of the CDMuellerMatrix class calculates

the angle  $\alpha$  to go from facet local to exitant ray polarization coordinates. The function `makeLocalToGlobalProjector` computes the required Mueller matrix to put a Stoke's vector expressed in a ray polarization coordinates into a facet local polarization coordinate system. This function accepts the facet normal and ray direction vectors (assumed to be in global coordinates) as inputs. Similarly, the function `makeGlobalToLocalProjector` computes the required Mueller matrix to put a Stoke's vector expressed in a facet local polarization coordinate system into a global exitant ray polarization coordinate system.

### **CDGenericRadSolver**

The concept of getting the polarization coordinates consistent within `CDGenericRadSolver::compute` is to:

1. Rotate all source of incident radiance from incident ray polarization coordinates to facet local polarization coordinates (each incident ray considered will have it's own required Mueller matrix rotation)
2. Sum all sources of radiance (emitted, solar/lunar reflected, background reflected) in facet local polarization coordinates
3. Rotate final radiance from facet local to exitant ray polarization coordinates

It should be noted that the micro-facet based BRDFs (such as `ShellTarget`) have built in Mueller matrix rotations to go from facet local to micro-facet and back to facet local coordinate systems. Although similar, these rotations are not the same as the rotations required within Generic Rad Solver. In fact, it should be noted that the Mueller matrices produced by the polarized BRDFs assume the samples surfaces (aka facets) are flat to the ground, which is precisely why this facet local to ray polarization coordinate rotation is required!



# Appendix G

## Polarized Emissivity Measurement Procedure

This appendix is a concise description of the experimental technique and hardware utilized in this work to measure polarized emissivity.

### G.1 Required Equipment

The following equipment is required:

- Wire grid polarizer
- LWIR EZTherm camera
- Stage to hold camera and polarizer
- Reynolds brand aluminum foil
- Camera tripod
- Sample stage with tip/tilt capability
- Digital protractor
- Foil panel on a 1ft x 1ft piece of cardboard
- Aluminum foil pressed flat over a CD jewel case (glossy IR reflector)
- Crumpled aluminum foil wrapped over a CD jewel case

The pictures in Figures [G.1](#) and [G.2](#) show the camera stage and sample stage built for this work.



Figure G.1: Photo of camera and polarizer stage



Figure G.2: Photo of sample stage with tip-tilt capability

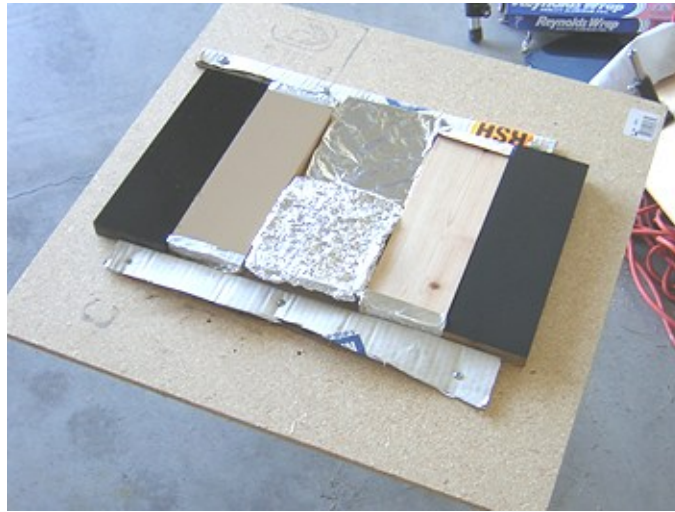


Figure G.3: Photo of sample stage loaded with material samples and foil targets

## G.2 Experimental Technique

1. Confirm that the sky is starlit and cloud-free (if not, abort!).
2. Place desired target material samples, glossy foil sample and a diffuse foil sample on sample stage. Figure G.3 shows an example of the sample stage loaded with 4 different painted wood panels and both foil targets. Note the ambient air temperature. For most material samples, it is helpful to put small pieces of aluminum foil at the corners as fiducial markers to aid in locating the samples in the images during the analysis process.
3. Turn on EZTherm camera and allow the sensor to reach thermal equilibrium (usually about 10 minutes).
4. Acquire an image of the blackbody cavity inside at room temperature.
5. Bring the camera and blackbody cavity outside and acquire images as the temperature of the cavity lowers to the ambient air temperature. Depending on the temperature difference between inside and outside, this may take anywhere from 10 - 20 minutes.
6. Assemble camera assembly by placing EZTherm on its mount and placing wire grid polarizer in its holder. Attach camera assembly to tripod at a height of about 4.5 feet. Using digital protractor tip camera assembly mount towards the ground at an angle of 45 degrees and positioned such that the camera is aiming at the sample stage.



Figure G.4: Photo of tripod (without camera and polarizer loaded), sample stage with targets, and foil placed behind stage to reflect sky

7. Allow the camera and wire grid polarizer about 10 minutes to reach thermal equilibrium
8. While the camera and polarizers are stabilizing, place aluminum foil on the ground underneath and surrounding the sample stage with a radius of about 2 meters.
9. Note the ambient air temperature again and compare to previous reading. If the temperature change over this approximately 20-30 minute period changes by more than a few degrees, it is likely that the temperature is still changing and it might be wise to hold off on the rest of the procedure until the temperature change rate slows down. If the experimental measurements continue while the ambient air temperature is changing at a high rate (less than 0.5 degree Fahrenheit per 5 minutes) it is assumed that the target sample temperatures are also changing at this rate and this will produce erroneous emissivity measurement results.
10. Placing the foil panel in front of the EZTherm camera, acquire a calibration image for polarizer orientations of 0, 45, 90, and 135 degrees.

11. Using the digital protractor, tip the sample stage towards the camera at an angle of 45 degrees. This orientation gives the camera a zenith angle of 0 degrees relative to the sample surface normals.
12. Acquire images with polarizer orientations of 0, 45, 90, and 135 degrees. For cold scenes, multiple images for each polarizer orientation are recommended (five images was sufficient for winter collects, while one was sufficient for summer collects). Collecting the images in the order: 0, 90, 45, and 135 was found to reduce the effects of target thermal drift in the  $S_1$  and  $S_2$  bands.
13. Using digital protractor, reposition sample stage to produce the next zenith angle of interest. For this dissertation work, image sets were collected for zenith angles of 0 to 70 degrees in 10 degree increments. In some cases where the samples were quite flat (such as painted wood samples), an image set at a zenith angle of 80 degrees was collected.
14. After all image collections are concluded, repeat the foil calibration panel collection for all four polarizer orientations and note the ambient air temperature.
15. Turn off camera and break down setup.



# Appendix H

## Detailed Critique of DIRSIG Simulations

This appendix is a detailed "what's different" between measured polarimetric thermal IR imagery and DIRSIG simulations. The intent is to explain what differences exist and the source of the difference (artifact, geometry difference etc.).

### H.1 Backyard Scene

Figure [H.1](#) compares the measured and DIRSIG simulation of the backyard target scene.

1. The diffuse and glossy IR reflector targets (aluminum foil) show contrast in the measured  $S_1$  image, but not in the simulated  $S_1$  image. The origin of the polarimetric contrast in the measured image is due to the reflection of the downwelled sky radiance, hence the positive value. The polarized emissivity of the reflector targets were not measured within the scope of this work, and was therefore not simulated in the DIRSIG scenes.

Figure [H.2](#) compares the measured and DIRSIG simulation of the backyard target scene.

1. The chair that is visible in the measured  $S_0$  image was not included in the simulated DIRSIG scene model.
2. The sawhorse that is visible in the measured  $S_0$  image was not included in the simulated DIRSIG scene model.
3. The diffuse and glossy IR reflector targets (aluminum foil) show contrast in the measured  $S_1$  image, but not in the simulated  $S_1$  image. The origin of

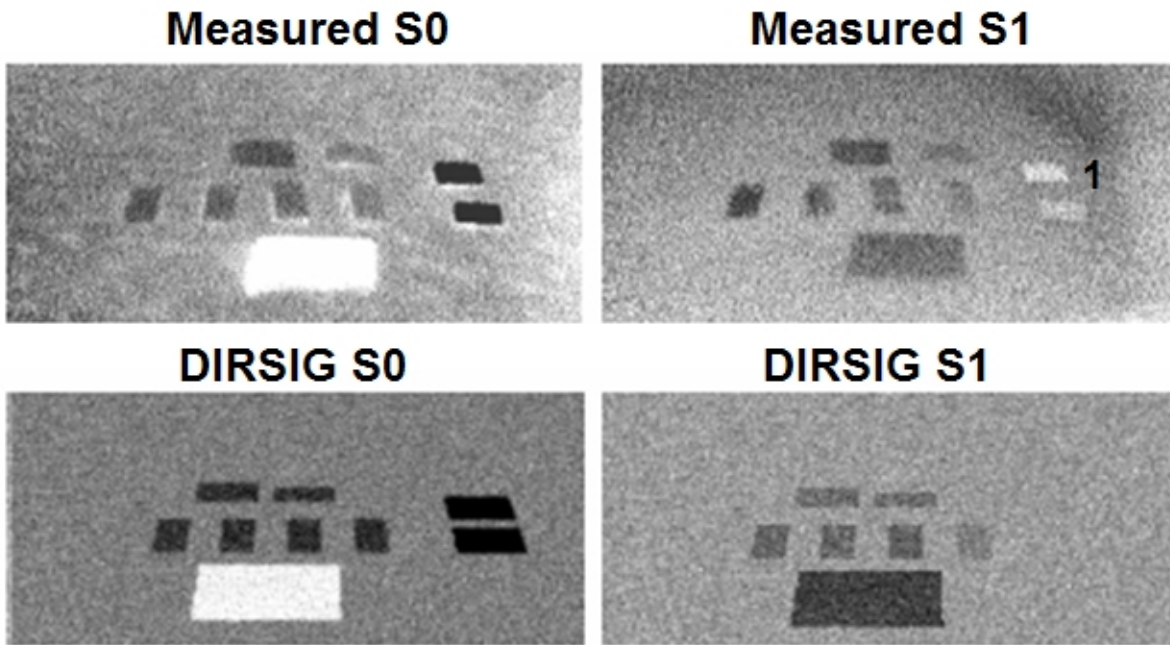


Figure H.1: Comparison of DIRSIG and measured thermal IR images of targets in backyard scene

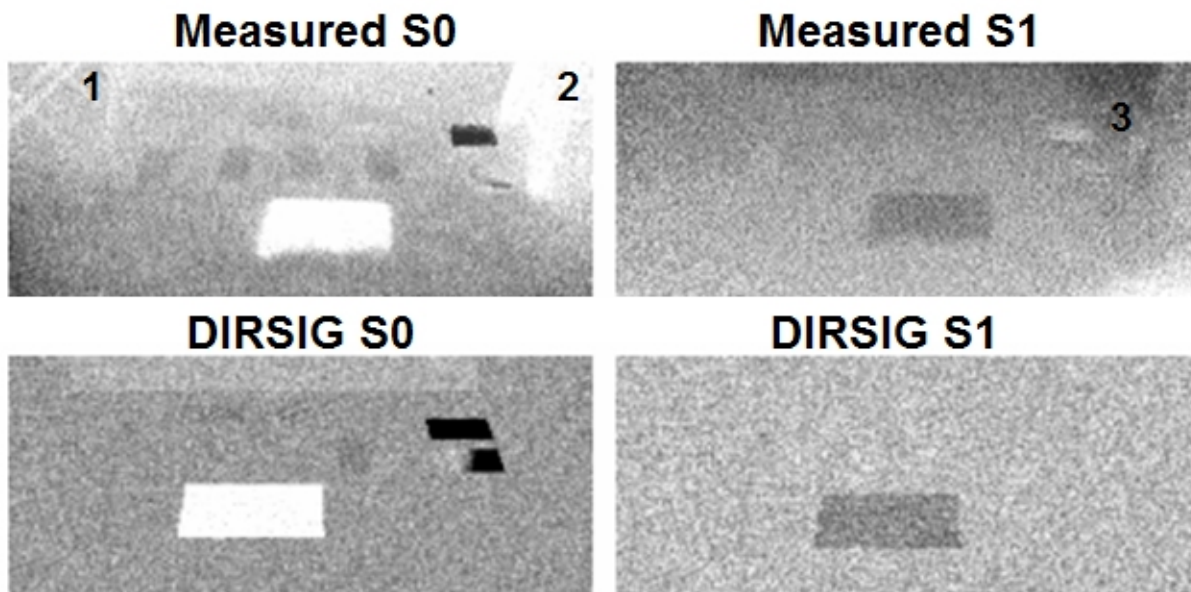


Figure H.2: Comparison of DIRSIG and measured thermal IR images of targets in backyard scene with a kiddie pool behind them

the polarimetric contrast in the measured image is due to the reflection of the downwelled sky radiance, hence the positive value. The polarized emissivity of the reflector targets were not measured within the scope of this work, and was therefore not simulated in the DIRSIG scenes.

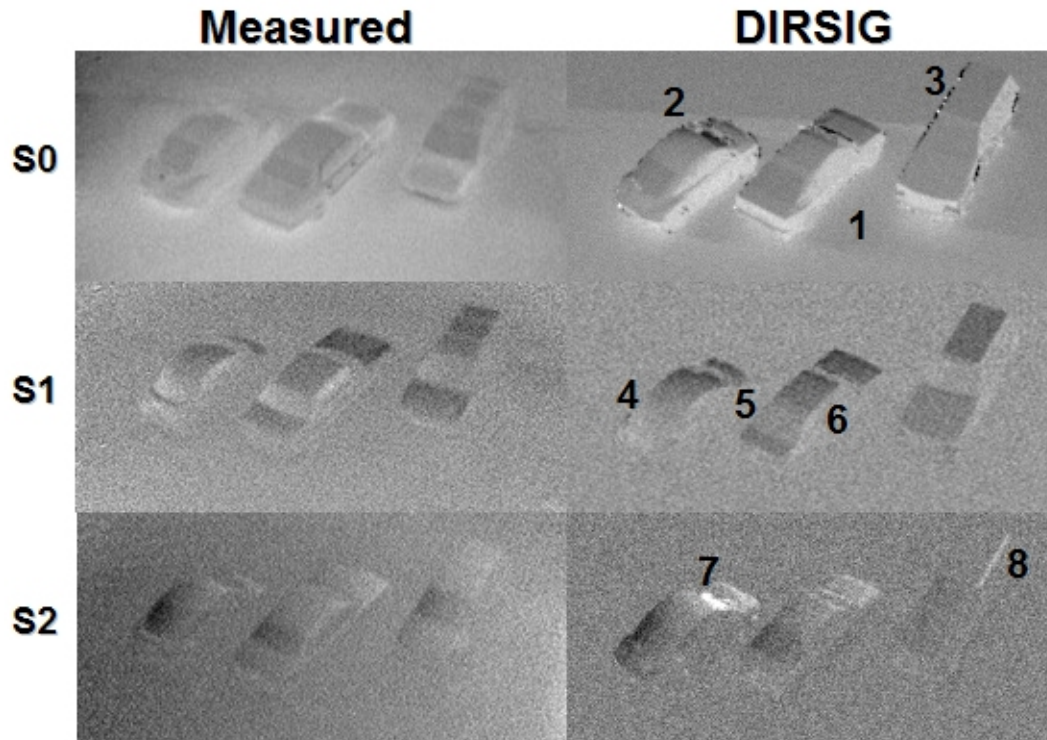


Figure H.3: Comparison of DIRSIG and measured thermal IR images of three automobiles on asphalt

## H.2 Car Scene

Figure H.3 compares the measured and DIRSIG simulation of the automobile scene.

1. Thermal shadows exist in the simulated scene that are not observed in the measured  $S_0$  image. It is likely that the Beetle and sedan arrived at a time closer to imaging compared to the SUV that has an obvious thermal shadow in the measured  $S_0$  image. Although DIRSIG has the capability to model objects leaving a scene before image time, I am not aware of being able to simulate the arrival of objects within a scene at specific times. Therefore, thermal shadows exist from the Beetle and sedan in the DIRSIG simulation that do not correspond to the measured data.
2. Grazing angle artifacts exist on the front windshield of the Beetle. It is likely that the origin of these artifacts is the lack of adequate background reflection sampling. This phenomenon was discovered during investigations leading to the results in Section 7.3.3. Although not presented it was found that Generic Rad Solver performance at grazing angles ( $\geq 85$  degrees) was poor due and likely due

to inadequate factorized representation of the polarized BRDF function.

3. Another grazing angle artifact on the side of the SUV. This could potentially be improved upon by oversampling the scene significantly, and then downsampling to the final image resolution.
4. The back windshield of the Beetle does not show the same level of brightening in the simulated  $S_1$  image compared to the measured  $S_1$  image. The source of this discrepancy may be inadequate modeling of the polarized emissivity of the glass. However the most likely reason for this difference is the difference in the geometric orientation of the back window. The back window is pointing (it's surface normal) more in the x-y plane in the measured image, while in the simulated DIRSIG image the back window seems to point more in the z direction (up).
5. The back windshield of the sedan does not show the same level of brightening in the simulated  $S_1$  image compared to the measured  $S_1$  image. The source of this difference is likely the same as for the previous item, a difference in the geometric orientation of the window between measured and simulated scenes.
6. There is some brightening along the sedan roof to sedan car side in the measured  $S_1$  image that does not exist in the simulated  $S_1$  image. The source of this discrepancy may be that the background reflections are entirely canceling the polarized  $S_1$  signature of the emitted polarization in the simulated scene, while in the measured scene there is a small region close to the roof of the sedan where the background reflections are not entirely canceling the emitted polarization signature. Another reason for the difference may be due entirely to a difference in measured geometry at the sedan roof to side interface (gradual) and simulated geometry at this interface (very quick, sharp transition).
7. Another grazing angle artifact that manifests itself as a bright  $S_2$  signature on the front windshield of the Beetle that does not exist in the measured  $S_2$  image. Although there appears to be a slight brightening in the measured image, it is no where near as strong as the simulated image shows.
8. Although not a grazing angle artifact, there is significant contrast existing in the simulated  $S_2$  image at the SUV roof to car side interface that appears to be due to how the SUV is modeled. Specifically, there is a single facet that serves as the transition between the roof and car side, whereas the actual SUV has a more gradual geometric transition resulting in a different  $S_2$  signature.

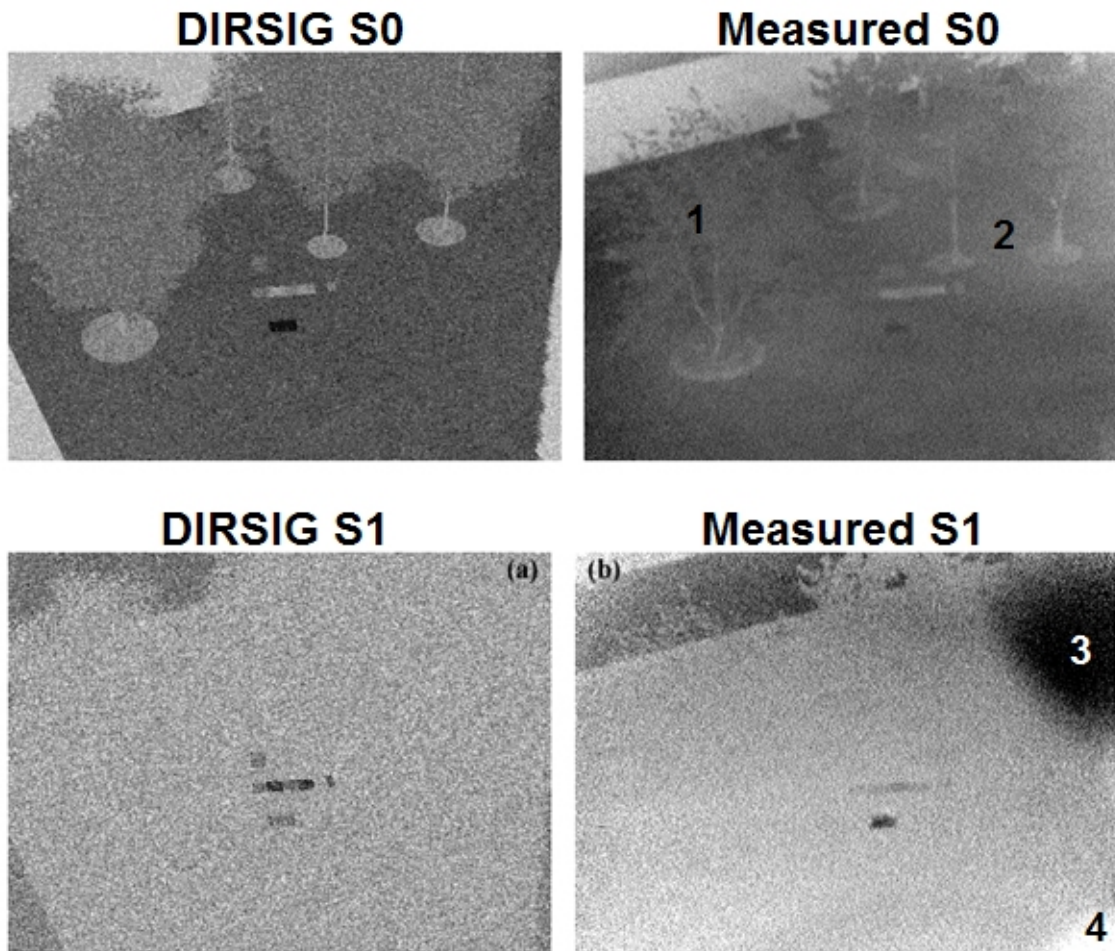


Figure H.4: Comparison of DIRSIG and measured thermal IR images of Building 76 target scene

### H.3 B76 Scene

Figure H.4 compares the measured and DIRSIG simulation of the building 76 target scene.

1. A notable difference between the measured and DIRSIG simulated  $S_0$  images is the level of foliage existing on the trees. The trees included with the DIRSIG simulated scene were leveraged from megascene and microscene for convenience.
2. Another notable difference is the  $S_0$  band brightening in the grass below each tree in the measured scene. In order to speed up the simulation time, the DIRSIG scene modeled the grass utilizing the Classic Emissivity property, (which did not appear to adequately capture the reflected tree radiance). Although this

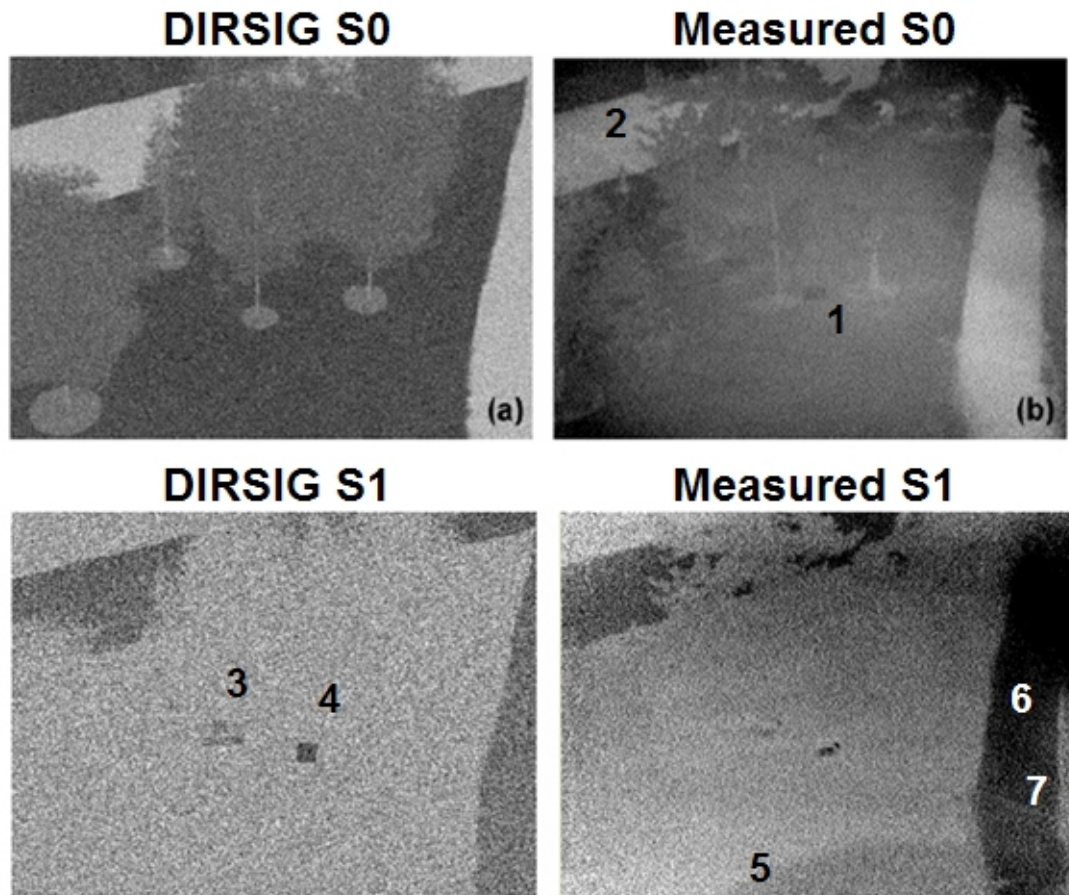


Figure H.5: Comparison of DIRSIG and measured thermal IR images of Building 76 target scene with targets embedded in trees

is a notable difference in the  $S_0$  band, there is no known effect in the  $S_1$  band and was therefore not considered significant enough to warrant modeling the grass utilizing the Generic Rad Solver and polarized BRDF.

3. An artifact due to the size of the wire grid polarizer (when angled towards the sky) relative to the camera aperture, not indicative of actual polarimetric contrast.
4. Another artifact due to the size of the wire grid polarizer relative to the camera aperture, again not indicative of actual polarimetric contrast.

Figure H.5 compares the measured and DIRSIG simulation of the building 76 target scene with targets embedded in trees.

1. Recent construction outside of building 76 (perhaps a pipe was laid) is obvious in the measured  $S_0$  image, but not modeled in the DIRSIG scene.
2. Recent construction that may be indicative of an underground pipe that is warmer than the ground. This was not modeled in the DIRSIG scene, as it was not deemed to have a significant impact of the polarimetric signatures in the scene.
3. The targets in the scene showed reduced polarimetric contrast relative to the same targets placed in the open (previous example Figure H.4). The DIRSIG simulated polarimetric contrast in the  $S_1$  band is slightly stronger for most of the targets compared to the actual measured  $S_1$  band, which may be due to one or both of the following: (1) dew on the target surfaces reducing the emitted polarized signature and/or (2) slight differences in the level of reflected background radiance between the modeled and measured scenes (the surrounding buildings were not included in the simulation, only the nearby trees).
4. There appears to be a specular reflection on the back half of the car hood that dampens the  $S_1$  signature significantly. This specular reflection (from one of the trees perhaps) is not adequately modeled in the DIRSIG scene and is likely due to a small difference in the placement of the trees in the scene and camera position.
5. An artifact resulting from the wire grid polarizer being slightly smaller than the camera aperture after it is tipped towards the sky (at about 45 degrees relative to camera aperture), therefore this is not indicative of actual polarimetric contrast.
6. An artifact resulting from the wire grid polarizer being slightly smaller than the camera aperture after it is tipped towards the sky (at about 45 degrees relative to camera aperture), therefore this is not indicative of actual polarimetric contrast.
7. A small amount of polarimetric contrast results from the possible underground pipe in the measured  $S_1$  band and is not modeled in the DIRSIG scene.

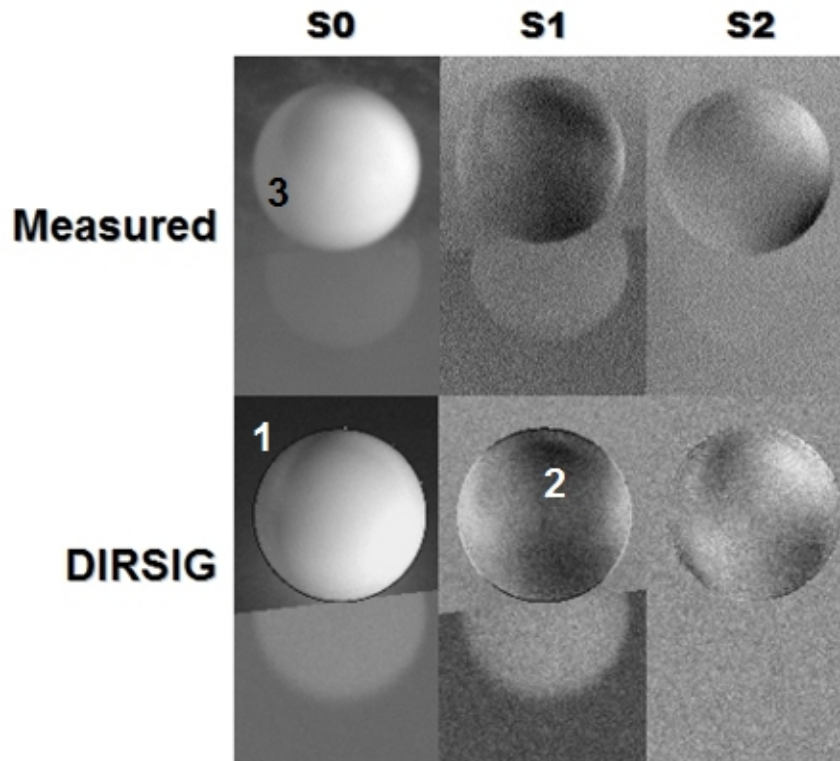


Figure H.6: Comparison of DIRSIG and measured thermal IR images of spheres during the day

## H.4 Spheres Scene

Figure H.6 compares the measured and DIRSIG simulation of spheres during the day.

1. A grazing angle artifact exists in the simulated  $S_0$  image that does not accurately represent the grazing angle response around the edge of the sphere in the measured  $S_0$  image.
2. Due to a larger than normal temporal difference between the collection of the I0 and I90 intensity images (utilized to derive the Stoke's images), there was actually some warming of the sphere surface between these two images. The result is the  $S_1$  image shows darkening over most of the sphere surface, not representing an actual polarimetric signature, but simply an artifact of the temporal nature of collecting the polarized images (the temperature of the sphere was changing). Therefore, the DIRSIG simulated  $S_1$  band was derived from two different DIRSIG simulations. The first simulation assumed the sphere was slightly colder when the I0 band was collected relative to the I90, I45, and I135

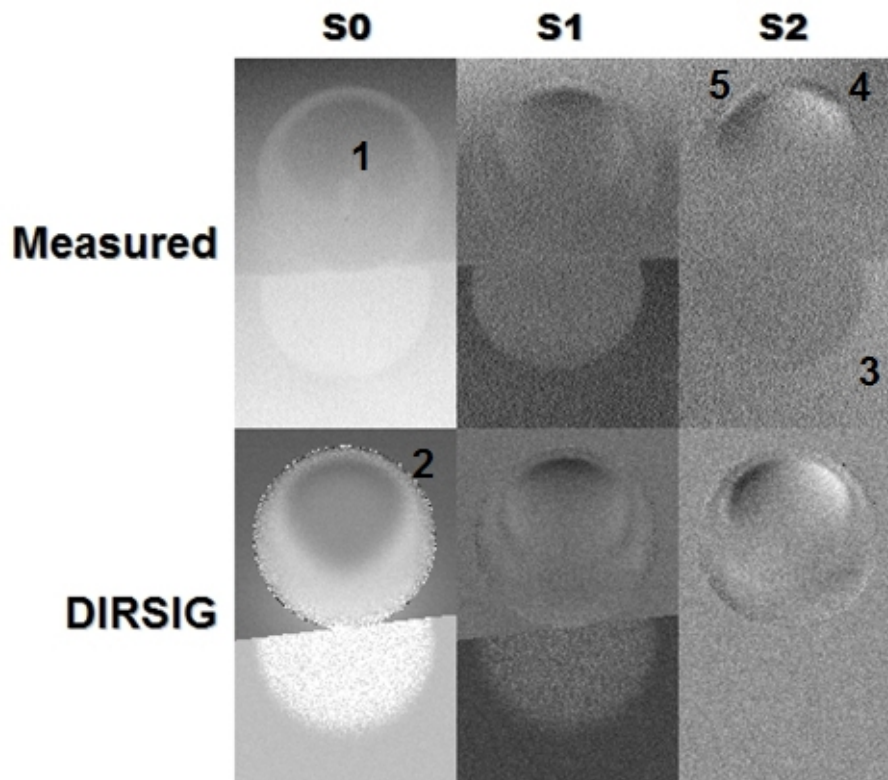


Figure H.7: Comparison of DIRSIG and measured thermal IR images of spheres at night

bands. The derived, simulated intensity bands were recombined into Stoke's images to simulate this effect.

3. It appears that the balance between the direct solar thermal load on the sphere surface and the background reflections were not exactly balanced in the simulated scene, resulting in a slight mismatch in the tones present in the simulated  $S_0$  image.

Figure H.7 compares the measured and DIRSIG simulation of spheres at night.

1. The reflection of the camera assembly and myself are visible in the center of the sphere in the measured  $S_0$  image, which is not modeled in the DIRSIG scene.
2. Similar to the daytime sphere scene, there are significant sampling artifacts in the simulated  $S_0$  band around the edge of the sphere.
3. There is a slight brightening on the right side of the reflecting panel in the measured  $S_2$  image that is not modeled in the DIRSIG  $S_2$  image. The origin

of this difference is likely due to reflection (we don't expect a  $S_2$  signature for thermally emitted radiance coming from a surface flat to the ground) of background radiance. The most significant source of background radiance included in the simulated scene was my house behind (but out of view) the sphere. So it is likely that the slight  $S_2$  signature noted on the right side of the panel is due to reflection of my house.

4. On the top right hand side of the sphere in the measured  $S_2$  image is a slight darkening at the very edge of the sphere. Most likely this darkening is due to reflection from my house, located behind the sphere. Although I did include my house in the simulated DIRSIG scene, the modeled temperature appears to be slightly too low compared to what would be required to generate the darkened nature at the edge of the top right hand side of the sphere.
5. On the top left hand side of the sphere in the measured  $S_2$  image is a slight brightening at the very edge of the sphere. Most likely this darkening is due to reflection from my house, located behind the sphere. Although I did include my house in the simulated DIRSIG scene, the modeled temperature appears to be slightly too low compared to what would be required to generate the brightened effect at the edge of the top left hand side of the sphere. I did try and increase the temperature of my house to generate this effect in the simulations, however the resulting phenomenology was not as what is observed in the measured  $S_2$  band. Most likely this effect was not modeled adequately due to the fact that currently the Generic Radiometry Solver is not modeling background reflections rigorously enough at grazing angles.

## H.5 DIRSIG Simulation Differences Summary

There were three main sources of differences between measured and DIRSIG simulated polarimetric thermal IR Stoke's images.

1. Inadequate sampling of background reflections by Generic Radiometry Solver at grazing angles. This is not a criticism of the Generic Radiometry Solver in DIRSIG, simply a realization of its limitations. This radiometry solver is not optimized for performance at grazing angles, but for fast and accurate performance for semi-diffuse materials at moderate scattering angles. Future development work may address and solve this issue.
2. Inadequate rigor in the modeled scene resulting in differences (primarily in the  $S_0$  images). In many cases, there were details in the scenes that were not modeled (such as the underground pipe in the Building 76 scene) due to the

fact that the level of effort required to implement outweighed the benefit of doing so.

3. Artifacts due to positioning and size of wire grid polarizer relative to the camera aperture were obvious in some the measured  $S_1$  and  $S_2$  bands, but not modeled in the DIRSIG simulations. The artifacts showed up as large dark and light areas around the edges of the scene.

# Bibliography

- [1] Alexander Berk et al, MODTRAN: A Moderate Resolution Model for LOWTRAN 7, Air Force Geophysics Lab, GL-TR-89-C122, April 1989.
- [2] N. Bruce, Calculations of the Mueller matrix for scattering of light from two-dimensional surfaces, *Waves in Random Media*, v8, pages 15-28, 1998.
- [3] F. Cremer, W. Jong, K. Schutte, Infrared polarization measurements and modeling applied to surface-laid antipersonnel landmines, *Optical Engineering*, v41 n5, pages 1021-1032, May 2002.
- [4] M. Duggin, G. Kinn, Vegetative target enhancement in natural scenes using multi-band polarization methods, *Proceedings of SPIE*, v4481, pages 281-291, 2002.
- [5] Adam Goodenough, CDGenericRadSolver Technical Brief, DIRS 05/06-1978-170, May 2006.
- [6] Matthew Fetrow et al, Results of a new polarization simulation, *Proceedings of the SPIE*, v4481, pages 149-162, 2002.
- [7] Matthew Fetrow, MODTRAN4-P: Developing a polarized version of MODTRAN, AFRL, Limited distribution, 2003.
- [8] Goran Forssell, Surface landmine and tripwire detection using calibrated polarization measurements in the LWIR and SWIR, *Subsurface and Surface Sensing Technologies and Applications III, Proceedings of SPIE Vol. 4491*, pages 41-51.
- [9] Michael Gartley *PhD Dissertation Proposal*, Rochester Institute of Technology, Center for Imaging Science, 2004.
- [10] Eugene Hecht, *Optics*, Addison-Wesley, 2nd Edition, 1987.
- [11] D. L. Jordan and G. Lewis, Measurements of the effect of surface roughness on the polarization state of thermally emitted radiation, *Optics Letters*, v19, n10, pages 692-694, May 1994.

- [12] D. L. Jordan, G. D. Lewis, and E. Jakeman, Emission polarization of roughened glass and aluminum surfaces, *Applied Optics*, v35 n19, pages 3583-3590, July 1996.
- [13] Jason Lawrence et al, Efficient BRDF importance sampling using a factored representation, *ACM Trans. Graph.*, v23 n3, pages 496-505, 2004.
- [14] Raymond Lee, Digital imaging of clear sky polarization, *Applied Optics*, v37 n9, pages 1465 - 1476, March 1998.
- [15] Yi Liu, Kenneth Voss, Polarized radiance distribution measurement of skylight. II. Experiment and data, *Applied Optics*, v36 n33, pages 8753-8764, November 1997.
- [16] J. R. Maxwell, J. Beard, S. Weiner, D. Ladd, and S. Ladd. Bidirectional reflectance model validation and utilization. Technical Report AFAL-TR-73-303, Environmental Research Institute of Michigan (ERIM), October 1973.
- [17] Jason P. Meyers *PhD Dissertation*, Rochester Institute of Technology, Center for Imaging Science, 2002.
- [18] Nonconventional Exploitation Factors (NEF) Modeling, NMA NEFmod9.4, July 2004.
- [19] C. Nguyen (Editor), Subsurface and Surface Sensing Technologies and Applications III, *Proceedings of SPIE Vol. 4491* (2001).
- [20] Mark Pesses and John Tan, Simulation of LWIR Polarimetric Observations of Space Objects, *Proceedings of the 31st Applied Imagery Pattern Recognition Workshop*, 2002.
- [21] Richard G. Priest and Thomas A. Germer. Polarimetric BRDF in the microfacet model: Theory and measurements. In *Proceedings of the 2000 Meeting of the Military Sensing Symposia Specialty Groupon Passive Sensors*, volume 1, pages 169181. Infrared Information Analysis Center, Ann Arbor, MI, 2000.
- [22] Richard G. Priest and Steven R. Meier. Polarimetric microfacet scattering theory with applications to absorptive and reflective surfaces. *Optical Engineering*, 41(5):988993, May 2002.
- [23] Timothy Rogne, Frederick Smith, James Rice, Passive target detection using polarized components of infrared signatures, *Proceedings of the SPIE*, v1317, pages 232-251.

- [24] Sadjadi, Passive polarimetric IR target classification, IEEE Transactions on Aerospace and Electronic Systems, v37 n2, pages 740-751, Apr 2001.
- [25] Firooz A. Sadjadi and Cornell S. L. Chun, *Optical Engineering*, v43 n10, pages 2283-2291, October 2004.
- [26] John R. Schott *Remote Sensing: The Image Chain Approach*, Oxford University Press, 1996.
- [27] Raymond Serway, *Physics for Scientists and Engineers*, 3rd Ed., Saunders College, 1990.
- [28] Joseph A. Shaw, Infrared Polarization in the Natural Earth Environment, pages 129-138, SPIE v4819, 2002.
- [29] James R. Shell *PhD Dissertation*, Rochester Institute of Technology, Center for Imaging Science, 2005.
- [30] M. Tamura et al, Infrared Polarization Signatures of Star Forming Regions, *The Astrophysical Journal*, v378, pages 611-627, September 10, 1991.
- [31] K.E. Torrance and E. M. Sparrow, Theory for off-specular reflection from roughened surfaces, *Journal of the Optical Society of America*, v57, n9, pages 1105-1114, 1967.
- [32] J. Scott Tyo et al, Review of passive imaging polarimetry for remote sensing applications, *Applied Optics*, v45 n22, pages 5453-5469, August 2006.
- [33] Lawrence Wolff, Andrew Lundberg, Renjie Tang, Image understanding from thermal emission polarization, IEEE, pages 625-631, 1998.
- [34] J. Young, H. Graham, E. Peterson, Wire Grid Infrared Polarizer, *Applied Optics*, v4 n8, p1023-1026, August 1965.
- [35] Electromagnetic Spectrum, [http://en.wikipedia.org/wiki/Electromagnetic\\_spectrum](http://en.wikipedia.org/wiki/Electromagnetic_spectrum), Feb 2007.
- [36] Indices of Refraction, [http://en.wikipedia.org/wiki/List\\_of\\_indices\\_of\\_refraction](http://en.wikipedia.org/wiki/List_of_indices_of_refraction), Feb 2007.
- [37] Moxtek General Information Datasheet, [http://www.moxtek.com/uploads/Gen\\_Data\\_Sheet\\_\(w](http://www.moxtek.com/uploads/Gen_Data_Sheet_(w) April 2007.
- [38] Polarization of Light, <http://en.wikipedia.org/wiki/Polarization>, Feb 2007.

- [39] Specific Heat Capacity, [http://en.wikipedia.org/wiki/Specific\\_heat\\_capacity](http://en.wikipedia.org/wiki/Specific_heat_capacity), Feb 2007.
- [40] Louis Keiner, Electromagnetic Spectrum, <http://en.wikipedia.org/wiki/Image:Electromagnetic-Spectrum.png>, Feb 2007.
- [41] Thermal Conductivity, [http://en.wikipedia.org/wiki/Thermal\\_conductivity](http://en.wikipedia.org/wiki/Thermal_conductivity), Feb 2007.
- [42] Wave-particle duality, [http://en.wikipedia.org/wiki/Wave-particle\\_duality](http://en.wikipedia.org/wiki/Wave-particle_duality), March 2007.